A NEAR-ZONE TO FAR-ZONE TRANSFORMATION PROCESS UTILIZING A FORMULATED EIGENFUNCTION EXPANSION OF SPHEROIDAL WAVE-HARMONICS

Gerald F. Ricciardi

Dissertation submitted to the Faculty of the
Virginia Polytechnic Institute and State University
in partial fulfillment of the requirements for the degree of

Doctor of Philosophy
in
Electrical Engineering

Dr. Warren L. Stutzman, Chair
Dr. William A. Davis
Dr. Sedki M. Riad
Dr. John F. Rossi
Dr. Ahmad Safaai-Jazi

September 21, 2000
Blacksburg, Virginia

Keywords: computational electromagnetics, eigenfunctions, FDTD, antennas

A NEAR-ZONE TO FAR-ZONE TRANSFORMATION PROCESS UTILIZING A FORMULATED EIGENFUNCTION EXPANSION OF SPHEROIDAL WAVE-HARMONICS

Gerald F. Ricciardi

(ABSTRACT)

In the field of antenna design and analysis, often the need arises to numerically extrapolate the far-zone performance of a radiating structure from its known (or assumed known) near-zone electromagnetic field. Mathematical processes developed to accomplish such a task are known in the literature as near-zone to far-zone transformations (NZ-FZTs) as well as near-field far-field (NF-FF) transformations. These processes make use of sampled near-zone field quantities along some virtual surface, viz., the transformation surface, that surrounds the radiating structure of interest. Depending upon the application, samples of the required near-zone field quantities are supplied via analytical, empirical, or computational means.

Over the years, a number of NZ-FZT processes have been developed to meet the demands of many applications. In short, their differences include, but are not limited to, the following: (1) the size and shape of the transformation surface, (2) the required near-zone field quantities and how they are sampled, (3) the computational methodology used, and (4) the imbedding of various application-driven features. Each process has its pros and cons depending upon its specific application as well as the type of radiation structure under consideration.

In this dissertation we put forth a new and original NZ-FZT process that allows the transformation surface along which the near-zone is sampled to be spheroidal in shape: namely a prolate or oblate spheroid. Naturally, there are benefits gained in doing so. Our approach uses a formulated eigenfunction expansion of spheroidal wave-harmonics to develop two distinct, yet closely related, NZ-FZT algorithms for each type of spheroidal transformation surface. The process only requires knowledge of the E-field along the transformation surface and does not need the corresponding H-field.

Given is a systematic exposition of the formulation, implementation, and verification of the newly developed NZ-FZT process. Accordingly, computer software is developed to implement both NZ-FZT algorithms. In the validation process, analytical and empirical radiation structures serve as computational benchmarks. Numerical models of both benchmark structures are created by integrating the software with a field solver, viz., a finite-difference time-domain (FDTD) code. Results of these computer models are compared with theoretical and empirical data to provide additional validation.

The highest result of education is tolerance.

Helen Keller (1880-1968)

ACKNOWLEDGMENTS

First and foremost, I need to thank God; for without divine inspiration and guidance, none of this work would have been possible.

Special thanks to my Ph.D. dissertation advisor, Professor Warren L. Stutzman, for allowing me to conduct this endeavor under his tutelage. It was through his patience and understanding that this research was able to be completed. I have truly benefited from his valuable technical advice throughout my studies here at Virginia Tech.

I would like to thank all of my Ph.D. committee members: Professor William A. Davis, Professor Sedki M. Riad, Professor John F. Rossi, and Professor Ahmad Safaai-Jazi. I appreciate the time and effort they put forth in serving on my committee. Over the years, all of them have contributed greatly to my growth academically and as a researcher; for that, I am truly grateful.

I wish to thank Naval Research Laboratory for furnishing the necessary formal reports that were key to the development of the spheroidal special function routines.

With regard to the microstrip patch antenna used as our empirical benchmark, I would be remiss if I did not acknowledge the following institutions and people that were instrumental to its development: Rogers Corporation, for donating the costly Duroid substrate material (their support of pure research should be commended); Randall Nealy, for fabricating and testing the microstrip antenna at Virginia Tech; and NASA Langley and Dr. Dave Shively, for providing the second set of pattern data.

I am deeply indebted to Dr. Boris Davidson and Matt Monkevich, who have consistently supported me during the most trying of times. At certain points, it was their friendship and sincerity that enabled me to continue with this work. In addition, I must also thank Boris for technically reviewing Chapter 2; his comments and suggestions are much appreciated.

Further, I must express my gratitude to Bernie Michaels for his much-needed assistance in preparing this document for electronic submission.

On a personal note, I would like to thank my parents and my family for always being there. And finally, I owe a heartfelt thank-you to my love, Suzanne, for her years of patience, sacrifice, support, and understanding throughout this long and arduous journey.

TABLE OF CONTENTS

CHAPTER 1. INTRODUCTION

In the field of antenna design and analysis, often the need arises to numerically extrapolate the far-zone performance of a radiating structure from its known (or assumed known) near-zone electromagnetic field. Mathematical processes developed to accomplish such a task are most popularly known in the literature as near-zone to far-zone transformations (NZ-FZTs) as well as near-field far-field (NF-FF) transformations. In general, most transformations make use of sampled near-zone field quantities along some particular closed surface that completely encloses the radiating structure of interest. Samples of the required near-zone field quantities are then supplied via analytical, empirical, or computational means. Yet, other transformations only use near-zone field samples along certain portions of a closed surface where the source of radiation is considered most concentrated; consequently, the near-zone quantities along the other less-contributory portions of the closed surface are approximated as zero. Either way, the far-zone response of the radiating structure is then computed from the sampled near-zone data using a numerical process that is well-rooted in electromagnetic theory. Throughout our discussion we shall refer to this virtual surface along which the near-zone field quantities are sampled as the transformation surface.

Over the years, a number of NZ-FZT processes have been developed to meet the demands of many different applications. For the most part, the differences in these processes include, but are not limited to, the following: (1) the size and shape of the transformation surface, (2) the required near-zone field quantities and the manner in which they are sampled, (3) the computational methodology used, and (4) the imbedding of various application-driven features into the NZ-FZT process. Each of the developed processes has its advantages and disadvantages depending upon its specific application as well as the type of radiation structure under consideration.

The thrust of this dissertation is to put forth a new and original NZ-FZT process that allows the transformation surface along which the near-zone is sampled to be spheroidal in shape: namely a prolate or oblate spheroid. Naturally, there are benefits

gained in doing so. Our approach makes use of a formulated eigenfunction expansion of spheroidal wave-harmonics to develop two distinct, yet closely related, NZ-FZT algorithms for each type of spheroidal transformation surface. Throughout this dissertation, we provide a systematic exposition of the formulation, implementation, and verification of our newly developed NZ-FZT process, as well as a demonstration of a novel application. Implementation of both algorithms involves the development of computer software able to carry out the entire NZ-FZT process from start-to-finish in a computationally efficient manner. Not only must this software include the calculation of the formulated eigenfunction expansion, but also the much difficult numerical evaluation of all required special functions. Remarkably, the process is quite practical from a numerical viewpoint in that it is able to be hosted in its entirety on an IBM compatible personal computer.

Verification and performance assessment of the new algorithms require the development of both an analytical and an empirical radiation structure to use as computational benchmarks. First, a proof-of-concept of the NZ-FZT process is achieved by seeing how well the algorithms are able to compute the far-zone of the analytical benchmark. The developed computer software is then integrated with a computational electromagnetic field solver (an additional piece of developed software) in order to create numerical models of both benchmark structures. Ultimately, results from these original computer models are compared with respective theoretical and empirical data to provide additional validation of our NZ-FZT process. Lastly, we would like to point out that although the joining of the newly developed NZ-FZT process with a computational electromagnetic field solver demonstrates one particular application of this work, the significance of this research is much more far-reaching and has yet to be explored.

1.1 BRIEF OVERVIEW OF NZ-FZT RESEARCH AND DEVELOPMENT

First, we would like to make it clear that it is not our intention to provide another exhaustive account of NZ-FZT research and development: for that, we refer the reader to the comprehensive survey articles by Johnson *et al.* [1] and Yaghjian [2]. Both of these works provide an excellent compendium of the many NZ-FZT methods with respect to their chronological development. Included in these seminal papers are the underlying theories behind each of the techniques as well as their various advantages and limitations. However, we shall delve briefly into the history of NZ-FZT methods so as to gain some contextual understanding of our newly developed NZ-FZT process.

Much of the research in this area is driven by the need to determine far-zone antenna patterns from measurements made in the near-zone. Often it is impractical or impossible to measure radiation patterns of an antenna on a conventional far-field range. Reasons for this difficulty can include, but are not limited to, the following: the distance to the far-zone may be too long for a given far-field range; or it may be just downright impractical to move the antenna from its operating environment to an antenna range [1]. For these and other reasons, it is this particular application that spawned initial development of NZ-FZT techniques and subsequently led to development of near-field antenna ranges.

According to [2], Richmond and Tice [3], [4] in 1955 put forth the earliest papers to research computation of far-zone radiation patterns from near-zone measurements. Their investigation used air and dielectric-filled open-ended rectangular waveguide probes for measuring the near-zone of microwave antennas; the calculated far-zone fields were then compared with those measured directly. Later, Kerns [5] used plane-wave analysis to predict the far-zone radiation pattern from near-zone data for a planar transformation surface and included probe compensation to account for the presence of the probe. Although sampling of fields along a planar transformation surface is usually conducted over a rectangular grid, Rahmat-Samii, Galindo-Israel, and Mittra [6] describe

an alternative NZ-FZT process that allows the sampling along the planar surface to occur using a plane-polar grid; the transformation is formulated in terms of a Jacobi-Bessel series expansion. Additionally, Williams and Rahmat-Samii [7] developed another NZ-FZT process that uses a bi-polar grid to sample the planar transformation surface. In 1961, Brown and Jull [8] put forth a two-dimensional NZ-FZT for a cylindrical transformation surface (no dependence on the z-coordinate) in which the radiating field is expanded in terms of cylindrical wave functions. However, it was not until Leach and Paris [9] of the Georgia Institute of Technology that the NZ-FZT theory for sampling the near-zone along a cylindrical surface was fully extended to three dimensions. Jensen [10] of the Technical University of Denmark developed a NZ-FZT for a spherical transformation surface that expands the radiating field in terms of spherical wave functions. Similarly, James and Longdon [11] describe an alternative method that obtains the expansion of spherical wave functions from measurements of the radial component of the E- and H-fields over the spherical transformation surface. Beyond just the theory, several institutions have also been extensively involved with the actual design and implementation of near-field ranges (including practical considerations): the National Institute of Standards and Technology (formerly the National Bureau of Standards) [12]; Georgia Institute of Technology [13]; the Technical University of Denmark [14]; and University of California, Los Angeles [15].

Although initial NZ-FZT research stemmed from the development of near-field ranges, these methods have continued to find their way into a host of other applications that are just too numerous to mention. However, we shall cite a few of these applications so as to illustrate the widespread use of NZ-FZT methods. While developing design techniques for Cassegrainian-fed paraboloids, Ludwig [16] formulated an inverse NZ-FZT for a spherical transformation surface that uses an expansion of spherical wave functions to transform the far-zone pattern of a given feed antenna to its respective near-zone pattern. In the same vein, Lee *et al.* used an inverse NZ-FZT for a planar transformation surface to locate defective elements in an array antenna [17]. Rahmat-Samii and Lemanczyk [18] made use of a NZ-FZT process to determine surface distortion

profiles of a parabolic reflector antenna. Moreover, NZ-FZT methods have also found their way into the realm of computational electromagnetics. Specifically, Taflove and Umashankar [19], [20] used the finite-difference time-domain (FDTD) method coupled with a NZ-FZT method based on field equivalence theory to analyze electromagnetic scattering from complex objects. Later, Luebbers *et al.* [21] expanded this particular approach to carry out the NZ-FZT in the time-domain. As one can see, NZ-FZT methods have and continue to play a significant role in the field of antenna design and analysis.

1.2 MOTIVATION FOR THE NEWLY DEVELOPED NZ-FZT PROCESS

One advantage that NZ-FZT methods with a spherical transformation surface have over those that are cylindrical and planar based is the ability to provide full coverage of the far-zone radiation pattern (i.e., in all directions). In general, methods that employ a planar transformation surface are confined to determining the fields within the forward solid angular region subtended by the edges of the radiating structure and the finite sampling area; consequently, there is limited sidelobe information and no backlobe information [2]. Similarly, NZ-FZT methods that use a cylindrical transformation surface must exclude the biconical angular region formed by the outer edges of the radiating structure and the cylindrical sample area of finite height; accordingly, sidelobe information is not available in the far-zone region that corresponds to the top and bottom of the cylindrical surface [2].

On the flip side, the spherical transformation surface must have a radius that is large enough to enclose the radiating structure of interest. For structures that are roughly the same size in all three Cartesian dimensions, the spherical transformation surface is, by nature, quite appropriate. In these instances, the near-zone is sampled (along the sphere) at distances from the structure that are more or less on the same order. Unfortunately, in cases where the radiating structure is planar or linear in shape, sampling of the near-zone must occur at some points (along the sphere) that are relatively distant from the radiating

structure. Depending upon the application, not being able to sample the fields close to the radiating structure may pose some difficulties. This lack in capability is one of the reasons why NZ-FZT methods based on planar and cylindrical transformation surfaces are often better suited for planar and linear radiating structures, respectively, than their spherical based counterparts.

All told, we desire a NZ-FZT process for linear and planar structures that is able to deliver the best of both worlds: full coverage of the far-zone radiation pattern while allowing all of the near-zone samples to remain close to the radiating structure. Toward this end, we consider geometrically *stretching* and *squashing* the spherical transformation surface into prolate and oblate spheroids, respectively. The advantage of doing so is that these particular transformation surfaces are capable of closely conforming to both linear and planar types of radiating structures: the prolate spheroid is better suited for linear structures (e.g., a dipole antenna), and the oblate spheroid is better suited for planar structures (e.g., a microstrip patch antenna). In essence, the spheroidal surface affords an extra degree of freedom over its spherical counterpart, thus providing the user with added control over the shape of the transformation surface. (Note that a sphere requires only one parameter, i.e., its radius, to describe its geometry; both the prolate and oblate spheroid require two parameters. This difference in specification follows because the sphere is actually a degenerate case of the spheroid.)

As we can see, developing a NZ-FZT process that employs a prolate and oblate spheroidal transformation surface can be extremely beneficial. However, Yaghjian [2] states that it is impractical to find the necessary dyadic Green's function for transformation surfaces that do not support orthogonal vector wave functions. Morse and Feshbach [22] show that there are only six coordinate systems that support orthogonal vector wave solutions: Cartesian, circular cylinder, spherical, elliptic cylinder, parabolic cylinder, and conical. Much to our chagrin, the two coordinate systems that are best suited to describe both spheroidal transformation surfaces, namely prolate spheroidal and oblate spheroidal, are not among these six special coordinate systems. Nevertheless, both spheroids (prolate and oblate) can still be made to successfully serve as transformation

surfaces despite not being able to support orthogonal vector wave functions. As we shall see in Chapter 2, our newly developed NZ-FZT process gets around this roadblock by employing a differential equation approach that solves the three-dimensional vector Helmholtz equation using a hybrid of coordinate systems.

Finally, we address the methodology behind the formulation of our newly developed NZ-FZT process. Although a much simpler NZ-FZT process for a spheroidal transformation surface could have been developed based on field equivalence theory, a major drawback of this approach is that it would require knowledge of both E- and H-fields along the transformation surface. The advantage of formulating our NZ-FZT process in terms of an eigenfunction expansion of spheroidal wave-harmonics is that only one of the two fields along the transformation surface has to be known, not both. Naturally, this reduction in informational content of the input to the NZ-FZT process can prove to be quite indispensable depending upon the application.

1.3 ORGANIZATION OF DISSERTATION

Essentially, the dissertation is divided into two parts. Chapters 2, 3, and 4 address the formulation and computational implementation of the newly developed NZ-FZT process. Thereafter, Chapters 5, 6, and 7 form the second part of this work that focuses on providing analytical and empirical validation of our spheroidal based NZ-FZT process. Lastly, Chapter 8 provides summary and conclusions of the research.

In detail, Chapter 2 discusses the formulation of the theory and algorithmic implementation of the newly developed NZ-FZT process. The first part of the chapter gives a detailed system overview of the NZ-FZT process and explicitly describes what the process actuality does. The remainder of the chapter presents a full discourse on the development of the computational algorithms along with all of the supporting electromagnetic theory. In addition, the appendices at the end of the document provide the necessary mathematical background that is key to the formulation of our NZ-FZT process.

Chapter 3 is devoted to the numerical evaluation of all required special functions associated with the eigenfunction expansion of spheroidal wave-harmonics. It addresses the details and issues regarding the development of numerical routines able to calculate these much involved special functions (i.e., while operating in the context of a working computational algorithm). Because this chapter can be read, for the most part, independently of the others, it is our hope that it provides the interested reader with some of the best ways to go about evaluating these complicated special functions (with regard to both accuracy and computational efficiency).

Chapter 4 addresses the formation of computer software based on our newly developed NZ-FZT process. Our software package employs the algorithms developed in Chapter 2 along with the special function routines developed in Chapter 3. In detail we examine the top-down design of the coded software and discuss the organization and particulars of its various constituent modules.

In Chapter 5, we provide a proof-of-concept of our NZ-FZT process by making use of an analytical benchmark. The selected radiating structure has electromagnetic fields that are analytically known in both the near- and far-zone regions. Accordingly, a software driver is written to sample the near-zone of our analytical benchmark along a user specified spheroidal transformation surface. Afterwards, the set of sampled near-zone data is able to be processed by the NZ-FZT software developed in Chapter 4. Ultimately, validation of the NZ-FZT process (and the software) is achieved by conducting a series of numerical tests that compares the algorithmic results with analytical (theoretical) results for an assortment of spheroidal transformation surfaces.

Chapters 6 and 7 have been included to provide further validation of our NZ-FZT process together with a successful demonstration of its application. First, Chapter 6 concentrates on developing a computational electromagnetic field solver, viz., a FDTD computer code, that is able to model the near-zone of a given radiating structure. Naturally, the field solver is designed to interface with the NZ-FZT software package developed in Chapter 4. Subsequently, an end-to-end test of the combined software is conducted using a computational model of our analytical benchmark (of Chapter 5) in

order to validate the overall coupled process. In Chapter 7, we use the combined software to model an empirical benchmark radiating structure that has been fabricated and then pattern tested at both NASA Langley and Virginia Tech. Additional validation of our NZ-FZT process is achieved by comparing the results from our computer simulation with the far-zone radiation patterns measured at both test facilities.

CHAPTER 2. FORMULATION OF THE THEORY AND ALGORITHMIC IMPLEMENTATION OF THE NEWLY DEVELOPED NEAR-ZONE TO FAR-ZONE TRANSFORMATION PROCESS

As previously stated, the aim of our developed NZ-FZT process is to extrapolate the far-zone of a radiating structure from near-zone field samples positioned along a spheroidal transformation surface. Specifically, the input to our process only requires the near-zone field samples to be of the time-harmonic E-field (that is, knowledge of its corresponding H-field is not required). Once supplied with this information, the NZ-FZT process is then able to determine the desired time-harmonic far-zone response. Because the process operates in the frequency-domain, all field quantities throughout the ensuing formulation are in time-harmonic form and thus suppress the $e^{j\omega t}$ time dependence.

A differential equation approach is taken in the development of our NZ-FZT process. The approach first requires us to pose boundary value problems that describe the physical process. The particular solution to each of these boundary value problems is then constructed using a suitable expansion of eigenfunctions. Ultimately, the formulated prolate and oblate spheroidal NZ-FZT algorithms use these eigenfunction expansions to compute the far-zone response. It is the objective of this chapter to present the theory and the algorithmic details behind the development of this new NZ-FZT process.

Throughout this development we shall observe that the formulations for both the prolate and oblate transformation surfaces closely parallel one another. Accordingly, it stands to reason to develop both formulations concurrently throughout this chapter. This is done in a step-by-step fashion by first stating equations and figures for the prolate case and then following them with their respective oblate counterpart. Both parallel sets of equations and figures share the same numbering with the only difference being an appended suffix, viz., an “a” or “b,” to distinguish between the prolate and oblate cases, respectively. For the sake of brevity, at some points in the development we choose to discuss only the prolate case since both spheroidal cases closely resemble one another.

Consequently, some of the prolate equations are not paired with their oblate counterpart. If need be, these omitted expressions pertaining to the oblate case can be easily derived from their disclosed prolate counterparts. Nevertheless, in these particular instances, we shall maintain the same numbering system and apply the appended suffix “a” to these prolate equations and figures even though their oblate counterparts have been excluded.

Lastly, it must be stated that the findings presented in this dissertation are application driven in nature. These results are directed toward applied physicists and engineers practicing computational electromagnetics, and not pure mathematicians. Accordingly, in the formulation that follows, the existence of solutions, completeness of sets of functions, and permissibility of interchanging order of integration operators and infinite summations (i.e., termwise integration) are all presumed, not demonstrated.

2.1 DETAILED SYSTEM OVERVIEW OF THE NZ-FZT PROCESS

2.1.1 NZ-FZT Process Input (Transformation Surfaces and Required Near-Zone Fields)

The first step in the development of any computational algorithm that approximates a given physical system is to understand the details regarding the system excitation (input) and the system response (output). Here, we examine the input information required to implement this new NZ-FZT process. Understanding the input to the process calls for descriptions of the transformation surfaces and the required near-zone fields. Regarding the desired output response, the section that immediately follows this one addresses its specific details.

For reasons beforehand mentioned in Chapter 1, there are advantages to choosing the transformation surface as either a prolate or oblate spheroid. In doing so, these surfaces must first be defined in their respective curvilinear coordinate systems along with their relation to Cartesian coordinates. In short, we shall briefly describe the details of both the prolate and oblate spheroidal coordinates that are immediately required.

However, the reader is referred to Appendix A for additional details regarding both of these closely related coordinate systems.

It must be stated that unlike the Cartesian and spherical coordinate systems, the pair of spheroidal coordinate systems does not universally conform to a conventional definition and notation. Consequently, one must be careful to avoid the pitfalls associated with inconsistent definitions and notations when using formulated results from multiple sources. Generally speaking, both the prolate and oblate spheroidal coordinate systems are generated by revolving the two-dimensional elliptic curvilinear coordinate system (where the orthogonal coordinates are comprised of a family of confocal ellipses and hyperbolas) about either the major axis (prolate case) or the minor axis (oblate case) of the confocal ellipses. Unfortunately, the lack of a single definition for the spheroidal coordinate system occurs because multiple versions exist that are able to satisfy this requirement.

Upon review of the various versions of spheroidal coordinate systems, we found that there are essentially two degrees of freedom responsible for creating the differences: the orientation of the family of ellipses (which determines the axis of revolution) and the reference axis (or plane) of the angular coordinate. Both Flammer [23], Morse and Feshbach [22], and Tai [24] define the z-axis as the axis of revolution for both the prolate and oblate spheroidal coordinate systems. As for *AMS-55* [25], the axis of revolution is defined as the x-axis in the prolate case and the y-axis in the oblate case. Although sources [22]-[24] remain consistent and designate the z-axis as the reference of the angular coordinate for the prolate spheroidal coordinate system, this is not the case for its oblate counterpart. Specifically, Tai [24] designates the x-y plane (effectively the ρ-axis) as the reference for the angular coordinate for the oblate spheroidal coordinate system; meanwhile, Flammer [23] and Morse and Feshbach [22] both retain the z-axis as the angular coordinate reference.

As we have shown, there are multiple definitions of the prolate and oblate spheroidal coordinate systems. In order to continue, we must select a pair of spheroidal coordinate systems that is best suited for our particular application: namely, the pair of

spheroidal coordinate systems defined by Flammer [23] and Morse and Feshbach [22]. First, since we are dealing with antenna radiation, it is beneficial to remain consistent with the practices of antenna theory and choose the z-axis as both the reference axis of the angular coordinate and the preferred axis of revolution. Second, this choice of reference axis (for the angular coordinate) remains consistent with spherical coordinates, which also defines its polar angle with respect to the z-axis. As we shall see later on in our discussion, having the spheroidal and the spherical coordinate systems share the z-axis as the preferred axis will prove to be convenient when relating these coordinate systems. Finally, most of the existing work on spheroidal wave functions is defined in terms of the z-axis preferred spheroidal coordinate system. Although this existing work can be made to account for another preferred axis, doing so has no apparent benefits.

The prolate and oblate spheroidal coordinate systems, shown in Figures 2.1a and 2.1b, respectively, are related to Cartesian coordinates by the following transformations [23]:

Prolate:
$$x = a\sqrt{\xi^2 - 1}\sqrt{1-\eta^2}\cos\varphi = a\sqrt{\xi^2 - 1}\sin\vartheta\cos\varphi \tag{2-1a}$$

$$y = a\sqrt{\xi^2 - 1}\sqrt{1-\eta^2}\sin\varphi = a\sqrt{\xi^2 - 1}\sin\vartheta\sin\varphi \tag{2-2a}$$

$$z = a\xi\eta = a\xi\cos\vartheta \tag{2-3a}$$

$$\text{and } -1 \le \eta \le 1 \ \ (0 \le \vartheta \le \pi),\ \ 1 \le \xi < \infty,\ \ 0 \le \varphi \le 2\pi; \tag{2-4a}$$

Oblate:
$$x = a\sqrt{\xi^2 + 1}\sqrt{1-\eta^2}\cos\varphi = a\sqrt{\xi^2 + 1}\sin\vartheta\cos\varphi \tag{2-1b}$$

$$y = a\sqrt{\xi^2 + 1}\sqrt{1-\eta^2}\sin\varphi = a\sqrt{\xi^2 + 1}\sin\vartheta\sin\varphi \tag{2-2b}$$

$$z = a\xi\eta = a\xi\cos\vartheta \tag{2-3b}$$

$$\text{and } -1 \le \eta \le 1 \ \ (0 \le \vartheta \le \pi),\ \ 0 \le \xi < \infty,\ \ 0 \le \varphi \le 2\pi; \tag{2-4b}$$

$$\text{where } \ \eta = \cos\vartheta \ \text{ in both cases.} \tag{2-5}$$

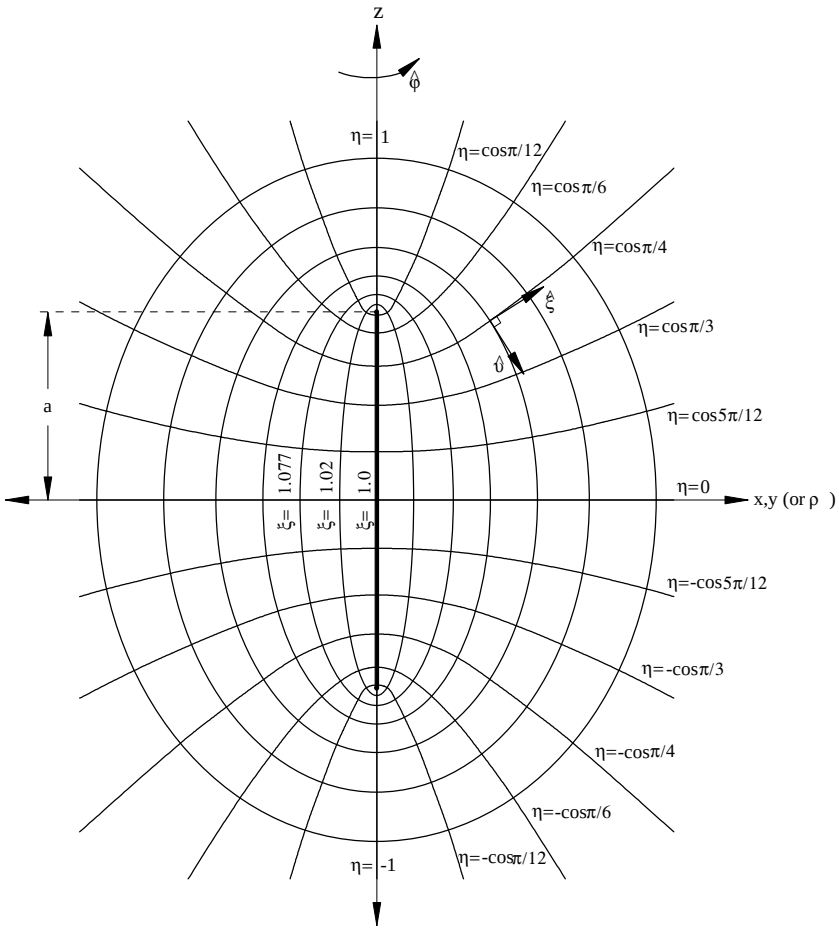

Figure 2.1a Prolate spheroidal coordinate system [23].

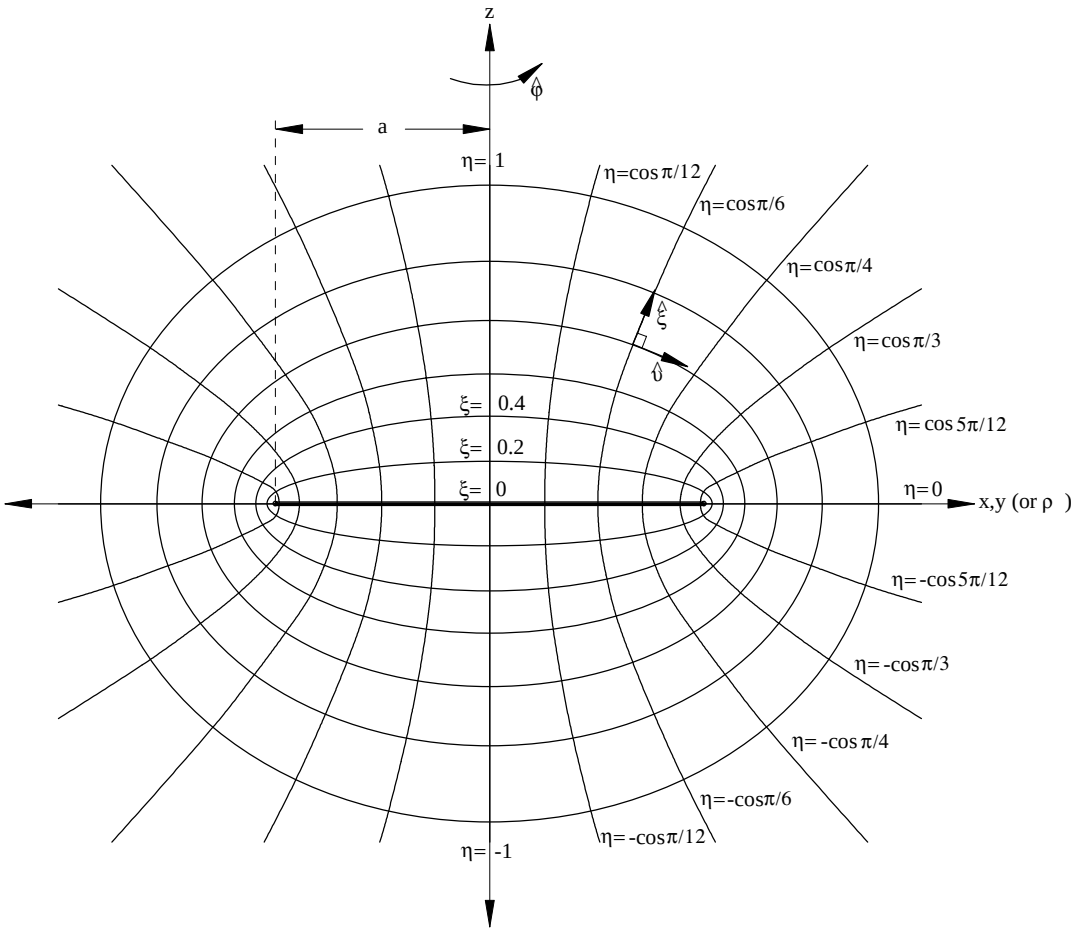

Figure 2.1b Oblate spheroidal coordinate system [23].

Both detailed spheroidal-to-Cartesian transformations, i.e., equations (2-1)-(2-5), indicate that the following parameters must be considered: ξ, η (or ϑ), φ, and a. The parameter a represents the distance from the focal point of the confocal ellipses and hyperbolas to the origin of the selected spheroidal coordinate system. Regarding the remaining parameters, they form an ordered triple that represents the coordinates for either spheroidal coordinate system: namely (ξ,η,φ) or (ξ,ϑ,φ) (the choice of which depends upon the angular parameter employed). Specifically, the parameter ξ serves as the radial coordinate for both spheroidal coordinate systems. However, unlike the spherical coordinate system, the radial coordinate of the spheroidal coordinate systems does not directly indicate the distance from the origin to the point-of-interest. Instead, ξ is a unitless quantity that implicitly represents the radial distance by indicating which confocal ellipsoid of revolution (i.e., $\xi = \xi_o = \text{constant}$ surface) intersects with the point-of-interest. In the case of the prolate spheroidal coordinate system, this ellipsoid of revolution (viz., a prolate spheroid) has a major axis of length $2a\xi$ and a minor axis of length $2a\sqrt{\xi^2-1}$. As for its oblate counterpart, its ellipsoid of revolution (viz., an oblate spheroid) has major and minor axes of lengths $2a\sqrt{\xi^2+1}$ and $2a\xi$, respectively. Regarding the parameters η and ϑ, either one can serve as the angular coordinate and is implicitly related to the angle between the point-of-interest and the z-axis. In the case of the prolate spheroidal coordinate system, the surface $|\eta| = |\eta_o| = \text{constant} < 1$ is a hyperboloid of revolution of two sheets with an asymptotic cone whose generating line passes through the origin and is inclined at the angle $\vartheta = \cos^{-1}\eta$ to the z-axis [23]. As for its oblate counterpart, the surface $|\eta| = |\eta_o| = \text{constant} < 1$ is in this case a hyperboloid of revolution of one sheet with an asymptotic cone whose generating line also passes through the origin and is inclined at the angle $\vartheta = \cos^{-1}\eta$ to the z-axis [23]. Since both parameters ϑ and η are dependent on one another and remain homeomorphic over their limited domains, i.e., maintain a one-to-one mapping, we are able to employ either one as

the angular coordinate during the formulation of our NZ-FZT process. Still, some care must be exercised whenever making this particular change-of-variable. Lastly, the coordinate φ represents the azimuthal angle between the x-z plane and the plane that passes through both the point-of-interest and the entire z-axis, i.e., $\varphi = \varphi_o = \text{constant}$ surface. The spheroidal coordinate φ is for all practical purposes the same as the azimuthal coordinate φ of both the cylindrical and spherical coordinate systems (or of any other rotational coordinate system).

In addition to describing both spheroidal coordinate systems in terms of their scalar coordinates, a review of their respective unit vectors is required. As illustrated in Figures 2.1a and 2.1b, the body-of-revolution confocal quadric surfaces (viz., spheroids and hyperboloids) intersect each other at right angles. In other words, the tangent planes of all three coordinate surfaces (viz., $\xi = \xi_o$, $\vartheta = \vartheta_o$, and $\varphi = \varphi_o$ constant parameter surfaces) passing through any point-of-interest $(\xi_o, \vartheta_o, \varphi_o)$ are mutually orthogonal [23]. Consequently, both the prolate and oblate spheroidal coordinate systems are classified as systems of orthogonal curvilinear coordinates. For both spheroidal coordinate systems, the unit vectors $\hat{\xi}$, $\hat{\vartheta}$, and $\hat{\varphi}$ form a right-handed system that is defined by the following cross products (see Figures 2.1a and 2.1b):

$$\hat{\xi} \times \hat{\vartheta} = \hat{\varphi} \tag{2-6}$$

$$\hat{\varphi} \times \hat{\xi} = \hat{\vartheta} \tag{2-7}$$

$$\hat{\vartheta} \times \hat{\varphi} = \hat{\xi} \tag{2-8}$$

where $\hat{\eta} = -\hat{\vartheta}$.

Having selected and defined an appropriate pair of spheroidal coordinate systems, we are now in a position to mathematically describe our spheroidal transformation surfaces. From our previous discussion of spheroidal coordinates, the prolate and oblate

spheroids are easily defined in their respective coordinate systems due to the fact that these surfaces are intrinsically the $\xi = \xi_o$ constant parameter surfaces. Accordingly, these spheroidal transformation surfaces can be formally described as follows:

Prolate Surface Ω_P: $$\vec{r}(\xi,\eta,\varphi)\big|_{\xi=\xi_o=\text{ constant}} = \vec{r}(\eta,\varphi) \tag{2-9a}$$

or defined parametrically as

$$\vec{r}(x(\eta,\varphi), y(\eta,\varphi), z(\eta,\varphi)) \tag{2-10a}$$

with $$x(\eta,\varphi) = a\sqrt{\xi_o^{\,2}-1}\sqrt{1-\eta^2}\cos\varphi$$

$$y(\eta,\varphi) = a\sqrt{\xi_o^{\,2}-1}\sqrt{1-\eta^2}\sin\varphi$$

$$z(\eta,\varphi) = a\xi_o\eta\,;$$

Oblate Surface Ω_o: $$\vec{r}(\xi,\eta,\varphi)\big|_{\xi=\xi_o=\text{ constant}} = \vec{r}(\eta,\varphi) \tag{2-9b}$$

or defined parametrically as

$$\vec{r}(x(\eta,\varphi), y(\eta,\varphi), z(\eta,\varphi)) \tag{2-10b}$$

with $$x(\eta,\varphi) = a\sqrt{\xi_o^{\,2}+1}\sqrt{1-\eta^2}\cos\varphi$$

$$y(\eta,\varphi) = a\sqrt{\xi_o^{\,2}+1}\sqrt{1-\eta^2}\sin\varphi$$

$$z(\eta,\varphi) = a\xi_o\eta\,.$$

In both of these descriptions of the prolate and oblate spheroidal transformation surfaces, the vector quantity $\vec{r}$ represents the position vector in the respective coordinate system.

With the transformation surfaces for the NZ-FZT process being mathematically described, our attention is now turned to the required near-zone field quantities.

Recalling from before that only the time-harmonic E-field along the spheroidal transformation surface is required, we describe the input to our NZ-FZT process as

$$\text{Prolate Process Input: } \vec{E}(\xi,\eta,\varphi)\Big|_{\Omega_P} = \vec{E}(\xi_o,\eta,\varphi); \tag{2-11a}$$

$$\text{Oblate Process Input: } \vec{E}(\xi,\eta,\varphi)\Big|_{\Omega_O} = \vec{E}(\xi_o,\eta,\varphi). \tag{2-11b}$$

It is important to understand that the transformation surface is virtual in nature and does not actually alter the operation of the electromagnetic system. That is, the fields emanating from the radiating structure are the same with or without the existence of the enclosing transformation surface. Accordingly, the electromagnetic fields sampled along this virtual boundary inherently must satisfy Maxwell's equations. The fact that all points on the transformation surface lie in free-space implies that the $\nabla \cdot \vec{E} = 0$ for the specified NZ-FZT process input.

2.1.2 NZ-FZT Process Output (Far-Zone Response)

In order to characterize the performance of an antenna, many figures-of-merit have been created and have subsequently evolved through the years to satisfy the needs of an ever-changing technology. Albeit an all inclusive list would be too large to mention, some of the basic parameters that characterize the performance of an antenna are as follows: radiation pattern, radiation intensity, directivity, gain, antenna efficiency, bandwidth, polarization, and input impedance. The reader is referred to any text on antenna theory, e.g., [26] or [27], for a more comprehensive review of these basic antenna performance parameters. Due to the fact that some of these parameters are interrelated, not all of them must be specified in order to give a complete characterization of antenna performance [27]. As a result, we shall use our NZ-FZT process to determine a quantity that is so essential that it serves as the foundation for many antenna performance parameters: the far-zone E-field. This fundamental quantity is so important because it

can subsequently be used to derive many of the aforementioned antenna performance parameters.

Despite having identified the far-zone time-harmonic E-field as the NZ-FZT process output, we now must consider the most suitable form for this quantity to assume. The first issue that must be addressed is the choice of coordinate system to express the process output. Upon first consideration, it logically appears that the NZ-FZT process input and output should share the same coordinate system: namely, the spheroidal coordinate system. Unfortunately, antenna researchers and designers do not operate in terms of this unusual coordinate system. Bearing this in mind, it is desirable to put the NZ-FZT process output, i.e., the far-zone E-field, in the more palatable spherical coordinate system and remain consistent with the conventions of antenna theory. This choice of using the spherical coordinate system to express the far-zone E-field will not only apply to the independent coordinates of the scalar functions, but also to its respective vector quantities.

In the far-zone of any radiating structure (in terms of spherical coordinates), it can be shown that the radial dependence, i.e., *r*, becomes separable from the angular dependence, i.e., θ and φ, and can be expressed as follows [27]:

$$\lim_{r\to\infty} \vec{E}(r,\theta,\varphi) = \vec{E}_{fz}(r,\theta,\varphi) = \vec{\bar{E}}_{fz}(\theta,\varphi)\frac{e^{-jkr}}{r} \tag{2-12}$$

where

$$\vec{\bar{E}}_{fz}(\theta,\varphi) = \bar{E}_{fz_\theta}(\theta,\varphi)\hat{\theta} + \bar{E}_{fz_\varphi}(\theta,\varphi)\hat{\varphi}\,. \tag{2-13}$$

It must be pointed out that these expressions are asymptotic approximations of the exact far-zone E-field representations. Even though higher-order terms of $1/r^n$ for $n>1$ do exist, in the far-zone they can be safely neglected because they vanish in the limit as

$r \to \infty$. Once again the reader is referred to any text on basic antenna theory regarding this matter.

Note that in expressions (2-12) and (2-13) a bar is placed over the E-field quantities in order to indicate within the notation the suppression of the radial factor $\left(e^{-jkr}/r\right)$. There are advantages to representing the far-zone E-field with a suppressed radial dependence in much of the same way that the $e^{j\omega t}$ time dependence is suppressed during the use of phasor notation. With regard to this particular notation, it allows us to avoid having to tote the cumbersome expression throughout the ensuing formulation, i.e., its presence is implied. Moreover, far-zone parameters most often characterize antenna performance with respect to only angular variations due to the fact that the form of the radial dependence is known. This is exemplified by the expression for radiation intensity which demonstrates that the radial dependence ultimately drops out of the definition [26], [27]:

$$U(\theta,\varphi) = \frac{r^2}{2\eta_o}\left|\vec{E}_{fz}(r,\theta,\varphi)\right|^2 \tag{2-14}$$

and subsequently,

$$U(\theta,\varphi) = \frac{1}{2\eta_o}\left|\bar{\vec{E}}_{fz}(\theta,\varphi)\right|^2 = \frac{1}{2\eta_o}\left[\left|\bar{E}_{fz_\theta}(\theta,\varphi)\right|^2 + \left|\bar{E}_{fz_\varphi}(\theta,\varphi)\right|^2\right] \tag{2-15}$$

where η_o is the intrinsic impedance of free-space.

Accordingly, we designate the far-zone E-field expressed in conventional spherical coordinates with a suppressed radial dependence, viz., equation (2-13), as the NZ-FZT process output. Note that the Sommerfeld radiation condition (see 2.2.6) implies that $\nabla \cdot \vec{E} = 0$ in the limit as $r \to \infty$ for the specified NZ-FZT process output.

2.2 FORMULATION OF THE NZ-FZT BOUNDARY VALUE PROBLEMS AND CONSTRUCTION OF THE SOLUTIONS

2.2.1 Governing Differential Equation (Three-Dimensional Vector Helmholtz Equation)

The first step in the formulation of the NZ-FZT process as a boundary value problem is to understand the differential equation that governs electromagnetic radiation in free-space. Our assumption of free-space radiation is justified because the region of interest that lies on and outside our closed boundary (i.e., the transformation surface) is considered to have no sources and/or any additional media other than free-space (i.e., μ_o, ε_o).

In order to derive the governing differential equation, we must begin with the time-harmonic, differential form of Maxwell's equations for free-space:

$$\nabla \times \vec{E} = -j\omega\mu_o \vec{H} \tag{2-16}$$

$$\nabla \times \vec{H} = j\omega\varepsilon_o \vec{E} \tag{2-17}$$

$$\nabla \cdot \vec{E} = 0 \tag{2-18}$$

$$\nabla \cdot \vec{H} = 0. \tag{2-19}$$

Note that equations (2-16)-(2-19) state Maxwell's equations in terms of only E- and H-fields and make use of the free-space constitutive relations $\vec{D} = \varepsilon_o \vec{E}$ and $\vec{B} = \mu_o \vec{H}$ (where free-space is obviously taken as both linear and isotropic). We begin decoupling equation (2-16) from (2-17) by applying the curl operator to both sides of (2-16):

$$\nabla \times \nabla \times \vec{E} = -j\omega\mu_o \nabla \times \vec{H}. \tag{2-20}$$

Equation (2-17) can then be substituted into (2-20) to obtain

$$\nabla \times \nabla \times \vec{E} = \omega^2 \mu_o \varepsilon_o \vec{E}. \tag{2-21}$$

Equation (2-22) states a needed vector identity:

$$\nabla \times \nabla \times \vec{E} = \nabla(\nabla \cdot \vec{E}) - \nabla^2 \vec{E} \,. \tag{2-22}$$

Applying the vector identity of (2-22) to expression (2-21) and assuming no charge density, i.e., $\nabla \cdot \vec{E} = 0$, we obtain the following [28]:

$$\nabla^2 \vec{E} + k^2 \vec{E} = 0 \tag{2-23}$$

where

$$k = \omega\sqrt{\mu_o \varepsilon_o} \,. \tag{2-24}$$

The second-order, linear, homogeneous partial differential equation expressed in (2-23) is often interchangeably referred to as either the vector wave equation [28] or the vector Helmholtz equation [22]. In the infinite domain exterior to the radiating structure, it is this differential equation in three dimensions that governs electromagnetic radiation into free-space.

2.2.2 Reduction of the Vector Helmholtz Equation Using a Hybrid of Coordinate Systems (Scalar Spheroidal/Vector Cartesian)

Now that we have resolved that the governing differential equation is the vector Helmholtz equation in three dimensions, our next step is to decide how to best apply this generalized differential equation to meet the system requirements of the NZ-FZT process, viz., its input and output. In expressions (2-11a) and (2-11b), we define the process input as being the near-zone time-harmonic E-field along either a prolate or oblate spheroidal transformation surface. Because these particular transformation surfaces form a boundary that is spheroidal in shape, the obvious approach is to solve the vector Helmholtz equation in spheroidal coordinates. However, as mentioned earlier (see 2.1.2), the process output (i.e., the far-zone time-harmonic E-field) is defined in terms of conventional spherical coordinates. Fortunately, this does not present a problem because

both spheroidal coordinate systems asymptotically approach that of the conventional spherical coordinate system in the far-zone (see Appendix A).

Although we have identified spheroidal coordinates as the coordinate system of choice for our particular process, an obstacle presents itself when trying to solve the vector Helmholtz equation in three dimensions. In coordinate systems other than Cartesian, the vector solution of the three-dimensional Helmholtz equation is not a straightforward extension of its respective scalar solution. This difficulty arises because the orientation of the curvilinear unit vector varies as a function of curvilinear coordinates such that, in general, the vector Laplacian is not easily expressed in terms of its three respective scalar Laplacians [28]:

$$\begin{aligned}\nabla^2\vec{E}(x_1,x_2,x_3) \neq\ & \nabla^2 E_{x_1}(x_1,x_2,x_3)\hat{x}_1 \\ & + \nabla^2 E_{x_2}(x_1,x_2,x_3)\hat{x}_2 \\ & + \nabla^2 E_{x_3}(x_1,x_2,x_3)\hat{x}_3 \end{aligned} \tag{2-25}$$

where in the special case of Cartesian coordinates (2-25) is an equality.

Unfortunately, the vector components of the vector Laplacian are mutually coupled (with the exception of Cartesian coordinates) and can be expressed in generalized three-dimensional curvilinear coordinates as follows:

$$\begin{aligned}\nabla^2\vec{E}(x_1,x_2,x_3) =\ & f(E_{x_1},E_{x_2},E_{x_3})\hat{x}_1 \\ & + g(E_{x_1},E_{x_2},E_{x_3})\hat{x}_2 \\ & + h(E_{x_1},E_{x_2},E_{x_3})\hat{x}_3 . \end{aligned} \tag{2-26}$$

Applying the generalized vector Laplacian (2-26) to the three-dimensional vector Helmholtz equation (2-23) yields the following system of scalar equations:

$$f(E_{x_1}, E_{x_2}, E_{x_3}) + k^2 E_{x_1} = 0$$

$$g(E_{x_1}, E_{x_2}, E_{x_3}) + k^2 E_{x_2} = 0$$

$$h(E_{x_1}, E_{x_2}, E_{x_3}) + k^2 E_{x_3} = 0\,. \qquad (2\text{-}27)$$

Upon inspection of the system of scalar equations (2-27), one can see that, in general, the vector components are not easily separated from one another. That is, it is difficult to decouple these equations and formulate them as a related system that has each of its three scalar equations expressed in terms of only one of the respective vector components.

Morse and Feshbach [22] indicate that only six of the eleven curvilinear coordinate systems which allow separation of the scalar Helmholtz equation in three dimensions are also capable of presenting separable solutions to the vector Helmholtz equation in three dimensions. Table 2.1 summarizes these eleven coordinate systems and notes their separable properties with regard to both the scalar and vector Helmholtz equations. These six special coordinate systems are vector-separable because one of their scale factors is unity, and the ratio of the other two scale factors is independent of the coordinate corresponding to the unity scale factor [22]. Even though there exists vector-separable solutions for each of these six special coordinates systems, constructing some of them can be quite formidable. In the case of spherical coordinates, various combinations of the solutions to the scalar wave equation (viz., spherical harmonics) can be used to construct a basis set of solution vectors in spherical coordinates (viz., vector spherical harmonics) [22], [29]. It must be mentioned that although these constructed basis sets of solution vectors maintain orthogonality, they are not unique. Arfken [29] and Morse and Feshbach [22] offer two different basis sets that are driven by a particular application. To digress, the vector spherical harmonics provided by Arfken [29] are used primarily in quantum mechanics in which angular momentum is a significant parameter;

Table 2.1 Summary of Three-Dimensional Curvilinear Coordinate Systems and Their Separable Properties Pertaining to Both the Scalar and Vector Helmholtz Equations

Coordinate System Number	Three-Dimensional Curvilinear Coordinate System	Provides Scalar-Separable Solution	Provides Vector-Separable Solution
1	Cartesian (rectangular)	yes	yes
2	circular cylinder	yes	yes
3	elliptic cylinder	yes	yes
4	parabolic cylinder	yes	yes
5	spherical	yes	yes*
6	conical	yes	yes*
7	parabolic	yes	no
8	***prolate spheroidal***	***yes***	***no***
9	***oblate spheroidal***	***yes***	***no***
10	ellipsoidal	yes	no
11	paraboloidal	yes	no

***** - Denotes that the coordinate system provides a separable solution to the vector Helmholtz equation only if the preferred coordinate is the radius.

meanwhile, Morse and Feshbach [22] describe another set of vector spherical harmonics that offers advantages with regard to separating wave propagation into longitudinal and transverse components.

As we have shown, solving the three-dimensional vector Helmholtz equation is significantly more involved than solving its scalar counterpart. And to further complicate matters, the coordinate systems of choice for our particular NZ-FZT process, viz., prolate and oblate spheroidal coordinates, are not among the six special curvilinear coordinate systems capable of providing a vector-separable solution. In order to circumvent this obstacle, we take an approach suggested by Morse and Feshbach [22] when attempting to solve the vector Helmholtz equation with one of the other five coordinate systems (viz., those that are scalar-separable, but not vector-separable): Formulate the overall solution

by taking three solutions of the scalar Helmholtz equation (in the scalar-separable/vector-not-separable coordinate system) as the three Cartesian components of the vector. Yet regarding this approach, Morse and Feshbach [22] express their reservations and warn that " ... the fitting of boundary conditions is well-nigh impossible of attainment." However, it must be pointed out that this comment more appropriately applies when solving boundary value problems in analytical form. Fortunately, because our particular NZ-FZT process is numerically based, the difficulties typically associated with the fitting of boundary conditions prove not to be an issue. At this point in our formulation, we implement this hybrid approach by reducing the vector Helmholtz equation into a system of three scalar Helmholtz equations in spheroidal coordinates with each representing a vector component in Cartesian coordinates:

$$\nabla^2 E_x(\xi,\eta,\varphi) + k^2 E_x(\xi,\eta,\varphi) = 0$$

$$\nabla^2 E_y(\xi,\eta,\varphi) + k^2 E_y(\xi,\eta,\varphi) = 0$$

$$\nabla^2 E_z(\xi,\eta,\varphi) + k^2 E_z(\xi,\eta,\varphi) = 0 \qquad \text{(2-28)}$$

where the scalar E-fields are in either spheroidal coordinate system.

2.2.3 Break Down of the Resulting Scalar Helmholtz Equations into a Set of Ordinary Differential Equations Using the Separation of Variables Method

Upon inspection of the system of scalar equations presented in (2-28), it is obvious that all three equations are of identical mathematical form. In essence, the vector problem has been reduced to three identical scalar problems of the following form:

Prolate: $$\nabla^2 \psi^P(\xi,\eta,\varphi) + k^2 \psi^P(\xi,\eta,\varphi) = 0\,; \qquad \text{(2-29a)}$$

Oblate: $$\nabla^2 \psi^O(\xi,\eta,\varphi) + k^2 \psi^O(\xi,\eta,\varphi) = 0\,. \qquad \text{(2-29b)}$$

Equations (2-29a) and (2-29b) are the scalar Helmholtz equation in prolate and oblate spheroidal coordinates, respectively. Fortunately, the scalar Helmholtz equation is separable in both of these coordinate systems (see Table 2.1). Since all three scalar equations of (2-28) are of the same mathematical form (namely, the scalar Helmholtz equation), we need to analyze their respective general solutions for both the prolate and oblate spheroidal coordinate systems, viz., $\psi^P(\xi,\eta,\varphi)$ and $\psi^O(\xi,\eta,\varphi)$. These general solutions can then be applied afterwards to each of the three scalar equations of (2-28) along with pertinent boundary conditions to formulate the respective particular solution of the system.

The first step in determining the general solutions of the scalar Helmholtz equation in both spheroidal coordinate systems is to expand each respective partial differential equation and express it in terms of the coordinate specific differential operators. This procedure requires that we determine the scalar Laplacians of equations (2-29a) and (2-29b) in their respective coordinate systems:

$$\nabla^2\psi^P(\xi,\eta,\varphi) =$$

$$\frac{1}{a^2(\xi^2-\eta^2)}\left[\frac{\partial}{\partial\xi}\left(\left(\xi^2-1\right)\frac{\partial\psi^P}{\partial\xi}\right)+\frac{\partial}{\partial\eta}\left(\left(1-\eta^2\right)\frac{\partial\psi^P}{\partial\eta}\right)+\frac{\left(\xi^2-\eta^2\right)}{\left(\xi^2-1\right)\left(1-\eta^2\right)}\frac{\partial^2\psi^P}{\partial\varphi^2}\right]; \tag{2-30a}$$

$$\nabla^2\psi^O(\xi,\eta,\varphi) =$$

$$\frac{1}{a^2(\xi^2+\eta^2)}\left[\frac{\partial}{\partial\xi}\left(\left(\xi^2+1\right)\frac{\partial\psi^O}{\partial\xi}\right)+\frac{\partial}{\partial\eta}\left(\left(1-\eta^2\right)\frac{\partial\psi^O}{\partial\eta}\right)+\frac{\left(\xi^2+\eta^2\right)}{\left(\xi^2+1\right)\left(1-\eta^2\right)}\frac{\partial^2\psi^O}{\partial\varphi^2}\right]. \tag{2-30b}$$

The scalar Laplacians in prolate and oblate spheroidal coordinates are found by employing their respective scale factors (provided in Appendix A) together with the generalized expression for the Laplacian in orthogonal curvilinear coordinates, i.e., (B-1).

The reader is referred to Appendix B for the details behind the derivation of expressions (2-30a) and (2-30b).

Having determined the necessary scalar Laplacians, we now apply expressions (2-30a) and (2-30b), respectively, to equations (2-29a) and (2-29b) to obtain the scalar Helmholtz partial differential equations in terms of coordinate specific differential operators [23]:

Prolate:

$$\frac{\partial}{\partial\xi}\left(\left(\xi^2-1\right)\frac{\partial\psi^P}{\partial\xi}\right)+\frac{\partial}{\partial\eta}\left(\left(1-\eta^2\right)\frac{\partial\psi^P}{\partial\eta}\right)+\frac{\left(\xi^2-\eta^2\right)}{\left(\xi^2-1\right)\left(1-\eta^2\right)}\frac{\partial^2\psi^P}{\partial\varphi^2}+h^2(\xi^2-\eta^2)\psi^P=0\,;$$

(2-31a)

Oblate:

$$\frac{\partial}{\partial\xi}\left(\left(\xi^2+1\right)\frac{\partial\psi^O}{\partial\xi}\right)+\frac{\partial}{\partial\eta}\left(\left(1-\eta^2\right)\frac{\partial\psi^O}{\partial\eta}\right)+\frac{\left(\xi^2+\eta^2\right)}{\left(\xi^2+1\right)\left(1-\eta^2\right)}\frac{\partial^2\psi^O}{\partial\varphi^2}+h^2(\xi^2+\eta^2)\psi^O=0\,;$$

(2-31b)

where $h\equiv ka\equiv(2\pi/\lambda_o)\,a\equiv 2\pi\,a_\lambda$. (2-32)

Within the literature, the independent variable of both partial differential equations has been designated by some with the variable *h* [22] and by others with the variable *c* [23]. Because of our particular application (i.e., the radiation of electromagnetic waves), we have opted to use the variable *h* instead of the variable *c* in order to avoid any confusion with the notation for the speed of light. Moreover, other notations also exist within the literature for this particular independent variable; for these, the interested reader should consult Table 21.11 of *AMS-55* [25] for a summary of the existing notations along with an itemized account of their originators. Finally, equation

(2-32) indicates that the independent variable *h* is directly related to the wavelength normalized focal point distance, i.e., $a_\lambda = a/\lambda_o$.

The general solutions of the scalar Helmholtz equation in spheroidal coordinates may be found by applying one of the oldest systematic methods for solving partial differential equations: separation of variables. This method allows a single partial differential equation to be reduced to a set of ordinary differential equations that are only coupled by separation constants. Although the separation of variables method is not always successful at solving a given partial differential equation, it will work in our case because we have *a priori* knowledge that the scalar Helmholtz equation is separable in both prolate and oblate spheroidal coordinates (see Table 2.1).

When applying the separation of variables method, one assumes the solution of the partial differential equation to be the product of distinct functions with each being only dependent on its respective single variable. In our case, we shall assume that the solutions of the partial differential equations of interest, viz., (2-31a) and (2-31b), are of the following form [23]:

Prolate: $$\psi^P(\xi,\eta,\varphi) = R_P(\xi)S_P(\eta)\Phi_P(\varphi); \tag{2-33a}$$

Oblate: $$\psi^O(\xi,\eta,\varphi) = R_O(\xi)S_O(\eta)\Phi_O(\varphi); \tag{2-33b}$$

where $R_P(\xi)$ and $R_O(\xi)$ are radial solutions,

$S_P(\eta)$ and $S_O(\eta)$ are angular solutions,

$\Phi_P(\varphi)$ and $\Phi_O(\varphi)$ are azimuthal solutions.

The assumed solutions presented in (2-33a) and (2-33b) are then substituted into their respective partial differential equations (2-31a) and (2-31b) to obtain the resulting corresponding systems of three ordinary differential equations [23], [25]:

Prolate:

$$\frac{d}{d\xi}\left[\left(\xi^2-1\right)\frac{d}{d\xi}R_P(\xi)\right]-\left[\lambda-h^2\xi^2+\frac{m^2}{\left(\xi^2-1\right)}\right]R_P(\xi)=0 \quad \text{where } 1\le\xi<\infty, \tag{2-34a}$$

$$\frac{d}{d\eta}\left[\left(1-\eta^2\right)\frac{d}{d\eta}S_P(\eta)\right]+\left[\lambda-h^2\eta^2-\frac{m^2}{\left(1-\eta^2\right)}\right]S_P(\eta)=0 \quad \text{where } -1\le\eta\le 1, \tag{2-35a}$$

$$\frac{d^2}{d\varphi^2}\Phi_P(\varphi)+m^2\Phi_P(\varphi)=0 \quad \text{where } 0\le\varphi\le 2\pi; \tag{2-36a}$$

Oblate:

$$\frac{d}{d\xi}\left[\left(\xi^2+1\right)\frac{d}{d\xi}R_O(\xi)\right]-\left[\lambda-h^2\xi^2-\frac{m^2}{\left(\xi^2+1\right)}\right]R_O(\xi)=0 \quad \text{where } 0\le\xi<\infty, \tag{2-34b}$$

$$\frac{d}{d\eta}\left[\left(1-\eta^2\right)\frac{d}{d\eta}S_O(\eta)\right]+\left[\lambda+h^2\eta^2-\frac{m^2}{\left(1-\eta^2\right)}\right]S_O(\eta)=0 \quad \text{where } -1\le\eta\le 1, \tag{2-35b}$$

$$\frac{d^2}{d\varphi^2}\Phi_O(\varphi)+m^2\Phi_O(\varphi)=0 \quad \text{where } 0\le\varphi\le 2\pi. \tag{2-36b}$$

During the separation of variables process, the azimuthal ordinary differential equations, i.e., (2-36a) and (2-36b), are the first to be separated from their respective partial differential equations with $-m^2$ designated as the first separation constant. Subsequently, the remaining respective radial and angular ordinary differential equations are separated from one another using the second separation constant λ (not to be confused with free-space wavelength). Although theory allows the separation constants to be arbitrarily chosen [30], these separation constants have been customarily selected as such because they best apply to the resulting solutions. The reason for using these specific separation

constants will become clearer as we explore the ensuing general solutions. We refer the interested reader to Appendix C for the explicit details behind applying the separation of variables method to derive both sets of ordinary differential equations presented in (2-34a)-(2-36a) and (2-34b)-(2-36b).

2.2.4 Review of Applicable Sturm-Liouville Theory and Self-Adjoint Boundary Value Problems

So that we may proceed with construction of the general solutions to the scalar Helmholtz equation in spheroidal coordinates, we must begin with some applicable Sturm-Liouville theory that is key to the understanding of the differential equations under consideration, viz., (2-34a)-(2-36a) and (2-34b)-(2-36b). It will become apparent that these differential equations are already subject to boundary conditions just based upon existing physical requirements. Consequently, it is necessary that we gain some insight of second-order self-adjoint boundary value problems and how they apply to the resulting differential equations coupled with their respective boundary conditions. This section provides a basic understanding of this type of boundary value problem in addition to their pertinent special properties. As we shall see, the special properties of self-adjoint boundary value problems play a crucial role when constructing the general solutions of the scalar Helmholtz equation in spheroidal coordinates.

Self-adjoint differential equations form a class of differential equations that fit a particular mathematical form. Sagan [31] provides an excellent treatment of the theory behind the origin of self-adjoint differential equations and their respective self-adjoint operators. It is here that we refer the reader to obtain the details regarding the origin of the definitions that are to follow. A differential operator of second-order, L, is considered self-adjoint if and only if it is equivalent to its adjoint operator, $\overline{\mathrm{L}}$, and has the following form [29], [31]:

$$\overline{\mathrm{L}}u(x) = \mathrm{L}u(x) = \frac{d}{dx}\left[p(x)\frac{du(x)}{dx} \right] + q(x)u(x) \tag{2-37}$$

where the functions $p(x)$ and $q(x)$ are real functions of x over the region of interest $a \le x \le b$; furthermore, $q(x)$ is continuous and $p(x)$ is twice differentiable (i.e., continuous first and second derivatives). Since the zeros of $p(x)$ will become singularities of the resulting differential equation, we must choose the interval $[a,b]$ so that no singularities are contained in the interior of the interval. However, theory allows for the existence of singular points on either one or both boundaries of the interval [29], [30].

Having defined the differential operator of second-order, we can now express the generalized form of the differential equation (known as the Sturm-Liouville equation) [29], [31]:

$$\mathrm{L}u(x) + \lambda w(x)u(x) = 0, \tag{2-38}$$

or more explicitly as (applying (2-37) to (2-38))

$$\frac{d}{dx}\left[p(x)\frac{du(x)}{dx} \right] + q(x)u(x) + \lambda\, w(x)u(x) = 0. \tag{2-39}$$

In these expressions, λ serves as a constant and $w(x)$ is a known function of x, referred to as a density or weighting function [29]. It is required that $w(x) > 0$, except possibly at isolated points at which $w(x) = 0$ [29]. If boundary conditions are imposed at both endpoints of the interval, solutions to (2-38) will be limited to a discrete set of $u(x)$ functions. Each one of these functions is referred to as an eigenfunction and corresponds to a specific value of λ, known as an eigenvalue. It is important to note that only the discrete set of eigenfunctions (each paired with its respective eigenvalue) is able to satisfy the self-adjoint differential equation of (2-38).

Now that we have an understanding of self-adjoint differential equations of second-order, our attention shall focus on some of the underlying boundary conditions that are possible for second-order, homogeneous, self-adjoint boundary value problems.

The boundary conditions are specified at the endpoints of the interval $[a,b]$ and shall be classified by us for easy reference as one of the following for homogeneous boundary value problems [30], [31]:

Type I boundary conditions:

$$c_{11}u(a)+c_{12}u'(a)=0$$
$$c_{21}u(b)+c_{22}u'(b)=0\,; \tag{2-40}$$

Type II boundary conditions:

$$c_{11}u(a)+c_{12}u'(a)+d_{11}u(b)+d_{12}u'(b)=0$$
$$c_{21}u(a)+c_{22}u'(a)+d_{21}u(b)+d_{22}u'(b)=0\,; \tag{2-41}$$

Type III boundary conditions:

$$c_{11}u(a)+c_{12}u'(a)=0$$
$$u(b)\,,\ u'(b) \quad \text{bounded as } x\to b\,; \tag{2-42}$$

Type IV boundary conditions:

$$u(a)\,,\ u'(a) \quad \text{bounded as } x\to a$$
$$u(b)\,,\ u'(b) \quad \text{bounded as } x\to b\,. \tag{2-43}$$

The task of solving the Sturm-Liouville equation, i.e., (2-38), under one of these general types of imposed boundary conditions, viz., (2-40)-(2-43), is referred to as a homogeneous self-adjoint boundary value problem of second-order [30], [31]. However, these generalized boundary conditions, with the exception of Type I, cannot guarantee that the resulting boundary value problem is self-adjoint; that is, there is still an additional condition that must be satisfied.

Let $u_1(x)$ and $u_2(x)$ represent every pair of sufficiently differentiable solutions to the self-adjoint differential equation (2-38) that satisfies the given type of boundary condition such that we can formulate the following condition [29]-[31]:

$$\left(\mathrm{L}u_1(x), u_2(x)\right) = \left(u_1(x), \mathrm{L}u_2(x)\right). \tag{2-44}$$

Note that nomenclature (f, g) represents the complex inner product over the interval $[a, b]$ defined as follows [30]:

$$(f, g) = \int_a^b f(x) g^*(x) dx \tag{2-45}$$

where * denotes complex conjugate of the function.

A boundary value problem specified by the Sturm-Liouville equation and any one of the defined boundary condition types is considered to be self-adjoint (i.e., on a case-by-case basis) if the crucial condition (2-44) can be shown to be valid [29]-[31].

Now that we have a basic understanding of what constitutes a homogeneous self-adjoint boundary value problem of second-order, we are now somewhat able to classify them. First of all, self-adjoint boundary value problems can be divided into one of two types: regular, where no singularities exist anywhere in the interval $[a, b]$ including the boundaries; and singular, where singularities exist at either one or both of the boundaries [30]. Type I and II boundary conditions shall apply to regular self-adjoint boundary value problems, while the less restrictive Type III and IV boundary conditions are necessary to solve the singular self-adjoint boundary value problem.

We first consider the second-order self-adjoint boundary value problem that is regular with separated boundary conditions, viz., Type I (2-40). These linear homogeneous boundary conditions are said to be separated because each condition involves only one of the endpoints of the interval [30]. Note that these self-adjoint boundary value problems are considered extraordinary because sweeping generalizations can be made about them without having to explicitly investigate each particular one on a

case-by-case basis. An example being that the identity specified in (2-44) is always true in the particular case that the problem is regular with separated boundary conditions [30], [31]. Unfortunately, this type of self-adjoint boundary value problem does not apply to the differential equations under consideration. However, the regular self-adjoint boundary value problem with the unseparated linear homogeneous boundary conditions, i.e., Type II (2-41), is of importance to us. As we shall see, it is this type of boundary conditions that enables us to address the periodic boundary conditions that result when formulating the azimuthal solutions of the scalar Helmholtz equation in spheroidal coordinates.

Finally, we must consider singular, homogeneous self-adjoint boundary value problems with the less restrictive Type III or IV boundary conditions, i.e., (2-42) and (2-43). In general, Type I and II boundary conditions are not able to be applied in the singular case because they will only yield the trivial solution [30]. When the endpoints are singular, the boundary condition must be somewhat relaxed and only require that the possible solutions and their first derivatives remain finite (or bounded). Regarding the regular endpoint, Type III makes use of a separated boundary condition. It must be emphasized that the singular problem must also satisfy the condition put forth in (2-44).

According to Boyce and DiPrima [30], a striking difference between regular and singular self-adjoint boundary value problems is that the singular problem may not yield discrete eigenvalues; that is, the problem might yield nontrivial solutions for continuous values of λ in some particular interval. Moreover, the problem might have a mixture of discrete and continuous eigenvalues. In cases where a singular self-adjoint boundary value problem has only a discrete set of eigenvalues and functions, the expansion of a given function in terms of a series of eigenfunctions is possible [30]. As we shall see, it is the case where a singular self-adjoint boundary value problem has a singularity at both endpoints, employs Type IV boundary conditions, and yields only discrete eigenvalues that is of utmost importance to us. It is this particular situation that arises when determining the angular solutions of the scalar Helmholtz equation in spheroidal coordinates.

Now that we have reviewed applicable types of self-adjoint boundary value problems of second-order, we are now ready to investigate their relevant special properties. These properties are of extreme importance in physics, both classical and quantum, and will be critical to the formulation of our NZ-FZT process [29]:

1. The eigenvalues of self-adjoint boundary value problems are real.

2. The eigenfunctions of self-adjoint boundary value problems are orthogonal.

3. The eigenfunctions of self-adjoint boundary value problems of second-order form a complete set.

An important caveat must be imposed on the validity of these properties. They always hold in the case of the regular self-adjoint problem. To the contrary, these properties are not guaranteed to remain true in the case of the singular self-adjoint problem. However, Boyce and DiPrima [30] indicate that it can be shown that these properties do remain valid in the special case that the singular self-adjoint problem has only discrete eigenvalues.

The first property is important because one needs to search for only real quantities in the process of finding the eigenvalues. As we shall see, this property is critical in cases where the eigenvalues must be numerically determined. The reader is referred to [29] and [30] for the proof of this property.

The second property regarding the orthogonality of eigenfunctions implies that the following inner product is true [29]:

$$\int_a^b u_i(x)u_j^*(x)w(x)dx = 0 \quad \text{where } i \neq j \text{ and } \lambda_i \neq \lambda_j . \tag{2-46}$$

(Notice how this inner product differs from the one previously defined in (2-45); namely, it includes the weighting function $w(x)$.) Essentially, the eigenfunctions $u_1(x)$ and

$u_2(x)$ are orthogonal with respect to the weighting function $w(x)$ over the interval $[a,b]$. Orthogonality is the fundamental property behind Sturm-Liouville theory because it makes possible the isolation of the eigenfunction expansion coefficients.

The inner product defined in (2-46) is predicated on the fact that the eigenvalues be simple; that is, each eigenvalue is distinct, i.e., $\lambda_i \neq \lambda_j$, and corresponds to only one linearly independent eigenfunction. As a result, expression (2-46) guarantees orthogonality in this case. However, the situation exists where there are multiple linearly independent eigenfunctions that correspond to the same eigenvalue; such a case is labeled degenerate [29]. Multiple eigenfunctions that correspond to a degenerate eigenvalue may or may not be orthogonal. In the degenerate case where the eigenfunctions happen not to be orthogonal, the Gram-Schmidt orthogonalization method can be used to construct an orthogonal basis set [29]. As we shall see, the self-adjoint boundary value problems that are under consideration do exhibit degenerate eigenvalues. Fortunately, construction of the general solutions to the scalar Helmholtz equation in spheroidal coordinates reveals that the pertinent eigenfunctions remain orthogonal. Consequently, we shall hereafter limit our discussion to the case where the eigenfunctions are orthogonal and the specified condition (2-46) remains true.

Finally, this leads us to the third property regarding the completeness of the set of eigenfunctions. In our context, this completeness implies that any well-behaved function, i.e., at least piecewise continuous, can be approximated by a series expansion of orthogonal eigenfunctions to any degree of accuracy [29]:

$$F(x) = \sum_{i=0}^{\infty} a_i \, u_i(x) \, . \tag{2-47}$$

In mathematical terms, the set of eigenfunctions is called complete if the limit of the mean square error vanishes [29]:

$$\lim_{I\to\infty}\int_a^b \left| F(x) - \sum_{i=0}^{I} a_i u_i(x) \right|^2 w(x)dx = 0 . \tag{2-48}$$

Notice that as the number of terms increases, (2-48) only requires that the integral of the error squared go to zero, not the magnitude of the error in $[a,b]$ [29]. This convergence in the mean is less restrictive than uniform convergence. (Note that uniform convergence implies convergence in the mean; however, the converse is not true.) According to Arfken [29], (2-48) is not upset with piecewise continuous functions, which by definition allows a finite number of finite discontinuities.

In order to evaluate the expansion coefficients of (2-47), we first consider normalization of eigenfunctions. The inner product expressed in (2-46) only addresses the case where the eigenfunctions are different, i.e., $i \neq j$. However, in the special case that the eigenfunctions are the same, i.e., $i = j$, the inner product can be expressed as follows:

$$\int_a^b u_i(x)u_i^*(x)w(x)dx = \int_a^b \left|u_i(x)\right|^2 w(x)dx = N_i . \tag{2-49}$$

Note that the square root of the resulting Sturm-Liouville normalization constant N_i is often referred to as the norm of the eigenfunction. Moreover, the value of this normalization constant can be arbitrarily chosen. This degree of freedom exists because each eigenfunction is a solution to a given linear, homogenous differential equation, viz., the Sturm-Liouville equation; that is, basic differential equation theory indicates that we may multiply a solution by any constant, and it will still be a solution. A common normalization scheme requires that each eigenfunction be multiplied by $1/\sqrt{N_i}$, i.e., the reciprocal of its norm, so that the inner product expressed in (2-49) yields unity; these rescaled orthogonal eigenfunctions are then said to be orthonormal. In addition to the just described orthonormal scheme, we shall also employ other normalization schemes during

the formulation of the NZ-FZT process where the Sturm-Liouville normalization constant is not taken as unity.

Now that we have addressed the issue of normalization, the individual cases expressed in (2-46) and (2-49) can be combined to yield the single orthogonality relation:

$$\int_a^b u_i(x)u_j{}^*(x)w(x)dx = N_i\delta_{i,j} \tag{2-50}$$

where $\delta_{i,j}$ represents a Kronecker delta. Finally, we can evaluate the expansion coefficients of (2-47) by using the following expression:

$$a_j = \frac{1}{N_j}\int_a^b F(x)u_j{}^*(x)w(x)dx\,. \tag{2-51}$$

This expression follows by multiplying both sides of (2-47) by $[u_j{}^*(x)w(x)]$ and integrating over the interval $[a,b]$. We then proceed to make use of (2-50) and employ the discrete version of the sifting property (due to the Kronecker delta) in order to isolate the j^{th} term. At this point in the discussion, it is quite obvious that it is orthogonality that enables the eigenfunction expansion method to be such an effective analytical approach.

2.2.5 General Solutions of the Scalar Helmholtz Equation in Spheroidal Coordinates

We are now ready to begin construction of the general solutions to the scalar Helmholtz equation in spheroidal coordinates by applying Sturm-Liouville theory to the separated differential equations, i.e., (2-34a)-(2-36a) and (2-34b)-(2-36b). Physical requirements impose two sets of boundary conditions that limit the general solutions to a discrete set of eigenfunctions with corresponding eigenvalues: single-valuedness of the azimuthal solutions and finiteness of the angular solutions (specifically at the poles of the spheroid) [23]. Consequently, self-adjoint boundary value problems must be formulated that address both the azimuthal and the angular solutions of the separated differential

Table 2.2 Overview of the Azimuthal and Angular Self-Adjoint Boundary Value Problems

Differential Equation	$p(x)$	$q(x)$	$w(x)$	$[a,b]$	Boundary Conditions	λ (eigenvalues)
Prolate Angular (2-35a)	$1-\eta^2$	$-\frac{m^2}{1-\eta^2}-h^2\eta^2$	1	$[-1,1]$ (singular)	Type IV (2-43) (finite at both boundaries)	$\lambda_{m,l}(h)$
Oblate Angular (2-35b)	$1-\eta^2$	$-\frac{m^2}{1-\eta^2}+h^2\eta^2$	1	$[-1,1]$ (singular)	Type IV (2-43) (finite at both boundaries)	$\lambda_{m,l}(-jh)$
Prolate/Oblate Azimuthal (SHO) (2-36a)/(2-36b)	1	0	1	$[0,2\pi]$ (regular)	Type II (2-41) (periodic)	m^2

Note: $p(x)$, $q(x)$, and $w(x)$ are with regard to the Sturm-Liouville equation (2-38).

equations. An overview of these self-adjoint boundary value problems is provided in Table 2.2. Regarding the radial solution, its behavior is driven by the results of the azimuthal and angular self-adjoint boundary value problems; that is, the allowable azimuthal and angular solutions (i.e., the eigenfunctions) dictate the corresponding permissible separation constants (which directly correspond to the eigenvalues). Accordingly, the radial solution can be understood using conventional differential equation theory only after analyzing the azimuthal and angular self-adjoint boundary value problems.

Let us first address the separated differential equations that pertain to the azimuthal solution, namely, (2-36a) and (2-36b). Since both of these equations are mathematically identical, it is only necessary to analyze their form. The form of these azimuthal differential equations is quite common and has been traditionally referred to as the simple harmonic oscillator (SHO) [29]. As we can see, the SHO is easily put into self-adjoint form, i.e., satisfies the Sturm-Liouville equation (2-38). The interval of the azimuthal coordinate φ is designated as $[0,2\pi]$ by definition (see 2.1.1). As we have

previously stated, physical requirements demand that the azimuthal solution be single-valued, i.e.,

$$\Phi(\varphi + 2\pi) = \Phi(\varphi)\,. \tag{2-52}$$

The constraint imposed by (2-52) is equivalent to requiring the azimuthal solution to have a period of 2π or some integral multiple of it [29]. This physical requirement can be represented as the following periodic boundary conditions for the interval $[0, 2\pi]$ [30]:

$$\Phi(0) - \Phi(2\pi) = 0 \text{ and } \Phi'(0) - \Phi'(2\pi) = 0\,. \tag{2-53}$$

Notice that the boundary conditions of (2-53) actually are of Type II, i.e., (2-41). Furthermore, it is easy to show that the SHO under these particular Type II boundary conditions satisfies the condition required for all second-order self-adjoint boundary value problems, viz., (2-44). Since there are no singularities at the endpoints, our azimuthal self-adjoint boundary value problem is considered regular.

The eigenvalues of the azimuthal self-adjoint boundary value problem can be shown from basic differential equation theory to be [30]:

$$\lambda_m = m^2 \qquad \text{where } m = 0, 1, 2, \ldots. \tag{2-54}$$

This result is consistent with Sturm-Liouville theory. Differential equation theory can also be used to determine the allowable azimuthal solutions (i.e., the eigenfunctions) [29]:

$$\begin{Bmatrix} \sin m\varphi \\ \cos m\varphi \end{Bmatrix}. \tag{2-55}$$

In addition to (2-55), differential equation theory also allows us to express the azimuthal eigenfunctions as the following linearly independent complex exponentials [29]:

$$\left\{ e^{+jm\varphi} \right\}. \tag{2-56}$$

As we shall see, these complex exponentials will be the form of choice during our construction of the general solutions. Upon review of (2-55) and (2-56), one may recognize the linearly independent solutions as the basis sets for both the trigonometric Fourier series and its corresponding exponential Fourier series, respectively.

It is important to note that there are two linearly independent eigenfunctions corresponding to each nonzero eigenvalue; that is, with the exception of $\lambda_0 = 0$, the remaining eigenvalues are two-fold degenerate. Although Sturm-Liouville theory cannot guarantee orthogonality of eigenfunctions that correspond to a particular degenerate eigenvalue, direct evaluation of (2-50) with the exponential form of the eigenfunctions does confirm that all solutions are orthogonal; this leads us to the following needed orthogonality relation [29]:

$$\int_0^{2\pi} e^{+jm\varphi} \left(e^{+jm'\varphi} \right)^* \, d\varphi = 2\pi\delta_{m,m'} \tag{2-57}$$

where $N_m = 2\pi$ and $w(x) = 1$.

We shall now turn our attention to the separated differential equations that pertain to the angular solutions, namely, (2-35a) and (2-35b). Gaining insight into the behavior of both of these angular differential equations under their imposed boundary conditions is much more involved than their azimuthal counterparts. At this point in our discussion, we shall predominately rely on the monograph put forth by Flammer [23] (which is considered one of the most comprehensive works on the subject) and the text by Morse and Feshbach [22] to develop the required understanding of these angular solutions. Furthermore, we shall subsequently refer to both of these works regarding the corresponding radial solutions.

Upon review of the prolate and oblate separated differential equations for the radial and angular solutions, i.e., (2-34a)/(2-34b) and (2-35a)/(2-35b), it is important to

note that the oblate differential equations can be obtained from their prolate counterparts using the following transformation [23]:

$$h \to -jh \text{ (or } +jh\text{); and } \xi \to +j\xi \text{ (or } -j\xi\text{).} \tag{2-58}$$

Since these sets of differential equations are closely related through this simple transformation, much of the oblate solution development closely parallels that of its prolate counterpart. Consequently, for the sake of brevity, throughout the ensuing development there will be instances where the results of the oblate case are obtained from the prolate case using the aforementioned transformation. However, as always, one must exercise caution and not apply this transformation blindly; there will be points (especially in the computational process) where the approaches between the two cases differ. Because the separated differential equations are so closely related, many investigators have included these transformations within the notation of the solutions and their respective eigenvalues to distinguish between the prolate and oblate cases.

The separated angular differential equations, i.e., (2-35a) and (2-35b), can be put into self-adjoint form such that both satisfy the Sturm-Liouville equation. By definition, the interval of the angular coordinate η for both the prolate and oblate cases is designated as $[-1,1]$ (see 2.1.1). Upon inspection of the angular differential equations, we are able to see that singularities exist at both endpoints of the interval: $\eta = \pm 1$. Since physical requirements demand that the angular solutions of both the prolate and oblate case remain finite over the specified interval in the presence of these endpoint singularities, we must appropriately apply Type IV boundary conditions. These boundary conditions coupled with their respective differential equations enable us to formulate the needed angular self-adjoint boundary value problems (which happen to be singular in both spheroidal cases).

Determining the eigenvalues of the angular self-adjoint boundary value problems is much more complicated than finding those of their azimuthal counterparts (i.e., the SHO). As a matter of fact, computation of the exact eigenvalues is not straightforward

and requires the use of a sophisticated numerical process that is subsequently addressed in Chapter 3. However, some relevant points regarding these eigenvalues and how they relate to the angular solutions can be made at this point in our discussion.

In the limiting case that $h = 0$, both angular differential equations (2-35a) and (2-35b) approach the form of the associated Legendre equation [29]:

$$\frac{d}{d\eta}\left[\left(1-\eta^2\right)\frac{d}{d\eta}S(\eta)\right] - \frac{m^2}{\left(1-\eta^2\right)}S(\eta) + \underbrace{\lambda}_{\equiv l(l+1)} S(\eta) = 0 \qquad \text{(2-59)}$$

where $-1 \le \eta \le 1$.

The associated Legendre equation is the ordinary differential equation that results when solving the scalar Helmholtz equation in spherical coordinates (after applying the separation of variables method). Essentially, the associated Legendre equation is a special case of both angular differential equations; this intuitively makes sense because a sphere is a special case of a spheroid. We shall use the insight gained from this special case as a springboard to extend our understanding to the more general angular self-adjoint boundary value problems for both the prolate and oblate cases.

The eigenvalues of the self-adjoint boundary value problem associated with this special case (which also requires the solution to remain bounded over the interval) are known to be [29]:

$$\lambda_{m,l}(h=0) = l(l+1) \quad \text{where } -l \le m \le +l \text{ and } l = 0, 1, 2, \ldots. \qquad \text{(2-60)}$$

Equation (2-60) indicates that each real eigenvalue is referenced by a two-dimensional index where the index *m* is considered the *order* (based upon the azimuthal separation constant, $-m^2$) and the index *l* is referred to as the *degree* (based upon the angular separation constant, $\lambda = l(l+1)$). Table 2.3 depicts a portion of an infinite two-dimensional matrix where the elements are the eigenvalues with indices that correspond to the order and degree, respectively. Inspection of both (2-60) and Table 2.3 reveals that

Table 2.3 Portion of Infinite Two-Dimensional Eigenvalue Matrix for the Special Case where $\lambda_{m,l}(h=0)$

Index	l =0	1	2	3
m = -3	-	-	-	12
-2	-	-	6	12
-1	-	2	6	12
0	0	2	6	12
1	-	2	6	12
2	-	-	6	12
3	-	-	-	12

Note: A hyphen denotes no corresponding eigenvalue.

for the special case where $h=0$, the eigenvalues are independent of the order *m* and thus are degenerate; namely, the eigenfunctions of (2-59) having the same order *m* happen to share the same eigenvalue. In addition, equation (2-60) implies that all of the eigenvalues form a monotonic increasing sequence for a given order *m*:

$$\lambda_{m,l}(h=0) < \lambda_{m,l+1}(h=0). \tag{2-61}$$

The eigenfunctions of the self-adjoint boundary value problem associated with this special case (which also requires the solution to remain bounded over the interval) are well known and are referred to as the associated Legendre functions of the first kind [29]: $P_l^m(\eta)$, where *m* is the order and *l* is the degree. Both indices are the same as those used to reference the corresponding eigenvalue. Throughout this dissertation, we shall always employ Ferrer's definition of the associated Legendre functions of the first kind when the argument is on the $-1 < x < 1$ branch cut, namely,

$$P_l^m(x) = (1-x^2)^{m/2}\frac{d^m}{dx^m}P_l(x) \qquad \text{(Ferrer's definition),} \qquad (2\text{-}62)$$

and Hobson's definition when the argument lies elsewhere in the finite complex plane, namely,

$$P_l^m(z) = (z^2-1)^{m/2}\frac{d^m}{dz^m}P_l(z) \qquad \text{(Hobson's definition).} \qquad (2\text{-}63)$$

Notice how both definitions approach the same values at the ± 1 branch points. It is at this point in our discussion that we refer the reader to Appendix D for a more comprehensive understanding of Legendre functions.

It is important for us to understand that for negative orders of *m*, these eigenfunctions are not linearly independent from their positive order counterparts. This statement remains consistent with the associated Legendre equation (2-59) because the solutions are symmetric with respect to the order *m* (due to the m^2 term). Accordingly, the associated Legendre functions of the first kind with negative orders are proportional to their positive order counterparts as follows [29]:

$$P_l^{-m}(\eta) = (-1)^m \frac{(l-m)!}{(l+m)!}P_l^m(\eta)\,. \qquad (2\text{-}64)$$

Note that the presence of a proportionality constant between the positive and negative order solutions is justified based upon differential equation theory. This is so because a linear combination of solutions of a linear homogeneous differential equation is also a solution of the equation [30]. One advantage of using this particular constant of proportionality is that it enables the recurrence relations that are valid for $0 \le m \le l$ to remain valid for $-l \le m < 0$ [29].

Once again Sturm-Liouville theory cannot guarantee orthogonality of eigenfunctions corresponding to a particular degenerate eigenvalue. However, the eigenvalues are distinct with respect to order because they form a monotonic increasing sequence for any given order *m*, i.e., (2-61). The fact that all of the eigenvalues for a

given order *m* differ from one another implies that the corresponding eigenfunctions for a given order *m* are mutually orthogonal. This assertion is demonstrated by Arfken [29] when he shows that the associated Legendre functions of the first kind for a given order *m* are indeed mutually orthogonal and satisfy the following orthogonality relation:

$$\int_{-1}^{1} P_l^m(\eta) P_{l'}^m(\eta) d\eta = \frac{2}{2l+1} \frac{(l+m)!}{(l-m)!} \delta_{l,l'} \tag{2-65}$$

where $N_{m,l} \equiv \frac{2}{2l+1} \frac{(l+m)!}{(l-m)!}$ and $w(x) = 1$.

Since the eigenfunctions and the eigenvalues are referenced by the indices *m* and *l*, it is logical that we do the same for the corresponding Sturm-Liouville normalization constants. Moreover, we would like to point out that the normalization given in (2-65) is the one that has been customarily used for associated Legendre functions of the first kind. Even though it is possible to develop an orthogonality relation for these associated Legendre functions for a given degree *l* (with differing orders *m*), its usefulness is limited because in physical problems orthogonality of the azimuthal dependence ties together the possible orders *m* and thus leads to (2-65) [29].

If we lift the condition imposed on the associated Legendre self-adjoint boundary value problem that requires the solutions to remain finite, a second set of linearly independent solutions becomes acceptable [29]. These solutions are logarithmic in nature, i.e., become infinite at the boundaries of the interval, and are referred to as the associated Legendre functions of the second kind, $Q_l^m(\eta)$. However, these solutions are seldom used in the angular context, i.e., over the interval $[-1,1]$, because of the imposed physical requirements.

Having explored the behavior of the solutions for the special case where $h = 0$, we are now in a better position to understand the more general solutions to the angular self-adjoint boundary value problems. In the general case where $h \neq 0$, the eigenvalues are now a function of both indices, *m* and *l*, in addition to the independent variable *h* [23].

Because of these dependencies, the eigenvalues can be represented for the prolate and oblate cases within the notation as $\lambda_{m,l}(h)$ and $\lambda_{m,l}(-jh)$, respectively [23]. Unlike the special case, the eigenvalues need to be evaluated numerically because they do not have closed form representations. However, both angular differential equations, i.e., (2-35a) and (2-35b), indicate that corresponding positive and negative order eigenfunctions share the same eigenvalue for a given order *m* (just like the special case where $h = 0$) [23]:

Prolate: $\lambda_{-m,l}(h) = \lambda_{m,l}(h)$; (2-66a)

Oblate: $\lambda_{-m,l}(-jh) = \lambda_{m,l}(-jh)$. (2-66b)

Once again, this occurs because the solutions to both self-adjoint boundary value problems are symmetric with respect to the order *m* due to the m^2 term (see Table 2.2). Another important similarity between the general and special cases is that eigenvalues for the general cases also form a monotonic increasing sequence for a given order *m* [22]:

Prolate: $\lambda_{m,l}(h) < \lambda_{m,l+1}(h)$; (2-67a)

Oblate: $\lambda_{m,l}(-jh) < \lambda_{m,l+1}(-jh)$; (2-67b)

where $-l \le m \le +l$ and $l = 0, 1, 2, \ldots$.

Making use of the symmetry of the eigenvalues with respect to the order *m* (i.e., 2-66a and 2-66b), we are able to display in Table 2.4 a portion of the infinite two-dimensional eigenvalue matrix for both the prolate and oblate cases.

As for the eigenfunctions of the self-adjoint boundary value problems associated with the general cases (i.e., where $h \neq 0$), they are not so well known and have been referred to as prolate and oblate spheroidal angle functions of the first kind: $S_{m,l}^{(1)}(h,\eta)$ and $S_{m,l}^{(1)}(-jh,\eta)$, respectively [23]. Once again, indices *m* and *l* are still the same as those used to reference the corresponding eigenvalue. However, unlike the

Table 2.4 Portion of Infinite Two-dimensional Eigenvalue Matrix for the Prolate and Oblate Cases ($h \neq 0$)

Index	l =0	1	2
m = -2	-	-	$\lambda_{2,2}(h)$; $\lambda_{2,2}(-jh)$
-1	-	$\lambda_{1,1}(h)$; $\lambda_{1,1}(-jh)$	$\lambda_{1,2}(h)$; $\lambda_{1,2}(-jh)$
0	$\lambda_{0,0}(h)$; $\lambda_{0,0}(-jh)$	$\lambda_{0,1}(h)$; $\lambda_{0,1}(-jh)$	$\lambda_{0,2}(h)$; $\lambda_{0,2}(-jh)$
1	-	$\lambda_{1,1}(h)$; $\lambda_{1,1}(-jh)$	$\lambda_{1,2}(h)$; $\lambda_{1,2}(-jh)$
2	-	-	$\lambda_{2,2}(h)$; $\lambda_{2,2}(-jh)$

Note: A hyphen denotes no corresponding eigenvalue.

eigenfunctions for the special case, i.e., $P_l^m(\eta)$, the spheroidal angle functions of the first kind not only depend on the angular parameter η, but also on the independent variable *h*. Flammer [23] states that both spheroidal angle functions of the first kind can be expressed as an infinite expansion of associated Legendre functions of the first kind:

Prolate: $$S_{m,l}^{(1)}(h,\eta) = \sum_{r=0,1}^{\infty}{}' d_r^{m,l}(h) P_{m+r}^m(\eta) \text{ where } 0 \le m \le l ; \quad (2\text{-}68a)$$

Oblate: $$S_{m,l}^{(1)}(-jh,\eta) = \sum_{r=0,1}^{\infty}{}' d_r^{m,l}(-jh) P_{m+r}^m(\eta) \text{ where } 0 \le m \le l . \quad (2\text{-}68b)$$

In these expressions and from this point forward, the prime over the summation sign indicates that the summation is over only even values of *r* when (*l* - *m*) is even, and over only odd values of *r* when (*l* - *m*) is odd. Consequently, spheroidal angle functions are themselves even functions when (*l* - *m*) is even, and odd functions when (*l* - *m*) is odd.

Later, we shall exploit this property to improve the computational efficiency of the special function routines and the overall NZ-FZT computer software.

Like the special case where $h = 0$, the eigenfunctions of the general case, i.e., the spheroidal angle functions, that correspond to negative orders of *m* are also not linearly independent from their positive order counterparts. Once again, this is so because the solutions to the prolate and oblate self-adjoint boundary value problems are symmetric with respect to the order *m* (see Table 2.2). Similarly, the eigenfunctions that correspond to negative orders of *m* are also directly proportional to their positive order counterparts. Regarding the proportionality constant between the positive and negative order eigenfunctions, Flammer [23] recommends using a constant that is identical to the one used for the associated Legendre functions of the first kind, i.e., contained in (2-64). This particular proportionality constant would allow the infinite expansions provided in (2-68a) and (2-68b) to remain valid for negative orders of *m*. However, for our particular application, it will facilitate our development if we assume a proportionally constant of unity:

Prolate: $$S_{-m,l}^{(1)}(h,\eta) \equiv S_{m,l}^{(1)}(h,\eta)\,; \tag{2-69a}$$

Oblate: $$S_{-m,l}^{(1)}(-jh,\eta) \equiv S_{m,l}^{(1)}(-jh,\eta)\,. \tag{2-69b}$$

As before, we are justified in doing so based upon fundamental differential equation theory. The advantage of assuming a unity proportionality constant is that it prevents us from having to unnecessarily tote around an additional factor for negative values of *m*; this factor for negative orders of *m* would make no difference in our final formulation because it would ultimately end up being absorbed into the eigenfunction expansion coefficients. Accordingly, we have appropriately applied the restriction $0 \le m \le l$ to the expansion representation of the spheroidal angle functions presented in (2-68a) and (2-68b).

Akin to the special case where $h = 0$, each of the angular self-adjoint boundary value problems also possesses a second set of linearly independent solutions for the general case. These respective sets of linearly independent solutions are referred to as the

prolate and oblate spheroidal angle functions of the second kind: $S_{m,l}^{(2)}(h,\eta)$ and $S_{m,l}^{(2)}(-jh,\eta)$, respectively [23]. These solutions are also logarithmic in nature and can be expressed as an infinite expansion of associated Legendre functions of the second kind, $Q_l^m(\eta)$ [23]. However, the physically imposed boundary condition requiring the solutions to remain finite precludes both $S_{m,l}^{(2)}(h,\eta)$ and $S_{m,l}^{(2)}(-jh,\eta)$ as acceptable solutions to their respective angular self-adjoint boundary value problem. Consequently, we shall refrain from any further discussion of spheroidal angle functions of the second kind. Because we will not be dealing with spheroidal angle functions of the second kind, we are now able to drop the superscript in the notation and subsequently avoid confusion when referring to the spheroidal angle functions of the first kind: $S_{m,l}(h,\eta) \equiv S_{m,l}^{(1)}(h,\eta)$ and $S_{m,l}(-jh,\eta) \equiv S_{m,l}^{(1)}(-jh,\eta)$.

We shall now turn our attention to orthogonality of the spheroidal angle functions of the first kind. Upon review of numerical results for selected values by Hanish and King [32] and the power-series expansions provided by Flammer [23], the degenerate eigenvalues for the special case (i.e., $h = 0$) appear to become distinct and simple for both the prolate and oblate general cases. Furthermore, expressions (2-67a) and (2-67b) indicate that in both general cases the eigenvalues are distinct with respect to order because they too form a monotonic increasing sequence for any given order *m*. By way of Sturm-Liouville theory, this fact implies that the eigenfunctions corresponding to a given order *m* are mutually orthogonal. Flammer [23] supports this assertion by stating that spheroidal angle functions of the first kind for a given order *m* remain mutually orthogonal such that they satisfy the following orthogonality relations:

Prolate: $$\int_{-1}^{1} S_{m,l}(h,\eta) S_{m,l'}(h,\eta) d\eta = N_{m,l}(h)\delta_{l,l'}; \tag{2-70a}$$

Oblate: $$\int_{-1}^{1} S_{m,l}(-jh,\eta) S_{m,l'}(-jh,\eta) d\eta = N_{m,l}(-jh)\delta_{l,l'}. \tag{2-70b}$$

This leads us to the last issue pertaining to the angular solutions that must be addressed: normalization. Since we are dealing with linear homogeneous differential equations in the angular self-adjoint boundary value problems, the possible solutions, i.e., the eigenfunctions, can be scaled by any arbitrary constant. In the special case where $h = 0$, the solutions (i.e., the associated Legendre functions of the first kind) already have a universally accepted normalization scheme. However, in both general cases of the angular self-adjoint boundary value problems, we are not so fortunate. Several different normalization schemes have been presented within the literature and are tabulated by Flammer [23]. The one thing that is common among almost all of the tabulated normalization schemes (with the exception of one) is that they somehow scale the spheroidal angle function to behave like the associated Legendre function of the first kind (i.e., the special case solution where $h = 0$) with regard to a certain parameter.

For the sake of brevity, we shall only discuss the popular normalization schemes put forth by Flammer [23] and Morse and Feshbach [22]. Flammer [23] presents a normalization scheme that dictates the following as $\eta \to 0$: all even spheroidal angle functions behave like their corresponding associated Legendre functions, and all first derivatives of odd spheroidal angle functions behave as the first derivatives of their respective associated Legendre functions. In mathematical terms,

Prolate: $S_{m,l}(h,0) = P_l^m(0)$ for $(l-m)$ even, (2-71a)

$S'_{m,l}(h,0) = P_l'^m(0)$ for $(l-m)$ odd; (2-72a)

Oblate: $S_{m,l}(-jh,0) = P_l^m(0)$ for $(l-m)$ even, (2-71b)

$S'_{m,l}(-jh,0) = P_l'^m(0)$ for $(l-m)$ odd. (2-72b)

As for Morse and Feshbach [22], their normalization scheme stipulates that the spheroidal angle functions behave like their corresponding associated Legendre functions as $\eta \to 1$:

Prolate: $$\left[\left(1-\eta^2\right)^{-\frac{m}{2}} S_{m,l}(h,\eta)\right]_{\eta=1} = \left[\left(1-\eta^2\right)^{-\frac{m}{2}} P_l^m(\eta)\right]_{\eta=1}; \qquad \text{(2-73a)}$$

Oblate: $$\left[\left(1-\eta^2\right)^{-\frac{m}{2}} S_{m,l}(-jh,\eta)\right]_{\eta=1} = \left[\left(1-\eta^2\right)^{-\frac{m}{2}} P_l^m(\eta)\right]_{\eta=1}. \qquad \text{(2-73b)}$$

In general, conversion factors between any pair of normalization schemes can be developed. Furthermore, the choice of the normalization scheme is immaterial because the eigenfunction expansion coefficients will ultimately assume their proper values based on the normalization of the eigenfunctions. An important point that may not be quite so obvious is that the Sturm-Liouville normalization constants, i.e., $N_{m,l}(h)$ and $N_{m,l}(-jh)$, are also dependent on the normalization scheme chosen. In the ensuing theoretical development of our NZ-FZT process, we shall maintain generality and assume an arbitrary normalization scheme. However, in Chapters 3 and 4 when we address computational details of the NZ-FZT process, we shall opt to use the normalization scheme of Morse and Feshbach for the computation of the spheroidal angle functions (including their respective Sturm-Liouville normalization constants).

Equipped with an understanding of the solutions to the azimuthal and angular self-adjoint boundary value problems, we are now able to address the radial solutions to the scalar Helmholtz equation in spheroidal coordinates. As we mentioned earlier in this section, the allowable radial solutions are driven by the possible separation constants (which directly correspond to the eigenvalues of the azimuthal and angular self-adjoint boundary value problems; see Table 2.2).

Two sets of linearly independent solutions exist that satisfy the radial differential equations presented in (2-34a) and (2-34b). These linearly independent solutions sets are referred to as the prolate and oblate spheroidal radial functions of the first and second kind: $\{ R_{m,l}^{(1)}(h,\xi),\ R_{m,l}^{(2)}(h,\xi) \}$ and $\{ R_{m,l}^{(1)}(-jh, j\xi),\ R_{m,l}^{(2)}(-jh, j\xi) \}$, respectively. These functions appear to be universally defined so that in the special case where $h = 0$, both sets of spheroidal radial functions approach the spherical Bessel and Neumann functions

$\{ j_l(\xi),\ n_l(\xi) \}$ [22], [23]. Based upon differential equation theory, both sets of linearly independent radial solutions can be combined to produce a complex form of these solutions referred to as the prolate and oblate spheroidal radial functions of the third and fourth kind: $\{ R_{m,l}^{(3)}(h,\xi),\ R_{m,l}^{(4)}(h,\xi) \}$ and $\{ R_{m,l}^{(3)}(-jh, j\xi),\ R_{m,l}^{(4)}(-jh, j\xi) \}$, respectively. The spheroidal radial functions of the third and fourth kind are related to those of the first and second kind by the following expressions [23]:

Prolate: $$R_{m,l}^{(3),(4)}(h,\xi) = R_{m,l}^{(1)}(h,\xi) \pm jR_{m,l}^{(2)}(h,\xi); \tag{2-74a}$$

Oblate: $$R_{m,l}^{(3),(4)}(-jh, j\xi) = R_{m,l}^{(1)}(-jh, j\xi) \pm jR_{m,l}^{(2)}(-jh, j\xi). \tag{2-74b}$$

It must be noted that the spheroidal radial functions of the third and fourth kind are somewhat analogous to complex exponentials. As a matter of fact, both of these spheroidal radial functions asymptotically approach complex exponentials as $\xi \to \infty$ [23]:

Prolate: $$\lim_{\xi\to\infty} R_{m,l}^{(3),(4)}(h,\xi) = \frac{1}{h\xi}\exp\pm j\left[h\xi - \frac{1}{2}(l+1)\pi\right]; \tag{2-75a}$$

Oblate: $$\lim_{\xi\to\infty} R_{m,l}^{(3),(4)}(-jh, j\xi) = \frac{1}{h\xi}\exp\pm j\left[h\xi - \frac{1}{2}(l+1)\pi\right]. \tag{2-75b}$$

As we shall see, both of these asymptotic expressions will prove useful later on in our development. Furthermore, these functions also appear to be universally defined so that in the special case that $h = 0$, both complex sets of spheroidal radial functions approach the spherical Hankel functions of the first and second kind $\{ h_l^{(1)}(\xi),\ h_l^{(2)}(\xi) \}$ [23].

Just like the spheroidal angle functions, the spheroidal radial functions that correspond to negative orders of *m* are not linearly independent from their positive order counterparts. This is so because the solutions to the both the prolate and oblate radial differential equations, i.e., (2-34a) and (2-34b), are also symmetric with respect to the

order *m* due to the m^2 term. As for the proportionality constant between the positive and negative order solutions, our development is simplified if we define it to be unity:

Prolate: $$R_{-m,l}^{(3),(4)}(h,\xi) \equiv R_{m,l}^{(3),(4)}(h,\xi)\,; \tag{2-76a}$$

Oblate: $$R_{-m,l}^{(3),(4)}(-jh, j\xi) \equiv R_{m,l}^{(3),(4)}(-jh, j\xi)\,. \tag{2-76b}$$

Once again, we are at liberty to do so because a linear combination of solutions of a linear homogeneous differential equation is also a solution of the equation [30].

The spheroidal radial functions of the third and fourth kind have significant meaning in the study of wave phenomena when using the spheroidal coordinate systems. Both of these linearly independent solutions, i.e., $R_{m,l}^{(3)}$ and $R_{m,l}^{(4)}$, represent incoming and outgoing traveling waves, respectively. Note that the mathematical form of the complex exponentials in the asymptotic relations of (2-75a) and (2-75b) is consistent with this physical interpretation of the spheroidal radial functions.

Now that the separated solutions for the scalar Helmholtz equation in spheroidal coordinates have been understood, we are at the point where the overall general solutions can be constructed. Referring back to (2-33a) and (2-33b), the overall solution is obtained by taking the product of the separated solutions. However, our investigation has revealed that the possible solutions are limited to a discrete set of eigenfunctions based upon the order *m* and the degree *l*. Therefore, the general solutions must be expressed as a linear combination of these resulting eigenfunctions [23]:

Prolate: $$\psi^{P}(\xi,\eta,\varphi) = \sum_{m,l} a_{m,l}\psi_{m,l}^{P}(\xi,\eta,\varphi) \tag{2-77a}$$

where $$\psi_{m,l}^{P}(\xi,\eta,\varphi) = \begin{Bmatrix} R_{m,l}^{(3)}(h,\xi) \\ R_{m,l}^{(4)}(h,\xi) \end{Bmatrix} \{S_{m,l}(h,\eta)\} \begin{Bmatrix} e^{+jm\varphi} \\ e^{-jm\varphi} \end{Bmatrix}; \tag{2-78a}$$

Oblate: $$\psi^{O}(\xi,\eta,\varphi)=\sum_{m,l} a_{m,l}\psi^{O}_{m,l}(\xi,\eta,\varphi) \tag{2-77b}$$

where $$\psi^{O}_{m,l}(\xi,\eta,\varphi)=\begin{Bmatrix} R^{(3)}_{m,l}(-jh,j\xi) \\ R^{(4)}_{m,l}(-jh,j\xi) \end{Bmatrix}\{S_{m,l}(-jh,\eta)\}\begin{Bmatrix} e^{+jm\varphi} \\ e^{-jm\varphi} \end{Bmatrix}. \tag{2-78b}$$

Note that we have opted to use the exponential form of the solutions in the expressions for the general solutions.

By evoking Sturm-Liouville theory, we are allowed to approximate the solution to the scalar Helmholtz equation in spheroidal coordinates to any degree of accuracy with an expansion of its respective eigenfunctions. In expressions (2-78a) and (2-78b), the functions encased in the brackets are understood to be the basis sets of the eigenfunction expansions. Based upon differential equation theory, a particular solution can be formulated from the general solutions only after imposing boundary conditions. Further in our development, we shall apply the specific boundary conditions to our general solutions to formulate the particular eigenfunction expansion needed for our NZ-FZT process. Lastly, having presumed the completeness of these developed basis sets, we can expect convergence in the mean for an eigenfunction expansion of a well-behaved particular solution.

2.2.6 Statement of Boundary Conditions Imposed by the NZ-FZT Process

In the previous section, we applied the boundary conditions imposed by physical requirements when constructing both general solutions of the scalar Helmholtz equation in spheroidal coordinates (viz., single-valuedness of the azimuthal solutions and finiteness of the angular solutions). One can recall that it was these boundary conditions that limited the general solutions to a discrete set of eigenfunctions. However, in order to construct the particular solutions to our overall prolate and oblate spheroidal NZ-FZT boundary value problems, we must further impose additional boundary conditions. It is here that we state these additional boundary conditions, as well as express their impact on narrowing the general solutions to the desired particular solutions.

As stated at the outset of this chapter, the purpose of our NZ-FZT process is to use near-zone E-field samples along a spheroidal transformation surface (which surrounds the radiating structure) to extrapolate the far-zone response. The first significant boundary condition is implicitly contained within this objective. Specifically, the fact that the spheroidal transformation surface fully encompasses the radiating structure of interest implies spatial causality with respect to wave and energy propagation; that is, at all points outside the closed spheroidal transformation surface (i.e., the source region), only outgoing traveling waves must exist. Enforcing this boundary condition on a surface at infinity was first introduced by Sommerfeld and is referred to as the "radiation condition" [33]. As indicated by Felsen and Marcuvitz [33], the Sommerfeld radiation condition also implies that the transverse components of a spherically diverging wave propagating in a homogeneous medium behave as $\left(e^{-jkr}/r\right)$.

By virtue of the Sommerfeld radiation condition, the particular solutions to our overall spheroidal NZ-FZT boundary value problems must only contain the outward traveling spheroidal radial functions of the fourth kind, viz., $R_{m,l}^{(4)}(h,\xi)$ and $R_{m,l}^{(4)}(-jh, j\xi)$. Furthermore, these radial functions must also remain consistent with the radiation condition and behave as $\left(e^{-jkr}/r\right)$ in the far-zone; this is demonstrated by the following asymptotic expressions for spheroidal radial functions of the fourth kind:

Prolate: $$\lim_{\xi\to\infty} R_{m,l}^{(4)}(h,\xi) = \frac{j^{l+1}}{k}\left(e^{-jkr}/r\right); \tag{2-79a}$$

Oblate: $$\lim_{\xi\to\infty} R_{m,l}^{(4)}(-jh, j\xi) = \frac{j^{l+1}}{k}\left(e^{-jkr}/r\right). \tag{2-79b}$$

(Note that these equations can be found from the asymptotic expressions of (2-75a) and (2-75b) together with the fact that $h\xi \to k\,r$ in the far-zone.) It should be emphasized that these expressions prove to be very important in the development of our NZ-FZT process. They essentially mean that the radial dependence of the field in the far-zone will

approach that of a spherically diverging wave (expressed in spherical coordinates) regardless of the independent variable *h*. Moreover, the far-zone behavior of the radial dependence is identical for both the prolate and oblate cases.

Having discussed the boundary condition imposed on the spheroidal surface at infinity, we now must address the boundary condition that exists on the spheroidal transformation surface. The NZ-FZT process input specifies the E-field on this boundary. As a result, the particular field solutions for both the prolate and oblate cases must be constructed to match the near-zone along their respective transformation surface. Using the mathematical description of the spheroidal transformation surfaces provided earlier (see 2.1.1), we express these Dirichlet boundary conditions as follows:

Prolate: $$\psi^{P}(\xi,\eta,\varphi)\big|_{\Omega_P} \equiv \psi^{P}(\xi_o,\eta,\varphi) = known; \tag{2-80a}$$

Oblate: $$\psi^{O}(\xi,\eta,\varphi)\big|_{\Omega_O} \equiv \psi^{O}(\xi_o,\eta,\varphi) = known. \tag{2-80b}$$

The boundary conditions imposed by (2-80a) and (2-80b) are classified as Dirichlet boundary conditions because they specify the values of a function on a given boundary [29].

2.2.7 Development of Spheroidal Wave-Harmonics

In order to facilitate construction of the particular solutions to our overall NZ-FZT boundary value problems, we must first develop an understanding of spheroidal wave-harmonics for both the prolate and oblate cases. Since no reference appears to address them, we must take some time to develop and define our own. Fortunately, we have a logical starting point to base our development: conventional spherical harmonics, i.e., the special case where $h = 0$. Furthermore, we shall define our spheroidal wave-harmonics with a notation that somewhat resembles that of conventional spherical harmonics.

In the section that follows, the particular solutions to our overall NZ-FZT boundary value problems have to be expanded on the spheroidal transformation surface in

terms of their azimuthal and angular eigenfunctions. Because of this requirement, it is logical to develop a two-dimensional basis set (dependent on azimuthal and angular coordinates) for both the prolate and oblate cases that remains orthonormal over a given spheroidal surface. This spheroidal wave-harmonic for both spheroidal cases can be obtained by taking the product of their respective normalized azimuthal and angular eigenfunctions.

We can express the azimuthal eigenfunctions presented in (2-56) using the following orthonormal scheme:

$$\overline{\Phi}_m(\varphi) = \frac{1}{\sqrt{2\pi}} e^{+jm\varphi} \tag{2-81}$$

$$\int_0^{2\pi} \overline{\Phi}_m(\varphi)\overline{\Phi}_{m'}^{*}(\varphi)d\varphi = \delta_{m,m'} \tag{2-82}$$

where $-l \le m \le +l$.

Here we have used the overbar to indicate that the eigenfunction has been normalized. Additionally, we are able to include both sets of complex exponentials by extending the index *m* over positive and negative orders.

Regarding the angular eigenfunctions, we would like to replace the angular parameter η with ϑ. As mentioned beforehand, the two angular parameters are mutually related by the transformation given in equation (2-5), i.e., $\eta = \cos\vartheta$. Employing this change of variable together with the orthonormal scheme, we can express both angular eigenfunctions and their orthogonality relations as follows:

Prolate: $$\overline{S}_{m,l}(h,\cos\vartheta) = \frac{1}{\sqrt{N_{m,l}(h)}} S_{m,l}(h,\cos\vartheta) \tag{2-83a}$$

$$\int_0^{\pi} \overline{S}_{m,l}(h,\cos\vartheta)\overline{S}_{m,l'}(h,\cos\vartheta)\sin\vartheta d\vartheta = \delta_{l,l'}; \tag{2-84a}$$

Oblate: $$\bar{S}_{m,l}(-jh,\cos\vartheta)=\frac{1}{\sqrt{N_{m,l}(-jh)}}S_{m,l}(-jh,\cos\vartheta) \tag{2-83b}$$

$$\int_0^{\pi}\bar{S}_{m,l}(-jh,\cos\vartheta)\bar{S}_{m,l'}(-jh,\cos\vartheta)\sin\vartheta\,d\vartheta=\delta_{l,l'}\,. \tag{2-84b}$$

Once again we have used the overbar to denote normalization of the eigenfunction. In the orthogonality relations presented in (2-84a) and (2-84b), it is important to understand that the $\sin\vartheta$ integration factor that arises from the change of variable is consistent with Sturm-Liouville theory. One can show by performing a change of independent variable, viz., $\eta\rightarrow\vartheta$, on the differential equations for both angular self-adjoint boundary value problems (prolate and oblate) leads to a non-unity weighting function that is equal to the $\sin\vartheta$ integration factor.

As previously stated in the definitions of (2-69a) and (2-69b), we have assumed a unity proportionality constant relating positive and negative orders of spheroidal angle functions. This implies that the Sturm-Liouville normalization constants that correspond to the positive orders of spheroidal angle functions must be equal to their negative order counterparts:

Prolate: $$N_{m,l}(h)\equiv N_{-m,l}(h)\,; \tag{2-85a}$$

Oblate: $$N_{m,l}(-jh)\equiv N_{-m,l}(-jh)\,. \tag{2-85b}$$

Therefore, the normalized angular eigenfunctions expressed in (2-83a) and (2-83b) must also possess a unity proportionality constant between the positive and negative orders *m*.

We can now define our spheroidal wave-harmonics for both the prolate and oblate cases by taking the product of their corresponding normalized azimuthal and angular eigenfunctions:

Prolate: $$Y_{m,l}(h,\vartheta,\varphi)=\frac{1}{\sqrt{2\pi N_{m,l}(h)}}S_{m,l}(h,\cos\vartheta)e^{+jm\varphi} \tag{2-86a}$$

where $-l\le m\le +l$,

$$\iint_{\Omega_P} Y_{m,l}(h,\vartheta,\varphi)Y^{*}_{m',l'}(h,\vartheta,\varphi)\;\; d\Omega_P = \delta_{m,m'}\delta_{l,l'} \tag{2-87a}$$

where $\{\,\Omega_P:\ 0\le\vartheta\le\pi,\ 0\le\varphi\le 2\pi$, and $d\Omega_P=\sin\vartheta\, d\vartheta\, d\varphi\,\}$,

$$Y^{*}_{m,l}(h,\vartheta,\varphi)=Y_{-m,l}(h,\vartheta,\varphi)\,; \tag{2-88a}$$

Oblate: $$Y_{m,l}(-jh,\vartheta,\varphi)=\frac{1}{\sqrt{2\pi N_{m,l}(-jh)}}S_{m,l}(-jh,\cos\vartheta)e^{+jm\varphi} \tag{2-86b}$$

where $-l\le m\le +l$,

$$\iint_{\Omega_O} Y_{m,l}(-jh,\vartheta,\varphi)Y^{*}_{m',l'}(-jh,\vartheta,\varphi)\;\; d\Omega_O = \delta_{m,m'}\delta_{l,l'} \tag{2-87b}$$

where $\{\,\Omega_O:\ 0\le\vartheta\le\pi,\ 0\le\varphi\le 2\pi$, and $d\Omega_O=\sin\vartheta\, d\vartheta\, d\varphi\,\}$,

$$Y^{*}_{m,l}(-jh,\vartheta,\varphi)=Y_{-m,l}(-jh,\vartheta,\varphi)\,. \tag{2-88b}$$

As we can see, the spheroidal wave-harmonics defined in (2-86a) and (2-86b) are valid over the orders where $-l\le m\le +l$; it is in this instance that our unity proportionality constant relating positive and negative orders of the angular solutions proves to be convenient. The two-dimensional orthogonality relations provided in (2-87a) and (2-87b) are derived by taking the product of the azimuthal orthogonality relation, (2-82), and their respective angular orthogonality relations, (2-84a) and (2-84b). These resulting orthogonality relations demonstrate that the defined spheroidal wave-harmonics are orthonormal over their respective spheroidal surfaces. The fact that the complex

conjugate of a spheroidal wave-harmonic is equal to its respective negative order, i.e., (2-88a) and (2-88b), follows by inspection.

Finally, something must be said about why we choose to refer to the product of the angular and azimuthal spheroidal solutions for the prolate and oblate cases as "spheroidal wave-harmonics." Traditionally, the term "harmonic" referred to solutions of the Laplace equation (i.e., the static equation where $k = 0$) because they were called harmonic functions [29]. When solving both the Helmholtz and Laplace equations in spherical coordinates, the angular and azimuthal Helmholtz solutions happen to exactly match those of the Laplace solutions. It is the product of these angular and azimuthal solutions that are often referred to as "spherical harmonics" [29]. Thus, in this particular case, the solutions to the Helmholtz equation happen to be referred to as "harmonics." However, when solving the Helmholtz and Laplace equations in the prolate and oblate spheroidal coordinate systems, the angular part of the solution is no longer the same for the two partial differential equations. This is why the angular solutions (as well as the radial solutions) of the scalar Helmholtz equation (i.e., the wave equation) in both spheroidal coordinate systems are referred to as "spheroidal wave functions" [23]. In short, we label the product of these angular and azimuthal solutions as "spheroidal wave-harmonics." We do so in order to maintain some sort of kinship with conventional spherical harmonics, yet still convey that the two-dimensional basis sets are solutions to the scalar Helmholtz equation (i.e., the wave equation).

2.2.8 Construction of the Particular Solutions Using Expansions of Spheroidal Wave-Harmonics

Equipped with the developed spheroidal wave-harmonics and their related properties, we are now ready to continue with the construction of the particular solutions to our overall NZ-FZT boundary value problems (i.e., for the prolate and oblate cases). Construction of the particular solutions begins with applying the Sommerfeld radiation condition to both sets of general solutions. Application of this boundary condition leads to the appropriate expansions of spheroidal wave-harmonics. Both of these expansions

have coefficients that can be determined only after applying their respective Dirichlet boundary conditions. To do so, each particular solution, i.e., the expansion of spheroidal wave-harmonics, must be forced to match the known field quantities (specified by the NZ-FZT process input) along its respective spheroidal boundary. Lastly, we approximate each of these particular solutions in the far-zone region by using the appropriate asymptotic expression, viz., (2-79a) or (2-79b).

We recall that the Sommerfeld radiation condition has limited our radial solutions to only outward traveling waves, viz., $R_{m,l}^{(4)}(h,\xi)$ and $R_{m,l}^{(4)}(-jh,j\xi)$; this eliminates the spheroidal radial functions of the third kind, i.e., $R_{m,l}^{(3)}(h,\xi)$ and $R_{m,l}^{(3)}(-jh,j\xi)$, from both sets of possible solutions. Applying this boundary condition to the general solutions expressed in (2-77a)-(2-78a) and (2-77b)-(2-78b), we can construct both particular solutions in terms of the following spheroidal wave-harmonic expansions:

Prolate: $$\psi^{P}(\xi,\vartheta,\varphi)=\sum_{l=0}^{\infty}\sum_{m=-l}^{+l}b_{m,l}(h)R_{m,l}^{(4)}(h,\xi)Y_{m,l}(h,\vartheta,\varphi)\,; \qquad (2\text{-}89a)$$

Oblate: $$\psi^{O}(\xi,\vartheta,\varphi)=\sum_{l=0}^{\infty}\sum_{m=-l}^{+l}b_{m,l}(-jh)R_{m,l}^{(4)}(-jh,j\xi)Y_{m,l}(-jh,\vartheta,\varphi)\,. \qquad (2\text{-}89b)$$

Note that both expansions represent the linear combination of all possible linearly independent solutions to their respective boundary value problem. The limits of the indices m and l are based upon the possible eigenvalues and the definition of the developed spheroidal wave-harmonics.

Our next step is to determine the expansion coefficients for both the prolate and oblate cases. In order to accomplish this task, we must first enforce each respective Dirichlet boundary condition over its corresponding spheroidal boundary. This essentially means that both particular solutions must match the known field quantities along their respective spheroidal transformation surface (i.e., the $\xi=\xi_o$ constant parameter surface):

Prolate:

$$\psi^{P}(\xi_o,\vartheta,\varphi) = known = \sum_{l=0}^{\infty}\sum_{m=-l}^{+l} b_{m,l}(h) R_{m,l}^{(4)}(h,\xi_o) Y_{m,l}(h,\vartheta,\varphi)\,; \tag{2-90a}$$

Oblate:

$$\psi^{O}(\xi_o,\vartheta,\varphi) = known = \sum_{l=0}^{\infty}\sum_{m=-l}^{+l} b_{m,l}(-jh) R_{m,l}^{(4)}(-jh, j\xi_o) Y_{m,l}(-jh,\vartheta,\varphi)\,. \tag{2-90b}$$

We can now multiply each of these equations by its respective conjugated spheroidal wave-harmonic, $Y_{m',l'}^{*}(h,\vartheta,\varphi)$ or $Y_{m',l'}^{*}(-jh,\vartheta,\varphi)$, and then integrate over its corresponding spheroidal surface:

Prolate:

$$\iint_{\Omega_P} \psi^{P}(\xi_o,\vartheta,\varphi) Y_{m',l'}^{*}(h,\vartheta,\varphi)\ \ d\Omega_P$$

$$= \iint_{\Omega_P} \sum_{l=0}^{\infty}\sum_{m=-l}^{+l} b_{m,l}(h) R_{m,l}^{(4)}(h,\xi_o) Y_{m,l}(h,\vartheta,\varphi) Y_{m',l'}^{*}(h,\vartheta,\varphi)\ \ d\Omega_P\ ; \tag{2-91a}$$

Oblate:

$$\iint_{\Omega_O} \psi^{O}(\xi_o,\vartheta,\varphi) Y_{m',l'}^{*}(-jh,\vartheta,\varphi)\ \ d\Omega_O$$

$$= \iint_{\Omega_O} \sum_{l=0}^{\infty}\sum_{m=-l}^{+l} b_{m,l}(-jh) R_{m,l}^{(4)}(-jh, j\xi_o) Y_{m,l}(-jh,\vartheta,\varphi) Y_{m',l'}^{*}(-jh,\vartheta,\varphi)\ \ d\Omega_O\,. \tag{2-91b}$$

Assuming the permissibility of termwise integration, we first interchange the integration operator and the summation on the right-hand side of the equation. Having performed

this operation, we then make use of the orthogonality relation for prolate spheroidal wave-harmonics, i.e., (2-87a), such that we are able to employ the discrete version of the sifting property to isolate each expansion coefficient:

Prolate:

$$\begin{aligned}
&\iint_{\Omega_P} \psi^P(\xi_o,\vartheta,\varphi) Y^*_{m',l'}(h,\vartheta,\varphi)\ \ d\Omega_P \\
&= \sum_{l=0}^{\infty}\sum_{m=-l}^{+l} b_{m,l}(h) R^{(4)}_{m,l}(h,\xi_o) \iint_{\Omega_P} Y_{m,l}(h,\vartheta,\varphi) Y^*_{m',l'}(h,\vartheta,\varphi)\ \ d\Omega_P \\
&= \sum_{l=0}^{\infty}\sum_{m=-l}^{+l} b_{m,l}(h) R^{(4)}_{m,l}(h,\xi_o) \delta_{m,m'}\delta_{l,l'} \\
&= b_{m',l'}(h) R^{(4)}_{m',l'}(h,\xi_o)\,. \qquad \text{(2-92a)}
\end{aligned}$$

For the oblate case, similar mathematical operations can be performed to yield the following:

Oblate:

$$\begin{aligned}
&\iint_{\Omega_O} \psi^O(\xi_o,\vartheta,\varphi) Y^*_{m',l'}(-jh,\vartheta,\varphi)\ \ d\Omega_O \\
&= b_{m',l'}(-jh) R^{(4)}_{m',l'}(-jh, j\xi_o)\,. \qquad \text{(2-92b)}
\end{aligned}$$

We are now able to drop the prime from the indices and express the coefficients for both expansions of spheroidal wave-harmonics, i.e., (2-89a) and (2-89b), as follows:

Prolate:

$$b_{m,l}(h) = \frac{1}{R^{(4)}_{m,l}(h,\xi_o)} \iint_{\Omega_P} \psi^P(\xi_o,\vartheta,\varphi) Y^*_{m,l}(h,\vartheta,\varphi)\ \ d\Omega_P\ ; \qquad \text{(2-93a)}$$

Oblate:

$$b_{m,l}(-jh) = \frac{1}{R^{(4)}_{m,l}(-jh, j\xi_o)} \iint_{\Omega_O} \psi^O(\xi_o,\vartheta,\varphi) Y^*_{m,l}\ (-jh,\vartheta,\varphi)\ d\Omega_O\,. \qquad \text{(2-93b)}$$

Since the objective of our NZ-FZT process is to compute the far-zone response of a radiating structure, we shall approximate the developed spheroidal wave-harmonic

expansions in the far-zone region by using asymptotic expressions for the spheroidal radial functions of the fourth kind, i.e., $R_{m,l}^{(4)}(h,\xi)$ and $R_{m,l}^{(4)}(-jh,j\xi)$. The far-zone behavior of these radial functions has already been examined and is described in expressions (2-79a) and (2-79b). The asymptotic expression for the prolate spheroidal radial function of the fourth kind can then be applied to (2-89a) to yield the following far-zone spheroidal wave-harmonic expansion for the prolate case:

$$\begin{aligned}
\text{Prolate:} \qquad \psi_{fz}^{P} &= \lim_{\xi\to\infty} \psi^{P}(\xi,\vartheta,\varphi) \\
&= \sum_{l=0}^{\infty}\sum_{m=-l}^{+l} b_{m,l}(h) Y_{m,l}(h,\vartheta,\varphi)\left[\lim_{\xi\to\infty} R_{m,l}^{(4)}(h,\xi)\right] \\
&= \sum_{l=0}^{\infty}\sum_{m=-l}^{+l} b_{m,l}(h) Y_{m,l}(h,\vartheta,\varphi)\left[\frac{j^{l+1}}{k}\left(e^{-jkr}/r\right)\right] \\
&= \sum_{l=0}^{\infty}\sum_{m=-l}^{+l} \underbrace{\left[\frac{j^{l+1}}{k} b_{m,l}(h)\right]}_{\equiv a_{m,l}(h)} Y_{m,l}(h,\vartheta,\varphi)\left(e^{-jkr}/r\right). \qquad \text{(2-94a)}
\end{aligned}$$

For the sake of simplicity, we have elected to incorporate the complex factor $\left[j^{l+1}/k\right]$ into our new expansion coefficient $a_{m,l}(h)$. Furthermore, notice how the presence of the $\left(e^{-jkr}/r\right)$ radial dependence is consistent with the Sommerfeld radiation condition. For reasons expressed earlier (see 2.1.2), we shall once again suppress the $\left(e^{-jkr}/r\right)$ radial factor. In short, by using a bar over the scalar field quantity to indicate suppression of the radial dependence, we express the far-zone prolate spheroidal wave-harmonic expansion with its expansion coefficients as follows:

Prolate:

$$\overline{\psi}^{P}_{fz}(\vartheta,\varphi)=\sum_{l=0}^{\infty}\sum_{m=-l}^{+l}a_{m,l}(h)Y_{m,l}(h,\vartheta,\varphi) \tag{2-95a}$$

where

$$a_{m,l}(h)=\frac{j^{l+1}}{k\,R^{(4)}_{m,l}(h,\xi_o)}\iint_{\Omega_P}\psi^{P}(\xi_o,\vartheta,\varphi)Y^{*}_{m,l}(h,\vartheta,\varphi)\;\;d\Omega_P\;\;. \tag{2-96a}$$

Likewise, following similar mathematical operations and rationale, we are also able to express the far-zone oblate spheroidal wave-harmonic expansion with its expansion coefficients:

Oblate:

$$\overline{\psi}^{O}_{fz}(\vartheta,\varphi)=\sum_{l=0}^{\infty}\sum_{m=-l}^{+l}a_{m,l}(-jh)Y_{m,l}(-jh,\vartheta,\varphi) \tag{2-95b}$$

where

$$a_{m,l}(-jh)=\frac{j^{l+1}}{k\,R^{(4)}_{m,l}(-jh,j\xi_o)}\iint_{\Omega_O}\psi^{O}(\xi_o,\vartheta,\varphi)Y^{*}_{m,l}(-jh,\vartheta,\varphi)\;\;d\Omega_O\;. \tag{2-96b}$$

Having satisfied all of the imposed boundary conditions, both of these spheroidal wave-harmonic expansions individually form the particular solution to their respective NZ-FZT boundary value problem.

2.3 THE NZ-FZT ALGORITHMS FOR THE PROLATE AND OBLATE SPHEROIDAL CASES

2.3.1 Algorithmic Implementation of the Constructed Particular Solutions

In this section we take the constructed prolate and oblate particular solutions and reduce each of them to a numerical algorithm capable of being implemented by a computer code. The first step in the formulation of the algorithms requires that each expansion of spheroidal wave-harmonics be expressed only in terms of special functions that are able to be numerically evaluated. This is followed by addressing the particulars regarding the sampling of the known near-zone E-field along the respective spheroidal transformation surface, including how these samples are incorporated into our computational process. Finally, numerical algorithms are put forth that enable the calculation of the prolate and oblate particular solutions for our NZ-FZT process. Recalling that both particular solutions have been constructed for the scalar case, we explain in the section that immediately follows (i.e., 2.3.2) how these algorithms are extended to the vector case using our hybrid of coordinate systems approach (see 2.2.2).

At this point in the development of our NZ-FZT process, it has become evident that the formulations for both the prolate and oblate cases have begun to closely resemble one another. Prior to now, we have elected to explicitly state results for both spheroidal cases throughout our discussion on behalf of providing a theoretical development that is both thorough and complete. Furthermore, this approach of stating the results for both spheroidal cases in a side-by-side manner has also allowed us to compare the two formulations, as well as define their respective nomenclature and special functions. However, we shall now depart from this practice in the following discussion regarding the development of the NZ-FZT algorithms. For the sake of brevity, the discussion that ensues shall only provide a step-by-step development of the numerical algorithm for the prolate case, not the oblate case. Since these numerical algorithms closely parallel one another, details regarding development of the algorithm for the oblate case can easily be

derived from the discussion of its prolate counterpart. Nonetheless, we shall still disclose both prolate and oblate numerical algorithms at the conclusion of this discussion.

Since the Dirichlet boundary condition specifies the field quantities on the prolate spheroidal surface (i.e., the $\xi = \xi_o$ constant parameter surface), we define this boundary condition as a function of only angular and azimuthal parameters:

$$\psi^P(\xi,\vartheta,\varphi)\big|_{\Omega_P} \equiv \psi^P(\xi_o,\vartheta,\varphi) \equiv f^P(\vartheta,\varphi). \tag{2-97a}$$

As we shall ultimately see, this two-dimensional function will serve as the NZ-FZT process input for each respective Cartesian vector component of the near-zone E-field. We can now substitute this two-dimensional function into our expression for the wave-harmonic expansion coefficients presented in (2-96a):

$$a_{m,l}(h) = \frac{j^{l+1}}{k\,R^{(4)}_{m,l}(h,\xi_o)} \iint\limits_{\Omega'_P} f^P(\vartheta',\varphi') Y^*_{m,l}(h,\vartheta',\varphi')\; d\Omega'_P \;. \tag{2-98a}$$

It is important to note that in (2-98a), the variables of integration, viz., ϑ' and φ', have been primed in order to distinguish them as boundary parameters that exist along the prolate spheroidal transformation surface; they are considered in the near-zone. As for their unprimed counterparts, i.e., ϑ and φ, they represent the far-zone observation parameters in the prolate spheroidal coordinate system. Thus, we can now substitute (2-98a) into the far-zone prolate wave-harmonic expansion presented in (2-95a) to obtain

$$\overline{\psi}^P_{fz}(\vartheta,\varphi) = \sum_{l=0}^{\infty} \sum_{m=-l}^{+l} \frac{j^{l+1}}{k\,R^{(4)}_{m,l}(h,\xi_o)} \iint\limits_{\Omega'_P} f^P(\vartheta',\varphi') Y^*_{m,l}(h,\vartheta',\varphi')\; Y_{m,l}(h,\vartheta,\varphi)\, d\Omega'_P \;. \tag{2-99a}$$

Once again presuming the permissibility of interchanging the summation with the integration operator, we yield

$$\overline{\psi}^{\,P}_{fz}(\vartheta,\varphi)=\iint_{\Omega'_P}\left[\sum_{l=0}^{\infty}\frac{j^{l+1}}{k}\sum_{m=-l}^{+l}\frac{Y^{*}_{m,l}(h,\vartheta',\varphi')\;Y_{m,l}(h,\vartheta,\varphi)}{R^{(4)}_{m,l}(h,\xi_o)}\right]f^{\,P}(\vartheta',\varphi')d\Omega'_P\;.$$

(2-100a)

At this juncture in our development, we make use of the following crucial identity derived in Appendix E:

$$\sum_{m=-l}^{+l}\frac{Y^{*}_{m,l}(h,\vartheta',\varphi')\;Y_{m,l}(h,\vartheta,\varphi)}{R^{(4)}_{m,l}(h,\xi_o)}$$

$$=\frac{1}{2\pi}\left[\frac{S_{0,l}(h,\cos\vartheta)S_{0,l}(h,\cos\vartheta')}{N_{0,l}(h)R^{(4)}_{0,l}(h,\xi_o)}+2\sum_{m=1}^{l}\frac{S_{m,l}(h,\cos\vartheta)S_{m,l}(h,\cos\vartheta')}{N_{m,l}(h)R^{(4)}_{m,l}(h,\xi_o)}\cos m(\varphi-\varphi')\right].$$

(2-101a)

It is this double- to single-sided wave-harmonic identity that enables us to reduce our eigenfunction expansion into a mathematical form that is expressed only in terms of computable special functions. We do so by substituting (2-101a) into (2-100a):

$$\overline{\psi}^{\,P}_{fz}(\vartheta,\varphi)=$$

$$\iint_{\Omega'_P}\left[\sum_{l=0}^{\infty}\frac{j^{l+1}}{2\pi k}\left(\begin{array}{l}\dfrac{S_{0,l}(h,\cos\vartheta)S_{0,l}(h,\cos\vartheta')}{N_{0,l}(h)R^{(4)}_{0,l}(h,\xi_o)}\\ +2\displaystyle\sum_{m=1}^{l}\dfrac{S_{m,l}(h,\cos\vartheta)S_{m,l}(h,\cos\vartheta')}{N_{m,l}(h)R^{(4)}_{m,l}(h,\xi_o)}\cos m(\varphi-\varphi')\end{array}\right)\right]f^{\,P}(\vartheta',\varphi')d\Omega'_P\;.$$

(2-102a)

Assuming that we are able to termwise integrate the resulting expression, we reduce it to an eigenfunction expansion in terms of a set of indexed integrals dependent upon the Dirichlet boundary condition function $f^{\,P}(\vartheta',\varphi')$:

$$\overline{\psi}^{\,P}_{fz}(\vartheta,\varphi)$$

$$= \sum_{l=0}^{\infty} \frac{j^{l+1}}{2\pi k} \left(\begin{array}{l} \dfrac{S_{0,l}(h,\cos\vartheta)}{N_{0,l}(h) R^{(4)}_{0,l}(h,\xi_o)} \iint\limits_{\Omega'_P} f^{\,P}(\vartheta',\varphi') S_{0,l}(h,\cos\vartheta') d\Omega'_P \\ +2\sum\limits_{m=1}^{l} \dfrac{S_{m,l}(h,\cos\vartheta)}{N_{m,l}(h) R^{(4)}_{m,l}(h,\xi_o)} \iint\limits_{\Omega'_P} f^{\,P}(\vartheta',\varphi') S_{m,l}(h,\cos\vartheta') \cos m(\varphi-\varphi') d\Omega'_P \end{array} \right)$$

$$= \sum_{l=0}^{\infty} \frac{j^{l+1}}{2\pi k} \left(\frac{S_{0,l}(h,\cos\vartheta)}{N_{0,l}(h) R^{(4)}_{0,l}(h,\xi_o)} I_{0,l}(h) + 2\sum_{m=1}^{l} \frac{S_{m,l}(h,\cos\vartheta)}{N_{m,l}(h) R^{(4)}_{m,l}(h,\xi_o)} I_{l,m}(h,\varphi) \right)$$

(2-103a)

where

$$I_{0,l}(h) = \iint\limits_{\Omega'_P} f^{\,P}(\vartheta',\varphi') S_{0,l}(h,\cos\vartheta') d\Omega'_P \quad \text{for } l \geq 0 \tag{2-104a}$$

and

$$I_{m,l}(h,\varphi) = \iint\limits_{\Omega'_P} f^{\,P}(\vartheta',\varphi') S_{m,l}(h,\cos\vartheta') \cos m(\varphi-\varphi') d\Omega'_P \quad \text{for } 1 \leq m \leq l\,.$$

(2-105a)

Now that we have expressed the expansion of prolate spheroidal wave-harmonics in terms of computable special functions, the next order of business is to determine how to best approximate the indexed two-dimensional integrals of (2-104a) and (2-105a) in terms of the sampled near-zone E-field along the prolate spheroidal transformation surface. As illustrated in Figure 2.2a, let us first partition the surface of the prolate spheroid (i.e., the $\xi = \xi_o$ constant parameter surface) into uniform surface elements $\Delta S'_{i,j}$ (with respect to ϑ' and φ' dimensions) that are centered at $(\vartheta'_i, \varphi'_j)$ and have respective widths $\Delta\vartheta'$ and $\Delta\varphi'$. If we allow the subscripts *i* and *j* to index the surface elements in the angular and azimuthal directions, respectively, we can define the center of each surface element as follows:

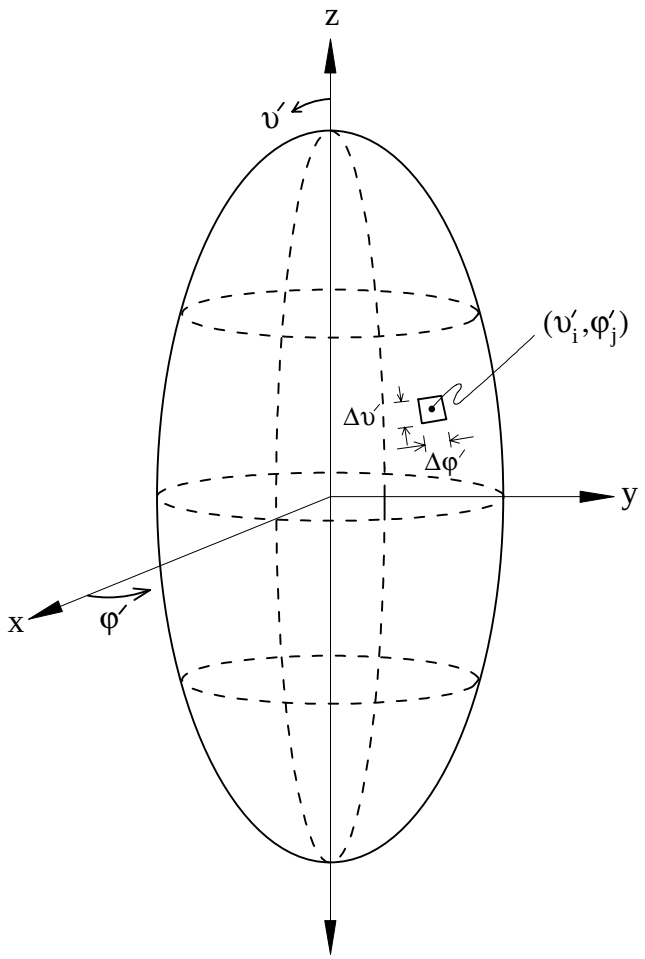

Figure 2.2a The i^{th}, j^{th} surface element $\Delta S'_{i,j}$ of the partitioned prolate spheroidal transformation surface (i.e., the $\xi = \xi_o$ constant parameter surface).

Angular: $\Delta\vartheta' = \pi / I$ (2-106a)

$\vartheta'_i = (i - \frac{1}{2})\Delta\vartheta'$ (2-107a)

where I = total number of samples in the angular direction and $i = 1, 2, \ldots, I$;

Azimuthal: $\Delta\varphi' = 2\pi / J$ (2-108a)

$\varphi'_j = (j - \frac{1}{2})\Delta\varphi'$ (2-109a)

where J = total number of samples in the azimuthal direction and $j = 1, 2, \ldots, J$.

As we can see, expressions (2-104a) and (2-105a) both require an integration operation that must be performed over the entire prolate spheroidal transformation surface. Because we have partitioned the spheroidal surface into $(I \times J)$ surface elements, these integration operations can be broken down into a finite summation of individual integration operations performed over each surface element $\Delta S'_{i,j}$:

$$I_{0,l}(h) = \sum_{i,j} \iint_{\Delta S'_{i,j}} f^{P}(\vartheta', \varphi') S_{0,l}(h, \cos\vartheta') d\Omega'_p \tag{2-110a}$$

$$I_{m,l}(h, \varphi) = \sum_{i,j} \iint_{\Delta S'_{i,j}} f^{P}(\vartheta', \varphi') S_{m,l}(h, \cos\vartheta') \cos m(\varphi - \varphi') d\Omega'_p . \tag{2-111a}$$

We shall now presuppose that the two-dimensional function $f^{P}(\vartheta', \varphi')$ varies slowly over any particular surface element $\Delta S'_{i,j}$ provided that the size of its area is made fine enough. This assumption allows us to approximate the function $f^{P}(\vartheta', \varphi')$ over the entire prolate spheroidal transformation surface as a mosaic of constant values with each one corresponding to an individual surface element $\Delta S'_{i,j}$. Furthermore, these values

shall equal the function $f^{P}(\vartheta',\varphi')$ sampled at the center of each respective surface element: in mathematical terms, $f_{i,j}^{P} \equiv f^{P}(\vartheta_i',\varphi_j') \equiv constant$. Using this approximation of the two-dimensional function $f^{P}(\vartheta',\varphi')$, we approximate the finite summation of individual integration operations defined in (2-110a) and (2-111a) in terms of the indexed samples:

$$I_{0,l}(h) \cong \sum_{i,j} \iint_{\Delta S_{i,j}'} f_{i,j}^{P} S_{0,l}(h,\cos\vartheta')d\Omega_p'$$

$$= \sum_{i,j} f_{i,j}^{P} \iint_{\Delta S_{i,j}'} S_{0,l}(h,\cos\vartheta')d\Omega_p', \tag{2-112a}$$

$$I_{m,l}(h,\varphi) \cong \sum_{i,j} \iint_{\Delta S_{i,j}'} f_{i,j}^{P} S_{m,l}(h,\cos\vartheta')\cos m(\varphi-\varphi')d\Omega_p'$$

$$= \sum_{i,j} f_{i,j}^{P} \iint_{\Delta S_{i,j}'} S_{m,l}(h,\cos\vartheta')\cos m(\varphi-\varphi')d\Omega_p'. \tag{2-113a}$$

Note that the indexed samples $f_{i,j}^{P}$ can be brought outside both integrals because they remain constant with respect to the variables of integration ϑ' and φ' over each individual surface element $\Delta S_{i,j}'$ (by definition of the approximation for the two-dimensional function $f^{P}(\vartheta',\varphi')$).

So that we may further reduce the approximated integrations of (2-112a) and (2-113a), each of the individual integration operations (with respect to *i* and *j*) must first be explicitly performed over its corresponding surface element $\Delta S_{i,j}'$:

$$\iint_{\Delta S'_{i,j}} S_{0,l}(h,\cos\vartheta')\,d\Omega'_p$$

$$= \int_{\left[\varphi'_j-\frac{\Delta\varphi'}{2}\right]}^{\left[\varphi'_j+\frac{\Delta\varphi'}{2}\right]} \int_{\left[\vartheta'_i-\frac{\Delta\vartheta'}{2}\right]}^{\left[\vartheta'_i+\frac{\Delta\vartheta'}{2}\right]} S_{0,l}(h,\cos\vartheta')\sin\vartheta'\,d\vartheta'\,d\varphi'$$

$$= \Delta\varphi' \int_{\left[\vartheta'_i-\frac{\Delta\vartheta'}{2}\right]}^{\left[\vartheta'_i+\frac{\Delta\vartheta'}{2}\right]} S_{0,l}(h,\cos\vartheta')\sin\vartheta'\,d\vartheta' \text{ for } l \geq 0, \tag{2-114a}$$

$$\iint_{\Delta S'_{i,j}} S_{m,l}(h,\cos\vartheta')\cos m(\varphi-\varphi')\,d\Omega'_p$$

$$= \int_{\left[\varphi'_j-\frac{\Delta\varphi'}{2}\right]}^{\left[\varphi'_j+\frac{\Delta\varphi'}{2}\right]} \int_{\left[\vartheta'_i-\frac{\Delta\vartheta'}{2}\right]}^{\left[\vartheta'_i+\frac{\Delta\vartheta'}{2}\right]} S_{m,l}(h,\cos\vartheta')\cos m(\varphi-\varphi')\sin\vartheta'\,d\vartheta'\,d\varphi'$$

$$= \frac{2}{m}\sin\left[m\frac{\Delta\varphi'}{2}\right]\cos m(\varphi'_j-\varphi) \int_{\left[\vartheta'_i-\frac{\Delta\vartheta'}{2}\right]}^{\left[\vartheta'_i+\frac{\Delta\vartheta'}{2}\right]} S_{m,l}(h,\cos\vartheta')\sin\vartheta'\,d\vartheta' \text{ for } 1 \leq m \leq l.$$

(2-115a)

Using these explicit results for the individual integration operations and the approximated integrations of (2-112a) and (2-113a), we can now present the overall approximations for the indexed integrals of (2-104a) and (2-105a):

$$I_{0,l}(h) \cong \Delta\varphi' \sum_{i,j} f_{i,j}^{\,P}\ IS_{0,l,i}^{P} \text{ for } l \geq 0 \tag{2-116a}$$

$$\text{where } IS_{0,l,i}^{P} \equiv \int_{\left[\vartheta'_i-\frac{\Delta\vartheta'}{2}\right]}^{\left[\vartheta'_i+\frac{\Delta\vartheta'}{2}\right]} S_{0,l}(h,\cos\vartheta')\sin\vartheta'\,d\vartheta', \tag{2-117a}$$

$$I_{m,l}(h,\varphi) \cong \frac{2}{m}\sin\left[m\frac{\Delta\varphi'}{2}\right]\sum_{i,j} f^{P}_{i,j}\cos m(\varphi'_j-\varphi)\ IS^{P}_{m,l,i} \quad \text{for } 1\le m\le l \tag{2-118a}$$

$$\text{where}\quad IS^{P}_{m,l,i} \equiv \int_{\left[\vartheta'_i-\frac{\Delta\vartheta'}{2}\right]}^{\left[\vartheta'_i+\frac{\Delta\vartheta'}{2}\right]} S_{m,l}(h,\cos\vartheta')\sin\vartheta' d\vartheta'. \tag{2-119a}$$

From a computational viewpoint, these approximations require numerical integrations of a function, viz., the prolate spheroidal angle function of the first kind, that in and of itself must be numerically evaluated. At first glance, these numerical integrations may appear to be computationally costly. However, as we shall see, these computations are quite plausible and will only need to be calculated once for each particular spheroidal transformation surface, regardless of the number of far-zone observation angles. As a matter of fact, these numerical integrations do not account for a majority of the computation time for an average computational run. Particulars regarding these numerical integrations are addressed in Chapter 3, which focuses on computations of the required special functions.

An alternative approach to approximating the indexed integrals of (2-104a) and (2-105a) could have been to use standard Riemann sums and thus avoid the required numerical integrations. Unfortunately, a drawback of this approach is that the convergence of the integration is then coupled to the order and degree, i.e., *m* and *l*, of the two-dimensional basis functions; that is, the more oscillatory wave-harmonics (dependent on *l* and *m*) would require finer sampling of the Dirichlet boundary condition function $f^{P}(\vartheta',\varphi')$ regardless of how slow or fast the function varies over the prolate spheroidal transformation surface. The approach that we have elected to use, i.e., (2-116a)-(2-119a), effectively allows us to more efficiently sample the two-dimensional function $f^{P}(\vartheta',\varphi')$.

Now that we have determined how to best approximate the indexed two-dimensional integrals of (2-104a) and (2-105a), we return our attention to our expansion of prolate spheroidal wave-harmonics. As explained earlier, we want our extrapolated

far-zone field response to be in conventional spherical coordinates (see 2.1.2). Fortunately, the angular coordinate for both the prolate and oblate cases approaches that of the spherical coordinate system in the far-zone (see Appendix A); this means that in the far-zone, i.e., where $\xi \to \infty$, we can apply the following coordinate transformation:

$$\vartheta \to \theta . \tag{2-120}$$

As for the azimuthal parameter, it obviously remains unchanged by definition of the involved coordinate systems, i.e., $\varphi \equiv \varphi$. Since the far-zone prolate spheroidal wave-harmonic expansion presented in (2-103a) exists in the far-zone by definition, we can apply (2-120) to transform only the variables that represent the angular observation parameter, viz., ϑ (recalling that the angular boundary parameter ϑ' is not in the far-zone):

$$\overline{\psi}^{P}_{fz}(\theta,\varphi) = \sum_{l=0}^{\infty} \frac{j^{l+1}}{2\pi k} \left(\frac{S_{0,l}(h,\cos\theta)}{N_{0,l}(h) R^{(4)}_{0,l}(h,\xi_o)} I_{0,l}(h) + 2\sum_{m=1}^{l} \frac{S_{m,l}(h,\cos\theta)}{N_{m,l}(h) R^{(4)}_{m,l}(h,\xi_o)} I_{l,m}(h,\varphi) \right). \tag{2-121a}$$

The far-zone prolate spheroidal wave-harmonic expansion in (2-121a) presents itself as an infinite series expansion. In order for the expansion to be useable from an applied perspective, we must be able to truncate it at some prescribed order and degree, i.e., *m* and *l*, and still obtain valid results; that is, the truncated wave-harmonic expansion needs to converge upon a solution as higher-order terms of *m* and *l* are considered. Having presumed the completeness of the developed basis sets (i.e., the spheroidal wave-harmonics) implies that the formulated spheroidal wave-harmonic expansion will render convergence in the mean for well-behaved solutions. As a result, we are able to truncate both series of (2-121a) at some user prescribed degree *L* (since the range of the order *m* is dependent on the degree *l*) and still achieve valid results.

At this point, we are able to insert our overall approximations for the indexed integrals, viz., (2-116a) and (2-118a), into the truncated version of (2-121a) to obtain the following finite expansion of wave-harmonics:

$$\overline{\psi}_{fz}^{P}(\theta,\varphi) \cong$$

$$\frac{\lambda_o}{(2\pi)^2}\left[\begin{array}{l}\displaystyle\sum_{l=0}^{L}(\sqrt{-1})^{l+1}\Delta\varphi'\frac{S_{0,l}(h,\cos\theta)}{N_{0,l}(h)R_{0,l}^{(4)}(h,\xi_o)}\sum_{i,j}f_{i,j}^{P}\ IS_{0,l,i}^{P} \\ \displaystyle+4\sum_{l=1}^{L}\sum_{m=1}^{l}(\sqrt{-1})^{l+1}\frac{\sin m(\Delta\varphi'/2)}{m}\frac{S_{m,l}(h,\cos\theta)}{N_{m,l}(h)R_{m,l}^{(4)}(h,\xi_o)}\sum_{i,j}f_{i,j}^{P}\cos m(\varphi_j'-\varphi)\ IS_{m,l,i}^{P}\end{array}\right]. \tag{2-122a}$$

(Note that we replaced the complex factor j^{l+1} with $(\sqrt{-1})^{l+1}$ in order to avoid any confusion with the azimuthal sample index j.) Because the expansion of (2-122a) is finite, we can interchange the order of the summations and then factor out the indexed samples $f_{i,j}^{P}$ (which are independent of *l* and *m*):

$$\overline{\psi}_{fz}^{P}(\theta,\varphi) \cong$$

$$\frac{\lambda_o}{(2\pi)^2}\sum_{i,j}f_{i,j}^{P}\times\left[\begin{array}{l}\displaystyle\sum_{l=0}^{L}\left[\frac{(\sqrt{-1})^{l+1}\Delta\varphi'}{N_{0,l}(h)R_{0,l}^{(4)}(h,\xi_o)}\right]\left[IS_{0,l,i}^{P}\right]\left[S_{0,l}(h,\cos\theta)\right] \\ \displaystyle+\sum_{l=1}^{L}\sum_{m=1}^{l}\left[4\frac{(\sqrt{-1})^{l+1}\sin m(\Delta\varphi'/2)}{mN_{m,l}(h)R_{m,l}^{(4)}(h,\xi_o)}\right]\left[IS_{m,l,i}^{P}\right]\left[S_{m,l}(h,\cos\theta)\cos m(\varphi_j'-\varphi)\right]\end{array}\right]. \tag{2-123a}$$

For both spheroidal cases, we are now able to put forth the algorithmic implementations of the constructed particular solutions capable of computing a Cartesian vector component of the desired far-zone E-field. Shown in Tables 2.5a and 2.5b are the required computations (including the overall finite wave-harmonic expansions for both the prolate and oblate cases) and the memory storage format of the NZ-FZT process for

Table 2.5a Prolate Spheroidal NZ-FZT Algorithm for Each Cartesian Vector Component

$$\overline{\psi}_{fz}^{\,P}(\theta,\varphi) \cong$$

$$C1\sum_{i=1}^{I}\sum_{j=1}^{J} f_{i,j}^{\,P} \times \left[\begin{array}{l} \sum_{l=0}^{L}\left[C2_{l}^{\,P}\right]\left[IS_{0,l,i}^{\,P}\right]\left[S_{0,l}(h,\cos\theta)\right] \\ +\sum_{l=1}^{L}\sum_{m=1}^{l}\left[C3_{m,l}^{\,P}\right]\left[IS_{m,l,i}^{\,P}\right]\left[S_{m,l}(h,\cos\theta)\cos m(\varphi_{j}'-\varphi)\right] \end{array} \right] \qquad \text{(2-124a)}$$

Notation	Definition	Indices	Memory Storage Format
$C1$	$\left[\dfrac{\lambda_o}{(2\pi)^2}\right]$	none	scalar constant
$\left[C2_{l}^{\,P}\right]$	$\left[\dfrac{(\sqrt{-1})^{l+1}\Delta\varphi'}{N_{0,l}(h)R_{0,l}^{(4)}(h,\xi_o)}\right]$	$(l=0,1,\ldots,L)$	complex vector: $(L+1)$ elements
$\left[C3_{m,l}^{\,P}\right]$	$\left[4\dfrac{(\sqrt{-1})^{l+1}\sin m(\Delta\varphi'/2)}{mN_{m,l}(h)R_{m,l}^{(4)}(h,\xi_o)}\right]$	$(l=1,2,\ldots,L)$; $(m=1,2,\ldots,l)$	complex matrix: $L\times L$ elements {upper triangular}
$\left[IS_{0,l,i}^{\,P}\right]$	$\int_{\left[\vartheta_i'-\frac{\Delta\vartheta'}{2}\right]}^{\left[\vartheta_i'+\frac{\Delta\vartheta'}{2}\right]} S_{0,l}(h,\cos\vartheta')\sin\vartheta'\,d\vartheta'$	$(l=0,1,\ldots,L)$; $(i=1,2,\ldots,I)$	real matrix: $(L+1)\times I$ elements
$\left[IS_{m,l,i}^{\,P}\right]$	$\int_{\left[\vartheta_i'-\frac{\Delta\vartheta'}{2}\right]}^{\left[\vartheta_i'+\frac{\Delta\vartheta'}{2}\right]} S_{m,l}(h,\cos\vartheta')\sin\vartheta'\,d\vartheta'$	$(l=1,2,\ldots,L)$; $(m=1,2,\ldots,l)$; $(i=1,2,\ldots,I)$	real hyper-matrix: $L\times L\times I$ elements {triangular prism}
$f_{i,j}^{\,P}$	$f^{\,P}(\vartheta_i',\varphi_j')$	$(i=1,2,\ldots,I)$; $(j=1,2,\ldots,J)$	complex matrix: $I\times J$ elements

Table 2.5b Oblate Spheroidal NZ-FZT Algorithm for Each Cartesian Vector Component

$$\overline{\psi}^{O}_{fz}(\theta,\varphi) \cong$$

$$C1\sum_{i=1}^{I}\sum_{j=1}^{J} f^{O}_{i,j} \times \left[\begin{array}{l} \sum_{l=0}^{L}\left[C2^{O}_{l}\right]\left[IS^{O}_{0,l,i}\right]\left[S_{0,l}(-jh,\cos\theta)\right] \\ +\sum_{l=1}^{L}\sum_{m=1}^{l}\left[C3^{O}_{m,l}\right]\left[IS^{O}_{m,l,i}\right]\left[S_{m,l}(-jh,\cos\theta)\cos m(\varphi'_{j}-\varphi)\right] \end{array} \right] \quad \text{(2-124b)}$$

Notation	Definition	Indices	Memory Storage Format
$C1$	$\left[\frac{\lambda_o}{(2\pi)^2}\right]$	none	scalar constant
$\left[C2^{O}_{l}\right]$	$\left[\frac{(\sqrt{-1})^{l+1}\Delta\varphi'}{N_{0,l}(-jh)R^{(4)}_{0,l}(-jh,\, j\xi_o)}\right]$	$(l=0,1,\ldots,L)$	complex vector: $(L+1)$ elements
$\left[C3^{O}_{m,l}\right]$	$\left[4\frac{(\sqrt{-1})^{l+1}\sin m(\Delta\varphi'/2)}{mN_{m,l}(-jh)R^{(4)}_{m,l}(-jh,\, j\xi_o)}\right]$	$(l=1,2,\ldots,L)$; $(m=1,2,\ldots,l)$	complex matrix: $L\times L$ elements {upper triangular}
$\left[IS^{O}_{0,l,i}\right]$	$\int_{\left[\vartheta'_i-\frac{\Delta\vartheta'}{2}\right]}^{\left[\vartheta'_i+\frac{\Delta\vartheta'}{2}\right]} S_{0,l}(-jh,\cos\vartheta')\sin\vartheta'\,d\vartheta'$	$(l=0,1,\ldots,L)$; $(i=1,2,\ldots,I)$	real matrix: $(L+1)\times I$ elements
$\left[IS^{O}_{m,l,i}\right]$	$\int_{\left[\vartheta'_i-\frac{\Delta\vartheta'}{2}\right]}^{\left[\vartheta'_i+\frac{\Delta\vartheta'}{2}\right]} S_{m,l}(-jh,\cos\vartheta')\sin\vartheta'\,d\vartheta'$	$(l=1,2,\ldots,L)$; $(m=1,2,\ldots,l)$; $(i=1,2,\ldots,I)$	real hyper-matrix: $L\times L\times I$ elements {triangular prism}
$f^{O}_{i,j}$	$f^{O}(\vartheta'_i,\varphi'_j)$	$(i=1,2,\ldots,I)$; $(j=1,2,\ldots,J)$	complex matrix: $I\times J$ elements

the scalar case. In the next section, we show how to extend these algorithms to the vector case using our approach that employs a hybrid of coordinate systems.

Upon review of the algorithms disclosed in Tables 2.5a and 2.5b, important observations can be made regarding the implementation of the required computations. For any user selected spheroidal transformation surface, i.e., specified by h and ξ_o, all of the respective constants, vectors, and matrices only need to be computed once, regardless of the number of desired far-zone observation angles (θ,φ). From the viewpoint of computational efficiency (with respect to computation time and the total number of floating point operations), this algorithmic feature is quite beneficial because most of these quantities require many evaluations of computationally demanding special functions. However, this improvement in computational efficiency is only gained at the expense of memory storage. Fortunately, present technology does possess the memory storage capabilities required to implement these algorithms using the outlined storage scheme. It is important to note that some of the matrices, specifically, $\left[C3^{P}_{m,l}\right]$, $\left[IS^{P}_{m,l,i}\right]$, $\left[C3^{O}_{m,l}\right]$, and $\left[IS^{O}_{m,l,i}\right]$, could be more efficiently stored than the disclosed matrix format if need be.

Further inspection of both algorithms reveals that for each desired far-zone observation angle θ, the only special functions that need to be recalculated are their respective spheroidal angle functions, viz., $S_{m,l}(h,\cos\theta)$ or $S_{m,l}(-jh,\cos\theta)$, where $(l=0,1,\ldots,L)$ and $(m=0,1,\ldots,l)$. Correspondingly, for each user requested far-zone observation angle there are a total of $(L+1)(L+2)/2$ additional evaluations of the respective spheroidal angle functions.

Finally, the prolate or oblate wave-harmonic expansions of (2-124a) and (2-124b) must be summed for each user requested far-zone observation angle (θ,φ). It is in these summations that temporary storage can be exploited to further improve computational efficiency.

2.3.2 Extension of the Algorithmic Implementation for the Constructed Particular Solutions to the Required Vector Solutions

The final step in completing the newly developed NZ-FZT process is to extend the developed algorithms so that they can handle the computation of the required vector solutions. We do so by using the hybrid of coordinate systems approach discussed earlier in this chapter (see 2.2.2). The approach requires us to solve the vector Helmholtz equation by using its scalar solution (which corresponds to the scalar Helmholtz equation in spheroidal coordinates) to individually represent all three vector components in Cartesian coordinates. The overall vector solution is then obtained by using vector addition in Cartesian coordinates to combine all three scalar solutions.

The algorithms put forth in Tables 2.5a and 2.5b are capable of computing each Cartesian vector component of the far-zone E-field for both spheroidal transformation surfaces. Both algorithms individually operate on each Cartesian vector component of the Dirichlet boundary condition in one-to-one correspondence in order to extrapolate all three Cartesian vector components of the far-zone E-field. In essence, the same exact algorithm operates on $E_x(\vartheta_i', \varphi_j')$ to yield $\overline{E}_{fz_X}(\theta, \varphi)$, $E_y(\vartheta_i', \varphi_j')$ to yield $\overline{E}_{fz_Y}(\theta, \varphi)$, and $E_z(\vartheta_i', \varphi_j')$ to yield $\overline{E}_{fz_Z}(\theta, \varphi)$; we mathematically describe this process as follows:

Prolate:
$$\begin{Bmatrix} \overline{E}_{fz_X}(\theta, \varphi) \\ \overline{E}_{fz_Y}(\theta, \varphi) \\ \overline{E}_{fz_Z}(\theta, \varphi) \end{Bmatrix} = \overline{\psi}^P_{fz}(\theta, \varphi)\Big|_{f^P_{i,j}} \tag{2-125a}$$

where

$$f^P_{i,j} = f^P(\vartheta_i', \varphi_j') = \psi^P(\xi_o, \vartheta_i', \varphi_j') = \begin{Bmatrix} E_x(\vartheta_i', \varphi_j') \\ E_y(\vartheta_i', \varphi_j') \\ E_z(\vartheta_i', \varphi_j') \end{Bmatrix}; \tag{2-126a}$$

Oblate:
$$\left\{\begin{matrix}\overline{E}_{fz_x}(\theta,\varphi)\\ \overline{E}_{fz_y}(\theta,\varphi)\\ \overline{E}_{fz_z}(\theta,\varphi)\end{matrix}\right\} = \overline{\psi}^{O}_{fz}(\theta,\varphi)\Big|_{f^{O}_{i,j}} \tag{2-125b}$$

where

$$f^{O}_{i,j} = f^{O}(\vartheta'_i,\varphi'_j) = \psi^{O}(\xi_o,\vartheta'_i,\varphi'_j) = \left\{\begin{matrix}E_x(\vartheta'_i,\varphi'_j)\\ E_y(\vartheta'_i,\varphi'_j)\\ E_z(\vartheta'_i,\varphi'_j)\end{matrix}\right\}. \tag{2-126b}$$

It should be reiterated that the bar over each Cartesian component of the far-zone E-field indicates the suppression of the radial dependence (see 2.1.2). Meanwhile, each Cartesian component of the Dirichlet boundary condition is the near-zone E-field sampled on the spheroidal transformation surface in spheroidal coordinates.

Since each Cartesian component employs the same exact algorithm, the overall NZ-FZT process can take advantage of eliminating redundant computations. Specifically, we have formulated the required computations (i.e., the constants, vectors, matrices, spheroidal angle function evaluations, and part of the wave-harmonic expansion) to be independent of the samples of the Dirichlet boundary conditions, i.e., $E_x(\vartheta'_i,\varphi'_j)$, $E_y(\vartheta'_i,\varphi'_j)$, and $E_z(\vartheta'_i,\varphi'_j)$. However, the overall wave-harmonic summation, i.e., (2-124a) or (2-124b), still has to be performed individually for each Cartesian component. Nevertheless, elimination of these redundant computations does significantly improve the computational efficiency of the overall NZ-FZT process. Specific details regarding the best way to implement these computations are addressed in the subsequent chapter on NZ-FZT software development (see Chapter 4).

Now that each Cartesian vector component of the far-zone E-field has been determined, we are able to put the resulting far-zone E-field in spherical coordinates as specified by the NZ-FZT process output, i.e., equation (2-13):

$$\overline{E}_{fz_\theta}(\theta,\varphi) =$$
$$\cos\theta\cos\varphi\,\overline{E}_{fz_x}(\theta,\varphi) + \cos\theta\sin\varphi\,\overline{E}_{fz_y}(\theta,\varphi) - \sin\theta\,\overline{E}_{fz_z}(\theta,\varphi) \qquad (2\text{-}127)$$

$$\overline{E}_{fz_\varphi}(\theta,\varphi) = -\sin\varphi\,\overline{E}_{fz_x}(\theta,\varphi) + \cos\varphi\,\overline{E}_{fz_y}(\theta,\varphi)\,. \qquad (2\text{-}128)$$

This final step concludes the rigorous development of our newly formulated NZ-FZT process. Figure 2.3 summarizes the entire NZ-FZT process for both prolate and oblate spheroidal transformation surfaces by depicting an overall system diagram.

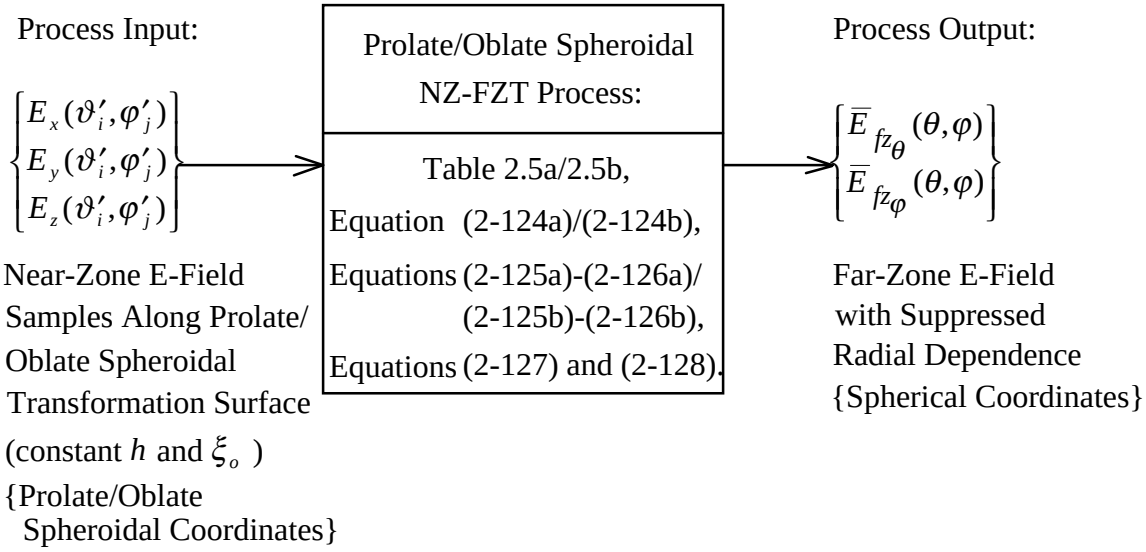

Figure 2.3 Overall system diagram of the newly developed NZ-FZT process for both prolate and oblate spheroidal transformation surfaces.

CHAPTER 3. NUMERICAL EVALUATION OF REQUIRED SPECIAL FUNCTIONS

Successful implementation of the newly developed NZ-FZT algorithms put forth in the preceding chapter requires the evaluation of special functions pertaining to prolate and oblate spheroidal wave functions. Unfortunately, calculating them is far from a simple process. Yet without the ability to evaluate these much needed special functions in an efficient and accurate manner, the scope of our developed algorithms would unfortunately remain confined to only theoretical applications. This chapter addresses the details and issues regarding the development of numerical routines capable of efficiently calculating these special functions while operating in the context of a working computational algorithm. As we shall see, these numerical routines are quite involved with respect to their computational procedures, as well as their interactions with one another. Since the development of these numerical routines is application driven, our discussion shall be procedurally based, thus leaving the interested reader to examine the supporting references for the theoretical details.

One of the major difficulties that must be avoided in the development of these numerical routines is the numerical roundoff error that often occurs in computational processes. As any individual experienced in the field of scientific computing will attest, theoretical expressions for desired quantities do not always lend themselves well to numerical techniques. Accordingly, our concern becomes whether or not these numerical routines for the special functions can furnish results that are precise enough for the NZ-FZT algorithms. Moreover, these routines must be able to provide accurate results for all orders m and degrees l that are necessary to achieve convergence of the spheroidal wave-harmonic expansions contained within our algorithms. Lastly, we do not want to rely on esoteric computer platforms that have more precision than that which is generally available for a typical IEEE-compliant 32-bit machine. For the most part, the accessibility of such extraordinary machines is quite often limited and costly. Fortunately, we are able with much finesse to implement these routines using double

precision on a standard IBM compatible personal computer (considered a typical IEEE-compliant 32-bit machine). At the time of writing, the use of this particular platform is considered quite advantageous because it is relatively inexpensive and, more often than not, readily available.

3.1 OVERVIEW OF SPECIAL FUNCTION NUMERICAL ROUTINES

3.1.1 Description and Organization of Top-Level Numerical Routines

As mentioned at the outset of this chapter, the numerical routines necessary to accurately evaluate these special functions are extremely involved. This is partly so because computation of some of these functions requires the evaluation of other constituent special functions that, in and of themselves, are complicated. Furthermore, the level of complexity for some of these special function routines is increased by virtue of having totally different computational approaches for different regions of interest. In this section, we describe the required top-level numerical routines and their relationship to one another; we do so in order to gain an understanding of the overall computational process for the special functions. So as to be concise, the scope of our discussion is limited to the required top-level numerical routines. Toward that end, we have intentionally excluded details concerning the supporting lower-level routines.

Many of the developed special function routines make use of computational approaches (including the resultant numerical experience) described in a series of formal reports published by the Acoustics Division of the Naval Research Laboratory (NRL) [32], [34]-[36]. Additionally, some of the routines are streamlined versions of Fortran subroutines presented in *Numerical Recipes in FORTRAN* [37]. And finally, others are developed directly from the outcomes of many numerical experiments, which were so conducted in order to determine the best computational approaches. By using this eclectic mix of methods and routines, an altogether numerical process is developed that

computes the required special functions in the best possible way, i.e., in terms of accuracy and efficiency, for our specific application.

Shown in Figures 3.1a and 3.1b are structure charts depicting the overall organization of the top-level numerical routines that is necessary to compute the prolate and oblate special functions. The name of each routine is chosen to somewhat reflect its respective computational objective. Accompanying these figures are Tables 3.1a and 3.1b, which furnish an overview of the top-level routines by providing a brief functional description of each routine. To facilitate our discussion, we have chosen to tag each numerical routine with a reference index. Although the meaning of the lettered prefix contained within the reference index may be somewhat obvious, we nevertheless describe its interpretation and bearing on the routine referenced: "P," only needed in the prolate special function computational process; "O," only needed in the oblate special function computational process; and "B," needed in both computational processes.

Upon review of Figures 3.1a and 3.1b, we recognize that there are essentially five primary numerical routines for each spheroidal case. All of the primary routines have been assigned a reference index with a numbered suffix so as to distinguish them from the remaining secondary routines. The computational objectives of the primary routines are as follows: (P-1) and (O-1) compute an initial approximation of all desired eigenvalues; (P-2) and (O-2) compute the Sturm-Liouville normalization constants for the respective spheroidal angle function; (P-3) and (O-3) evaluate the respective spheroidal radial function of the first and second kind along with both of their first derivatives; (P-4) and (O-4) evaluate the respective spheroidal angle functions; (P-5) and (O-5) compute the integral of the respective spheroidal angle functions over a given interval. As we can see, these routines provide all of the computations necessary to implement the prolate and oblate spheroidal NZ-FZT algorithms of Chapter 2. All of the secondary numerical routines, i.e., those that have a reference index that contains a lettered suffix, essentially support the computation of one or more of these primary routines.

It is important to note that although the first derivatives of the spheroidal radial functions are not used directly by the NZ-FZT algorithms, they are nevertheless provided

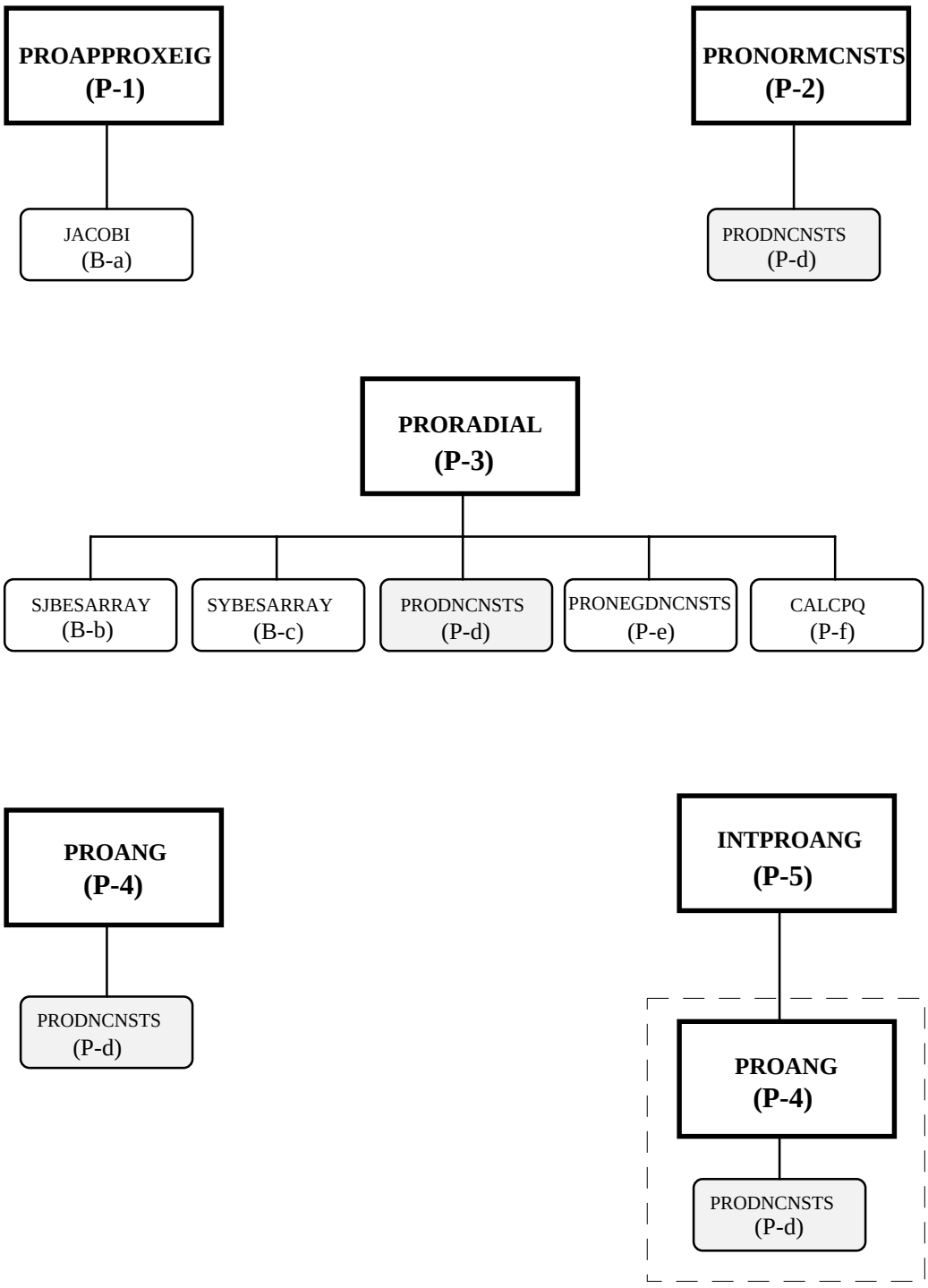

Figure 3.1a Structure chart indicating organization of top-level numerical routines required to compute the prolate spheroidal special functions.

Table 3.1a Overview of Top-Level Numerical Routines Required to Compute the Prolate Spheroidal Special Functions

Reference Index	Top-level Routine Name	Top-level Routine Functional Description
(P-1)	PROAPPROXEIG	Provides an initial approximation to all desired prolate spheroidal eigenvalues.
(P-2)	PRONORMCNSTS *	Provides Sturm-Liouville normalization constants for prolate spheroidal angle functions.
(P-3)	PRORADIAL	Evaluates the prolate spheroidal radial functions of the first and second kind along with their respective first derivatives.
(P-4)	PROANG *	Evaluates the prolate spheroidal angle function.
(P-5)	INTPROANG *	Computes the integral of the prolate spheroidal angle function over a given interval.
(B-a)	JACOBI	Employs the Jacobi transformation method to solve eigenvalues of a real symmetric matrix.
(B-b)	SJBESARRAY	Evaluates required values of spherical Bessel functions.
(B-c)	SYBESARRAY	Evaluates required values of spherical Neumann functions.
(P-d)	PRODNCNSTS *	Computes $d_r^{m,l}(h)$ expansion coefficients. Also, given an initial approximation to the prolate eigenvalue, this routine replaces it with one that has a higher degree of accuracy.
(P-e)	PRONEGDNCNSTS *	Computes $d_{-r}^{m,l}(h)$ and $d_{\rho/r}^{m,l}(h)$ expansion coefficients.
(P-f)	CALCPQ	Computes the required values of associated Legendre functions of the first and second kind for real arguments that do not lie on the $(-1 < x < +1)$ branch cut or the $x = \pm 1$ singular points.

* - Denotes that the routine yields results in terms of the Morse and Feshbach normalization scheme.

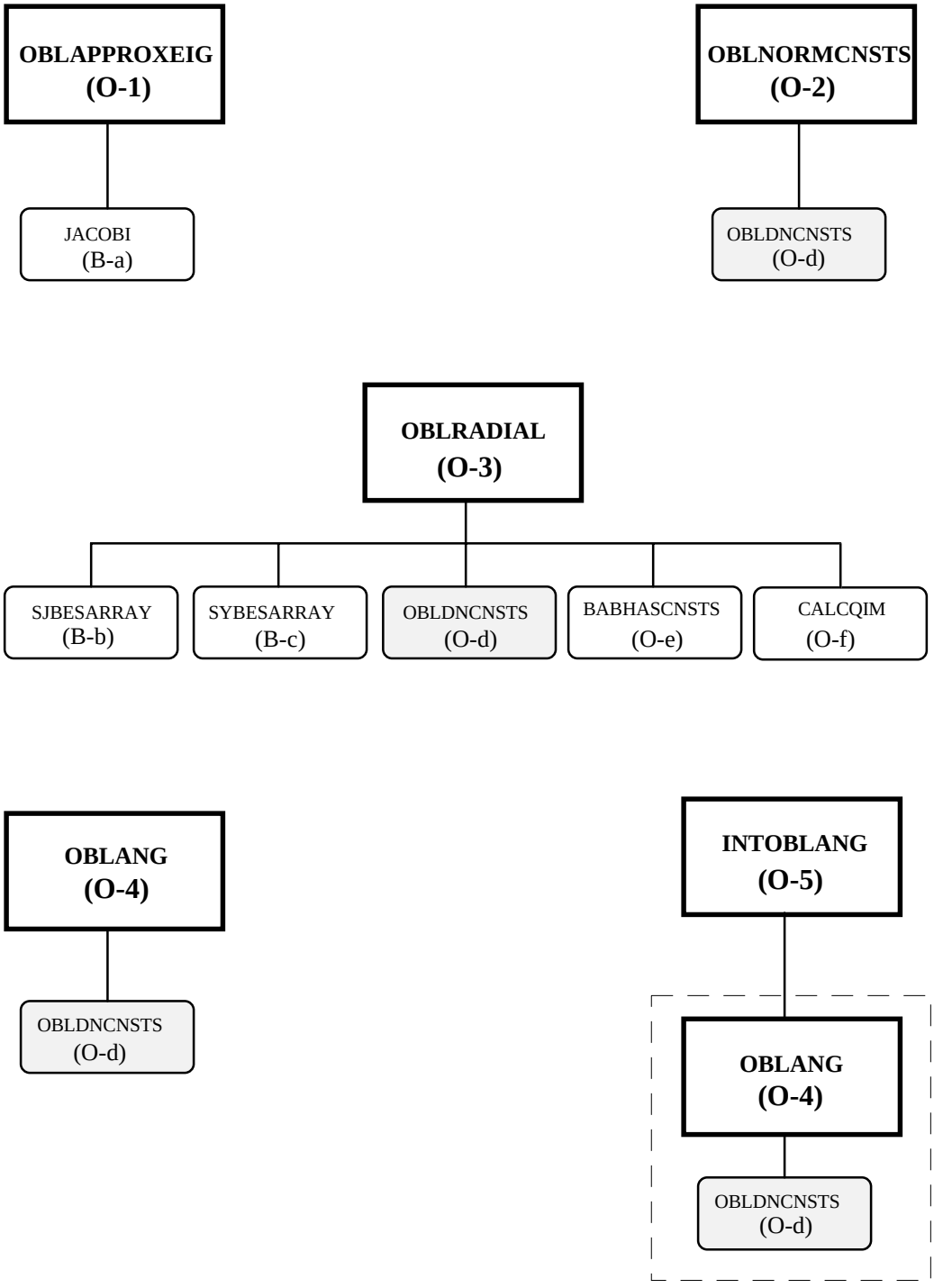

Figure 3.1b Structure chart indicating organization of top-level numerical routines required to compute the oblate spheroidal special functions.

Table 3.1b Overview of Top-Level Numerical Routines Required to Compute the Oblate Spheroidal Special Functions

Reference Index	Top-level Routine Name	Top-level Routine Functional Description
(O-1)	OBLAPPROXEIG	Provides an initial approximation to all desired oblate spheroidal eigenvalues.
(O-2)	OBLNORMCNSTS *	Provides Sturm-Liouville normalization constants for oblate spheroidal angle functions.
(O-3)	OBLRADIAL	Evaluates the oblate spheroidal radial functions of the first and second kind along with their respective first derivatives.
(O-4)	OBLANG *	Evaluates the oblate spheroidal angle function.
(O-5)	INTOBLANG *	Computes the integral of the oblate spheroidal angle function over a given interval.
(B-a)	JACOBI	Employs the Jacobi transformation method to solve eigenvalues of a real symmetric matrix.
(B-b)	SJBESARRAY	Evaluates required values of spherical Bessel functions.
(B-c)	SYBESARRAY	Evaluates required values of spherical Neumann functions.
(O-d)	OBLDNCNSTS *	Computes $d_r^{m,l}(-jh)$ expansion coefficients. Also, given an initial approximation to the oblate eigenvalue, this routine replaces it with one that has a higher degree of accuracy.
(O-e)	BABHASCNSTS	Computes Baber and Hasse normalized expansion coefficients $\left(\boldsymbol{A}_r^{m,l} / \boldsymbol{A}_{-m}^{m,l}\right)$.
(O-f)	CALCQIM	Computes the required values of associated Legendre functions of the second kind for purely imaginary arguments that do not lie on the $(-1 < x < +1)$ branch cut (i.e., excludes $x = 0$)

* - Denotes that the routine yields results in terms of the Morse and Feshbach normalization scheme.

to the user. As fortune would have it, this feature does not have a negative impact on computational efficiency because determination of these first derivatives is required in the process of computing their respective spheroidal radial functions. Since the first derivatives of the spheroidal radial functions are computational by-products and come at no expense, they are provided in order to make the set of numerical routines more versatile and complete.

Regarding the primary numerical routines that directly or indirectly involve the spheroidal angle functions, namely, (P-2), (P-4), (P-5), (O-2), (O-4), and (O-5), they render their results in terms of the Morse and Feshbach normalization scheme (see 2.2.5). Consequently, some of the secondary routines, viz., (P-d), (P-e), and (O-d), also furnish their results in terms of Morse and Feshbach normalization. Notwithstanding, it should be made clear that even though our special function routines happen to employ this particular normalization scheme, both of our developed NZ-FZT algorithms work properly regardless of the normalization selected. However, the use of a different normalization scheme would ultimately require all of our special functions that are dependent on the Morse and Feshbach normalization to be modified accordingly.

Upon further review of the structure charts shown in Figures 3.1a and 3.1b, it is important to note that there is an element of redundancy within the overall computational process for the special functions. For each spheroidal case, four of the five primary numerical routines share a common secondary routine: namely, PRODNCNSTS (P-d) in the prolate case, and OBLDNCNSTS (O-d) in the oblate case. Furthermore, in each spheroidal case one of the primary routines evokes another primary routine. In particular, the routines that compute the integration of the spheroidal angle functions must each use the routine that calculates the respective spheroidal angle function, viz., INTPROANG (P-5) uses PROANG (P-4), and INTOBLANG (O-5) uses OBLANG (O-4).

Finally, we would like to highlight that the computational processes for both prolate and oblate special functions do have some significant differences. Some of the routines for the oblate special functions can be derived from their respective prolate counterparts with some minor modifications. However, other routines require totally

different numerical approaches. The principal difference between both sets of numerical routines occurs when evaluating the respective spheroidal radial functions, viz., (P-3) and (O-3), as well as a few of their supporting secondary routines. Further details concerning these differences are addressed in the sections of this chapter that discuss each of the spheroidal radial function routines.

3.1.2 Numerical Precision and Accuracy

As a numerical algorithm progresses through its computations, the possibility exists that inherent roundoff error will cause the accuracy of each passing stage of floating-point computations to continually degrade until the overall results become completely swamped with erroneous calculations [37]. In these catastrophic cases where numerical algorithms fail to converge upon usable results, the computations are said to have become numerically unstable. More often than not, it is very difficult to characterize these numerical errors and predict the performance of a given algorithm without conducting numerical experiments. Furthermore, a given algorithm may work well for one particular region of operating parameters while failing miserably for others.

The ultimate goal of our NZ-FZT process is to provide single precision results for the far-zone E-field response (i.e., between six and seven significant digits on a typical IEEE-compliant 32-bit machine). However, numerical experience has shown that computation of the NZ-FZT algorithms should be conducted in double precision (i.e., between fifteen and sixteen significant digits on a typical IEEE-compliant 32-bit machine) in order to achieve the desired single precision results. In particular, the use of double precision is instrumental in minimizing the roundoff error when summing the spheroidal wave-harmonic expansions.

Since our NZ-FZT algorithms need to be performed with double precision, logic dictates that our special function routines must also support double precision. Besides using double precision to achieve more accurate results for the special functions, its use is also required in certain instances to avoid underflow/overflow errors. As we shall see,

some of the numerical routines require expansions of functions that contain values that lie outside the permissible range of magnitude for single precision, viz., $(10^{-38} < |x| < 10^{+38})$ for a typical IEEE-compliant 32-bit machine [37]. By using double precision, the range of magnitude can be extended to $(10^{-308} < |x| < 10^{+308})$ on a typical IEEE-compliant 32-bit machine [37].

During the development of the numerical routines for the special functions, each of the secondary routines is individually tested and validated before being integrated with its respective primary routine. Results from the secondary routines are compared with published tabulated data whenever available to help confirm their accuracy. Following the validation and integration of the secondary routines, the overall primary routines are then tested. First, the results of the primary routines are compared with tabulated data for a given set of parameters whenever possible. Unfortunately, most of the published data sets that are available are limited with respect to the number of decimal places provided and the number of test cases presented.

In some cases, we make use of computational checks to further corroborate the accuracy of the developed routines. Some of these computational checks consist of comparing the results of the developed primary routines with other routines that calculate the same special functions by way of a different numerical approach. In general, these other approaches were not considered the method of choice because of their lack of computational efficiency and limited range of validity. Nonetheless, the development of these less efficient routines is not in vain because they still contribute to our overall validation process.

The remaining computational checks consist of comparing the results of both spheroidal radial function routines with their known Wronskian value. Specifically, both routines take advantage of the Wronskian check and use it during the computational process to ensure the accuracy of their results. Details regarding this process are addressed in the sections pertaining to the prolate and oblate spheroidal radial functions.

As mentioned earlier, these numerical routines must be able to provide accurate results for all orders m and degrees l necessary to achieve convergence of the spheroidal wave-harmonic expansions. Naturally, the number of terms required to achieve convergence depends on the functions that are to be expanded, viz., the Dirichlet boundary conditions that exist on the spheroidal transformation surface. However, computational testing for reasonable values of h (viz., where $h < 20$) indicates that a ceiling of 50 should be imposed on all orders m and degrees l (i.e., $L \leq 50$) so as to ensure that the numerical routines safely provide reasonable results. We do so because the special function routines may deliver questionable results for wave-harmonics that lie beyond this imposed ceiling. Fortunately, experience shows that for our particular application, the prolate and oblate spheroidal wave-harmonic expansions converge well before reaching the imposed ceiling with a considerable margin of allowable orders and degrees remaining.

3.2 PROLATE AND OBLATE SPHEROIDAL EIGENVALUES

3.2.1 PROAPPROXEIG (P-1) and OBLAPPROXEIG (O-1) Numerical Routines

The first step in evaluating all of the prolate and oblate spheroidal wave functions is the determination of their respective eigenvalues: $\lambda_{m,l}(h)$ and $\lambda_{m,l}(-jh)$. It should be noted that each of the other primary numerical routines for the special functions must first be supplied with its respective eigenvalues before it can proceed with its calculations. As previously pointed out in Chapter 2, computation of these eigenvalues is not straightforward and involves the use of a complicated numerical process. The computational approach that we have decided to incorporate into our numerical routines is that which is used and explained in NRL formal reports [32], [34]-[36]. Our experience shows that this approach performs the best with regard to computational efficiency and accuracy. The approach is essentially a two-step process that first requires the eigenvalues to be determined approximately and then subjects them to a refining

process to improve their accuracy. Both numerical routines addressed in this section only carry out the first part of this process (this explains the choice of their names). The second part of the process that refines the eigenvalues for each spheroidal case is performed by the commonly shared secondary routines PRODNCNSTS (P-d) and OBLDNCNSTS (O-d); details concerning refinement of the eigenvalues are addressed in the subsequent section that features both of these routines (see 3.3.2).

Hanish and King [32] present the detailed theory behind the computational process that provides an initial approximation to the spheroidal eigenvalues. Although this intricate theory lies outside the scope of our discussion, the interested reader is referred here to gain further insight into the theoretical basis of this computational process. With regard to practicality, the other NRL formal reports, viz., [34]-[36], describe the matrix methods required to compute an initial approximation of both sets of spheroidal eigenvalues.

These matrix methods are able to compute an accurate initial approximation of the eigenvalues for both spheroidal cases by solving a set of linear algebra eigenvalue problems. In keeping with the nomenclature of fundamental linear algebra, these eigenvalue problems can be expressed using the following standard matrix equations [35]:

Prolate: $$[\mathbf{L}(h,m) - \lambda(h)\mathbf{I}]\vec{d}(h) = 0\,; \tag{3-1a}$$

Oblate: $$[\mathbf{L}(-jh,m) - \lambda(-jh)\mathbf{I}]\vec{d}(-jh) = 0\,. \tag{3-1b}$$

In these matrix equations, the parameters are defined as follows: $\mathbf{L}(h,m)$ and $\mathbf{L}(-jh,m)$ are infinite square real symmetric matrices dependent on h and m; $\vec{d}(h)$ and $\vec{d}(-jh)$ are possible eigenvectors that represent $d_r^{m,l}(h)$ and $d_r^{m,l}(-jh)$ expansion coefficients with respect to normalized associated Legendre functions; $\lambda(h)$ and $\lambda(-jh)$ represent the desired spheroidal eigenvalues for a given order m, i.e., $l = m, m+1, \ldots$, when arranged in

a monotonic increasing sequence; and $\mathbf{I}$ is the corresponding identity matrix. Accordingly, a separate eigenvalue problem must be solved for each desired order m so that all of the needed eigenvalues can be determined.

In order to continue with our discussion of the eigenvalue problems at hand, we must first explore the matrices $\mathbf{L}(h,m)$ and $\mathbf{L}(-jh,m)$ in more detail. Although both of these matrices are infinite in size, King *et al.* [35] have indicated that truncated matrices of modest proportions will yield an initial approximation of the eigenvalues accurate enough to supply the refining part of the computational process. More specifically, their experience has found that in the prolate case a truncated matrix of size (50×50) delivers good approximations of the eigenvalues for $l = m, m+1, \ldots, m+49$ when $h < 10$. However, as h increases in magnitude, the size of the truncated matrix must also increase in order to supply approximations for the lowest 50 eigenvalues that are sufficiently accurate. According to [35], truncated matrices of size (90×90) have been shown to deliver sufficiently accurate approximations for the lowest 50 eigenvalues for the specific case where $h = 80$. Because the size of the truncated matrix required to deliver an acceptable approximation of the eigenvalues is not known exactly, King *et al.* [35] provide a practical approach to solve this problem. Their approach selects the size of the truncated matrix $(K\times K)$ between $50 \le K \le 100$ by using a linear function of h that passes through the two numerical benchmarks, namely, ($h = 0$, $K = 50$) and ($h = 80$, $K = 90$). Although King *et al.* [35] cite this practical approach for only the prolate spheroidal case, another NRL formal report, viz., [34], extends the approach (with slightly different numerical benchmarks) to its oblate counterpart. Based upon the success of their experiences for both spheroidal cases, we have chosen to adopt their approach using ($h = 0$, $K = 51$) and ($h = 80$, $K = 91$) to determine the size of our truncated $\mathbf{L}(h,m)$ and $\mathbf{L}(-jh,m)$ matrices.

Now that we have an understanding of how to truncate the matrices $\mathbf{L}(h,m)$ and $\mathbf{L}(-jh,m)$, we proceed to examine the content of their elements. King *et al.* [34], [35]

explicitly put forth in their computational procedures the following expressions for the elements of the truncated matrices:

Prolate:

$$\mathbf{L}_{\mathrm{i,j}}(h,m) =$$

$$\left\{\begin{array}{ll} i=j: & \left[p(p+1)+h^2\,\dfrac{2p(p+1)-2m^2-1}{(2p-1)(2p+3)}\right] \\ \left.\begin{array}{l} i=j+2 \\ j=i+2 \end{array}\right\}: & \left[\dfrac{h^2}{(2p+3)}\sqrt{\dfrac{(p+m+2)(p+m+1)(p-m+2)(p-m+1)}{(2p+1)(2p+5)}}\right] \\ \text{elsewhere:} & 0 \ \text{(other elements)} \end{array}\right\};$$

(3-2a)

Oblate:

$$\mathbf{L}_{\mathrm{i,j}}(-jh,m) =$$

$$\left\{\begin{array}{ll} i=j: & \left[p(p+1)-h^2\,\dfrac{2p(p+1)-2m^2-1}{(2p-1)(2p+3)}\right] \\ \left.\begin{array}{l} i=j+2 \\ j=i+2 \end{array}\right\}: & \left[\dfrac{-h^2}{(2p+3)}\sqrt{\dfrac{(p+m+2)(p+m+1)(p-m+2)(p-m+1)}{(2p+1)(2p+5)}}\right] \\ \text{elsewhere:} & 0 \ \text{(other elements)} \end{array}\right\};$$

(3-2b)

where $i, j = 0,1,2,\ldots,K$ and $p = m+i$ for both cases.

Upon inspection of these expressions, we are able to recognize an important property of the matrices $\mathbf{L}(h,m)$ and $\mathbf{L}(-jh,m)$: the only nonzero elements are those situated on the principal diagonal (i.e., $i=j$), the second subdiagonal (i.e., $i=j+2$), and the second

superdiagonal (i.e., $j = i + 2$). From a viewpoint of filling these matrices, its symmetry can be used to easily derive elements of the second subdiagonal from those of the second superdiagonal, e.g., $\mathbf{L}_{5,7} = \mathbf{L}_{7,5}$, or vice-versa. One should also note that the matrix for the oblate case (3-2b) can be easily derived from its prolate counterpart (3-2a) by using the previously mentioned transformation $h \to -jh$.

Having discussed the matrix method for approximating the set of eigenvalues for a given order *m*, we now must address its connection to the eigenvalue matrix described in Table 2.4 (which differs from the matrices $\mathbf{L}(h, m)$ and $\mathbf{L}(-jh, m)$). Each row of the eigenvalue matrix (i.e., corresponding to a given order *m*) is approximated by solving a separate linear algebra eigenvalue problem. Disregarding the negative orders of the eigenvalue matrix (due to its symmetry with respect to the order *m*; see 2.2.5), we are left with solving $(L+1)$ separate linear algebra eigenvalue problems in order to fill the desired eigenvalue matrix with its respective initial approximations (recalling from Chapter 2 that *L* represents the user prescribed degree as to where the wave-harmonic expansion is truncated). This eigenvalue matrix is then stored in memory for non-negative orders of *m* (including *m* = 0) using a $(L+1)\times(L+1)$ two-dimensional matrix; note that zero-fill is used for elements that do not have an eigenvalue corresponding to the indices *m* and *l*.

3.2.2 JACOBI (B-a) Numerical Routine

In the process of computing an initial approximation of the spheroidal eigenvalues, the matrix methods employed in both PROAPPROXEIG (P-1) and OBLAPPROXEIG (O-1) call for a number of linear algebra eigenvalue problems to be solved for numerically. Since both of these primary routines provide the computational setup for the resulting eigenvalue problems, a generic numerical process is then needed to individually solve them. As a result, it is the purpose of this supporting secondary routine to numerically evaluate the eigenvalues for a given $\mathbf{L}(h, m)$ or $\mathbf{L}(-jh, m)$ truncated matrix.

There are many existing numerical techniques and routines available able to compute the eigenvalues of a given matrix. The computational advantage of any one of these techniques over another depends on some *a priori* knowledge of the matrix under consideration. This is so because many of these numerical techniques are specially designed to handle a specific class of matrices possessing certain characteristics. More often than not, these specialized numerical techniques perform much better for their intended class of matrices than their generalized counterparts. Naturally, it is our intent to use the eigenvalue technique that is the most beneficial for our particular application.

As mentioned earlier, the truncated $\mathbf{L}(h,m)$ and $\mathbf{L}(-jh,m)$ matrices employed during the matrix method of (P-1) and (O-1) routines are real and symmetric. Accordingly, the Jacobi method proves to be a suitable eigenvalue technique for our particular application because it takes advantage of both of these matrix characteristics. The method employs a sequence of orthogonal similarity transformations (i.e., Jacobi rotations) with each one being a plane rotation designed to eliminate one of the off-diagonal matrix elements [37]. Although successive transformations undo previously set zeros, the off-diagonal elements do continue to get smaller with each passing iteration until the matrix is diagonal to machine precision. The on-the-fly product (i.e., the matrix multiplication) of these successive transformations leads to the overall transformation matrix that is comprised of its corresponding eigenvectors. After applying the similarity transformation to the original matrix, the resulting elements of the final diagonal matrix are the eigenvalues. The interested reader is referred to *Numerical Recipes in FORTRAN* [37] for further details regarding this robust eigenvalue numerical technique.

According to [37], the Jacobi method is considered absolutely foolproof for all real symmetric matrices. Although they do mention that the algorithm can be significantly slower than others when considering large matrices, they also cite that the Jacobi method is much simpler than these other more efficient methods. Because our application requires us to compute the set of eigenvalues only once for a given transformation surface, the additional computational expense associated with this numerical method does not seriously lengthen our overall computation time.

The JACOBI (B-a) numerical routine is a streamlined version of the one presented in [37]. Since our application does not derive the eigenvectors from this portion of the process, we have chosen to eliminate the eigenvector feature from their routine. Furthermore, this routine puts the eigenvalues in monotonic increasing order as required by our application.

3.3 STURM-LIOUVILLE NORMALIZATION CONSTANTS FOR THE PROLATE AND OBLATE SPHEROIDAL ANGLE FUNCTIONS

3.3.1 PRONORMCNSTS (P-2) and OBLNORMCNSTS (O-2) Numerical Routines

We now proceed with the development of the two primary routines that compute the Sturm-Liouville normalization constants for the prolate and oblate spheroidal angle functions. As mentioned beforehand, both of these numerical routines provide normalization constants that are consistent with the Morse and Feshbach normalization scheme. In order for these routines to operate properly, they must be supplied with initial approximations to all eigenvalues corresponding to the desired normalization constants. Furthermore, the Sturm-Liouville normalization constants only have to be computed once for a given spheroidal transformation surface.

A computational by-product of these primary routines, i.e., (P-2) and (O-2), is that the approximate eigenvalues that are supplied to these routines (computed by the primary routines (P-1) and (O-1)) are replaced afterwards with more accurate values. In essence, it is the execution of these routines that serves as the second part of the eigenvalue computation process that refines the initial set of approximate eigenvalues. This refinement occurs because the secondary routines PRODNCNSTS (P-d) and OBLDNCNSTS (O-d), which directly perform the eigenvalue refinement portion of the process, must be used by these primary routines. It should be noted that if the initial approximation of any eigenvalue happens to match the refined eigenvalue within the

precision provided by either of the secondary routines (P-d) and (O-d), then its value virtually remains unchanged by the routine.

Our numerical experience indicates that the best way to compute the Sturm-Liouville normalization constants for both spheroidal angle functions is to use the following expansions presented by Flammer [23]:

Prolate: $$N_{m,l}(h) = 2\sum_{r=0,1}^{\infty}{}' \left[d_r^{m,l}(h)\right]^2 \frac{(2m+r)!}{(2m+2r+1)r!}; \qquad (3\text{-}3a)$$

Oblate: $$N_{m,l}(-jh) = 2\sum_{r=0,1}^{\infty}{}' \left[d_r^{m,l}(-jh)\right]^2 \frac{(2m+r)!}{(2m+2r+1)r!}; \qquad (3\text{-}3b)$$

where the prime over the summation sign indicates that the summation is over only even values of r when $(l-m)$ is even, and over only odd values of r when $(l-m)$ is odd. Both of these expressions can be derived from taking the inner product of their respective spheroidal angle function while representing them with their appropriate expansion of associated Legendre functions, viz., equations (2-68a) and (2-68b). In deriving expansions (3-3a) and (3-3b), the factorial expressions are a result of using the orthogonality property of the associated Legendre functions of the first kind, i.e., equation (2-65). The routines PRODNCNSTS (P-d) and OBLDNCNSTS (O-d) are summoned to deliver the $d_r^{m,l}(h)$ and $d_r^{m,l}(-jh)$ expansion coefficients. It must be pointed out that during the computational process the ratio of factorial expressions must be evaluated carefully in order to avoid overflow conditions. Furthermore, convergence of these expansions is quite rapid due to the fact that the $d_r^{m,l}(h)$ and $d_r^{m,l}(-jh)$ coefficients are squared.

Flammer [23] presents tabulated values of the Sturm-Liouville normalization constants for the prolate spheroidal angle functions, yet for some reason does not provide values of the normalization constants for the oblate case. Consequently, we take a two-pronged approach when validating these primary routines. In the prolate spheroidal case,

we naturally make use of the available tabulated data (after accounting for the difference in normalization schemes) to validate the PRONORMCNSTS (P-2) routine. In general, results of the prolate routine are fairly consistent with the tabulated values. As for the oblate spheroidal case, we must resort to some sort of computational check. Specifically, our computational check consists of a conducting numerical integration of the square of the oblate spheroidal angle function over the $[-1,1]$ interval; the results are then compared to those obtained from the OBLNORMCNSTS (O-2) routine, i.e., found by using (3-3b). For the cases tested, the two different methods yield results that match one another extremely well.

3.3.2 PRODNCNSTS (P-d) and OBLDNCNSTS (O-d) Numerical Routines

These secondary routines compute their respective set of $d_r^{m,l}(h)$ and $d_r^{m,l}(-jh)$ expansion coefficients using the Morse and Feshbach normalization scheme for a given order *m*, degree *l*, and independent parameter *h*. Because these routines are called by many of the primary routines, they are essentially at the core of all special function computations. In the organization of this chapter, the discussion of these routines could have easily been placed in any of the other sections that describe the primary routines for which they support. However, we have chosen to include their discussion here because PRONORMCNSTS (P-2) and OBLNORMCNSTS (O-2) are chronologically the first primary routines in our NZ-FZT process to evoke these much shared secondary routines.

Both routines make use of a variational method devised by Bouwkamp in [38] and further described in [23], [34], [35]. Also, it must be mentioned that this variational method was developed independently by Blanch [39]. In order for the Bouwkamp/Blanch method to function properly, it requires an initial approximation of the eigenvalue, viz., $\lambda_{m,l}^{(1)}(h)$ or $\lambda_{m,l}^{(1)}(-jh)$; this requirement explains the necessity of both the PROAPPROXEIG (P-1) and OBLAPPROXEIG (O-1) numerical routines. The Bouwkamp/Blanch method is essentially an iterative numerical process that converges upon the desired eigenvalue within some desired degree of accuracy using an initial

approximation of the eigenvalue as its starting point. Moreover, in the process of improving the accuracy of the approximate eigenvalue, the method simultaneously renders the much needed $d_r^{m,l}(h)$ and $d_r^{m,l}(-jh)$ expansion coefficients. Thus, both of these numerical routines intrinsically carry out the second part of the eigenvalue computational process that refines the eigenvalue.

Since the computational procedures to calculate the expansion coefficients for both spheroidal cases, i.e., $d_r^{m,l}(h)$ and $d_r^{m,l}(-jh)$, closely parallel one another, we shall from this point forward (for the remainder of this section) only discuss in detail the process that corresponds to the prolate spheroidal case. Regarding the process that computes the expansion coefficients for the oblate spheroidal case, it can be easily derived from its prolate counterpart using the ubiquitous $h \to -jh$ transformation. Accordingly, both PRODNCNSTS (P-d) and OBLDNCNSTS (O-d) routines essentially use the same procedure with the only exception being the difference in sign between some of the terms containing the independent parameter *h*.

The first step in computing the $d_r^{m,l}(h)$ expansion coefficients is to compute the correction term $\delta\lambda_{m,l}(h)$ to the initial approximation of the eigenvalue $\lambda_{m,l}^{(1)}(h)$. After finding this correction term, it can be applied to the approximate eigenvalue as follows to determine a more accurate numerical representation of the eigenvalue [23]:

$$\lambda_{m,l}(h) = \lambda_{m,l}^{(1)}(h) + \delta\lambda_{m,l}(h) . \qquad \text{(3-4a)}$$

With the accuracy of the eigenvalue improved, the process can then be applied again to further refine its initial result. According to Flammer [23], one or two applications of this iterative method will lead to remarkably accurate eigenvalues. Moreover, Flammer [23] indicates that Bouwkamp [38] showed the method to improve the approximate eigenvalue from two- to six-decimal accuracy with only one iteration of the process.

Recalling that the $d_r^{m,l}(h)$ expansion coefficients exist for only even terms when $(l-m)$ is even and only odd terms when $(l-m)$ is odd, we formally state

$$r = \begin{cases} 0, 2, 4, \ldots & \text{for } (l-m) \text{ even}, \\ 1, 3, 5, \ldots & \text{for } (l-m) \text{ odd}. \end{cases} \tag{3-5a}$$

Bearing this property in mind, we now make use of two closely related forms of a three-term recurrence relation (derived from one another using a shift of index) [35]:

$$\Lambda_r^m = \frac{-\beta_r^m}{\gamma_r^m - \lambda_{m,l}^{(1)}(h) + \Lambda_{r+2}^m} \text{ for } r \geq 2, \tag{3-6a}$$

$$\Lambda_r^m = -\gamma_{r-2}^m + \lambda_{m,l}^{(1)}(h) - \frac{\beta_{r-2}^m}{\Lambda_{r-2}^m} \text{ for } r \geq 4, \tag{3-7a}$$

where

$$\gamma_r^m = (m+r)(m+r+1) + \tfrac{1}{2}h^2\left[1 - \frac{4m^2-1}{(2m+2r-1)(2m+2r+3)}\right] \text{ for } r \geq 0, \tag{3-8a}$$

$$\beta_r^m = \frac{r(r-1)(2m+r)(2m+r-1)}{(2m+2r-1)^2(2m+2r-3)(2m+2r+1)}h^4 \text{ for } r \geq 2. \tag{3-9a}$$

The difference between these two forms of the recurrence relation is the direction in which they compute the Λ_r^m terms: recurrence relation (3-6a) works its way downward (i.e., backward); as opposed to recurrence relation (3-7a), which works its way upward (i.e., forward). The fact that both recurrence expressions relate a given term to another term that differs in index by two is consistent with (3-5a).

Upon review of (3-6a), one can see that the downward recurrence relation can be written as a continued fraction. Since Flammer [23] indicates that $\lim_{r\to\infty} \Lambda_r^m = 0$, the continued fraction can be safely terminated at some reasonable large value for the index *r*, viz., $r = r_{term}$ (remembering to select the appropriate even or odd index), by letting $\Lambda_{r_{term}+2}^m = 0$. As a result, the starting point for the downward recurrence relation can be taken as [34]:

$$\Lambda^m_{r_{term}} = \frac{-\beta^m_{r_{term}}}{\gamma^m_{r_{term}} - \lambda^{(1)}_{m,l}(h)}. \tag{3-10a}$$

Using this starting point, the remaining values in the Λ^m_r sequence can then be determined by working downward using the recurrence relation (3-6a).

Likewise, the upward recurrence relation (3-7a) can also be written in terms of a continued fraction. In this case, we can exploit the fact that both β^m_0 and β^m_1 equal zero in order to terminate the sequence; thus, we are led to the following starting point [34]:

$$\Lambda^m_2 = -\gamma^m_0 + \lambda^{(1)}_{m,l}(h) \text{ for } (l-m) \text{ even},$$

$$\Lambda^m_3 = -\gamma^m_1 + \lambda^{(1)}_{m,l}(h) \text{ for } (l-m) \text{ odd}. \tag{3-11a}$$

Accordingly, the Λ^m_r terms can be computed by working upward from the appropriate starting point using the recurrence relation (3-7a).

With these upward and downward recurrence relations, we are now able to compute the correction term $\delta\lambda_{m,l}(h)$ to the initial approximation of the eigenvalue $\lambda^{(1)}_{m,l}(h)$. First, the initial approximation for the eigenvalue $\lambda^{(1)}_{m,l}(h)$ is used by both recurrence relations to compute two numerical values for Λ^m_{l-m+2}: Λdw^m_{l-m+2} by (3-6a) and Λup^m_{l-m+2} by (3-7a). In addition, the routine must store in memory all of these upward and downward intermediate Λ^m_r terms used in the process of determining both numerical values for Λ^m_{l-m+2} (beginning with each of their respective starting points). Using all of these numerical results, we are then able to determine the eigenvalue correction term as follows [23], [34], [35]:

$$\delta\lambda_{m,l}(h) =$$

$$\frac{\Lambda dw^{m}_{l-m+2} - \Lambda up^{m}_{l-m+2}}{\left[1+\frac{\beta^{m}_{l-m}}{\left(\Lambda up^{m}_{l-m}\right)^{2}}+\frac{\beta^{m}_{l-m}\beta^{m}_{l-m-2}}{\left(\Lambda up^{m}_{l-m}\right)^{2}\left(\Lambda up^{m}_{l-m-2}\right)^{2}}+\cdots\right]+\left[\frac{\left(\Lambda dw^{m}_{l-m+2}\right)^{2}}{\beta^{m}_{l-m+2}}+\frac{\left(\Lambda dw^{m}_{l-m+2}\right)^{2}\left(\Lambda dw^{m}_{l-m+4}\right)^{2}}{\beta^{m}_{l-m+2}\beta^{m}_{l-m+4}}+\cdots\right]}.$$

(3-12a)

Each of the series in the denominator for this expression is computed until convergence has been achieved. Lastly, the entire Bouwkamp/Blanch process, i.e., described by (3-4a)-(3-12a), is repeated until $\lambda_{m,l}(h)$ reaches the desired accuracy.

Now that the Bouwkamp/Blanch method has been used to refine the initial approximation of the eigenvalue, we return our attention to the main objective of the PRODNCNSTS (P-d) secondary routine: computing the much needed set of $d_r^{m,l}(h)$ expansion coefficients for a particular order *m* and degree *l*. Fortunately, these expansion coefficients are related to the Λ_r^m terms (taken from the respective upward and downward intermediate terms) by the following relation [35]:

$$\frac{d_r^{m,l}(h)}{d_{r-2}^{m,l}(h)} = \Lambda_r^m \frac{(2m+2r-1)(2m+2r+1)}{(2m+r)(2m+r-1)h^2} \text{ for } r \geq 2\,. \tag{3-13a}$$

It is important to point out that repeated applications of the Bouwkamp/Blanch method will not only refine a particular eigenvalue $\lambda_{m,l}(h)$, but also its corresponding Λ_r^m terms. Equation (3-13a) relates the computed Λ_r^m terms to the ratio of consecutive $d_r^{m,l}(h)$ expansion coefficients. The list of the expansion coefficients normalized with respect to its first term in the sequence, i.e., $d_0^{m,l}(h)$ or $d_1^{m,l}(h)$, can be easily determined from this sequence of ratios by using the appropriate finite product [23]:

$$\frac{d_r^{m,l}(h)}{d_0^{m,l}(h)} = \left(\frac{d_2^{m,l}}{d_0^{m,l}}\right)\left(\frac{d_4^{m,l}}{d_2^{m,l}}\right)\cdots\left(\frac{d_r^{m,l}}{d_{r-2}^{m,l}}\right) \text{ for } (l-m) \text{ even and } r \geq 2,$$

$$\frac{d_r^{m,l}(h)}{d_1^{m,l}(h)} = \left(\frac{d_3^{m,l}}{d_1^{m,l}}\right)\left(\frac{d_5^{m,l}}{d_3^{m,l}}\right)\cdots\left(\frac{d_r^{m,l}}{d_{r-2}^{m,l}}\right) \text{ for } (l-m) \text{ odd and } r \geq 3. \qquad \text{(3-14a)}$$

As we can see, all of the computed expansion coefficients of (3-14a) are normalized with respect to the first term in their sequence. Thus, by applying its respective first term as a scaling constant, i.e., $d_0^{m,l}(h)$ or $d_1^{m,l}(h)$, to the entire computed sequence, i.e., $d_r^{m,l}(h)/d_0^{m,l}(h)$ or $d_r^{m,l}(h)/d_1^{m,l}(h)$, the list of $d_r^{m,l}(h)$ expansion coefficients can be found explicitly. However, before being able to do so, we must first determine the first term in the sequence.

Up to this point, the process for computing the $d_r^{m,l}(h)$ expansion coefficients has been independent of the chosen Sturm-Liouville normalization scheme. However, the selected normalization scheme will have a direct bearing on this next and final step in this computational process. Since we have chosen to implement our NZ-FZT process using the normalization scheme of Morse and Feshbach [22], the first term of the sequence can be found by appropriately using one the following normalizing relations [35]:

$$d_0^{m,l}(h) = \frac{(l+m)!}{(l-m)!}\left[\sum_{r=0}^{\infty}{}' \frac{d_r^{m,l}(h)}{d_0^{m,l}(h)}\frac{(2m+r)!}{r!}\right]^{-1} \text{ for } (l-m) \text{ even},$$

$$d_1^{m,l}(h) = \frac{(l+m)!}{(l-m)!}\left[\sum_{r=1}^{\infty}{}' \frac{d_r^{m,l}(h)}{d_1^{m,l}(h)}\frac{(2m+r)!}{r!}\right]^{-1} \text{ for } (l-m) \text{ odd}. \qquad \text{(3-15a)}$$

To digress for a moment, other normalization schemes would require the use of different normalization relations. As an example, Flammer [23] presents a different pair of normalization relations to be used with the scheme presented in his monograph (recalling that his particular normalization scheme for prolate spheroidal angle functions is

described in equations (2-71a) and (2-72a) of Chapter 2). Once again, care must be exercised when evaluating the ratio of factorial expressions in (3-15a) in order to avoid overflow conditions.

The first step in validating both PRODNCNSTS (P-d) and OBLDNCNSTS (O-d) numerical routines consists of checking the accuracy of the refined prolate and oblate spheroidal eigenvalues. Results of these routines are compared to computed values made available in [35], [36]. Comparisons with these data sets indicate that for the cases tested both numerical routines refine their respective eigenvalues to better than twelve-decimal accuracy.

The next step in validating both PRODNCNSTS (P-d) and OBLDNCNSTS (O-d) routines is to check the accuracy of the $d_r^{m,l}(h)$ and $d_r^{m,l}(-jh)$ expansion coefficients. Fortunately, Flammer [23] provides tabulated data for both of these expansion coefficients that ranges anywhere between four- and eight-decimal accuracy. Results from both of our routines fare extremely well when compared with this available data (i.e., after accounting for the difference in normalization schemes). Nevertheless, the ultimate validation is left to how well these routines support their respective primary routines.

3.4 PROLATE SPHEROIDAL RADIAL FUNCTIONS OF THE FIRST AND SECOND KIND

3.4.1 PRORADIAL (P-3) Numerical Routine

This numerical routine evaluates the prolate spheroidal radial functions of the first and second kind (both real quantities) together with their respective first derivatives for a given order *m*, degree *l*, and independent parameter *h*. However, upon review of our prolate spheroidal NZ-FZT algorithm (see Chapter 2), we recognize that its wave-harmonic expansion actually calls for the corresponding prolate spheroidal radial function of the fourth kind (a complex quantity). Fortunately, this seeming incompatibility does not present any real difficulty because the fourth kind solution is actually comprised of its

corresponding first and second kind solutions by way of (2-74a). Furthermore, because the prolate spheroidal radial function of the second kind is singular at $\xi = 1$, we have chosen to limit both radial functions of this numerical routine to arguments greater than unity, i.e., where $\xi > 1$. In this section, we choose to address only the computation of the spheroidal radial functions for the prolate case and not their oblate counterparts. We do so because the numerical approaches for computing both spheroidal cases are somewhat different. Consequently, our routine that handles computation of the oblate spheroidal radial functions, viz., OBLRADIAL (O-3), is later discussed in another section (see 3.5.1).

Since this primary routine also makes use of the shared secondary routine PRODNCNSTS (P-d) to compute the $d_r^{m,l}(h)$ expansion coefficients, it too must be provided with either an initial approximation of the respective eigenvalue or an already refined eigenvalue. In the case that an approximation of the eigenvalue is supplied to the routine, the numerical representation of the eigenvalue is replaced with a value that is more accurate.

Although the numerical process to compute an individual prolate spheroidal radial function is quite involved, its frequency of use is relatively limited in the course of computing the far-zone response for a single transformation surface. In fact, PRORADIAL (P-3) only has to calculate the set of $R_{m,l}^{(4)}(h,\xi)$ functions once for all orders *m* and degrees *l* that are necessary to achieve convergence of the corresponding spheroidal wave-harmonic expansion (see Table 2.5a). It has therefore been our experience that this set of function evaluations only accounts for a small fraction of the total computation time for a given prolate spheroidal transformation surface.

This numerical routine is somewhat complicated because it makes use of one of two different approaches to compute the prolate spheroidal radial functions of the second kind and its first derivatives. The decision making process that determines which approach yields the most accurate results for a given region of input arguments is based upon the computational experience provided in *NRL Formal Report 7012* [35]. However,

in one particular input parameter region the approach that performs the best is not known decisively. Fortunately, we are able to use the known closed form of the Wronskian to validate the computed results in an on-the-fly manner when operating in this ambiguous region [35]. By comparing the numerically evaluated Wronskian (resulting from the computed prolate spheroidal radial functions and their first derivatives) from each numerical approach with the theoretical Wronskian (resulting from the known closed form), the approach which performs the best in this region of ambiguity is thus determined. It is this Wronskian check that lies behind the need for computing both first derivatives.

First, we shall focus on computing the prolate spheroidal radial function of the first kind together with its first derivative. To do so, King *et al.* [35] recommend using the following expansions of spherical Bessel functions $j_n(h\xi)$:

$$R_{m,l}^{(1)}(h,\xi) = \frac{(l-m)!}{(l+m)!}\left(\frac{\xi^2-1}{\xi^2}\right)^{m/2} {\sum_{r=0,1}^{\infty}}' j^{r+m-l}\; d_r^{m,l}(h)\frac{(2m+r)!}{r!} j_{r+m}(h\xi) \tag{3-16}$$

$$\frac{d}{d\xi}R_{m,l}^{(1)}(h,\xi) = \frac{(l-m)!}{(l+m)!}\left(\frac{\xi^2-1}{\xi^2}\right)^{m/2} \times$$

$$\left\{ h{\sum_{r=0,1}^{\infty}}' j^{r+m-l}\; d_r^{m,l}(h)\frac{(2m+r)!}{r!(2m+2r+1)}\begin{bmatrix}(m+r)\, j_{r+m-1}(h\xi)\\ -(m+r+1)\, j_{r+m+1}(h\xi)\end{bmatrix} \right.$$
$$\left. + \frac{m}{\xi(\xi^2-1)}{\sum_{r=0,1}^{\infty}}' j^{r+m-l}\; d_r^{m,l}(h)\frac{(2m+r)!}{r!} j_{r+m}(h\xi) \right\}. \tag{3-17}$$

The equation presented in (3-17) is easily derived from (3-16) by using a standard recurrence relation for spherical Bessel functions that relates the first derivative of the special function to those of other orders. In addition, one should note that the complex j^{r+m-l} term in both expressions can be misleading; that is, it belies the fact that the results of both expansions are always real quantities. This is so because the quantity $(r+m-l)$ is always an even integer; note that this property is consistent with (3-5a). As for the

required set of spherical Bessel function evaluations, it is supplied to this routine by the secondary routine SJBESARRAY (B-b).

From a perspective of reducing computations, we are able to take advantage of the fact that both (3-16) and (3-17) share many redundant computations: the foremost being that both expressions happen to contain an identical expansion of spherical Bessel functions. In removing these redundant computations, we are able to significantly improve the computational efficiency of this numerical routine. Moreover, all of the expansions contained within (3-16) and (3-17) are truncated at the point where numerical convergence has been achieved in order to eliminate non-contributory calculations. Once again, care must be taken when handling the ratios of the factorial expressions contained within these expansions.

As stated earlier, this numerical routine makes use of one of two different approaches to compute the prolate spheroidal radial functions of the second kind. The first approach closely resembles that which is taken to compute the prolate spheroidal radial function of the first kind, i.e., (3-16) and (3-17), with the only difference being the substitution of spherical Neumann functions for the spherical Bessel functions [35]:

$$R_{m,l}^{(2)}(h,\xi) = \frac{(l-m)!}{(l+m)!}\left(\frac{\xi^2-1}{\xi^2}\right)^{m/2} {\sum_{r=0,1}^{\infty}}' j^{r+m-l}\ d_r^{m,l}(h)\frac{(2m+r)!}{r!}n_{r+m}(h\xi) \tag{3-18}$$

$$\frac{d}{d\xi}R_{m,l}^{(2)}(h,\xi) = \frac{(l-m)!}{(l+m)!}\left(\frac{\xi^2-1}{\xi^2}\right)^{m/2} \times$$

$$\left\{ h{\sum_{r=0,1}^{\infty}}' j^{r+m-l}\ d_r^{m,l}(h)\frac{(2m+r)!}{r!(2m+2r+1)}\left[\begin{matrix}(m+r)n_{r+m-1}(h\xi)\\ -(m+r+1)n_{r+m+1}(h\xi)\end{matrix}\right] \right.$$
$$\left. + \frac{m}{\xi(\xi^2-1)}{\sum_{r=0,1}^{\infty}}' j^{r+m-l}\ d_r^{m,l}(h)\frac{(2m+r)!}{r!}n_{r+m}(h\xi) \right\}. \tag{3-19}$$

Unfortunately, the expansions of Neumann functions that are contained in these expressions do not converge well for small values of $h\xi$ [35]. The convergence of these

expansions is difficult in this region because the Neumann functions possess a singularity at the origin. As a matter of fact, Morse and Feshbach [22] indicate that these expansions are actually asymptotic series and are not absolutely convergent for any finite values of $h\xi$. As a result, the usefulness of the spherical Neumann expansion approach is limited to large values of $h\xi$.

An advantage of the spherical Neumann expansion approach is that we can exploit the fact that many of the calculations are identical to those required to compute its first kind counterpart. In fact, all of the overall expansion coefficients of the spherical Neumann expansion approach and the spherical Bessel expansion approach are exactly the same. As for the set of spherical Neumann function evaluations, it is provided to this primary routine by evoking the secondary routine SYBESARRAY (B-c). Because the spherical Neumann functions can assume extremely large magnitudes as their order increases, the resulting set of evaluations must be scaled by some large constant at some point in the sequence of functions in order to avert an impending floating-point overflow condition. This scaling scheme effectively expands the computational dynamic range of the spherical Neumann functions (i.e., allows magnitudes beyond 10^{+308}) and is critical to the successful implementation of this particular numerical approach. Essentially, each spherical Neumann function is an intermediate calculation of a particular term in the expansion. Accordingly, all expansion coefficients that correspond to the scaled spherical Neumann functions must now be scaled by the reciprocal of the scaling constant. This scaling scheme works because the combining of the spherical Neumann functions (with or without scaling) with their corresponding expansion coefficients (with or without scaling) yields expansion terms that lie within the range of magnitude afforded by double precision. All expansions contained within expressions (3-18) and (3-19) are also truncated at the point where numerical convergence has been achieved in order to eliminate non-contributory calculations.

Due to the limitations of the spherical Neumann function expansion approach, an alternative approach is necessary. Flammer [23] has shown that the prolate spheroidal

radial function of the second kind can be expressed in terms of associated Legendre functions:

$$R_{m,l}^{(2)}(h,\xi) = \frac{1}{\kappa_{m,l}^{(2)}(h)}\left[\sum_{\substack{r=-2m,\\ -2m+1}}^{\infty}{}' d_r^{m,l}\ (h) Q_{m+r}^m(\xi) + \sum_{\substack{r=2m+2,\\ 2m+1}}^{\infty}{}' d_{\rho/r}^{m,l}\ (h) P_{r-m-1}^m(\xi) \right] \tag{3-20}$$

$$\frac{d}{d\xi} R_{m,l}^{(2)}(h,\xi) = \frac{1}{\kappa_{m,l}^{(2)}(h)} \begin{bmatrix} \sum_{\substack{r=-2m,\\ -2m+1}}^{\infty}{}' d_r^{m,l}\ (h) \frac{d}{d\xi} Q_{m+r}^m(\xi) \\ + \sum_{\substack{r=2m+2,\\ 2m+1}}^{\infty}{}' d_{\rho/r}^{m,l}\ (h) \frac{d}{d\xi} P_{r-m-1}^m(\xi) \end{bmatrix}; \tag{3-21}$$

where

$$\kappa_{m,l}^{(2)}(h) =$$

$$\frac{(-1)^{(l-m)/2}}{(2m-1)h^{m-1}} \left[\frac{(2m)!}{m!}\right] \left[\frac{(l+m)!}{(l-m)!}\right] \left[\sum_{r=0}^{\infty}{}' \frac{(-1)^{r/2}\ (2m+r)!}{2^r \left(\frac{r}{2}\right)! \left(\frac{2m+r}{2}\right)!} d_r^{m,l}(h) \right]^{-1} d_{-2m}^{m,l}(h)$$

for (l - m) even,

$$\frac{(-1)^{(l-m+1)/2}}{(2m-1)(2m-3)h^{m-2}} \left[\frac{(2m)!}{m!}\right] \left[\frac{(l+m)!}{(l-m)!}\right]$$

$$\times \left[\sum_{r=1}^{\infty}{}' \frac{(-1)^{(r-1)/2}\ (2m+r+1)!}{2^r \left(\frac{r-1}{2}\right)! \left(\frac{2m+r+1}{2}\right)!} d_r^{m,l}(h) \right]^{-1} d_{-2m+1}^{m,l}(h)$$

for (l - m) odd.

(3-22)

Note that the expansions of (3-20) and (3-21) not only include the coefficients $d_r^{m,l}(h)$, but also contain the additional expansion coefficients $d_{\rho/r}^{m,l}(h)$. Moreover, both expressions also require the evaluation of $d_r^{m,l}(h)$ expansion coefficients for negative subscripts. Values of these additional expansion coefficients are supplied to this routine by the secondary routine PRONEGDNCNSTS (P-e).

Because both prolate spheroidal radial and angle functions of the second kind are integral functions and actually satisfy the same differential equation, i.e., (2-34a) and (2-35a), the two functions must be proportional to one another [23]. This constant of proportionally is referred to as the joining factor of the second kind $\kappa_{m,l}^{(2)}(h)$ and can be computed by the expression given in (3-22). Since this joining factor involves the prolate spheroidal angle function of the second kind, it must be dependent upon the selected Sturm-Liouville normalization scheme. Accordingly, the expression presented in (3-22) computes the joining factor for the desired Morse and Feshbach normalization scheme. One should note that expression (3-22) is actually derived from the one given in Flammer [23] by using a normalization conversion factor; the interested reader is referred here for further details and theory behind this particular joining factor.

Both expressions (3-20) and (3-21) involve expansions of associated Legendre functions of the first and second kind. However, caution must be exercised when working with these associated Legendre functions because their arguments are positive, real, and do not lie on the $(-1 < x < +1)$ branch cut (as defined by Erdelyi *et al.* [40]; see also Appendix D). As mentioned earlier, because the prolate spheroidal radial function of the second kind is singular at $\xi = 1$, the region of validity for these computations shall be limited to real arguments with values greater than unity, i.e., $\xi > 1$. Thus, evaluation of these associated Legendre functions of the first and second kind for this particular region requires the use of the specialized routine CALCPQ (P-e). It is this supporting secondary routine that provides the necessary set of associated Legendre functions for the expansions contained in (3-20) and (3-21).

Upon further review of (3-21), we recognize that the associated Legendre function expansion approach not only requires the evaluation of associated Legendre functions, but also their corresponding first derivatives. These derivatives are computed from the associated Legendre functions (i.e., provided by CALCPQ (P-e)) by way of the following recurrence formulas that are valid for real arguments that do not lie on the branch cut:

$$\frac{d}{d\xi} P_{r-m-1}^{m}(\xi) = \frac{m\xi}{\xi^2 - 1} P_{r-m-1}^{m}(\xi) + \frac{1}{\sqrt{\xi^2 - 1}} P_{r-m-1}^{m+1}(\xi) \tag{3-23}$$

$$\begin{aligned} \frac{d}{d\xi} Q_{m+r}^{m}(\xi) &= \frac{m\xi}{\xi^2 - 1} Q_{m+r}^{m}(\xi) + \frac{1}{\sqrt{\xi^2 - 1}} Q_{m+r}^{m+1}(\xi) \\ &= \frac{(2m+r)(r+1)}{\sqrt{\xi^2 - 1}} Q_{m+r}^{m-1}(\xi) - \frac{m\xi}{\xi^2 - 1} Q_{m+r}^{m}(\xi) . \end{aligned} \tag{3-24}$$

These expressions can be derived from the generalized complex variable form of the recurrence relations that are valid off the branch cut provided by Erdelyi *et al.* [40] (see equation (D-36) of Appendix D). Both recurrence formulas relate the derivative of the associated Legendre function for a given order m to the function itself and one of an adjacent order (all of which share the same degree).

Having discussed both approaches capable of computing the prolate spheroidal radial function of the second kind and its first derivative, we now need to determine which method is the most applicable (with respect to accuracy) for a given region of input parameters. As mentioned earlier, we shall take advantage of the computational experience of King *et al.* [35] when implementing this algorithmic decision making process. Supplied in Table 3.2 is a summary of their recommendations regarding which method to use when given a particular set of values for ξ and h.

As indicated by Table 3.2, the recommended method for one of the input parameter regions requires the selection of the best result from both numerical approaches using the Wronskian. Earlier in this section, we discussed that the numerically evaluated

Table 3.2 Best Method to Compute the Prolate Spheroidal Radial Function of the Second Kind $R_{m,l}^{(2)}(h,\xi)$ for a Given Input Parameter Region [35]

Input Parameter Region	Best Method
$1 < \xi \le 1.05$	Associated Legendre Function Expansion Approach
$1.05 < \xi \le 1.3$ or $h < 0.1$	Both (select better result using Wronskian)
$1.3 < \xi$ and $10 \le h$	Spherical Neumann Function Expansion Approach
$2 < \xi$ and $1 \le h$	Spherical Neumann Function Expansion Approach
$5 < \xi$ and $0.1 \le h$	Spherical Neumann Function Expansion Approach
ξ and h outside the above stated ranges	Associated Legendre Function Expansion Approach

Wronskian computed from each approach can be compared with the known theoretical Wronskian in order to determine which approach provides the better result; both of the needed formulations for the Wronskian check are expressed as follows [23]:

$$W_{numerical}(R_{m,l}^{(1)}(h,\xi), R_{m,l}^{(2)}(h,\xi)) = R_{m,l}^{(1)}(h,\xi)\frac{d}{d\xi}R_{m,l}^{(2)}(h,\xi) - R_{m,l}^{(2)}(h,\xi)\frac{d}{d\xi}R_{m,l}^{(1)}(h,\xi) \tag{3-25}$$

$$W_{theory}(R_{m,l}^{(1)}(h,\xi), R_{m,l}^{(2)}(h,\xi)) = \frac{1}{h(\xi^2 - 1)}. \tag{3-26}$$

Validation of this numerical routine consists of comparing its results with known published data provided by King *et al.* [35]. On the whole, this routine performs well (i.e., at least six-decimal accuracy) for reasonable values of h and ξ (viz., where $h < 20$ and $\xi > 1.01$). However, some difficulties do arise when the routine attempts to evaluate the prolate radial functions and their derivatives for some extreme regions of ξ and h that are not of interest for our particular application. In the unlikely case that the user attempts to push the routine past its numerical capabilities, the on-the-fly Wronskian check will warn the user of numerical results that fail to meet some specified level of

accuracy. An advantage of using the Wronskian check during the computational process of the routine is that it provides the user with an added level of confidence regarding the validity of the numerical results.

3.4.2 SJBESARRAY (B-b) and SYBESARRAY (B-c) Numerical Routines

These secondary routines provide the necessary evaluations of spherical Bessel and spherical Neumann functions. It is important to understand that both of these functions play an important role when computing the prolate and oblate spheroidal radial functions. As such, both of these secondary routines together must support each spheroidal radial function routine, viz., PRORADIAL (P-3) and OBLRADIAL (O-3). We choose to address the routines SJBESARRAY (B-b) and SYBESARRAY (B-c) here because PRORADIAL (P-3) is sequentially the first of the two primary routines in our discussion that utilizes these much needed secondary routines.

Both SJBESARRAY (B-b) and SYBESARRAY (B-c) must provide a truncated list of evaluations from a single family of their respective functions to the routines (P-3) and (O-3) (where a family is defined as the set of all orders of the function possessing the same argument). Furthermore, both of these secondary routines must also provide enough orders (i.e., from the zeroth order up to the point of truncation) from their respective families to enable convergence of the relevant expansions contained within both spheroidal radial function routines. Because the expansions of spherical Neumann functions are actually asymptotic expansions (see 3.4.1), they numerically converge much slower than their spherical Bessel function counterparts. Consequently, the spherical Neumann function routine SYBESARRAY (B-c) must furnish (to the spheroidal radial function routines) more orders from its family than its counterpart spherical Bessel function routine SJBESARRAY (B-b).

The routine SJBESARRAY (B-b) computes the spherical Bessel function using a bifurcated approach that is dependent upon the value of its argument. For arguments that

are relatively small (viz., $x < 0.4$), the following ascending series is used to compute the family of spherical Bessel functions [25]:

$$j_n(x) = \frac{x^n}{(2n+1)!!}\left\{1 - \frac{\frac{1}{2}x^2}{1!(2n+3)} + \frac{(\frac{1}{2}x^2)^2}{2!(2n+3)(2n+5)} - \ldots\right\} \tag{3-27}$$

where the double factorial notation denotes the product of only odd integers. For larger arguments (viz., $0.4 \le x < 100$), an approach suggested by Arfken [29] is employed that works downward (i.e., backward) from two starting values using the following recurrence relation:

$$j_n(x) = \frac{2n+3}{x} j_{n+1}(x) - j_{n+2}(x)\,. \tag{3-28}$$

The two consecutive starting values needed to implement this downward recurrence relation are chosen as some arbitrary constant and zero. As for the starting order of the downward recurrence relation, it should be somewhat greater than the highest order necessary. This procedural requirement is imposed because the initial values that result from the downward recurrence relation are not accurate and are needed to prime the downward computational pipeline. After this initial start-up procedure, the values for the remaining lower orders become extremely accurate. Since we choose an arbitrary constant as one of the starting values, the process yields a family of results that differs by a single scaling constant from that of the conventionally defined spherical Bessel functions. This situation leaves us with having to normalize the entire sequence of results as the last step in the spherical Bessel function computation process. Normalization is performed by comparing the sequence with either one of the known forms for $j_0(x)$ and $j_1(x)$ to determine the scaling constant [29]:

$$j_o(x) = \sin x / x \tag{3-29}$$

$$j_1(x) = \sin x / x^2 - \cos x / x\,. \tag{3-30}$$

In order to maintain the greatest accuracy possible for this approach, King *et al.* [35] recommend determining the scaling constant with the $j_1(x)$ form when the function $j_0(x)$ is in the neighborhood of a zero.

Regarding computation of the spherical Neumann functions, the routine SYBESARRAY (B-c) only makes use of the recurrence relation approach. However, this time around, the evaluation of the family of functions is determined by working upward (i.e., forward) using a recurrence relation similar to (3-28) [29]:

$$n_n(x) = \frac{2n-1}{x} n_{n-1}(x) - n_{n-2}(x) . \tag{3-31}$$

For obvious reasons, both $n_0(x)$ and $n_1(x)$ serve as the starting values and are computed from their respective closed form representations [29]:

$$n_o(x) = -\cos x / x \tag{3-32}$$

$$n_1(x) = -\cos x / x^2 - \sin x / x . \tag{3-33}$$

During our discussion of the routine PRORADIAL (P-3) (see 3.4.1), we mention that the spherical Neumann functions belonging to a given family have to be scaled at some point as their order increases so as to avoid an overflow condition. Correspondingly, the spherical Neumann function routine SYBESARRAY (B-c) at some point during the process of working upward with (3-31) must scale its results. Consequently, the spheroidal radial function routines not only must receive the family of spherical Neumann function evaluations, but also the index of the leading order in the sequence at which scaling had to be imposed. For obvious reasons, this additional piece of information is necessary for the spheroidal radial function routines to properly interpret the family of function evaluations.

These spherical Bessel and Neumann function routines are initially validated using the tabulated data provided in *AMS-55* [25]. Although the routines perform

extremely well with the tabulated data, we need to validate our routines for orders of the functions that are higher than those available in this particular data set. Toward that end, we compare the results of our routines with those computed by an alternative numerical routine for spherical Bessel and Neumann functions (namely, the one made available in *Numerical Recipes in FORTRAN* [37]). In terms of accuracy, our developed routines perform well when compared to the results of this alternative routine. It must be pointed out that the alternative routine provided in [37] was not selected for our particular application because its numerical approach is not the most computationally efficient way to evaluate a large family of spherical Bessel and spherical Neumann functions.

3.4.3 PRONEGDNCNSTS (P-e) Numerical Routine

This secondary routine computes the $d_r^{m,l}(h)$ expansion coefficients with negative subscripts and the expansion coefficients $d_{\rho/r}^{m,l}(h)$ that are necessary to compute the prolate spheroidal radial function of the second kind when employing the associated Legendre function expansion approach. Accordingly, this routine only has to support the PRORADIAL (P-3) primary routine. The inputs of this routine require two critical parameters for a given order m and degree l that are computed by the routine PRODNCNSTS (P-d): either $d_0^{m,l}(h)$ or $d_1^{m,l}(h)$, and the refined eigenvalue $\lambda_{m,l}(h)$.

The $d_r^{m,l}(h)$ expansion coefficients with negative subscripts are computed in a manner that is somewhat similar to its non-negative counterparts: the difference being that the procedure need not employ an iterative process because the eigenvalue is already assumed to be an accurate representation, not an initial approximation. Maintaining consistency with the expansions of associated Legendre functions of the second kind within (3-20) and (3-21), the range of the index r for the $d_r^{m,l}(h)$ expansion coefficients with negative subscripts can be formally stated as

$$r = \begin{cases} -2, -4, \ldots, -2m & \text{for } (l-m) \text{ even}, \\ -1, -3, \ldots, -2m+1 & \text{for } (l-m) \text{ odd}. \end{cases} \tag{3-34}$$

We now make use of another three-term recurrence relation using the already refined eigenvalue $\lambda_{m,l}(h)$ to determine the ratios of the $d_r^{m,l}(h)$ expansion coefficients with negative subscripts [23]:

$$\frac{d_r^{m,l}(h)}{d_{r+2}^{m,l}(h)} = \frac{-A_{r+2}^m}{B_r^{m,l} + C_{r-2}^m \left(\dfrac{d_{r-2}^{m,l}(h)}{d_r^{m,l}(h)} \right)} \tag{3-35}$$

where

$$A_r^m = \frac{(2m+r)(2m+r-1)}{(2m+2r-1)(2m+2r+1)} \tag{3-36}$$

$$B_r^{m,l} = \frac{2(m+r)(m+r+1) - 2m^2 - 1}{(2m+2r-1)(2m+2r+3)} + \frac{(m+r)(m+r+1) - \lambda_{m,l}(h)}{h^2} \tag{3-37}$$

$$C_r^m = \frac{(r+1)(r+2)}{(2m+2r+1)(2m+2r+3)}. \tag{3-38}$$

(Note that our recurrence constants differ slightly from those of Flammer [23] by a factor of h^{-2}. Since this alternative definition does not make a difference with respect to the recurrence relation of (3-35), we define the constants as such to minimize floating-point operations.) The fact that both recurrence constants A_{-2m}^m and A_{-2m+1}^m vanish (by inspection of (3-36)) implies that both expansion coefficient ratios $\dfrac{d_{-2m-2}^{m,l}(h)}{d_{-2m}^{m,l}(h)}$ and $\dfrac{d_{-2m-1}^{m,l}(h)}{d_{-2m+1}^{m,l}(h)}$ also must vanish. Using a zero value for either of these expansion coefficient ratios along with the recurrence relation of (3-35) leads us to the following starting points:

$$\frac{d_{-2m}^{m,l}(h)}{d_{-2m+2}^{m,l}(h)} = \frac{-A_{-2m+2}^{m}}{B_{-2m}^{m,l}} \quad \text{for } (l-m) \text{ even},$$

$$\frac{d_{-2m+1}^{m,l}(h)}{d_{-2m+3}^{m,l}(h)} = \frac{-A_{-2m+3}^{m}}{B_{-2m+1}^{m,l}} \quad \text{for } (l-m) \text{ odd}. \tag{3-39}$$

We are now able to compute the sequence of $d_r^{m,l}(h)$ expansion coefficients ratios with negative subscripts by working upward (i.e., forward) with recurrence relation (3-35) using the appropriate starting point of (3-39) for all required indices of r stated in (3-34).

Now that we have determined the $d_r^{m,l}(h)$ expansion coefficient ratios with negative subscripts, the list of expansion coefficients normalized with respect to either $d_0^{m,l}(h)$ or $d_1^{m,l}(h)$ can be determined by using one of the following appropriate expressions [23]:

$$\frac{d_r^{m,l}(h)}{d_0^{m,l}(h)} = \left(\frac{d_{-2}^{m,l}}{d_0^{m,l}}\right)\left(\frac{d_{-4}^{m,l}}{d_{-2}^{m,l}}\right)\cdots\left(\frac{d_r^{m,l}}{d_{r+2}^{m,l}}\right) \text{ for } (l-m) \text{ even and } -2m \le r \le -2,$$

$$\frac{d_r^{m,l}(h)}{d_1^{m,l}(h)} = \left(\frac{d_{-1}^{m,l}}{d_1^{m,l}}\right)\left(\frac{d_{-3}^{m,l}}{d_{-1}^{m,l}}\right)\cdots\left(\frac{d_r^{m,l}}{d_{r+2}^{m,l}}\right) \text{ for } (l-m) \text{ odd and } -2m+1 \le r \le -1. \tag{3-40}$$

We now appropriately apply either $d_0^{m,l}(h)$ or $d_1^{m,l}(h)$, i.e., calculated by PRODNCNSTS (P-d), to properly scale the list and explicitly provide the desired sequence of $d_r^{m,l}(h)$ expansion coefficients with negative subscripts. In our particular case, the values provided for $d_0^{m,l}(h)$ or $d_1^{m,l}(h)$ correspond to those required for the Morse and Feshbach normalization scheme.

Having addressed the $d_r^{m,l}(h)$ expansion coefficients with negative subscripts, we now turn our attention to the numerical procedure put forth by Flammer [23] that is necessary to compute the $d_{\rho/r}^{m,l}(h)$ expansion coefficients. It is important to understand

that the $d_{\rho/r}^{m,l}(h)$ expansion coefficients are related to the $d_{r}^{m,l}(h)$ expansion coefficients, albeit for a different range of subscripts, through the following relation [23]:

$$d_{\rho/r}^{m,l}(h) = \lim_{\rho\to 0} d_{-r+\rho}^{m,l} \Big/ \rho \tag{3-41}$$

where

$$r = \begin{cases} 2m+2, 2m+4, \ldots & \text{for } (l-m) \text{ even}, \\ 2m+1, 2m+3, \ldots & \text{for } (l-m) \text{ odd}. \end{cases} \tag{3-42}$$

Note that the range of indices specified in (3-42) remains consistent with the expansions of associated Legendre functions of the first kind included in expressions (3-20) and (3-21). We can now apply (3-41) to the three-term recurrence relation of (3-35) to obtain an expression for the first element in the sequence of $d_{\rho/r}^{m,l}(h)$ ratios:

$$\frac{d_{\rho/2m+2}^{m,l}(h)}{d_{-2m}^{m,l}(h)} = \frac{-\left[(1+2m)(1-2m)\right]^{-1}}{B_{-2m-2}^{m,l} + C_{-2m-4}^{m}\left(\dfrac{d_{\rho/2m+4}^{m,l}(h)}{d_{\rho/2m+2}^{m,l}(h)}\right)} \quad \text{for } (l-m) \text{ even},$$

$$\frac{d_{\rho/2m+1}^{m,l}(h)}{d_{-2m+1}^{m,l}(h)} = \frac{-\left[(1-2m)(3-2m)\right]^{-1}}{B_{-2m-1}^{m,l} + C_{-2m-3}^{m}\left(\dfrac{d_{\rho/2m+3}^{m,l}(h)}{d_{\rho/2m+1}^{m,l}(h)}\right)} \quad \text{for } (l-m) \text{ odd}; \tag{3-43}$$

where the recurrence constants are computed using equations (3-36)-(3-38). Moreover, the numerator in each expression is derived from evaluating the respective limiting formulation: $\lim_{\rho\to 0} A_{-2m+\rho}^{m} \Big/ \rho$ or $\lim_{\rho\to 0} A_{-2m+1+\rho}^{m} \Big/ \rho$. Note that both expressions of (3-43) can be written as continued fractions and may be computed to any degree of accuracy by truncating the fractions after a sufficient number of terms [23]. We now make use of the following three-term recurrence relation to work downward (i.e., backward) to the second element in the sequence of $d_{\rho/r}^{m,l}(h)$ ratios:

$$\frac{d_{\rho/r}^{m,l}(h)}{d_{\rho/r-2}^{m,l}(h)} = \frac{-A_{-r+2}^{m}}{B_{-r}^{m,l} + C_{-r-2}^{m}\left(\dfrac{d_{\rho/r+2}^{m,l}(h)}{d_{\rho/r}^{m,l}(h)}\right)} \quad \text{for } r \geq 2m+3. \tag{3-44}$$

The first element in the sequence, i.e., $\dfrac{d_{\rho/2m+2}^{m,l}(h)}{d_{-2m}^{m,l}(h)}$ or $\dfrac{d_{\rho/2m+1}^{m,l}(h)}{d_{-2m+1}^{m,l}(h)}$, can then be computed from the second element by using the appropriate expression of (3-43).

The fact that Flammer [23] indicates that the continued fraction may be safely truncated implies that the sequence of $d_{\rho/r}^{m,l}(h)$ ratios continues to get smaller in magnitude as the index r increases, i.e., $\lim_{r\to\infty} \dfrac{d_{\rho/r+2}^{m,l}(h)}{d_{\rho/r}^{m,l}(h)} = 0$. By terminating the continued fraction at some reasonable large value for the index r, viz., $r = r_{term}$ (remembering to choose the appropriate even or odd index), and using the approximation $\dfrac{d_{\rho/r_{term}+2}^{m,l}(h)}{d_{\rho/r_{term}}^{m,l}(h)} = 0$, we create the following starting point for the downward recurrence relation of (3-44):

$$\frac{d_{\rho/r_{term}}^{m,l}(h)}{d_{\rho/r_{term}-2}^{m,l}(h)} = \frac{-A_{-r_{term}+2}^{m}}{B_{-r_{term}}^{m,l}}. \tag{3-45}$$

From this calculated list of $d_{\rho/r}^{m,l}(h)$ expansion coefficient ratios, the sequence of expansion coefficients normalized with respect to either $d_{-2m}^{m,l}(h)$ or $d_{-2m+1}^{m,l}(h)$ can be found by appropriately applying one of the following expressions (where the index r still conforms to the range defined in (3-42)) [23]:

$$\frac{d^{m,l}_{\rho/r}(h)}{d^{m,l}_{-2m}(h)} = \left(\frac{d^{m,l}_{\rho/2m+2}}{d^{m,l}_{-2m}}\right)\left(\frac{d^{m,l}_{\rho/2m+4}}{d^{m,l}_{\rho/2m+2}}\right)\cdots\left(\frac{d^{m,l}_{\rho/r}(h)}{d^{m,l}_{\rho/r-2}(h)}\right)$$

for $(l-m)$ even and $r \geq 2m+2$,

$$\frac{d^{m,l}_{\rho/r}(h)}{d^{m,l}_{-2m+1}(h)} = \left(\frac{d^{m,l}_{\rho/2m+1}}{d^{m,l}_{-2m+1}}\right)\left(\frac{d^{m,l}_{\rho/2m+3}}{d^{m,l}_{\rho/2m+1}}\right)\cdots\left(\frac{d^{m,l}_{\rho/r}(h)}{d^{m,l}_{\rho/r-2}(h)}\right)$$

for $(l-m)$ odd and $r \geq 2m+1$.

(3-46)

At this point, we scale the entire computed sequence by either $d^{m,l}_{-2m}(h)$ or $d^{m,l}_{-2m+1}(h)$ to explicitly determine the desired $d^{m,l}_{\rho/r}(h)$ expansion coefficients. Fortunately, the necessary scaling constant has already been computed by the first part of this routine that calculates the $d^{m,l}_{r}(h)$ expansion coefficients with negative subscripts. Consequently, the values of the $d^{m,l}_{\rho/r}(h)$ expansion coefficients also must correspond to the Morse and Feshbach normalization scheme.

Validation of this routine consists of comparing both the computed $d^{m,l}_{r}(h)$ expansion coefficients with negative subscripts and the computed expansion coefficients $d^{m,l}_{\rho/r}(h)$ to tabulated data provided by Flammer [23]. Results for both computed sets of expansion coefficients do extremely well when compared with this available data (i.e., after accounting for the difference in normalization schemes). However, the ultimate validation is once again left to how well this routine supports the expansions of associated Legendre function expansions contained within expressions (3-20) and (3-21).

3.4.4 CALCPQ (P-f) Numerical Routine

This secondary routine provides the necessary evaluations of the associated Legendre functions of the first and second kind to the PRORADIAL (P-3) routine. These

computations are only necessary when invoking the associated Legendre function expansion approach of (3-20) and (3-21) to compute the prolate spheroidal radial function of the second kind. An essential feature of this routine is that both associated Legendre functions must be evaluated for positive real arguments (in terms of the radial parameter) that do not lie on the $(-1 < x < +1)$ branch cut or at the $x = \pm 1$ singular points, viz., where $\xi > 1$.

Expressions (3-20) and (3-21) coupled with the recurrence formulas of (3-23) and (3-24) indicate that the associated Legendre function expansion approach requires the evaluation of the *m*, $m+1$, and $m-1$ order families for the associated Legendre functions. (By definition, a family is considered to be a set of associated Legendre functions that correspond to a given order *m*.) Specifically, the approach only requires evaluations of the *m* and $m+1$ families in the case of the associated Legendre functions of the first kind, and evaluations of all three families in the case of the associated Legendre functions of the second kind. Even though the expansions of (3-20) and (3-21) only call for every other member of a particular associated Legendre function family (i.e., either even or odd degrees), this routine shall nevertheless provide consecutive members to the PRORADIAL (P-3) routine in the interest of being more versatile and complete. Since this secondary routine only provides the necessary computations for a given order *m*, PRORADIAL (P-3) must again evoke this routine in order to compute the $m+1$ and $m-1$ order families.

Evaluation of the associated Legendre function of the first kind for real arguments that do not lie on the branch cut can be performed in a variety of ways. These approaches include the use of closed form expressions, viz., found by using (D-20), as well as other explicit series expansions. Unfortunately, these techniques do not lend themselves well to the numerical evaluation of this function from a viewpoint of coding efficiency and numerical accuracy. Instead, we make use of the ingenious computational approach recommended by *Numerical Recipes in FORTRAN* [37].

Although the computational approach presented in [37] is made to address real arguments that are either on the branch cut or at the singular points, with slight

modifications this method can be augmented to also handle real arguments that are off the branch cut. *Numerical Recipes in FORTRAN* [37] recommends using the following numerically stable recurrence relation to compute a family of associated Legendre functions of the first kind for a given order *m* by working upward (i.e., forward) with respect to the degree *l*:

$$P_l^m(\xi) = \xi \frac{(2l-1)}{(l-m)} P_{l-1}^m(\xi) - \frac{(l+m-1)}{(l-m)} P_{l-2}^m(\xi) . \tag{3-47}$$

As fortune would have it, in this instance this particular recurrence relation not only applies to real arguments that lie on the branch cut, but also to those that exist off the branch cut. For that reason, recurrence relation (3-47) can be directly incorporated into our numerical routine. The fact that (3-47) remains valid off the branch cut for real arguments can be shown using the generalized complex variable form of the recurrence relation, i.e., (D-34), provided by Erdelyi *et al.* [40]. It must be noted that having a recurrence relation hold for real arguments on and off the branch cut is generally not true for associated Legendre functions (see Appendix D).

We now employ a closed form expression that is valid for real arguments off the branch cut as one of the two starting values needed for the recurrence relation (3-47):

$$P_m^m(\xi) = (2m-1)!!(\xi^2 - 1)^{m/2} . \tag{3-48}$$

This expression can be derived from a finite power series representation of the associated Legendre function of the first kind (found in *MTP-1945* [41]) which terminates quickly when $l = m$. Using (3-47) and setting $P_{m-1}^m(\xi) = 0$, we can determine the second starting value [37]:

$$P_{m+1}^m(\xi) = (2m+1)\xi \; P_m^m(\xi) . \tag{3-49}$$

Working upward with (3-47) from these two starting values, we are able to generate an entire family of associated Legendre functions of the first kind for a given order *m*, i.e., $l = m, m+1, \ldots$, with a single pass. As we can see, this method is remarkably efficient for our particular application.

We now turn our attention to evaluating the associated Legendre functions of the second kind for positive real arguments that do not lie on the branch cut or at the singular points, i.e., $\xi > 1$. These functions must be computed for both positive and negative degrees *l*, i.e., $l = -m, -m+1, \ldots, 0, 1, \ldots$, when the given order *m* is greater than zero (as opposed to just non-negative degrees *l* when $m = 0$). Let us first address the computation of the required set of associated Legendre functions of the second kind with non-negative degrees (i.e., $l \geq 0$).

Due to the associated Legendre function of the second kind being singular at $x = 1$, computation of the necessary set of these functions becomes progressively more difficult as the argument ξ gets closer to unity. As a result, we found that using a two-pronged approach that is based upon the value of the argument is the best way to compute the set of associated Legendre functions of the second kind with non-negative degrees for a given order *m*, i.e., where $l = 0, 1, \ldots$.

For the region $1 < \xi < 1.1$ where the positive real argument is close to the singular point, the set of associated Legendre functions of the second kind with non-negative degrees is individually computed for all respective degrees of *l* using the following general explicit expression (based upon the example case given in *MTP-1945* [41]):

$$Q_l^m(\xi) = \tfrac{1}{2} P_l^m(\xi) \ln \frac{\xi+1}{\xi-1}$$

$$+ \frac{m!}{2} \sum_{s=1}^{m} \frac{(-1)^s}{s(m-s)!} P_l^{m-s}(\xi) \left[\frac{(\xi+1)^s - (\xi-1)^s}{(\xi^2-1)^{s/2}} \right]$$

$$- \sum_{q=0}^{Int\left[\frac{1}{2}(l-1)\right]} \frac{(2l-4q-1)}{(2q+1)(l-q)} P_{l-2q-1}^m(\xi) \text{ for } l \geq 1; \qquad (3\text{-}50)$$

where $Int[x]$ is considered the greatest integer function.

Note that expression (3-50) reduces to the following when $l = 0$ and $m = 0$ (convention drops the superscript for the zeroth order):

$$Q_0(\xi) = \tfrac{1}{2} \ln \frac{\xi+1}{\xi-1}. \qquad (3\text{-}51)$$

The expression (3-50) is derived from the definitive expression for the zeroth-order associated Legendre function of the second kind $Q_l(\xi)$, viz., (D-4), and the differentiation formula that relates $Q_l(\xi)$ for a given degree l to its higher-order counterparts, viz., (D-22). One makes use of Leibnitz's formula for the n^{th} derivative of a product, i.e., (D-40), to remove the resulting derivatives and reduce the explicit expression for the associated Legendre functions of the second kind to the form presented in (3-50).

When using this explicit approach to compute the set of functions with non-negative degrees, the necessary evaluations of the associated Legendre functions of the first kind are provided by using the approach outlined in (3-47)-(3-49). In addition, it must be pointed out that this explicit approach is not very efficient because it requires each function to be individually evaluated using a computationally intensive formula. Unfortunately, we are limited to this approach when operating so close to the singularity.

Regarding the region where $\xi \geq 1.1$, the argument has been numerically determined to be far enough from the singularity to successfully implement the following more computationally efficient approach. In order to compute the set of associated Legendre functions of the second kind with non-negative degrees for $\xi \geq 1.1$, we shall take advantage of the following downward (i.e., backward) traveling recurrence relation (with respect to the degree l) that is valid off the branch cut for a given order m [40]:

$$Q_l^m(\xi) = \xi \frac{(2l+3)}{(l+m+1)} Q_{l+1}^m(\xi) - \frac{(l-m+2)}{(l+m+1)} Q_{l+2}^m(\xi). \tag{3-52}$$

Note that (3-52) is of similar form to the upward traveling recurrence relation of (3-47) with the exception of a shift of indices. Numerical experience has shown that the recurrence relation of (3-52) is numerically stable when traveling in the downward direction for this particular function.

In order to begin working downward to $Q_0^m(\xi)$ using the recurrence relation (3-52), we need to have two consecutive starting values. These two starting values must be situated at some point far enough from $l = 0$ to provide enough members of the family to ensure convergence of the associated Legendre functions of the second kind expansions contained within (3-20) and (3-21). Furthermore, we can take advantage of some known expressions for associated Legendre functions of the second kind to compute both of these starting values. These expressions are in open form and can be represented in terms of the Gauss hypergeometric function (defined for a complex argument z) [25]:

$$F(a,b;c;z) = \sum_{k=0}^{\infty} \left(\frac{(a+k-1)!}{(a-1)!} \right) \left(\frac{(b+k-1)!}{(b-1)!} \right) \left(\frac{(c-1)!}{(c+k-1)!} \right) \frac{z^k}{k!}. \tag{3-53}$$

The region of convergence for this function without exception includes all values of the complex argument z enclosed within the unit circle, i.e., $|z| < 1$, and excludes all values which lie outside it. Regarding complex arguments situated on the unit circle boundary, convergence of the hypergeometric function is dictated by a set of conditional rules

dependent upon the parameters *a*, *b*, and *c*. Fortunately, having knowledge of whether or not a particular hypergeometric function theoretically converges on the unit circle is beyond our computational purposes given the fact that it would be numerically imprudent to operate the expansion at this boundary. Consequently, the interested reader is referred to *AMS-55* [25] for the details regarding convergence of the hypergeometric function for complex arguments situated on the unit circle.

According to *MTP-1945* [41], the following hypergeometric expression is the one to use when computing the associated Legendre function of the second kind with an argument whose modulus is less than or equal to three:

$$Q_l^m(\xi) = B(m,l,\xi)F\left(\tfrac{1}{2}+m, \tfrac{1}{2}-m;\, l+\tfrac{3}{2};\, -t\right) \tag{3-54}$$

where

$$B(m,l,\xi) = \frac{(-1)^m 4^l}{(l+\frac{1}{2})\sqrt{2(\xi^2-1)^{1/2}}\left(\xi+\sqrt{\xi^2-1}\right)^{l+\frac{1}{2}}}\left(\frac{l!(l+m)!}{(2l)!}\right)$$

$$t = \frac{\xi-\sqrt{\xi^2-1}}{2\sqrt{\xi^2-1}}.$$

However, it can be shown that the hypergeometric expression of (3-54) possesses a convergence boundary at $\xi = \frac{3}{4}\sqrt{2} \approx 1.06$ (found by setting the modulus of $-t$ to unity). Since (3-54) is valid for positive real arguments off the branch cut that are greater than this convergence boundary, our routine makes use of this hypergeometric expression to compute both starting values when operating in the $1.1 \le \xi \le 3$ region.

As for arguments that have a modulus greater than three, *MTP-1945* [41] recommends using the following less complicated, but slower converging,

Table 3.3 Summary of Approach Used to Compute the Set of Associated Legendre Functions of the Second Kind with Non-Negative Degrees for a Given Order *m*

Region of Argument ξ	Approach Used to Compute Set of $Q_l^m(\xi)$ functions for $l \geq 0$	Formula Used to Compute Starting Values
$1 < \xi < 1.1$	Explicit Expression Approach (use (3-50) and (3-51) to individually compute all members of set)	NA
$1.1 \leq \xi \leq 3$	Recurrence Relation Approach (use (3-52) to work downward from starting values)	Hypergeometric Expression (3-54)
$\xi > 3$	Recurrence Relation Approach (use (3-52) to work downward from starting values)	Hypergeometric Expression (3-55)

hypergeometric expression when computing the associated Legendre functions of the second kind:

$$Q_l^m(\xi) = A(m,l,\xi)F\left(\tfrac{1}{2}(l-m+2), \tfrac{1}{2}(l-m+1);\ l+\tfrac{3}{2};\ \xi^{-2}\right) \qquad (3\text{-}55)$$

where

$$A(m,l,\xi) = \frac{(-1)^m 2^{l-1}}{(l+\frac{1}{2})(\xi^2-1)^{m/2}\xi^{l-m+1}}\left(\frac{l!(l+m)!}{(2l)!}\right).$$

Accordingly, (3-55) is employed by this routine to compute both starting values when the argument is in the $\xi > 3$ region. Although these hypergeometric expressions can be used to individually evaluate each function of the set, the recurrence relation approach is much more computationally efficient. Having completed the discussion of our approach for computing the set of associated Legendre functions of the second kind with non-negative degrees, we present a summary of its details in Table 3.3.

We now turn our attention to computing the set of associated Legendre functions of the second kind with negative degrees *l*, viz., $l = -m, -m+1, \ldots, -1$, for a given order *m* (i.e., when $m > 0$). These computations are done by using the recurrence relation (3-52) to work downward from the starting values $Q_0^m(\xi)$ and $Q_1^m(\xi)$ until $Q_{-m}^m(\xi)$ is reached. Note that both starting values have already been determined from the part of the routine that computes the set of associated Legendre functions of the second kind with non-negative degrees (see Table 3.3).

The results of this routine are first compared to tabulated data available in *MTP-1945* [41] (i.e., six-decimal accuracy) for both sets of associated Legendre functions. For all of the test cases, the routine performs extremely well and yields results that agree with the published data. In order to further validate the performance of our routine, additional computational checks are made. First, the associated Legendre functions of the first kind are computed by the CALCPQ (P-f) routine and then compared to results obtained from a select set of closed form representations: both sets of results match one another extremely well. As for the associated Legendre functions of the second kind, we continue our validation process by conducting consistency checks between the computational methods. For arguments situated in the regions where $\xi \geq 1.1$, results obtained from the recurrence relation approach are compared to those computed directly with the hypergeometric expression appropriate for its region, viz., (3-54) and (3-55). For both of these regions, i.e., $1.1 \leq \xi \leq 3$ and $\xi > 3$, the two computational approaches are in excellent agreement (i.e., match to better than twelve decimal places) for the cases that are tested. As a result, it is these additional tests that allow us to gain additional confidence in the developed CALCPQ (P-f) numerical routine.

3.5 OBLATE SPHEROIDAL RADIAL FUNCTIONS OF THE FIRST AND SECOND KIND

3.5.1 OBLRADIAL (O-3) Numerical Routine

With similarity to its prolate counterpart, this numerical routine computes the oblate spheroidal radial functions of the first and second kind with their first derivatives for a given order *m*, degree *l*, and independent parameter *h*. The oblate spheroidal radial function of the fourth kind, which is required by the NZ-FZT algorithm for the oblate case, is then determined from both of these computed radial solutions by way of (2-74b). Because this primary routine makes use of the shared secondary routine OBLDNCNSTS (O-d) to compute the $d_r^{m,l}(-jh)$ expansion coefficients, it too must be provided with either an initial approximation of the respective eigenvalue or an already refined eigenvalue. In the case that an approximation of the eigenvalue is supplied to the routine, the numerical representation of the eigenvalue is replaced with a value that is more accurate. As we shall see, the principal difference between the prolate and oblate approaches presents itself when computing the spheroidal radial function of the second kind and its first derivative.

Even though both oblate spheroidal radial functions are defined (i.e., not singular) at $\xi = 0$, we have elected to confine this routine to those arguments that are greater than zero, i.e., $\xi > 0$. In the limiting case where $\xi = 0$, the oblate spheroidal surface becomes a circular disc of infinitesimal thickness (refer to Figure 2.1b). From an applied perspective, the usefulness of this particular transformation surface is somewhat limited because of the difficulty it has with enclosing a realistic radiating structure possessing finite dimensions. Furthermore, evaluating both oblate spheroidal radial functions and their first derivatives at $\xi = 0$ requires the use of special formulas [36]. In fact, the two radial solutions no longer remain linearly independent in this limiting case [36]. Taking into account these reasons, we decided that being able to evaluate these functions at $\xi = 0$ is beyond what is really necessary for our particular application.

Computation of the oblate spheroidal radial function of the first kind and its first derivative uses essentially the same procedure as its prolate counterpart with the exception of some sign reversals in the expressions containing the spherical Bessel function expansions [36]:

$$R_{m,l}^{(1)}(-jh, j\xi) = \frac{(l-m)!}{(l+m)!}\left(\frac{\xi^2+1}{\xi^2}\right)^{m/2} \sum_{r=0,1}^{\infty}{}' j^{r+m-l}\ d_r^{m,l}(-jh)\frac{(2m+r)!}{r!} j_{r+m}(h\xi) \tag{3-56}$$

$$\frac{d}{d\xi}R_{m,l}^{(1)}(-jh, j\xi) = \frac{(l-m)!}{(l+m)!}\left(\frac{\xi^2+1}{\xi^2}\right)^{m/2} \times$$

$$\left\{ h\sum_{r=0,1}^{\infty}{}' j^{r+m-l}\ d_r^{m,l}(-jh)\frac{(2m+r)!}{r!(2m+2r+1)}\begin{bmatrix}(m+r)\, j_{r+m-1}(h\xi)\\ -(m+r+1)\, j_{r+m+1}(h\xi)\end{bmatrix} \right\}. \tag{3-57}$$
$$\left\{ -\frac{m}{\xi(\xi^2+1)}\sum_{r=0,1}^{\infty}{}' j^{r+m-l}\ d_r^{m,l}(-jh)\frac{(2m+r)!}{r!} j_{r+m}(h\xi) \right\}$$

Evaluation of these expressions is performed in the same manner as that which is done for the prolate case, i.e., using (3-16) and (3-17), and need not be discussed any further.

This numerical routine makes use of two different approaches to compute the oblate spheroidal radial function of the second kind and its first derivative much in the same way as its prolate counterpart. This time around, the decision making process that determines the best approach to use is based upon the computational experience provided in *NRL Report 6959* [36]. Once again, the Wronskian check (using the appropriate oblate form) plays a significant role.

The first of these two approaches uses essentially the same procedure as its prolate counterpart with the exception of some sign reversals in the expressions containing the spherical Neumann function expansions [36]:

$$R_{m,l}^{(2)}(-jh, j\xi) = \frac{(l-m)!}{(l+m)!}\left(\frac{\xi^2+1}{\xi^2}\right)^{m/2} \sum_{r=0,1}^{\infty}{}' j^{r+m-l}\ d_r^{m,l}(-jh)\frac{(2m+r)!}{r!}n_{r+m}(h\xi)$$

(3-58)

$$\frac{d}{d\xi}R_{m,l}^{(2)}(-jh, j\xi) = \frac{(l-m)!}{(l+m)!}\left(\frac{\xi^2+1}{\xi^2}\right)^{m/2} \times$$

$$\left\{ h\sum_{r=0,1}^{\infty}{}' j^{r+m-l}\ d_r^{m,l}(-jh)\frac{(2m+r)!}{r!(2m+2r+1)}\begin{bmatrix}(m+r)n_{r+m-1}(h\xi)\\ -(m+r+1)n_{r+m+1}(h\xi)\end{bmatrix} \right.$$
$$\left. -\frac{m}{\xi(\xi^2+1)}\sum_{r=0,1}^{\infty}{}' j^{r+m-l}\ d_r^{m,l}(-jh)\frac{(2m+r)!}{r!}n_{r+m}(h\xi) \right\}. \quad (3\text{-}59)$$

Because the evaluation of these expressions is performed in the same exact manner as that which is done for the prolate case, i.e., using (3-18) and (3-19), it too will not be discussed in any further depth.

Just like its prolate counterpart, the usefulness of the spherical Neumann function expansion approach of (3-58) and (3-59) is limited to large values of $h\xi$ because of the spherical Neumann functions. Accordingly, Van Buren *et al.* [36] put forth another approach capable of evaluating the oblate spheroidal radial function of the second kind and its first derivative when given small values of $h\xi$. Their approach fundamentally differs from its prolate counterpart, i.e., equations (3-20)-(3-24), and requires the use of an expression presented by Flammer [23] that expands the oblate spheroidal radial function of the third kind only in terms of associated Legendre functions of the second kind [36]:

$$R_{m,l}^{(3)}(-jh, j\xi) = \underbrace{e^{j(h\xi-(l+1)(\pi/2))}}_{\equiv\alpha+j\beta} \times \underbrace{\frac{j^{2m+1}}{m!h}\sum_{r=-m}^{\infty}\left(\frac{A_r^{m,l}}{A_{-m}^{m,l}}\right)Q_{m+r}^{m}(j\xi)}_{\equiv\gamma+j\delta} \quad (3\text{-}60)$$

where $r = -m, -m+1, \ldots.$

As a point of information, this expression is developed from a special expansion for the oblate spheroidal angle function of the first kind discovered by Baber and Hasse; the interested reader is referred to [23], [36] regarding the specific details. Contrary to the other expansions explored within this chapter, the summation in this case is over each consecutive value of r as opposed to every other value of r. The Baber and Hasse normalized expansion coefficients $\left(\boldsymbol{A}_r^{m,l} / \boldsymbol{A}_{-m}^{m,l}\right)$ are computed using another three-term recurrence relation that is employed in the secondary routine BABHASCNSTS (O-e); these computations are detailed in the next section (see 3.5.2).

Upon inspection of (3-60), one can see that this expression can be represented as the product of two complex quantities: $(\alpha + j\beta)$ and $(\gamma + j\delta)$. The oblate spheroidal radial function of the second kind can now be related to its first kind counterpart using the following expression derived from (2-74b) and (3-60) [36]:

$$R_{m,l}^{(2)}(-jh, j\xi) = \alpha\delta + \frac{\beta}{\alpha}\left[R_{m,l}^{(1)}(-jh, j\xi) + \beta\delta\right]. \tag{3-61}$$

This expression allows us to compute the oblate spheroidal radial function of the second kind from the results of (3-56), i.e., $R_{m,l}^{(1)}(-jh, j\xi)$, after determining the parameters α, β, and δ from (3-60). While the computation of the parameters α and β is straightforward, this is not the case for the parameter δ. Evaluation of the quantity $(\gamma + j\delta)$ requires the complex summation of an expansion of associated Legendre functions of the second kind. Although the $\left(\boldsymbol{A}_r^{m,l} / \boldsymbol{A}_{-m}^{m,l}\right)$ normalized expansion coefficients are real quantities, the summation is complex because the associated Legendre functions of the second kind $Q_{m+r}^{m}(j\xi)$ can be either a real or purely imaginary quantity. The calculation of this complex set of associated Legendre functions of the second kind is provided by the CALCQIM (O-f) secondary routine and is discussed later (see 3.5.3).

Regarding the first derivative of the oblate radial function of the second kind, it can be computed from its first kind counterpart (determined from (3-57)) using the following expressions [36]:

$$\frac{d}{d\xi} R_{m,l}^{(2)}(-jh, j\xi) = \alpha\nu + \frac{\beta}{\alpha}\left[\frac{d}{d\xi} R_{m,l}^{(1)}(-jh, j\xi) + \beta\nu\right] \tag{3-62}$$

where

$$\mu + j\nu = \sum_{r=-m}^{\infty}\left(\frac{\boldsymbol{A}_r^{m,l}}{\boldsymbol{A}_{-m}^{m,l}}\right)\left(\begin{array}{l} Q_{m+r}^{m}(j\xi)\left[(m+r)\dfrac{\xi}{\xi^2+1} + jh\right] \\ + j\dfrac{(2m+r)}{\xi^2+1} Q_{m+r-1}^{m}(j\xi) \end{array}\right). \tag{3-63}$$

By taking the imaginary part of the complex expansion (3-63), expression (3-62) is provided with the necessary parameter ν. Both of these expressions can be found from (3-60) and (3-61) using the following recurrence relation involving the derivative of the associated Legendre function of the second kind that is valid for arguments that are off the branch cut and are purely imaginary:

$$\frac{d}{d\xi} Q_{m+r}^{m}(j\xi) = (m+r)\frac{\xi}{\xi^2+1} Q_{m+r}^{m}(j\xi) + j\frac{(2m+r)}{\xi^2+1} Q_{m+r-1}^{m}(j\xi). \tag{3-64}$$

This recurrence relation can be derived from its generalized complex variable form, i.e., (D-35), provided by Erdelyi *et al.* [40]. One should take note that (3-64) relates the first derivative of this radial function to only associated Legendre functions of the second kind that correspond to the same family of a given order *m*. Practically speaking, this feature means that the evaluation of the derivative only requires associated Legendre functions of the second kind from a single family when using formulations (3-62) and (3-63). Moreover, this family of functions is the same as the one used when computing its corresponding oblate spheroidal radial function of the second kind with (3-60) and (3-61). As a result, the routine CALCQIM (O-f) only needs to be evoked once when using the

Table 3.4 Best Method to Compute the Oblate Spheroidal Radial Function of the Second Kind $R_{m,l}^{(2)}(-jh, j\xi)$ for a Given Input Parameter Region

Input Parameter Region	Best Method
$0 < \xi \leq 1$ or $h\xi \leq 10$	Baber and Hasse Expansion Approach
ξ and h outside the above stated ranges	Both Spherical Neumann Function Expansion Approach and Baber and Hasse Expansion Approach (select better result using the Wronskian)

Baber and Hasse expansion approach to compute this particular radial function and its first derivative.

Now that we have discussed both approaches capable of computing the oblate spheroidal radial function of the second kind and its first derivative, our attention must focus on which method is the best with respect to accuracy for a given region of input parameters. Taking advantage of the computational experience of Van Buren *et al.* [36], Table 3.4 summarizes their recommendations regarding the best method to use when given a particular set of values for ξ and h.

Upon inspection of Table 3.4, we notice that the second input parameter region requires the selection of the best result from both numerical approaches by comparing their numerical Wronskians. This computational check, which is initially described in the section pertaining to the PRORADIAL (P-3) numerical routine, consists of comparing the numerical Wronskian of each approach with the known theoretical Wronskian to determine which approach yields the better result. Using the Wronskian formulation that corresponds to the oblate case, we obtain the necessary expressions for the Wronskian check [23]:

$$W_{numerical}\left(R_{m,l}^{(1)}(-jh, j\xi), R_{m,l}^{(2)}(-jh, j\xi)\right) =$$

$$R_{m,l}^{(1)}(-jh, j\xi)\frac{d}{d\xi}R_{m,l}^{(2)}(-jh, j\xi) - R_{m,l}^{(2)}(-jh, j\xi)\frac{d}{d\xi}R_{m,l}^{(1)}(-jh, j\xi) \tag{3-65}$$

$$W_{theory}\left(R_{m,l}^{(1)}(-jh, j\xi), R_{m,l}^{(2)}(-jh, j\xi)\right) = \frac{1}{h(\xi^2+1)}. \tag{3-66}$$

Validation of the OBLRADIAL (O-3) routine consists of comparing its results with published data provided by Van Buren *et al.* [36]. The routine performs extremely well (i.e., at least twelve-decimal accuracy) when compared to this data set. Once again, we choose to implement the Wronskian check in an on-the-fly manner such that the routine can warn the user of results that fail to meet some specified level of accuracy. We do so in order to provide the user with an added level of confidence regarding the validity of the computed results.

3.5.2 BABHASCNSTS (O-e) Numerical Routine

This routine computes the Baber and Hasse normalized expansion coefficients $\left(\boldsymbol{A}_r^{m,l} / \boldsymbol{A}_{-m}^{m,l}\right)$ required to implement the approach outlined in equations (3-60)-(3-63). In order to perform these computations, our routine makes use of the technique put forth by Van Buren *et al.* [36]. Like the other special function expansion coefficients, this technique also evokes the use of a three-term recurrence relation that relates consecutive expansion coefficients. We begin computing these normalized expansion coefficients by using the following downward (i.e., backward) traveling form of the three-term recurrence relation [36]:

$$\left(\frac{A_r^{m,l}}{A_{-m}^{m,l}}\right) = -\frac{U_{r+1}^{m}\left(\frac{A_{r+2}^{m,l}}{A_{-m}^{m,l}}\right) + V_{r+1}^{m,l}\left(\frac{A_{r+1}^{m,l}}{A_{-m}^{m,l}}\right)}{W_{r+1}^{m}} \tag{3-67}$$

where

$$U_r^m = \frac{2(r+m+1)(r+2m+1)}{(2r+2m+3)} \tag{3-68}$$

$$V_r^{m,l} = \frac{\lambda_{m,l}(-jh) - (r+m)(r+m+1)}{h} + h \tag{3-69}$$

$$W_r^m = \frac{-2r(r+m)}{(2r+2m-1)}. \tag{3-70}$$

Note that (3-69) requires this routine to be provided with a refined version of the respective oblate spheroidal eigenvalue. In order to begin working downward with the recurrence relation of (3-67), we must generate two consecutive starting values. Just like we do when computing the spherical Bessel functions, these consecutive starting values are arbitrarily chosen as some constant and zero. The index of the starting values should then be chosen somewhat greater than the highest index required to achieve convergence of the expansions in (3-60) and (3-63). As before, this procedural requirement must be imposed because the initial values that result from the downward recurrence relation are not accurate and are needed to prime the downward computational pipeline. However, the values of the lower indices do become extremely accurate after the initial start-up procedure. Because we have chosen an arbitrary constant as one of the starting values, this procedure yields expansion coefficients that are only accurate relative to one another; that is, they still need to be scaled by a correction constant to achieve the proper results.

Unfortunately, this particular three-term recurrence relation may not provide accurate results for the entire pass in the downward direction. From a computational viewpoint, one would prefer to work a recurrence relation in the direction of increasing magnitude (of the related terms) in order to minimize the loss of precision. However in

this particular case, the set of normalized expansion coefficients $\left(\boldsymbol{A}_r^{m,l} \big/ \boldsymbol{A}_{-m}^{m,l}\right)$ is not always guaranteed to be continually increasing in the downward direction. To overcome this difficulty, Van Buren *et al.* [36] suggest using the downward traveling recurrence relation to compute the coefficients only as long as the they continue to increase in magnitude. Accordingly, it is possible that the entire set of normalized coefficients could be computed using a single downward pass. However, if the normalized coefficients should begin to decrease in magnitude during the downward traveling computations, then those remaining coefficients need to be computed differently. This second part of the approach requires that the remaining lower indexed portion of the normalized coefficients be evaluated from $r = -m$ up to this resulting cross-over index (i.e., the point where the terms begin to get smaller with respect to the downward direction) using the following upward traveling form of the three-term recurrence relation [36]:

$$\left(\frac{\boldsymbol{A}_r^{m,l}}{\boldsymbol{A}_{-m}^{m,l}}\right) = -\frac{V_{r-1}^{m,l}\left(\dfrac{\boldsymbol{A}_{r-1}^{m,l}}{\boldsymbol{A}_{-m}^{m,l}}\right) + W_{r-1}^{m}\left(\dfrac{\boldsymbol{A}_{r-2}^{m,l}}{\boldsymbol{A}_{-m}^{m,l}}\right)}{U_{r-1}^{m}}. \tag{3-71}$$

The two consecutive starting values necessary to begin working upward with (3-71) are given as follows: $\left(\dfrac{\boldsymbol{A}_{-m}^{m,l}}{\boldsymbol{A}_{-m}^{m,l}}\right) = 1$ and $\left(\dfrac{\boldsymbol{A}_{-m+1}^{m,l}}{\boldsymbol{A}_{-m}^{m,l}}\right) = -\dfrac{V_{-m}^{m,l}}{U_{-m}^{m}}$. The first starting value is unity for obvious reasons, and the second starting value can be found directly from (3-71) using the fact that $W_{-m}^{m} = 0$ by way of (3-70). Since both of these starting values are correct in absolute terms, the normalized coefficients that are computed using the upward recurrence relation need not be scaled by a correction constant.

Having determined the normalized expansion coefficients using both forms of the three-term recurrence relation, we must now address the fact that the upper portion of the coefficients computed using the downward form (3-67) must be scaled by a correction constant. Since the normalized coefficients that are computed by the upward form (3-71) are accurate in absolute terms (as opposed to relative terms), the necessary correction

constant can be found by reconciling the difference between the two differently computed portions at the resulting cross-over index. In the special case that all of the normalized coefficients are computed using the downward recurrence relation, the correction constant is then determined using the fact that the first normalized coefficient in the set is unity.

We are not able to directly validate this routine because of the lack of available published data for these obscure normalized expansion coefficients. Once again, the ultimate validation is left to how well this routine supports its respective primary routine, i.e., OBLRADIAL (O-3).

3.5.3 CALCQIM (O-f) Numerical Routine

This secondary routine provides the necessary evaluations of the associated Legendre functions of the second kind to the OBLRADIAL (O-3) routine. In particular, CALCQIM (O-f) evaluates a family of these functions for a given order *m* with degrees corresponding to $l = -1, 0, 1, \ldots$. This supporting routine is always called by (O-3) because the overall approach to computing the oblate spheroidal radial function of the second kind requires the evaluation of the Baber and Hasse expansions of (3-60) and (3-63) (see Table 3.4). Furthermore, CALCQIM (O-f) must provide enough members of the family to ensure convergence of both of these expansions. A unique feature of this routine is that it evaluates the associated Legendre functions of the second kind for a purely imaginary argument, viz., $Q_l^m(j\xi)$. Correspondingly, the formulations used in this routine are derived from generalized complex variable expressions for the associated Legendre functions of the second kind that are valid off the $(-1 < x < +1)$ branch cut. In keeping with the requirements of OBLRADIAL (O-3), this supporting routine is confined to purely imaginary arguments that lie on the positive half of the imaginary axis, viz., where $j\xi > 0$.

Initially, we discuss the how and when of the three different methods used by this routine to directly evaluate the associated Legendre functions of the second kind for purely imaginary arguments with non-negative degrees (i.e., $l \geq 0$). As we will see, the

methods for computing the associated Legendre functions of the second kind for purely imaginary arguments somewhat resemble those methods that address real arguments greater than unity (see 3.4.4). These similarities exist because the methods are fundamentally derived from the same generalized complex variable expressions. Although using these direct evaluation methods to calculate the entire set of complex-valued associated Legendre functions of the second kind is very feasible, doing so is still computationally costly. For that reason, we proceed to explain how to improve the computational efficiency of this routine by fusing the direct evaluation methods with a recurrence relation approach. Finally, we address computation of the lone function with a negative degree, viz., $Q_{-1}^{m}(j\xi)$.

When directly evaluating the associated Legendre functions of the second kind with non-negative degrees for purely imaginary arguments, the routine selects one of the three following methods depending upon the modulus of the argument $j\xi$. For arguments in the region where $0 < \xi < 0.01$, our numerical experience shows that the following explicit expression performs well:

$$
\begin{aligned}
Q_l^m(j\xi) = \; & jP_l^m(j\xi)(\tan^{-1}\xi - \pi/2) \\
& + \frac{m!}{2}\sum_{s=1}^{m}\frac{j^s}{s(m-s)!}P_l^{m-s}(j\xi)\times\begin{Bmatrix} 2j\,\mathrm{Im}\left[\left(\dfrac{1+j\xi}{\sqrt{\xi^2+1}}\right)^s\right], s\,\text{even} \\ 2\,\mathrm{Re}\left[\left(\dfrac{1+j\xi}{\sqrt{\xi^2+1}}\right)^s\right], s\,\text{odd} \end{Bmatrix} \\
& - \sum_{q=0}^{Int\left[\frac{1}{2}(l-1)\right]}\frac{(2l-4q-1)}{(2q+1)(l-q)}P_{l-2q-1}^{m}(j\xi) \;\text{ for } l \geq 1; \qquad (3\text{-}72)
\end{aligned}
$$

where $Int[x]$ is considered the greatest integer function.

Note that (3-72) reduces to the following when $l = 0$ and $m = 0$ (convention drops the superscript for the zeroth order):

$$Q_0(j\xi) = j(\tan^{-1}\xi - \pi/2). \tag{3-73}$$

The explicit expression of (3-72) can be found directly (with some reduction) from its prolate counterpart (3-50) by way of the $\xi \to j\xi$ transformation.

Although the Baber and Hasse expansion approach does not explicitly use the associated Legendre functions of the first kind, the evaluation of these functions for a purely imaginary argument is necessary when using (3-72) to directly compute the associated Legendre function of the second kind. Fortunately, we are able to expand the previously outlined approach that computes the associated Legendre functions of the first kind for real arguments off the branch cut to handle purely imaginary arguments (which also happen to be off the branch cut). These modifications consist of applying the $\xi \to j\xi$ transformation to equations (3-47)-(3-49) to yield the following complex equations:

$$P_l^m(j\xi) = j\xi\frac{(2l-1)}{(l-m)}P_{l-1}^m(j\xi) - \frac{(l+m-1)}{(l-m)}P_{l-2}^m(j\xi) \tag{3-74}$$

$$P_m^m(j\xi) = j^m(2m-1)!!(\xi^2+1)^{m/2} \tag{3-75}$$

$$P_{m+1}^m(j\xi) = j\xi(2m+1)P_m^m(j\xi). \tag{3-76}$$

Using these modified equations in a manner identical to that which is performed for real arguments off the branch cut, we begin working upward with the complex recurrence relation of (3-74) from the starting values provided by (3-75) and (3-76). This process allows us to evaluate the required associated Legendre functions of the first kind for a purely imaginary argument $j\xi$. It is important to recognize that the evaluation of this

particular function for a purely imaginary argument yields either a real or purely imaginary result whose phase behaves as j^l.

We now consider direct computation of the associated Legendre functions of the second kind for purely imaginary arguments $j\xi$ where $\xi \geq 0.01$. Our numerical experience shows that the hypergeometric approaches recommended by *MTP-1945* [41] perform extremely well in the $\xi \geq 0.01$ region when modified to handle purely imaginary arguments. For the case where $0.01 \leq \xi \leq 3$, we make use of the following complex hypergeometric expression (obtained from (3-54) using the $\xi \rightarrow j\xi$ transformation):

$$Q_l^m(j\xi) = B(m,l,j\xi)F\left(\tfrac{1}{2}+m, \tfrac{1}{2}-m; l+\tfrac{3}{2}; -t\right) \tag{3-77}$$

where

$$B(m,l,j\xi) = \frac{j^{-(l+2m+1)}\,4^l}{(l+\frac{1}{2})\sqrt{2(\xi^2+1)^{1/2}}\left(\xi+\sqrt{\xi^2+1}\right)^{l+\frac{1}{2}}}\left(\frac{l!(l+m)!}{(2l)!}\right)$$

$$t = \frac{\xi-\sqrt{\xi^2+1}}{2\sqrt{\xi^2+1}}.$$

We are able to employ (3-77) for purely imaginary arguments $j\xi$ in this particular region because its respective hypergeometric function converges for all positive values of ξ.

Regarding the region where $\xi > 3$, we make use of the less complicated, but slower converging, complex hypergeometric expression to directly compute the associated Legendre function of the second kind (obtained from (3-55) using the $\xi \rightarrow j\xi$ transformation):

$$Q_l^m(j\xi) = A(m,l,j\xi)F\left(\tfrac{1}{2}(l-m+2), \tfrac{1}{2}(l-m+1); l+\tfrac{3}{2}; -\xi^{-2}\right) \qquad (3\text{-}78)$$

where

$$A(m,l,j\xi) = \frac{j^{-(l+2m+1)}\,2^{l-1}}{(l+\frac{1}{2})(\xi^2+1)^{m/2}\,\xi^{l-m+1}}\left(\frac{l!(l+m)!}{(2l)!}\right).$$

Because expression (3-78) converges for all positive values of ξ greater than unity, it is capable of directly evaluating the associated Legendre function of the second kind for purely imaginary arguments $j\xi$ in the region where $\xi > 3$.

Having discussed the three methods used to directly evaluate the associated Legendre functions of the second kind for purely imaginary arguments, we are now able to improve the computational efficiency of this routine by incorporating the following recurrence relation approach. We begin computing these complex-valued functions by taking advantage of the following downward (i.e., backward) traveling complex recurrence relation that is valid for purely imaginary arguments (obtained from (3-52) using the $\xi \to j\xi$ transformation):

$$Q_l^m(j\xi) = j\xi\frac{(2l+3)}{(l+m+1)}Q_{l+1}^m(j\xi) - \frac{(l-m+2)}{(l+m+1)}Q_{l+2}^m(j\xi). \qquad (3\text{-}79)$$

Yet before we can begin working downward with this complex recurrence relation, we must first have two consecutive starting values. In a manner that is similar to the procedure used when computing the spherical Bessel functions, the moduli of these consecutive starting values are chosen as some arbitrary constant and zero. However, this time around, the nonzero starting value is either real or purely imaginary. We know this is the case because the phase of the associated Legendre function of the second kind for purely imaginary arguments behaves as $j^{-(l+2m+1)}$. As a result, we are able to assign the correct phase to the nonzero starting value such that the resulting correction constant is a scalar quantity, not a complex quantity. (Recall from before that a correction constant is

needed because the nonzero starting value is arbitrarily chosen.) Once again, the index l of the nonzero starting value, i.e., the degree of the associated Legendre function, should be chosen somewhat greater than the highest index required to achieve convergence of the expansions in (3-60) and (3-63). Like the process for computing the spherical Bessel functions, this procedural requirement must be imposed because the initial values that result from the downward recurrence relation are not considered usable and are necessary to prime the downward computational pipeline.

Regarding the complex recurrence relation of (3-79), numerical experiments indicate that it may not always yield accurate results for the entire pass in the downward direction. This difficulty occurs because a given family of associated Legendre functions of the second kind with a purely imaginary argument may not provide a sequence of moduli that is always continually increasing in the downward direction. As previously mentioned, one would prefer to work a recurrence relation in the direction of increasing magnitude (of the related terms) in order to minimize the loss of precision. In order to sidestep this difficulty, we make use of a procedure that somewhat resembles the approach used when computing the Baber and Hasse normalized expansion coefficients (see 3.5.2). We begin by using the downward traveling complex recurrence relation to evaluate the family of functions only as long as the moduli of the functions continue to increase. Once again, it is conceivable that the entire family of associated Legendre functions of the second kind is computed using a single downward pass. However, if the moduli of these functions should begin to decrease during the downward traveling computations, then those remaining functions of the family (viz., those with the lower degrees) need to be computed differently. Our numerical experience shows that the best way to evaluate this lower portion of the family from $l = 0$ to this cross-over index is by individually calculating each function using direct evaluation; in essence, the remaining lower indexed portion of the family is forward filled by appropriately using one of the three direct evaluation approaches that depends upon the modulus of the argument.

Now that the family of associated Legendre functions of the second kind has been computed using either the recurrence relation or the direct evaluation approach, we turn

our attention to applying the proper correction constant to the upper indexed portion of the family that is computed using the downward recurrence relation of (3-79). Since the lower indexed portion of the family (computed by using direct evaluation) is correct in absolute terms (as opposed to relative terms), the proper correction constant is easily found by reconciling the difference between the two differently computed portions at the resulting cross-over index (this procedural step closely parallels that which is used in the BABHASCNSTS (O-e) routine). In the special case that all of the functions are computed using the downward recurrence relation, the second element in the sequence (which corresponds to $l = 1$) is reconciled with its direct evaluation counterpart in order to determine the proper correction constant. In order to obtain the proper set of results, we then apply the computed correction constant to the portion of the family that is computed using the downward recurrence relation (3-79).

Numerical testing reveals that the use of this particular recurrence relation approach can provide a significant savings in computation time for these much needed evaluations of the associated Legendre functions of the second kind. In the cases where a majority of the functions are able to be computed using the recurrence relation approach, a better than ten-fold savings in computation time has been observed when compared to only using the direct evaluation approach. However, for obvious reasons there is little or no improvement in computation time for the cases where most of the associated Legendre functions must be found using direct evaluation. Since the computation time of the functions is reduced on average with the recurrence relation approach, we have prudently chosen to incorporate this time-saving technique into our routine. Unfortunately, further testing of the recurrence relation approach indicates that its effectiveness is limited to arguments where $\xi \leq 5$ due to computational difficulties that occur when operating beyond this region (viz., numerical overflow conditions); consequently, we exclusively employ the direct evaluation approach to compute the family of functions when $\xi > 5$. Table 3.5 summarizes our overall numerical approach to evaluating the required family of

Table 3.5 Summary of Overall Approach to Compute the Set of Associated Legendre Functions of the Second Kind with Non-Negative Degrees for a Given Order m and Purely Imaginary Argument $j\xi$

Region of Argument $j\xi$	Approach Used to Compute the Set of $Q_l^m(j\xi)$ functions for $l \geq 0$	Appropriate Direct Evaluation Approach
$0 < \xi < 0.01$	Recurrence Relation Approach (3-79) Using the Appropriate Direct Evaluation Approach to Forward Fill	Explicit Expression (3-72) and (3-73)
$0.01 \leq \xi \leq 3$	Recurrence Relation Approach (3-79) Using the Appropriate Direct Evaluation Approach to Forward Fill	Hypergeometric Expression (3-77)
$3 < \xi \leq 5$	Recurrence Relation Approach (3-79) Using the Appropriate Direct Evaluation Approach to Forward Fill	Hypergeometric Expression (3-78)
$\xi > 5$	Direct Evaluation Approach to Compute All Members of the Required Set	Hypergeometric Expression (3-78)

associated Legendre functions of the second kind with non-negative degrees for a purely imaginary argument $j\xi$.

Finally, we must address the computation of the lone associated Legendre function of the second kind possessing a negative degree for a purely imaginary argument, i.e., $Q_{-1}^m(j\xi)$. Evaluation of this particular function is obtained by using the complex relation of (3-79) to work downward from the just computed $Q_0^m(j\xi)$ and $Q_1^m(j\xi)$ (viz., the first two members of the set of function evaluations computed via the procedure outlined in Table 3.5). In the special case where $m = 0$, the downward recurrence relation of (3-79) becomes undefined for $l = -1$ and cannot compute $Q_{-1}^0(j\xi)$. Fortunately, the expansion of (3-63) does not need this particular function because its respective expansion coefficient happens to conveniently vanish in this special case.

Validation of this routine includes the comparison of its results with tabulated data available in *MTP-1945* [41] (i.e., six-decimal accuracy tables of associated Legendre functions of the second kind with purely imaginary arguments). For all of our test cases, the routine performs extremely well and has results that match exactly with the published data. The routine is further validated by comparing the results obtained using the recurrence relation approach with those computed using only the direct evaluation approach (i.e., computed outside the normal operation of the routine). In general, the results provided by the two approaches match within twelve decimal places. Although the results provided by both methods are not as consistent when operating close to the origin, numerical tests indicate that in this region they still match one another within seven decimal places.

In the midst of establishing the proper combination of the two methods to use for the different regions of the argument, we are presented with an engineering tradeoff of accuracy (provided by direct evaluation) versus efficiency (provided by the recurrence relation). In short, accuracy of the routine could be improved in some regions at the expense of computation time by exclusively using the direct evaluation approach. Ultimately, our overall numerical approach strikes a practical balance between accuracy and computational efficiency for our particular application.

3.6 PROLATE AND OBLATE SPHEROIDAL ANGLE FUNCTIONS

3.6.1 PROANG (P-4) and OBLANG (O-4) Numerical Routines

Each of these primary routines evaluates its respective spheroidal angle function in terms of the Morse and Feshbach normalization scheme for a given order *m*, degree *l*, independent parameter *h*, and real argument η. In keeping with the definition of η put forth in Chapter 2, both numerical routines evaluate the spheroidal angle functions for arguments where $-1 \le \eta \le +1$. Furthermore, these primary routines must be supplied with either an initial approximation of the eigenvalue or a previously refined eigenvalue

for the particular function under consideration. Once again, this requirement stems from the fact that each of these primary routines must evoke the secondary routine which computes its respective expansion coefficients, viz., $d_r^{m,l}(h)$ or $d_r^{m,l}(-jh)$. With respect to the discussion that follows, we have chosen to address both routines concurrently throughout this section on account of how closely they parallel one another.

From a computational standpoint, it is important to understand that both spheroidal NZ-FZT algorithms need to recalculate their respective set of spheroidal angle functions for each far-zone observation angle under consideration (see Tables 2.5a and 2.5b). In addition, each of these primary routines must also provide support to its respective integration routine, i.e., INTPROANG (P-5) or INTOBLANG (O-5). By and large, the routines PROANG (P-4) and OBLANG (O-4) get an intensive workout in the course of computing the NZ-FZT process for their respective spheroidal transformation surface. Consequently, repeated execution of these routines accounts for a large share of the total computation time for the overall NZ-FZT process. It is for this reason that both routines must be able to evaluate their respective spheroidal angle functions in the best possible way with respect to computational efficiency.

In order to compute the spheroidal angle functions, we make use of the following expansions of associated Legendre functions of the first kind initially presented in (2-68a) and (2-68b):

Prolate: $$S_{m,l}(h,\eta) = \sum_{r=0,1}^{\infty}{}' d_r^{m,l}(h) P_{m+r}^m(\eta) \text{ where } 0 \le m \le l; \tag{3-80a}$$

Oblate: $$S_{m,l}(-jh,\eta) = \sum_{r=0,1}^{\infty}{}' d_r^{m,l}(-jh) P_{m+r}^m(\eta) \text{ where } 0 \le m \le l. \tag{3-80b}$$

Once more, the expansion coefficients $d_r^{m,l}(h)$ and $d_r^{m,l}(-jh)$ are provided by the secondary routines PRODNCNSTS (P-d) and OBLDNCNSTS (O-d). As a result, we are now left with having to compute the associated Legendre functions of the first kind that

are part of these expansions. However, this time around these functions must be evaluated for arguments that are either on the $(-1 < x < +1)$ branch cut or at the $x = \pm 1$ branch points. Fortunately, we are able to use the computational approach put forth in [37] without having to make any modifications. As before, we begin by using the upward (i.e., forward) traveling recurrence relation that relates associated Legendre functions of the first kind for a given order *m* [37]:

$$P_l^m(\eta) = \eta \frac{(2l-1)}{(l-m)} P_{l-1}^m(\eta) - \frac{(l+m-1)}{(l-m)} P_{l-2}^m(\eta) . \tag{3-81}$$

Note that this recurrence relation is identical in form to the one presented in (3-47) by virtue of being valid on and off the branch cut. We now employ the following closed form expressions that are valid for real arguments on the branch cut and at the branch points to determine the two necessary starting values [37]:

$$P_m^m(\eta) = (2m-1)!!(1-\eta^2)^{m/2} \tag{3-82}$$

$$P_{m+1}^m(\eta) = \eta(2m+1) P_m^m(\eta) . \tag{3-83}$$

Accordingly, the associated Legendre functions required to evaluate (3-80a) and (3-80b) are computed by working upward with the recurrence relation of (3-81) from these two starting values. With regard to computational efficiency, this numerical approach lends itself quite well to the evaluation of both spheroidal angle functions. This is so because the associated Legendre function of the first kind for each expansion term can be computed on an as-needed basis until convergence of the respective expansion, i.e., (3-80a) or (3-80b), is achieved. Namely, family members for a given order *m* are progressively computed on-the-fly using a single upward pass of the recurrence relation (3-81) until the expansion has converged; at this point, evaluation of the family of associated Legendre functions is then halted in order to eliminate any unnecessary

computations. Much to our satisfaction, both routines PROANG (P-4) and OBLANG (O-4) continually prove to be remarkably efficient.

Validation of the PROANG (P-4) routine consists of comparing its results with those computed by an alternative numerical method. We start by considering a numerical technique put forth in [37] capable of calculating the spheroidal eigenvalues. The approach consists of numerically solving the prolate angular self-adjoint boundary value problem of Chapter 2 (see Table 2.2) through the use of an ordinary differential equation (ODE) integrator. In our particular case, we happen to use the fifth-order Cash-Karp Runge-Kutta method with adaptive stepsize (also presented in [37]) as the ODE integrator. At length, we are then able to expand their numerical approach to a point where it can evaluate prolate spheroidal angle functions. Although this alternative method proved to be too slow for our particular algorithm, it still provides us with an excellent computational check. For the cases tested, results from PROANG (P-4) are quite consistent with those computed using this alternative numerical method: they match one another anywhere between seven and fourteen decimal places. In general, we consider the expansion approach employed in (P-4) to be more accurate than its alternative counterpart due to the limitations generally associated with ODE integrators.

In the case of OBLANG (O-4), validation of the routine consists of comparing its calculated results with tabulated data (i.e., four-decimal accuracy) provided by Flammer [23]. For the cases tested, the routine performs extremely well when compared to this published data (i.e., after accounting for the difference in normalization schemes).

3.7 INTEGRATION OF PROLATE AND OBLATE SPHEROIDAL ANGLE FUNCTIONS

3.7.1 INTPROANG (P-5) and INTOBLANG (O-5) Numerical Routines

Both of these primary routines integrate their respective spheroidal angle function over a specified interval for a given order *m*, degree *l*, independent parameter *h*, and lower/upper boundaries ϑ_{lw} and ϑ_{up}. This computational objective is met by conducting

a numerical integration of the specified function. In order to perform this operation, these routines must be able to sample the given spheroidal angle function at many different points over the specified interval. These samples are acquired through many repeated calls to their respective spheroidal angle function routine, viz., PROANG (P-4) or OBLANG (O-4).

Upon review of Tables 2.5a and 2.5b, we recognize that the amount of use each integration routine receives is based upon the NZ-FZT process input. For a single spheroidal transformation surface, the number of times the integration routine is called depends on the number of surface partitions in the angular direction and the total number of spheroidal wave-harmonics necessary for the expansion to achieve convergence. Fortunately, this set of integral evaluations only has to be computed once for a given spheroidal transformation surface despite the number of far-zone observation angles under consideration.

In developing these routines, our aim is to put together an overall approach capable of conducting these numerical integrations in the best possible way with respect to accuracy and computational efficiency. Consequently, both of these objectives prompt us to investigate already existing integration techniques to arrive at one which is well-suited for integrating the spheroidal angle functions. After conducting many numerical experiments, we are ultimately led to using Romberg integration (also referred to as Romberg quadrature). According to [37], this integration technique is very powerful for sufficiently smooth integrands which contain no singularities anywhere on the interval under consideration (including the endpoints). In our particular case, the integrand is either the prolate or oblate spheroidal angle function with the interval of interest being any segment of the $-1 \le \eta \le +1$ $(0 \le \vartheta \le \pi)$ domain. Since the behavior of the spheroidal angle functions satisfies both of these requirements, the Romberg integration technique is a natural for our specific application.

In particular, the routines INTPROANG (P-5) and INTOBLANG (O-5) make use of the Romberg integration routine provided in [37] (i.e., with some slight modifications). This integration routine employs Romberg's method of order $2K$ and is viewed as the

natural generalization of Simpson's rule (i.e., where $K = 2$). For a more comprehensive review of this standard integration technique, the interested reader is referred to [37] and/or any text on numerical analysis, e.g., [42].

Our investigation also reveals that Romberg integration performs extremely well (in terms of accuracy and convergence rate) for both spheroidal angle functions only after performing the $\eta = \cos\vartheta$ change of variable. Numerical testing demonstrates that convergence of these integrations can be considerably slower without carrying out this particular change of variable. As a result, both INTPROANG (P-5) and INTOBLANG (O-5) routines integrate their corresponding spheroidal angle functions with respect to the angular parameter ϑ. In mathematical terms, the numerical integrations implemented by these routines can be expressed as follows:

Prolate: $$I(h,m,l,\vartheta_{lw},\vartheta_{up}) = \int_{\vartheta_{lw}}^{\vartheta_{up}} S_{m,l}(h,\cos\vartheta')\sin\vartheta' d\vartheta'; \qquad (3\text{-}84a)$$

Oblate: $$I(-jh,m,l,\vartheta_{lw},\vartheta_{up}) = \int_{\vartheta_{lw}}^{\vartheta_{up}} S_{m,l}(-jh,\cos\vartheta')\sin\vartheta' d\vartheta'; \qquad (3\text{-}84b)$$

where $0 \le \vartheta_{lw} \le \pi$ and $0 \le \vartheta_{up} \le \pi$.

One may recall from Chapter 2 that the $\sin\vartheta'$ integration factor found in both integrals is introduced by the aforementioned change of variable, while the angular parameter has been primed to identify it as a variable of integration. Moreover, it is important to recognize that both of these integral representations are conveniently in the form necessary to implement our prolate and oblate spheroidal NZ-FZT algorithms (see Tables 2.5a and 2.5b).

Additional testing indicates that the Romberg integration technique does experience some difficulties when integrating the spheroidal angle functions over certain intervals in the defined domain. As we already know, the spheroidal angle functions

exhibit even or odd symmetry over the $-1 \le \eta \le +1$ domain based on whether $(l-m)$ is even or odd. Furthermore, these symmetries remain intact after performing the $\eta = \cos\vartheta$ change of variable in spite of the domain being mapped to $0 \le \vartheta \le \pi$. Consequently, this change of variable causes the spheroidal angle functions to now become symmetric about the point $(\pi/2, 0)$ instead of the origin $(0,0)$. This point of symmetry plays an important role in the implementation of these routines because numerical testing shows that Romberg integration has difficulties with integrating the spheroidal angle functions through this particular point, viz., where $\vartheta = \pi/2$. That is, the integration technique appears to breakdown when evaluating the integrals of (3-84a) and (3-84b) for cases where the boundaries ϑ_{lw} and ϑ_{up} lie in different halves of the $0 \le \vartheta \le \pi$ domain: namely $[0, \pi/2]$ and $[\pi/2, \pi]$ (it is important to recognize that the $\vartheta = \pi/2$ symmetry point is shared by both halves).

We overcome this computational difficulty for these special cases by dividing the troubled numerical integration into two separate integrals that share the $\vartheta = \pi/2$ symmetry point as a common boundary. Because Romberg integration has no problems integrating to this symmetry point (as opposed to integrating through it), both of these separate integrals can be numerically evaluated without a glitch. In essence, this approach allows the routines to piecewise integrate the spheroidal angle function over any given interval without ever having to pass through this menacing point. For obvious reasons, only a single integral must be evaluated for cases where both boundaries lie in the same half of the $0 \le \vartheta \le \pi$ domain.

When considering the special class of intervals where the boundaries ϑ_{lw} and ϑ_{up} are equidistant from the $\vartheta = \pi/2$ symmetry point and lie in different halves of the $0 \le \vartheta \le \pi$ domain, both routines exploit the symmetries of the spheroidal angle functions to reduce the computation time of the overall integration. If the spheroidal angle function happens to be even, only one of the two separate integrals (i.e., for the piecewise integration) needs to be computed because the overall integration is then found by

doubling the results. When the spheroidal angle function is odd, no calculations are necessary since the overall integration clearly vanishes for this special class of intervals.

As anticipated, no integral tables of the prolate and oblate spheroidal angle functions are able to be found. It is this lack of available data that prompts us to devise a computational check that is able to provide some validation of the INTPROANG (P-5) and INTOBLANG (O-5) routines. We choose to termwise integrate the expansions of (3-80a) and (3-80b) to procure an alternative, albeit much slower, approach to computing the integrals of (3-84a) and (3-84b). Essentially, Romberg integration is used to individually integrate the associated Legendre function identified with each term until convergence of the expansion is achieved. For the cases tested, results from the INTPROANG (P-5) and INTOBLANG (O-5) routines compare extremely well with those obtained using this alternative method; that is, they match one another within eleven decimal places (this level of accuracy is consistent with the fractional accuracy imposed on the Romberg integration routine).

CHAPTER 4. COMPUTER SOFTWARE BASED UPON THE NEWLY DEVELOPED NEAR-ZONE TO FAR-ZONE TRANSFORMATION PROCESS

Using the algorithms developed in Chapter 2 along with the special function routines developed in Chapter 3, we are now able to put together a software package capable of realizing the entire NZ-FZT process for both spheroidal cases. It is this stage of the project that allows our theoretical concept to emerge from the drawing board and be put into actual practice. Later on in our investigation, i.e., in the chapters that follow, we shall use the developed software to theoretically validate the overall NZ-FZT process as well as assess its computational performance. Because the software is constructed in a manner that is both generalized and computationally efficient, it has the capacity to handle a wide variety of radiation problems.

This chapter addresses the top-down design of the developed software by examining the organization and the particulars of its various constituent modules. In order to gain a broad understanding of the software without getting lost in the details, we elect to keep the discussion on a top-level by describing the entire process using pseudocode, i.e., a series of English-like statements. An additional benefit of such an approach is that it allows the computational process to be freely implemented using any structured, high-level computer language. Nevertheless, a section addressing the language and computer platform used during our investigation is included in order to provide a complete description of the software package. Finally, a memory storage technique used by the developed software to significantly improve its computational efficiency is discussed in the last section of this chapter.

4.1 OVERVIEW OF NZ-FZT COMPUTER SOFTWARE

4.1.1 Organization of Software

During the software development process, we found that using two separate computer codes to individually implement the NZ-FZT algorithms (for the prolate and oblate cases) is more practical than using one very large, all-encompassing code. Upon inspection of both algorithms (see Chapter 2), one can see that the top-level processes for both spheroidal cases are identical to each other with regard to structure, viz., memory storage formats, expansion formats, etc. As a result, both of the developed codes are very much the same with only one major difference: each code evokes a separate library of numerical routines when evaluating its respective special functions (one may recall from Chapter 3 that these numerical routines can vary significantly between the prolate and oblate cases). It is this common structure of both codes that prompts us to continue our discussion of the software package in a generalized manner; in particular, we describe both codes in terms of a generalized top-level procedure that applies to either spheroidal case. However, specific references to the pertinent algorithmic quantities, numerical routines, and special functions for each spheroidal case are included whenever applicable (using the nomenclature defined in Chapters 2 and 3).

At this point in our discussion, we feel that it is necessary to digress for a moment and reiterate that the NZ-FZT process from start-to-finish is designed to compute far-zone field quantities for a single spheroidal transformation surface. Consequently, the entire computational process must be performed each time a different transformation surface is considered. The developed software mirrors this process and handles only one spheroidal transformation surface per execution; thus, additional transformation surfaces require additional computer runs.

We now turn our attention to Figure 4.1 which uses a flowchart to depict the top-level modular design of the NZ-FZT computer codes for the prolate and oblate spheroidal transformation surfaces. Included in the flowchart for each module is a functional description along with a numerical tag. One can plainly see that the numbering of the

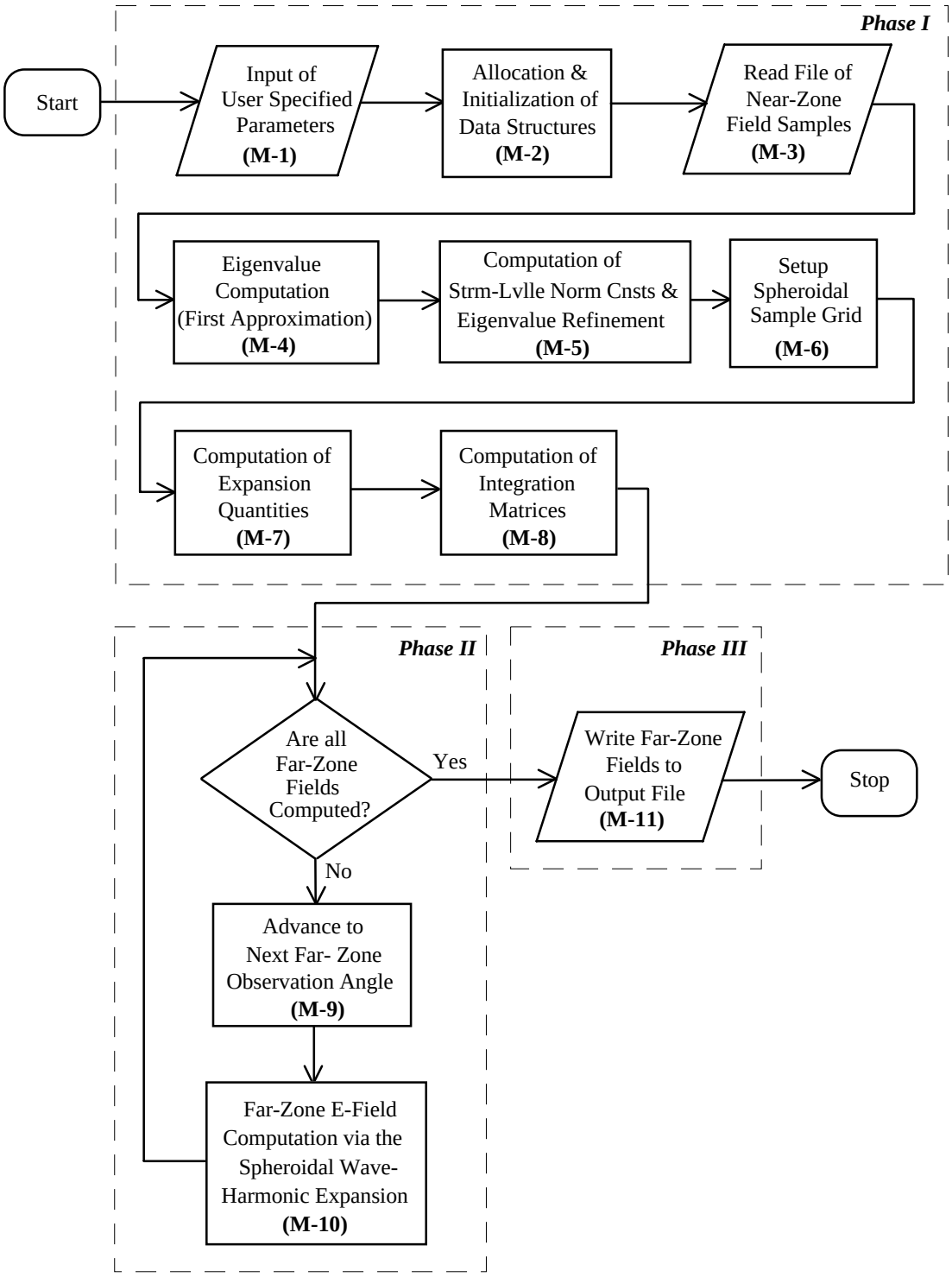

Figure 4.1 Flowchart of the NZ-FZT computer codes for the prolate and oblate spheroidal transformation surfaces.

modules corresponds to the sequential order in which they are initially encountered during the computational process. In addition, the functional descriptions of the modules are stated in pseudocode and are applicable to either spheroidal case.

The top-level modular design of both NZ-FZT computer codes is partitioned into three sequential phases so as to give us a better understanding of the developed software. As shown in Figure 4.1, Phase I is made up of the first eight modules, i.e., (M-1)-(M-8), and is executed only once for a given spheroidal transformation surface. The purpose of this phase is to take the information provided by the user and conduct the many one-time computations associated with the NZ-FZT process. Since the number of far-zone observation angles has no bearing on these one-time computations, we view the calculations of Phase I as computational overhead. In essence, the computational expense associated with these calculations is essentially fixed because it remains the same despite the number of desired far-zone field quantities. However, the computational expense contributed by Phase II does depend on the number of far-zone observation angles. The second phase consists of two modules, viz., (M-9) and (M-10), and forms a loop that must be repeated each time that a different far-zone field quantity is desired. It is this phase that accounts for most of the computation time when addressing a large number of far-zone field quantities. Lastly, Phase III is simply made up of the single module (M-11) and handles the output only after all of the desired far-zone field quantities have been computed. The computational expense contributed by this phase is relatively minor when compared to that of the previous two phases.

4.1.2 Numerical Precision

The developed software is designed to accept input data and to furnish output results with single precision. Despite this requirement, computations of the NZ-FZT process are nevertheless conducted with double precision in order to minimize the roundoff error associated with computing the spheroidal wave-harmonic expansion. Consequently, all of the software modules perform their calculations using double

precision. To meet this demand, the special function routines (developed in Chapter 3) must in turn provide double precision results to the modules. Ultimately, the NZ-FZT software rounds the final results to single precision at the conclusion of the entire process.

4.1.3 Computer Platform and Programming Language

One of our objectives is to take the developed NZ-FZT algorithms and map them to an IBM compatible personal computer. There are several distinct advantages in doing so. Just recently, personal computers have become powerful enough to host computationally intensive numerical algorithms. At present, both speed and memory storage of these machines have been steadily increasing while the base cost of these machines has continued to remain more or less the same. Accordingly, CPU time for personal computers is relatively inexpensive when compared to that of other alternative platforms, e.g., mainframes, workstations, etc. From a standpoint of availability, these machines are now much more accessible since becoming so pervasive throughout the scientific and industrial community. All things considered, the personal computer is easily the platform of choice for our specific application.

As for the programming language, we choose to implement the NZ-FZT computer software using Fortran albeit any structured, high-level language could be used (e.g., Pascal, C, etc.). The foremost reason for selecting Fortran stems from the fact that over time it has become the most commonly used programming language in the field of computational electromagnetics. Bearing this in mind, we opted to have our software conform to this industry standard.

Maintaining portability of our software also ranks high on our list of priorities. Portability between compilers can be improved by limiting the use of compiler-specific statements throughout the software. (Of course, achieving 100 percent portability is near impossible for a software project of this magnitude.) In addition, our concern extends beyond just portability of the code between compilers and addresses its portability to other structured, high-level languages. By limiting statements, control structures, and

data types that are only intrinsic to Fortran, we are able to develop a software package capable of being translated with minimal work to other structured, high-level languages. This approach gives our software the flexibility that it may need for future applications.

4.2 DESCRIPTION OF PHASE I MODULES

4.2.1 Module (M-1): Input of User Specified Parameters

By way of the computer terminal and an ASCII input file, this input module queries the user for information that is key to both ends of the NZ-FZT process (see Figure 2.3). Specifications requested through the terminal allow the software to configure the process output to that desired by the user. Meanwhile, data contained in the ASCII input file supplies the code with the necessary process input. The advantage of such an approach is that it allows the user to request a variety of output arrangements for a single input file. In addition, the information gathered by this module is also needed to internally configure the data structures necessary to implement the NZ-FZT process.

At the start of the module, the user must indicate the location of the ASCII input file by specifying its filename via the computer keyboard. Included in this input file is a header that contains parameters describing the geometry of the transformation surface as well as the configuration of the sampling scheme. The module then proceeds to open the file and read the following input parameters contained in the header: the free-space wavelength, λ_o; the focal point of the spheroidal transformation surface, a (related to independent parameter h by equation (2-32)); the radial coordinate of the spheroidal transformation surface, ξ_o; the total number of samples in the angular and azimuthal directions, I and J; and the widths of the partitioned surface elements, $\Delta\vartheta'$ and $\Delta\varphi'$. The remainder of the input file contains samples of the near-zone E-field that are to be read in by a subsequent module, viz., (M-3).

After reading the required input parameters, the code proceeds to query the user by way of the terminal for details regarding the computational process and its

corresponding output. One of the parameters that the user must provide is the degree at which he or she wants the spheroidal wave-harmonic expansion to be truncated during the computational process, viz., the parameter L of the NZ-FZT algorithms (see Tables 2.5a and 2.5b). In addition, the user must specify the desired pattern cuts of the far-zone E-field together with the preferred type of pattern normalization.

4.2.2 Module (M-2): Allocation and Initialization of Data Structures

The purpose of this housekeeping module is to first configure and then zero-initialize all data structures required to implement the NZ-FZT process. Referring to Tables 2.5a and 2.5b, one can see that the memory storage format of the data structures is dependent on the input parameters I, J, and L. However, it is the amount of available memory that dictates the maximum allowable size of these data structures (that is, assuming no software limitations are imposed by the compiler or the operating system). Thus, it is the memory capacity of the host platform that is the limiting factor when considering extremely fine sampling of the spheroidal transformation surface or a large number of orders and degrees for the spheroidal wave-harmonic expansion.

At the start of each run, this module employs dynamic memory allocation to configure all of the data structures to the exact size needed. The main advantage of using dynamic allocation over fixed allocation is that it enables the software to automatically manage the available memory. As a result, the code need not be recompiled every time the problem under consideration is larger than the present configuration or if the software is ported to a machine with a different memory capacity. Furthermore, by customizing the data structures to each problem under consideration, the software is able to make the most of the available memory resources.

4.2.3 Module (M-3): Read File of Near-Zone Field Samples

Having configured and initialized all of the necessary data structures, the code is now ready to read the remainder of the ASCII input file. This input module proceeds to

read in the near-zone E-field samples along the spheroidal transformation surface, i.e., $E_x(\vartheta_i', \varphi_j')$, $E_y(\vartheta_i', \varphi_j')$, and $E_z(\vartheta_i', \varphi_j')$, and then to place them in their respective data structures. We recall from Chapter 2 that each of these samples represents a Cartesian vector component in complex phasor form. The input samples are converted from single to double precision by zero-filling the additional significant figures.

4.2.4 Module (M-4): Eigenvalue Computation (First Approximation)

As indicated in Chapter 3, the first step in evaluating the prolate and oblate spheroidal wave functions is to compute their respective eigenvalues $\lambda_{m,l}(h)$ and $\lambda_{m,l}(-jh)$. Recalling from before, calculating these eigenvalues is a two-step process that initially requires a first approximation of the eigenvalue to be later refined using the Bouwkamp/Blanch method. This computational module only handles the first part of this process and produces the first approximation of all necessary eigenvalues, i.e., $\lambda_{m,l}^{(1)}(h)$ or $\lambda_{m,l}^{(1)}(-jh)$ where $(l = 0,1,\ldots,L)$ and $(m = 0,1,\ldots,l)$, by appropriately calling either the PROAPPROXEIG (P-1) or OBLAPPROXEIG (O-1) primary routine. The approximated eigenvalues are then stored in a $(L+1)\times(L+1)$ two-dimensional matrix that is subsequently refined during the execution of the next module.

4.2.5 Module (M-5): Computation of Sturm-Liouville Normalization Constants and Eigenvalue Refinement

The purpose of this computation module is essentially twofold. First, the module proceeds to compute all of the necessary Sturm-Liouville normalization constants for a given spheroidal transformation surface, i.e., $N_{m,l}(h)$ or $N_{m,l}(-jh)$ where $(l = 0,1,\ldots,L)$ and $(m = 0,1,\ldots,l)$, by appropriately evoking either the PRONORMCNSTS (P-2) or OBLNORMCNSTS (O-2) primary routine. These computed normalization constants are then stored in a $(L+1)\times(L+1)$ two-dimensional matrix that uses zero-fill for elements not having a corresponding normalization constant. Second, by way of performing these

calculations, the module proceeds to also refine the eigenvalue matrix (i.e., initially computed by the previous module), thus obtaining the necessary values of $\lambda_{m,l}(h)$ or $\lambda_{m,l}(-jh)$ (see Chapter 3). These refined eigenvalues are then used for the remainder of the NZ-FZT process.

4.2.6 Module (M-6): Setup Spheroidal Sample Grid

This computation module uses information provided in the header of the ASCII input file to calculate the samples points $(\vartheta_i', \varphi_j')$ along the spheroidal transformation surface in radian measure. The total number of samples in the angular and azimuthal directions (i.e., I and J, respectively) and the widths of the partitioned surface elements (i.e., $\Delta\vartheta'$ and $\Delta\varphi'$) are used with (2-107a) and (2-109a) to determine the spheroidal sample grid. These sample points coincide with the near-zone E-field samples provided by the ASCII input file.

4.2.7 Module (M-7): Computation of Expansion Quantities

The next step in the NZ-FZT process is to compute the following quantities associated with the spheroidal wave-harmonic expansion: $C1$, $\left[C2_l^P\right]$, and $\left[C3_{m,l}^P\right]$ for the prolate case; and $C1$, $\left[C2_l^O\right]$, and $\left[C3_{m,l}^O\right]$ for the oblate case. Tables 2.5a and 2.5b summarize the specifics regarding the computation and memory storage format of these quantities. In order to carry out these calculations, this module utilizes the respective Sturm-Liouville normalization constants together with the corresponding spheroidal radial functions of the fourth kind. At this point in the process, the normalization constants have already been computed and stored by the (M-5) software module. As for the required spheroidal radial functions, either PRORADIAL (P-3) or OBLRADIAL (O-3) supplies the necessary function evaluations.

4.2.8 Module (M-8): Computation of Integration Matrices

The final step of Phase I is to compute the following integration matrices of the spheroidal wave-harmonic expansion: $\left[IS^{P}_{0,l,i}\right]$ and $\left[IS^{P}_{m,l,i}\right]$ for the prolate case; and $\left[IS^{O}_{0,l,i}\right]$ and $\left[IS^{O}_{m,l,i}\right]$ for the oblate case. Details regarding the definition and memory storage format of these quantities are summarized in Tables 2.5a and 2.5b. We recall from Chapter 2 that each element of these matrices is related to the integration of a particular spheroidal angle function (indexed by *m* and *l*) over a given interval. In turn, these intervals correspond to a partition of the spheroidal transformation surface in the angular dimension (indexed by *i*). Accordingly, the integration matrices are computed (and filled) by individually evoking the appropriate integration routine, i.e., INTPROANG (P-5) or INTOBLANG (O-5), for all values of *m*, *l*, and *i*.

As discussed in Chapter 3 (see 3.7.1), both spheroidal angle functions exhibit even or odd symmetry over the $0 \le \vartheta \le \pi$ domain (i.e., about the $\vartheta = \pi/2$ symmetry point) based on whether $(l-m)$ is even or odd. In addition, the spheroidal transformation surface is uniformly partitioned in the angular dimension so that the resulting intervals in the upper-half of the spheroid (i.e., $[0,\pi/2]$) mirror those in the lower-half (i.e., $[\pi/2,\pi]$). Under these conditions, each of the integration matrices exhibits some form of combined symmetry. In the cases where the spheroidal angle function is even (i.e., when $(l-m)$ even), corresponding upper- and lower-half matrix elements are equivalent, viz., $IS^{P}_{m,l,i} = IS^{P}_{m,l,I+1-i}$ where $i = 1,2,\ldots,Int[(I+1)/2]$. Likewise, when the spheroidal angle function is odd (i.e., when $(l-m)$ odd), corresponding upper- and lower-half matrix elements are the same magnitude with a sign reversal, viz., $IS^{P}_{m,l,i} = -IS^{P}_{m,l,I+1-i}$ where $i = 1,2,\ldots,Int[(I+1)/2]$. By taking advantage of these symmetries, this module is able to cut the overall computation time roughly in half. Note that during the instances when the total number of partitions *I* is odd, the reduction

in the number of computations is a little less than a half because the middle partition, i.e., $i = (I+1)/2$, does not have a symmetrical counterpart.

4.3 DESCRIPTION OF PHASE II MODULES

4.3.1 Module (M-9): Advance to Next Far-Zone Observation Angle

The purpose of Phase II is to calculate the desired far-zone E-field response using the near-zone sample data together with the quantities computed during the first phase. As the first part of the Phase II loop, this module determines the sequence of observation angles (θ,φ) required to obtain the desired far-zone E-field pattern cuts. For each iteration of the loop, the next observation angle (θ,φ) in the sequence is fed to the second part of the loop that actually computes the far-zone E-field, viz., module (M-10). Module (M-9) also supplies the trigonometric constants associated with the coordinate transformation of (2-127) and (2-128) for each observation angle (θ,φ).

4.3.2 Module (M-10): Far-Zone E-Field Computation via the Spheroidal Wave-Harmonic Expansion

This second and final part of the Phase II loop computes the far-zone E-field for a particular observation angle (θ,φ) by employing the appropriate spheroidal wave-harmonic expansion (i.e., either prolate or oblate). We recall from Chapter 2 that the NZ-FZT process requires the overall expansion, i.e., either (2-124a) or (2-124b), to be individually evaluated for each Cartesian component of the E-field. Correspondingly, this computational module must evaluate three distinct expansions by individually employing each component of the near-zone field samples, viz., $E_x(\vartheta_i',\varphi_j')$, $E_y(\vartheta_i',\varphi_j')$, and $E_z(\vartheta_i',\varphi_j')$, as either $f_{i,j}^{P}$ or $f_{i,j}^{O}$; see (2-126a) and (2-126b). The results of these expansions yield all three Cartesian components of the far-zone E-field, viz., $\overline{E}_{fz_x}(\theta,\varphi)$, $\overline{E}_{fz_y}(\theta,\varphi)$, and $\overline{E}_{fz_z}(\theta,\varphi)$; see (2-125a) and (2-125b).

From a computational viewpoint, the manner in which these three expansions are evaluated can have a serious impact on the total computation time. As always, the issue at hand once again becomes an engineering tradeoff of computational efficiency versus memory storage. For a fixed amount of memory, the computational speed of the NZ-FZT process can be increased only at the expense of decreasing the maximum allowable problem size. In short, the computational efficiency is improved by storing intermediate results in order to minimize redundant calculations. However, storage of these intermediate results can be quite memory intensive depending upon the size of the problem under consideration. Because our goal is to put together a software package able to address as many realistic radiation problems as possible, we opt to implement all three expansions in a fashion that generally favors maximum allowable problem size over computational speed.

On the whole, the three expansions (corresponding to each Cartesian component) are implemented as they are written in (2-124a) and (2-124b). Yet, to reduce redundant calculations, we do take advantage of the fact that all three expansions share the same expansion coefficients, viz., the bracketed terms of (2-124a) and (2-124b). To minimize memory storage, this module computes the corresponding bracketed term on-the-fly and separately applies it to each of the samples $E_x(\vartheta_i', \varphi_j')$, $E_y(\vartheta_i', \varphi_j')$, and $E_z(\vartheta_i', \varphi_j')$; the results each contribute to their respective running summation (over the indices *i* and *j*).

Since the one-dimensional summation included in the bracketed term (over the degrees $l = 0,1,\ldots,L$) is only dependent on the index *i*, we are able to eliminate other redundant computations by using a simple storage scheme. By looping over all values of *j* for a given index *i*, the module buffers on-the-fly the part of the bracketed term that corresponds to the one-dimensional summation. Thus, all of the bracketed terms for a given index *i* can be computed without continually having to recompute this one-dimensional summation. The overall process is repeated over all values of *j* until contributions from all near-zone E-field samples have been included. When computing the bracketed term, the module evaluates the necessary prolate or oblate spheroidal angle functions by appropriately evoking either PROANG (P-4) or OBLANG (O-4). After

computing the far-zone E-field in Cartesian coordinates, module (M-10) then applies the coordinate transformation of (2-127) and (2-128) to yield the desired end-product for a given observation angle: the far-zone E-field in spherical coordinates with suppressed radial dependence, viz., $\overline{E}_{fz_\theta}(\theta,\varphi)$ and $\overline{E}_{fz_\varphi}(\theta,\varphi)$.

4.4 DESCRIPTION OF PHASE III MODULE

4.4.1 Module (M-11): Write Far-Zone Fields to Output File

After Phase II computes the desired far-zone E-field response, this single module phase applies the proper normalization (if any) to the computed results, i.e., $\overline{E}_{fz_\theta}(\theta,\varphi)$ and $\overline{E}_{fz_\varphi}(\theta,\varphi)$, and writes them to an ASCII output file. The choice of pattern normalization is specified by the user during the (M-1) input module and includes the following: (1) no normalization; (2) normalization with respect to the θ-component, $\left|\overline{E}_{fz_\theta}\right|$; (3) normalization with respect to the φ-component, $\left|\overline{E}_{fz_\varphi}\right|$; and (4) normalization with respect to the total magnitude, $\sqrt{\left|\overline{E}_{fz_\theta}\right|^2+\left|\overline{E}_{fz_\varphi}\right|^2}$. Since the far-zone E-field components are complex quantities, the ASCII output file expresses them in terms of both polar and rectangular formats.

4.5 IMPROVEMENT OF COMPUTATIONAL EFFICIENCY

4.5.1 Implementation of Memory Caching Technique

As we have just seen, the implementation of the overall NZ-FZT process is quite involved. The developed software package must go through a multitude of floating-point operations in order to arrive at the final results. Accordingly, we searched for additional ways to reduce the number of computations without seriously impacting the available

memory. After examining the manner in which the modules interface with the developed special function routines of Chapter 3, we are able to devise a memory storage technique that significantly improves the computational efficiency of both spheroidal codes.

The developed technique makes use of the fact that certain special functions utilize redundant sets of computed data at some points during the evaluation process. By buffering this common data, the software is able to eliminate a significant amount of floating-point operations. However, storage of this large amount of data will naturally have a negative impact on the overall memory capacity. In order to circumvent this difficulty, both codes have been designed to take advantage of the sequence in which their special function routines are called. The approach requires only one set of redundant data to be buffered at any point in the computational process. Using this buffered data, the software then proceeds to compute all of the connected special functions before computing and storing the next set of redundant data. With this technique, we are able to reduce the number of floating-point operations without seriously impacting the amount of available memory. However, the modules now have to be smart about the order in which they call these particular special function routines.

Inserted in these specific primary routines is a memory caching mechanism that stores the relevant data upon exit of the routine. Computation of this data is intrinsically based on some of the arguments passed to the numerical routine. Upon a subsequent call, each of these routines proceeds to compare the relevant arguments with those from the last call: in the instances where these arguments differ, the routine recomputes the necessary data; in the instances where these arguments match, the routine skips these lengthy computations and uses the data buffered from the previous call. As one can see, the technique is not very memory intensive because it only requires the code to buffer the relevant data one-step back. The specific primary routines able to take advantage of this technique consist of the following: PRORADIAL (P-3), OBLRADIAL (O-3), PROANG (P-4), and OBLANG (O-4).

In the case of PRORADIAL (P-3), the data from both families of spherical Bessel and spherical Neumann functions is buffered to speed up the computations of equations

(3-16)-(3-19). Since both of these families are evaluated for the single argument $h\xi_o$ and the software only addresses a single transformation surface at a time, these calculations are only performed once for a given computational run. In addition, this routine also buffers the associated Legendre functions of the first and second kind together with their first derivatives in order to reduce the number of computations associated with (3-20) and (3-21). It is important to note that all of the associated Legendre function data is based on a given order *m* and independent parameter *h*. Accordingly, module (M-7) is able to employ the memory caching technique to speed up the evaluation of expansion quantities that include the prolate spheroidal radial function: $\left[C2_l^P\right]$ and $\left[C3_{m,l}^P\right]$ (see Table 2.5a). However, this is where the software module must be smart about the sequential order in which it evokes PRORADIAL (P-3). The associated Legendre function data has to be recalculated every time a call to PRORADIAL (P-3) uses a given order *m* that differs from the one used during the previous call. In order to take advantage of the memory caching technique, module (M-7) must compute $\left[C2_l^P\right]$ and $\left[C3_{m,l}^P\right]$ by evaluating row-by-row the elements that correspond to all degrees of *l* for a given order *m* (this is done by using a nested loop with the degree *l* as the index for the internal loop).

As for OBLRADIAL (O-3), it employs the memory caching technique in much of the same way as its prolate counterpart. It too buffers the data from both families of spherical Bessel and spherical Neumann functions to speed up its respective computations, i.e., equations (3-56)-(3-59). However, this routine only has to buffer the associated Legendre functions of the second kind in order to reduce the number of computations associated with the Baber and Hasse approach, i.e., equations (3-60)-(3-63). In a manner that is identical to the prolate case, module (M-7) is also able to employ the memory caching technique to speed up the evaluation of expansion quantities that include the oblate spheroidal radial function: $\left[C2_l^O\right]$ and $\left[C3_{m,l}^O\right]$ (see Table 2.5b).

The primary routines PROANG (P-4) and OBLANG (O-4) make use of the memory caching technique to buffer their respective expansion coefficients $d_r^{m,l}(h)$ and

$d_r^{m,l}(-jh)$ for a given order *m*, degree *l*, and independent parameter *h*. By storing this data at the end of these routines, the software is able to significantly reduce the number of floating-point operations associated with the computation of the integration matrices: $\left[IS_{0,l,i}^{P}\right]$ and $\left[IS_{m,l,i}^{P}\right]$ for the prolate case; $\left[IS_{0,l,i}^{O}\right]$ and $\left[IS_{m,l,i}^{O}\right]$ for the oblate case. Module (M-8) computes these quantities by evoking the appropriate integration routine, i.e., INTPROANG (P-5) or INTOBLANG (O-5), for all values of *m*, *l*, and *i*. Each time a different pair of *m* and *l* is considered, these routines repeatedly evaluate the same spheroidal angle function in order to carry out the numerical integration. Although the angular parameter differs for each of these successive function evaluations, the expansion coefficients, i.e., $d_r^{m,l}(h)$ and $d_r^{m,l}(-jh)$, of (3-80a) and (3-80b) remain the same. As a result, the technique considerably speeds up the integration processes of INTPROANG (P-5) and INTOBLANG (O-5). However, in order to take full advantage of the memory caching technique (in this regard), module (M-8) should compute group-by-group the elements of the integration matrices that correspond to all values of *i* for a given order *m* and degree *l*.

CHAPTER 5. PROOF-OF-CONCEPT VIA AN ANALYTICAL BENCHMARK

In the preceding chapters, we fully disclose the details of the newly developed NZ-FZT process as well as the particulars necessary to put together a software package capable of carrying out its implementation. In keeping with the scientific method, the next step in the development process is to demonstrate the validity and viability of these new computational algorithms. This chapter addresses the first step in this validation process and consists of using a well-characterized radiation structure as an analytical benchmark. By applying the algorithms to a radiating structure with known near- and far-zone E-fields, we are able to setup and conduct multiple numerical tests that serve as a proof-of-concept for the newly developed NZ-FZT process.

Our first task at hand involves the choice of radiation structure to use as the analytical benchmark. Although the far-zone is often well-characterized for many realistic radiation structures, the near-zone is ordinarily only approximately understood. For our purposes, we want an analytical benchmark where the field quantities are exactly known in both the near- and far-zone regions. After searching, we are able to find such a radiating structure: a filament dipole with sinusoidal current distribution. Fortunately, Balanis [27] derives and presents an exact closed form representation for the surrounding E-field of this radiating structure (z-directed) that is valid everywhere including the near-zone. It is these exact field equations (after some manipulation) that are used to mathematically represent the analytical benchmark during our proof-of-concept experiments. Finally, in order to conduct these numerical experiments, we must create a software driver capable of sampling the near-zone of the analytic benchmark and then generating the corresponding ASCII input file required by the NZ-FZT software package. Comparisons of the algorithmic results are then made with their theoretically computed counterparts to assess the overall performance of the newly developed NZ-FZT process.

5.1 EXACT E-FIELD SURROUNDING A FILAMENT DIPOLE

5.1.1 Near-Zone E-Field

In defining the exact E-field for a filament dipole of length *l*, we choose to present the corresponding field equations in Cartesian form because it is the most suitable for our particular application. As described in Chapter 2, the NZ-FZT process input requires the near-zone E-field samples (situated along the spheroidal transformation surface) to be in vector Cartesian form, i.e., $E_x(\vartheta_i', \varphi_j')$, $E_y(\vartheta_i', \varphi_j')$, and $E_z(\vartheta_i', \varphi_j')$. Although the E-field must be sampled at specific points in the respective spheroidal coordinate system, viz., $(\vartheta_i', \varphi_j')$, defining the equations in terms of Cartesian parameters fortunately does not present any difficulties. In short, the spheroidal sample grid is easily converted to Cartesian coordinates by using the respective prolate or oblate spheroidal coordinate transformation, i.e., equations (2-1)-(2-5). After mathematically manipulating the exact field equations that are provided by Balanis [27], we obtain the following closed form representation for the near-zone E-field of a z-directed filament dipole with sinusoidal current distribution:

$$E_x(x_\lambda, y_\lambda, z_\lambda) = j\eta_o \frac{I_o}{4\pi\lambda_o}\left(\frac{x_\lambda}{x_\lambda^{\,2} + y_\lambda^{\,2}}\right)\times\left[\begin{array}{l}(z_\lambda - l_\lambda/2)\dfrac{e^{-j2\pi R1_\lambda(x_\lambda, y_\lambda, z_\lambda)}}{R1_\lambda(x_\lambda, y_\lambda, z_\lambda)} \\ +(z_\lambda + l_\lambda/2)\dfrac{e^{-j2\pi R2_\lambda(x_\lambda, y_\lambda, z_\lambda)}}{R2_\lambda(x_\lambda, y_\lambda, z_\lambda)} \\ -2z_\lambda \cos(l_\lambda\pi)\dfrac{e^{-j2\pi r_\lambda(x_\lambda, y_\lambda, z_\lambda)}}{r_\lambda(x_\lambda, y_\lambda, z_\lambda)}\end{array}\right] \qquad (5\text{-}1)$$

$$E_y(x_\lambda, y_\lambda, z_\lambda) = j\eta_o \frac{I_o}{4\pi\lambda_o}\left(\frac{y_\lambda}{{x_\lambda}^2 + {y_\lambda}^2}\right)\times\left[\begin{array}{l}(z_\lambda - l_\lambda/2)\dfrac{e^{-j2\pi R1_\lambda(x_\lambda, y_\lambda, z_\lambda)}}{R1_\lambda(x_\lambda, y_\lambda, z_\lambda)} \\ +(z_\lambda + l_\lambda/2)\dfrac{e^{-j2\pi R2_\lambda(x_\lambda, y_\lambda, z_\lambda)}}{R2_\lambda(x_\lambda, y_\lambda, z_\lambda)} \\ -2z_\lambda\cos(l_\lambda\pi)\dfrac{e^{-j2\pi r_\lambda(x_\lambda, y_\lambda, z_\lambda)}}{r_\lambda(x_\lambda, y_\lambda, z_\lambda)}\end{array}\right] \tag{5-2}$$

$$E_z(x_\lambda, y_\lambda, z_\lambda) = -j\eta_o \frac{I_o}{4\pi\lambda_o}\times\left[\begin{array}{l}\dfrac{e^{-j2\pi R1_\lambda(x_\lambda, y_\lambda, z_\lambda)}}{R1_\lambda(x_\lambda, y_\lambda, z_\lambda)} \\ +\dfrac{e^{-j2\pi R2_\lambda(x_\lambda, y_\lambda, z_\lambda)}}{R2_\lambda(x_\lambda, y_\lambda, z_\lambda)} \\ -2\cos(l_\lambda\pi)\dfrac{e^{-j2\pi r_\lambda(x_\lambda, y_\lambda, z_\lambda)}}{r_\lambda(x_\lambda, y_\lambda, z_\lambda)}\end{array}\right] \tag{5-3}$$

where

$$R1_\lambda(x_\lambda, y_\lambda, z_\lambda) = \sqrt{x_\lambda^2 + y_\lambda^2 + (z_\lambda - l_\lambda/2)^2} \tag{5-4}$$

$$R2_\lambda(x_\lambda, y_\lambda, z_\lambda) = \sqrt{x_\lambda^2 + y_\lambda^2 + (z_\lambda + l_\lambda/2)^2} \tag{5-5}$$

$$r_\lambda(x_\lambda, y_\lambda, z_\lambda) = \sqrt{x_\lambda^2 + y_\lambda^2 + z_\lambda^2}\ . \tag{5-6}$$

It is important to note that all spatial parameters of these equations have been normalized with respect to free-space wavelength (e.g., $x_\lambda = x/\lambda_o$). Normalizing these equations in this fashion enables our findings to be much more far-reaching because they now apply to spatial parameters that are defined relative to wavelength. In addition, the parameter η_o refers to the intrinsic impedance of free-space.

5.2 ASYMPTOTIC REDUCTION OF THE EXACT E-FIELD TO OBTAIN THE FAR-ZONE APPROXIMATION

5.2.1 Far-Zone E-Field

Although the field equations presented in (5-1)-(5-6) are valid for all regions surrounding the z-directed filament dipole, we would like to express the far-zone E-field in a form that is consistent with the NZ-FZT process output in order to facilitate our numerical studies. As indicated in Chapter 2 (see 2.1.2), the desired form of the far-zone E-field consists of expressing the field quantities in spherical coordinates (with respect to both independent coordinates and vector quantities) together with the suppression of the radial factor $\left(e^{-jkr}/r\right)$. By taking the limit as $r \to \infty$, we are able to asymptotically approximate the field equations of (5-1)-(5-6) to obtain the following representation of the far-zone E-field [27]:

$$\overline{E}_{fz_\theta}(\theta,\varphi) = j\eta_o \frac{I_o}{2\pi}\left[\frac{\cos(l_\lambda \pi \cos\theta) - \cos(l_\lambda \pi)}{\sin\theta}\right] \tag{5-7}$$

$$\overline{E}_{fz_\varphi}(\theta,\varphi) = 0\,. \tag{5-8}$$

It is this far-zone E-field representation that serves as the theoretical yardstick for which the results of the NZ-FZT process are subsequently compared.

5.3 DEVELOPMENT OF AN ANALYTICAL BENCHMARK SOFTWARE DRIVER

5.3.1 Overview of Software Driver

The developed software driver samples the near-zone E-field of the z-directed filament dipole using equations (5-1)-(5-6) and then assembles the corresponding ASCII input file necessary to run the NZ-FZT software package (see Chapter 4). By way of the computer terminal, the user specifies the spheroidal transformation surface,

corresponding sampling scheme, free-space wavelength, and length of the filament dipole. Also included in the specification of the spheroidal transformation surface is its placement relative to the center of the filament dipole; that is, the center of the spheroidal surface can be offset from that of the dipole. As we shall subsequently see, this added feature allows us to further examine the effectiveness of the developed algorithms. Lastly, it must be mentioned that for all of our numerical studies we have arbitrarily assumed an I_o of unity when defining the E-field of the filament dipole.

5.4 COMPARISON OF ALGORITHMIC RESULTS WITH THEORETICAL RESULTS

5.4.1 Centered Dipole Numerical Tests

Our first set of numerical tests consists of using a z-directed filament dipole that is centered with respect to the spheroidal transformation surface. Both spheroidal algorithms are individually examined by repeatedly applying the developed NZ-FZT process to the analytical benchmark using a family of spheroidal transformation surfaces. By comparing the computed far-zone results with those that are theoretically known, i.e., computed using equations (5-7) and (5-8), we are able to quantify the performance of both the prolate and oblate spheroidal NZ-FZT algorithms.

Throughout all of the numerical studies the length of the dipole remains the same and is always taken as a tenth of a wavelength, i.e., $l = 0.1\lambda_o$. As for the focal point of the spheroidal coordinate system, it is taken as $a = 0.1\lambda_o$ for the prolate tests and $a = 1.0\lambda_o$ for the oblate tests. For the sake of clarity, we have depicted both of these test configurations in Figures 5.1a and 5.1b. Regarding the two families of spheroidal transformation surfaces, they range in our numerical studies from $\xi_o = 1.2$ to $\xi_o = 5.0$ for the prolate case and from $\xi_o = 0.15$ to $\xi_o = 0.80$ for the oblate case. In setting up these test configurations, we must pay close attention to the position of the radiating structure relative to that of the transformation surface so as to ensure that the two do not

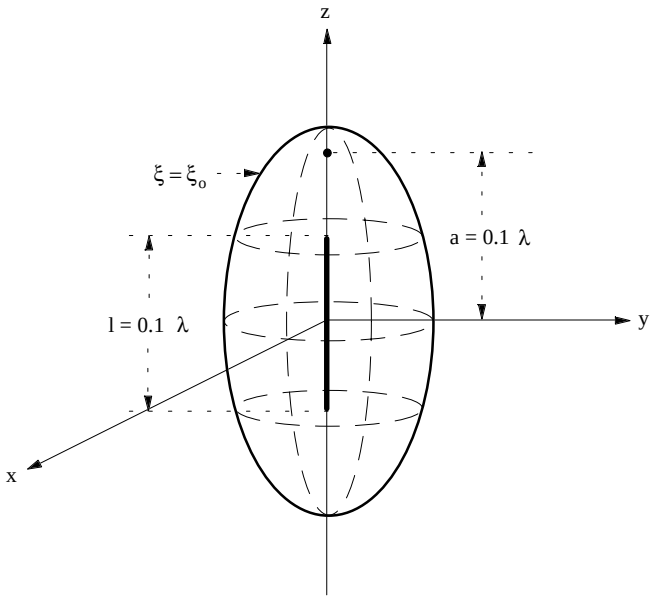

Figure 5.1a Configuration of centered dipole numerical tests for the prolate spheroidal case.

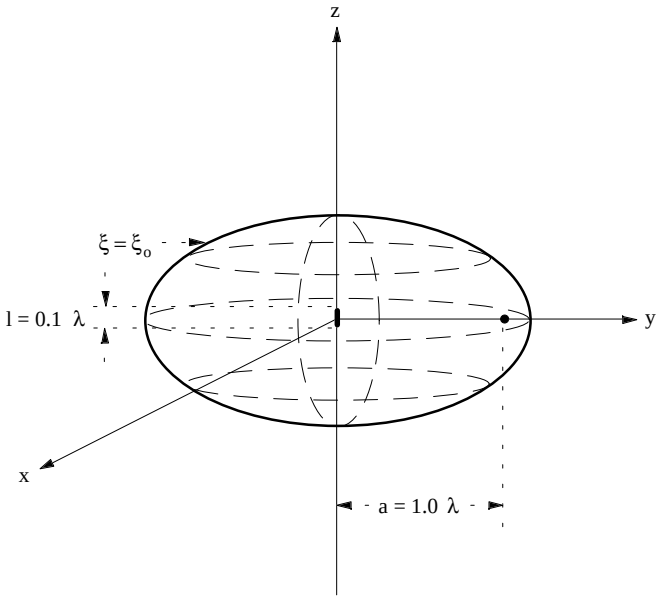

Figure 5.1b Configuration of centered dipole numerical tests for the oblate spheroidal case.

intersect. All of the numerical tests employ a uniform sample grid with 1^o intervals in both the ϑ and φ dimensions (i.e., $I \times J = 180 \times 360$). Lastly, we choose to compute the far-zone radiation patterns using 10^o increments in the θ-direction for two planar cuts: $\varphi = 0^o$ and $\varphi = 45^o$.

Having defined the configurations of the centered dipole numerical tests, we now turn our attention to assessing the performance of the developed algorithms implemented by the NZ-FZT software package. This performance evaluation is accomplished by conducting the following numerical studies: (1) an error analysis of the computed results; (2) an analysis of how well the algorithms approximate theoretical values of zero (i.e., establishing a numerical noise floor); and (3) a convergence study of the computed results. The error analysis consists of comparing the computed results with the known far-zone E-field of the centered dipole, i.e., specified by equations (5-7) and (5-8). Since the far-zone E-field is a complex quantity, it is logical to conduct the error analysis in polar form individually with respect to magnitude and phase. Because theory indicates that only the θ-component of the far-zone E-field is nonzero, we limit our error analysis to only $\overline{E}_{fz_\theta}(\theta,\varphi)$. Nevertheless, we still address its cross-polarized counterpart $\overline{E}_{fz_\varphi}(\theta,\varphi)$ by assessing how well both algorithms approximate its theoretical value of zero. In this regard, we must use this approach to evaluate the performance of the algorithms because conventional error analysis is rendered meaningless when its corresponding theoretical value vanishes. As for the convergence study, it consists of finding the value of *L* (i.e., the degree at which the spheroidal wave-harmonic expansion is truncated; see 2.3.1) where all nonzero results of $\overline{E}_{fz_\theta}(\theta,\varphi)$ have converged within single precision (i.e., between six and seven significant figures). Note that the convergence study is individually performed for each prolate and oblate spheroidal transformation surface under consideration.

For all of the error analyses, we use the following standard formula to compute the relative (or fractional) error in magnitude of $\overline{E}_{fz_\theta}(\theta,\varphi)$:

$$\text{Relative Error of } |\overline{E}_{fz_\theta}(\theta,\varphi)|\text{(ppm)} = \frac{|computed - theoretical|}{theoretical} \times 10^6 . \qquad (5\text{-}9)$$

As we shall see, we choose to express the relative error in parts per million (ppm) as opposed to percent (%) because it more fittingly describes the results of our numerical tests. Regarding the phase error of $\overline{E}_{fz_\theta}(\theta,\varphi)$, it is computed in terms of degrees as follows:

$$\text{Phase Error of } \angle\overline{E}_{fz_\theta}(\theta,\varphi)\text{ (deg)} = |computed - theoretical| . \qquad (5\text{-}10)$$

Using formulas (5-9) and (5-10) together with the results of the centered dipole numerical tests, we conduct the error analysis for both spheroidal cases. Presented in Tables 5.1a and 5.1b is a compilation of the findings. It is at this point that we would like to emphasize that our error analysis makes use of computed and theoretical data that are unnormalized with respect to both magnitude and phase; more precisely, unnormalized figures computed by the NZ-FZT algorithms are compared directly to those found using the theoretical expressions of (5-7) and (5-8).

Upon review of the compiled error analysis data, one can see that each algorithm delivers the same performance (with respect to itself) when predicting the E-field in the upper hemisphere of the far-zone as compared to that of the lower hemisphere. Furthermore, the performance of each algorithm is also the same when computing its respective far-zone E-field for both the $\varphi = 0^o$ and $\varphi = 45^o$ planar cuts. Both of these observations are exactly what should be expected for such a problem setup that has angular and azimuthal (rotational) symmetry. From a quantitative perspective, the worst

Table 5.1a Comparison of Prolate Spheroidal NZ-FZT Algorithmic Results with Theoretical Results for the Filament Dipole of $l_\lambda = 0.1$ (Centered with Respect to Transformation Surface): $\varphi = 0^o$ and 45^o

$l_\lambda = 0.1;\ a_\lambda = 0.1;$ $I \times J = 180 \times 360;$ $\Delta\vartheta' = \Delta\varphi' = 1^o$		Relative Error of $\lvert\overline{E}_{fz_\theta}(\theta,\varphi)\rvert$ (ppm) and Phase Error of $\angle\overline{E}_{fz_\theta}(\theta,\varphi)$ (deg) where $\varphi = <\begin{matrix}0^o\\45^o\end{matrix}$								
Prolate ξ_o	Convrgce L	$\theta = 10^o$ $\theta = 170^o$	$\theta = 20^o$ $\theta = 160^o$	$\theta = 30^o$ $\theta = 150^o$	$\theta = 40^o$ $\theta = 140^o$	$\theta = 50^o$ $\theta = 130^o$	$\theta = 60^o$ $\theta = 120^o$	$\theta = 70^o$ $\theta = 110^o$	$\theta = 80^o$ $\theta = 100^o$	$\theta = 90^o$
1.2	6	7 ppm; 0.0012 deg	7 ppm; 0.0012 deg	8 ppm; 0.0012 deg	9 ppm; 0.0012 deg	9 ppm; 0.0012 deg	10 ppm; 0.0012 deg	11 ppm; 0.0012 deg	11 ppm; 0.0012 deg	11 ppm; 0.0012 deg
1.5	6	8 ppm; 0.0012 deg	7 ppm; 0.0012 deg	6 ppm; 0.0012 deg	5 ppm; 0.0012 deg	3 ppm; 0.0012 deg	2 ppm; 0.0012 deg	< 1 ppm; 0.0012 deg	1 ppm; 0.0013 deg	1 ppm; 0.0013 deg
2.0	6	22 ppm; 0.0010 deg	21 ppm; 0.0010 deg	19 ppm; 0.0010 deg	17 ppm; 0.0010 deg	15 ppm; 0.0010 deg	13 ppm; 0.0010 deg	11 ppm; 0.0011 deg	10 ppm; 0.0011 deg	9 ppm; 0.0011 deg
3.0	6	32 ppm; 0.0008 deg	31 ppm; 0.0008 deg	29 ppm; 0.0008 deg	26 ppm; 0.0008 deg	24 ppm; 0.0008 deg	21 ppm; 0.0007 deg	19 ppm; 0.0007 deg	18 ppm; 0.0007 deg	17 ppm; 0.0007 deg
4.0	6	35 ppm; 0.0006 deg	34 ppm; 0.0006 deg	32 ppm; 0.0006 deg	30 ppm; 0.0006 deg	27 ppm; 0.0006 deg	24 ppm; 0.0006 deg	22 ppm; 0.0006 deg	21 ppm; 0.0005 deg	21 ppm; 0.0005 deg
5.0	6	37 ppm; 0.0005 deg	36 ppm; 0.0005 deg	34 ppm; 0.0005 deg	31 ppm; 0.0005 deg	29 ppm; 0.0005 deg	26 ppm; 0.0005 deg	24 ppm; 0.0004 deg	23 ppm; 0.0004 deg	22 ppm; 0.0004 deg

Table 5.1b Comparison of Oblate Spheroidal NZ-FZT Algorithmic Results with Theoretical Results for the Filament Dipole of $l_\lambda = 0.1$ (Centered with Respect to Transformation Surface): $\varphi = 0^o$ and 45^o

$l_\lambda = 0.1;\ a_\lambda = 1.0;$ $I \times J = 180 \times 360;$ $\Delta\vartheta' = \Delta\varphi' = 1^o$		Relative Error of $\lvert\overline{E}_{fz_\theta}(\theta,\varphi)\rvert$ (ppm) and Phase Error of $\angle\overline{E}_{fz_\theta}(\theta,\varphi)$ (deg) where $\varphi = <\begin{matrix}0^o\\45^o\end{matrix}$								
Oblate ξ_o	Convrgce L	$\theta = 10^o$ $\theta = 170^o$	$\theta = 20^o$ $\theta = 160^o$	$\theta = 30^o$ $\theta = 150^o$	$\theta = 40^o$ $\theta = 140^o$	$\theta = 50^o$ $\theta = 130^o$	$\theta = 60^o$ $\theta = 120^o$	$\theta = 70^o$ $\theta = 110^o$	$\theta = 80^o$ $\theta = 100^o$	$\theta = 90^o$
0.15	14	781 ppm; 0.1105 deg	826 ppm; 0.1002 deg	805 ppm; 0.0849 deg	677 ppm; 0.0679 deg	464 ppm; 0.0525 deg	225 ppm; 0.0406 deg	18 ppm; 0.0327 deg	119 ppm; 0.0283 deg	167 ppm; 0.0270 deg
0.20	14	494 ppm; 0.0527 deg	521 ppm; 0.0452 deg	505 ppm; 0.0358 deg	427 ppm; 0.0272 deg	314 ppm; 0.0209 deg	203 ppm; 0.0171 deg	118 ppm; 0.0151 deg	67 ppm; 0.0142 deg	51 ppm; 0.0139 deg
0.30	14	289 ppm; 0.0184 deg	307 ppm; 0.0138 deg	297 ppm; 0.0087 deg	254 ppm; 0.0052 deg	201 ppm; 0.0041 deg	164 ppm; 0.0047 deg	149 ppm; 0.0059 deg	147 ppm; 0.0070 deg	148 ppm; 0.0074 deg
0.40	14	207 ppm; 0.0072 deg	221 ppm; 0.0042 deg	213 ppm; 0.0009 deg	183 ppm; 0.0009 deg	151 ppm; 0.0006 deg	136 ppm; 0.0013 deg	140 ppm; 0.0037 deg	152 ppm; 0.0054 deg	157 ppm; 0.0060 deg
0.60	14	125 ppm; 0.0002 deg	135 ppm; 0.0018 deg	134 ppm; 0.0037 deg	121 ppm; 0.0044 deg	105 ppm; 0.0032 deg	102 ppm; 0.0006 deg	112 ppm; 0.0025 deg	126 ppm; 0.0048 deg	132 ppm; 0.0056 deg
0.80	14	71 ppm; 0.0027 deg	84 ppm; 0.0036 deg	94 ppm; 0.0047 deg	94 ppm; 0.0048 deg	87 ppm; 0.0036 deg	84 ppm; 0.0010 deg	89 ppm; 0.0021 deg	98 ppm; 0.0044 deg	102 ppm; 0.0053 deg

case magnitude and phase error for our centered dipole numerical tests is as follows: (a) prolate, 37 ppm and 0.0013 deg; (b) oblate, 826 ppm and 0.1105 deg. Moreover, the prolate algorithm converges more rapidly than the oblate algorithm for this particular radiating structure, i.e., L=6 for the prolate numerical tests as compared to L=14 for the oblate numerical tests.

Further inspection of Tables 5.1a and 5.1b reveals that the error analysis does not include performance of the algorithms at the far-zone observation angles $\theta = 0^o$ and $\theta = 180^o$. These particular observation angles have been omitted because the far-zone E-field pattern possesses a null at these points; as a result, the relative error in magnitude becomes a meaningless quantity at these observation angles (i.e., equation (5-9) becomes undefined when the value of the theoretical result vanishes). However, we do examine how well both algorithms approximate the null at these observation angles. For all of the test cases, both algorithms compute the null as values that are significantly below -120 dB from the main beam peak (i.e., which exists at $\theta = 90^o$). Regarding the cross-polarized far-zone E-field, both algorithms compute the theoretical zero of $\overline{E}_{fz_\varphi}(\theta,\varphi)$ as values that are also well below -120 dB from the main beam peak. In all of the instances where we examine how well the algorithms approximate the theoretical value of zero, the corresponding phase is ignored because it essentially represents some form of numerical phase noise.

5.4.2 Offset Dipole Numerical Tests

Having investigated how well the developed NZ-FZT algorithms address a problem setup that has both angular and azimuthal (rotational) symmetry, we would now like to assess their performance when considering an asymmetric problem. Fortunately, we can use the same analytical benchmark to generate such a test problem by simply offsetting the dipole with respect to the spheroidal transformation surface. By doing so, both algorithms must now address a near-zone E-field that is no longer symmetrically

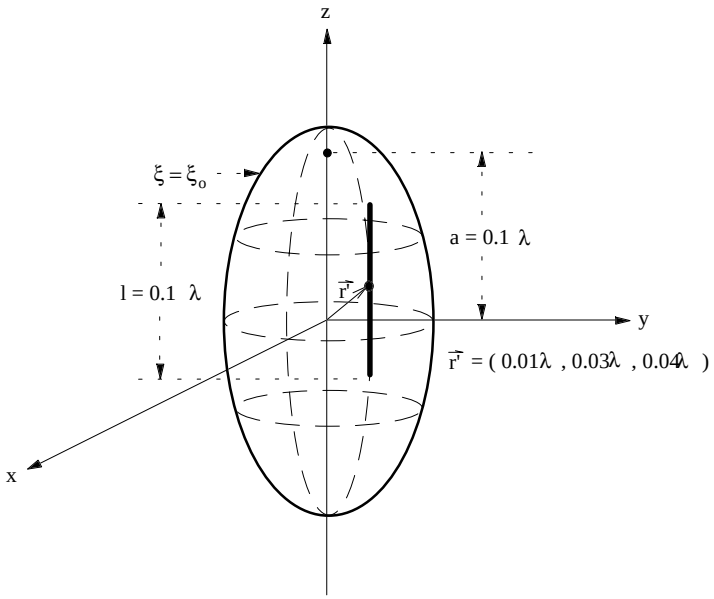

Figure 5.2a Configuration of offset dipole numerical tests for the prolate spheroidal case.

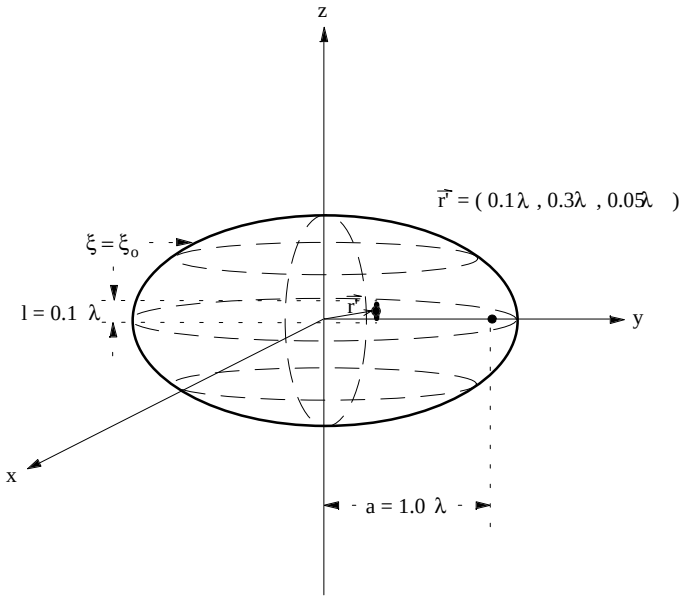

Figure 5.2b Configuration of offset dipole numerical tests for the oblate spheroidal case.

distributed over the spheroidal transformation surface. Consequently, it is specifically for this purpose that the dipole offset feature has been added to our analytical benchmark software driver (see 5.3.1).

In order to maintain a basis for comparison, we shall keep the parameters and test cases of the offset dipole numerical tests the same as those that are used for the centered dipole numerical tests. Essentially, the offset tests are identical to the centered tests with the only exception being the placement of the dipole. For these offset dipole numerical tests, the center of the dipole is translated from the center of the spheroidal transformation surface by the following offset vector: (a) $\vec{r}\,' = (x' = 0.01\lambda_o,\ y' = 0.03\lambda_o,\ z' = 0.04\lambda_o)$ for the prolate tests; (b) $\vec{r}\,' = (x' = 0.1\lambda_o,\ y' = 0.3\lambda_o,\ z' = 0.05\lambda_o)$ for the oblate tests. Portrayed in Figures 5.2a and 5.2b are the configurations of the offset dipole numerical tests for both spheroidal cases. Note that the offset in the x- and y-directions removes the azimuthal symmetry while the offset in the z-direction eliminates the angular symmetry. Once again we have ensured that the dipole and the spheroidal transformation surface do not intersect for any of the test cases.

Evaluating the performance of the NZ-FZT algorithms for the offset dipole numerical tests is done in the same way as that which is done for the centered dipole numerical tests. This time the error analysis consists of comparing the computed results with the known far-zone E-field of the offset dipole. Basic radiation theory indicates that the magnitude of the far-zone E-field remains unchanged for the offset dipole configuration when compared to that of the centered dipole configuration. As a result, the magnitude of equation (5-7) is still used directly to determine the theoretical data necessary to conduct the error analysis for the offset dipole numerical tests. However, the same basic radiation theory also indicates that the corresponding phase of the far-zone E-field differs between the offset and centered dipole configurations. Using the parallel ray approximation that is so often evoked in basic antenna theory (see Stutzman and Thiele [26]), one can show that the phase difference between the two dipole configurations is

Table 5.2a Comparison of Prolate Spheroidal NZ-FZT Algorithmic Results with Theoretical Results for the Filament Dipole of $l_\lambda = 0.1$ (Offset with Respect to Transformation Surface): $\varphi = 0^o$

Offset: $(x'_\lambda, y'_\lambda, z'_\lambda) = (0.01, 0.03, 0.04)$

$l_\lambda = 0.1;\ a_\lambda = 0.1;$ $I \times J = 180 \times 360;$ $\Delta\vartheta' = \Delta\varphi' = 1^o$		Relative Error of $\lvert\overline{E}_{fz_\theta}(\theta,\varphi)\rvert$(ppm) and Phase Error of $\angle\overline{E}_{fz_\theta}(\theta,\varphi)$ (deg) where $\varphi = 0^o$								
Prolate ξ_o	Convrgce L	$\theta = 10^o$	$\theta = 20^o$	$\theta = 30^o$	$\theta = 40^o$	$\theta = 50^o$	$\theta = 60^o$	$\theta = 70^o$	$\theta = 80^o$	$\theta = 90^o$
1.2	7	70 ppm; 0.0081 deg	50 ppm; 0.0044 deg	42 ppm; 0.0032 deg	38 ppm; 0.0026 deg	35 ppm; 0.0023 deg	32 ppm; 0.0021 deg	30 ppm; 0.0020 deg	28 ppm; 0.0020 deg	26 ppm; 0.0020 deg
1.5	7	9 ppm; 0.0063 deg	9 ppm; 0.0039 deg	10 ppm; 0.0031 deg	11 ppm; 0.0026 deg	12 ppm; 0.0023 deg	12 ppm; 0.0021 deg	13 ppm; 0.0019 deg	12 ppm; 0.0018 deg	11 ppm; 0.0017 deg
2.0	7	27 ppm; 0.0035 deg	20 ppm; 0.0024 deg	17 ppm; 0.0020 deg	13 ppm; 0.0017 deg	11 ppm; 0.0015 deg	8 ppm; 0.0014 deg	7 ppm; 0.0013 deg	5 ppm; 0.0013 deg	5 ppm; 0.0012 deg
3.0	7	41 ppm; 0.0016 deg	35 ppm; 0.0011 deg	31 ppm; 0.0009 deg	28 ppm; 0.0008 deg	24 ppm; 0.0007 deg	22 ppm; 0.0007 deg	19 ppm; 0.0007 deg	18 ppm; 0.0007 deg	17 ppm; 0.0007 deg
4.0	7	43 ppm; 0.0009 deg	38 ppm; 0.0006 deg	35 ppm; 0.0005 deg	32 ppm; 0.0004 deg	28 ppm; 0.0004 deg	26 ppm; 0.0004 deg	23 ppm; 0.0004 deg	22 ppm; 0.0004 deg	21 ppm; 0.0005 deg
5.0	7	43 ppm; 0.0006 deg	39 ppm; 0.0003 deg	36 ppm; 0.0003 deg	33 ppm; 0.0002 deg	30 ppm; 0.0002 deg	27 ppm; 0.0002 deg	25 ppm; 0.0003 deg	24 ppm; 0.0003 deg	23 ppm; 0.0004 deg

Table 5.2a (cont.) Comparison of Prolate Spheroidal NZ-FZT Algorithmic Results with Theoretical Results for the Filament Dipole of $l_\lambda = 0.1$ (Offset with Respect to Transformation Surface): $\varphi = 0^o$

Offset: $(x'_\lambda, y'_\lambda, z'_\lambda) = (0.01, 0.03, 0.04)$

$l_\lambda = 0.1;\ a_\lambda = 0.1;$ $I \times J = 180 \times 360;$ $\Delta\vartheta' = \Delta\varphi' = 1^o$		Relative Error of $\lvert\overline{E}_{fz_\theta}(\theta,\varphi)\rvert$(ppm) and Phase Error of $\angle\overline{E}_{fz_\theta}(\theta,\varphi)$ (deg) where $\varphi = 0^o$								
Prolate ξ_o	Convrgce L	$\theta = 90^o$	$\theta = 100^o$	$\theta = 110^o$	$\theta = 120^o$	$\theta = 130^o$	$\theta = 140^o$	$\theta = 150^o$	$\theta = 160^o$	$\theta = 170^o$
1.2	7	26 ppm; 0.0020 deg	23 ppm; 0.0020 deg	21 ppm; 0.0021 deg	19 ppm; 0.0022 deg	17 ppm; 0.0024 deg	14 ppm; 0.0027 deg	11 ppm; 0.0030 deg	4 ppm; 0.0037 deg	16 ppm; 0.0058 deg
1.5	7	11 ppm; 0.0017 deg	10 ppm; 0.0016 deg	9 ppm; 0.0016 deg	7 ppm; 0.0016 deg	5 ppm; 0.0017 deg	3 ppm; 0.0018 deg	< 1 ppm; 0.0020 deg	2 ppm; 0.0024 deg	7 ppm; 0.0037 deg
2.0	7	5 ppm; 0.0012 deg	6 ppm; 0.0012 deg	7 ppm; 0.0012 deg	9 ppm; 0.0012 deg	11 ppm; 0.0013 deg	13 ppm; 0.0013 deg	15 ppm; 0.0015 deg	17 ppm; 0.0017 deg	19 ppm; 0.0024 deg
3.0	7	17 ppm; 0.0007 deg	18 ppm; 0.0008 deg	18 ppm; 0.0008 deg	21 ppm; 0.0009 deg	23 ppm; 0.0010 deg	25 ppm; 0.0011 deg	27 ppm; 0.0012 deg	30 ppm; 0.0014 deg	32 ppm; 0.0018 deg
4.0	7	21 ppm; 0.0005 deg	21 ppm; 0.0006 deg	22 ppm; 0.0007 deg	24 ppm; 0.0008 deg	27 ppm; 0.0009 deg	29 ppm; 0.0010 deg	32 ppm; 0.0011 deg	34 ppm; 0.0012 deg	37 ppm; 0.0016 deg
5.0	7	23 ppm; 0.0004 deg	23 ppm; 0.0004 deg	25 ppm; 0.0005 deg	26 ppm; 0.0007 deg	28 ppm; 0.0008 deg	31 ppm; 0.0009 deg	34 ppm; 0.0010 deg	36 ppm; 0.0012 deg	38 ppm; 0.0014 deg

Table 5.3a Comparison of Prolate Spheroidal NZ-FZT Algorithmic Results with Theoretical Results for the Filament Dipole of $l_\lambda = 0.1$ (Offset with Respect to Transformation Surface): $\varphi = 45^o$

Offset: $(x'_\lambda, y'_\lambda, z'_\lambda) = (0.01, 0.03, 0.04)$

$l_\lambda = 0.1;\ a_\lambda = 0.1;$ $I \times J = 180 \times 360;$ $\Delta\vartheta' = \Delta\varphi' = 1^o$		Relative Error of $\lvert\overline{E}_{fz_\theta}(\theta,\varphi)\rvert$ (ppm) and Phase Error of $\angle\overline{E}_{fz_\theta}(\theta,\varphi)$ (deg) where $\varphi = 45^o$								
Prolate ξ_o	Convrgce L	$\theta = 10^o$	$\theta = 20^o$	$\theta = 30^o$	$\theta = 40^o$	$\theta = 50^o$	$\theta = 60^o$	$\theta = 70^o$	$\theta = 80^o$	$\theta = 90^o$
1.2	7	143 ppm; 0.0215 deg	86 ppm; 0.0111 deg	65 ppm; 0.0075 deg	55 ppm; 0.0057 deg	46 ppm; 0.0046 deg	40 ppm; 0.0039 deg	34 ppm; 0.0034 deg	29 ppm; 0.0031 deg	24 ppm; 0.0030 deg
1.5	7	13 ppm; 0.0146 deg	13 ppm; 0.0079 deg	14 ppm; 0.0056 deg	15 ppm; 0.0043 deg	15 ppm; 0.0035 deg	15 ppm; 0.0029 deg	15 ppm; 0.0025 deg	13 ppm; 0.0022 deg	11 ppm; 0.0021 deg
2.0	7	44 ppm; 0.0076 deg	27 ppm; 0.0043 deg	19 ppm; 0.0031 deg	15 ppm; 0.0025 deg	11 ppm; 0.0021 deg	8 ppm; 0.0017 deg	6 ppm; 0.0015 deg	5 ppm; 0.0013 deg	5 ppm; 0.0013 deg
3.0	7	57 ppm; 0.0033 deg	42 ppm; 0.0019 deg	35 ppm; 0.0014 deg	29 ppm; 0.0011 deg	25 ppm; 0.0009 deg	22 ppm; 0.0008 deg	19 ppm; 0.0007 deg	17 ppm; 0.0006 deg	17 ppm; 0.0006 deg
4.0	7	55 ppm; 0.0019 deg	44 ppm; 0.0011 deg	38 ppm; 0.0008 deg	33 ppm; 0.0006 deg	29 ppm; 0.0005 deg	26 ppm; 0.0004 deg	23 ppm; 0.0003 deg	22 ppm; 0.0003 deg	21 ppm; 0.0004 deg
5.0	7	53 ppm; 0.0014 deg	43 ppm; 0.0007 deg	39 ppm; 0.0005 deg	34 ppm; 0.0003 deg	30 ppm; 0.0002 deg	27 ppm; 0.0002 deg	25 ppm; 0.0002 deg	23 ppm; 0.0002 deg	23 ppm; 0.0002 deg

Table 5.3a (cont.) Comparison of Prolate Spheroidal NZ-FZT Algorithmic Results with Theoretical Results for the Filament Dipole of $l_\lambda = 0.1$ (Offset with Respect to Transformation Surface): $\varphi = 45^o$

Offset: $(x'_\lambda, y'_\lambda, z'_\lambda) = (0.01, 0.03, 0.04)$

$l_\lambda = 0.1;\ a_\lambda = 0.1;$ $I \times J = 180 \times 360;$ $\Delta\vartheta' = \Delta\varphi' = 1^o$		Relative Error of $\lvert\overline{E}_{fz_\theta}(\theta,\varphi)\rvert$ (ppm) and Phase Error of $\angle\overline{E}_{fz_\theta}(\theta,\varphi)$ (deg) where $\varphi = 45^o$								
Prolate ξ_o	Convrgce L	$\theta = 90^o$	$\theta = 100^o$	$\theta = 110^o$	$\theta = 120^o$	$\theta = 130^o$	$\theta = 140^o$	$\theta = 150^o$	$\theta = 160^o$	$\theta = 170^o$
1.2	7	24 ppm; 0.0030 deg	19 ppm; 0.0029 deg	14 ppm; 0.0030 deg	9 ppm; 0.0032 deg	3 ppm; 0.0036 deg	4 ppm; 0.0041 deg	15 ppm; 0.0051 deg	34 ppm; 0.0071 deg	88 ppm; 0.0129 deg
1.5	7	11 ppm; 0.0021 deg	9 ppm; 0.0020 deg	6 ppm; 0.0020 deg	4 ppm; 0.0021 deg	< 1 ppm; 0.0023 deg	3 ppm; 0.0027 deg	6 ppm; 0.0033 deg	12 ppm; 0.0046 deg	25 ppm; 0.0083 deg
2.0	7	5 ppm; 0.0013 deg	6 ppm; 0.0012 deg	7 ppm; 0.0013 deg	10 ppm; 0.0014 deg	12 ppm; 0.0016 deg	15 ppm; 0.0018 deg	17 ppm; 0.0022 deg	19 ppm; 0.0029 deg	22 ppm; 0.0049 deg
3.0	7	17 ppm; 0.0006 deg	17 ppm; 0.0007 deg	19 ppm; 0.0008 deg	21 ppm; 0.0009 deg	23 ppm; 0.0011 deg	26 ppm; 0.0013 deg	29 ppm; 0.0016 deg	32 ppm; 0.0020 deg	37 ppm; 0.0031 deg
4.0	7	21 ppm; 0.0004 deg	22 ppm; 0.0004 deg	23 ppm; 0.0006 deg	25 ppm; 0.0007 deg	27 ppm; 0.0009 deg	30 ppm; 0.0011 deg	33 ppm; 0.0013 deg	37 ppm; 0.0017 deg	42 ppm; 0.0025 deg
5.0	7	23 ppm; 0.0002 deg	23 ppm; 0.0003 deg	25 ppm; 0.0004 deg	27 ppm; 0.0006 deg	29 ppm; 0.0008 deg	32 ppm; 0.0010 deg	35 ppm; 0.0012 deg	38 ppm; 0.0015 deg	44 ppm; 0.0022 deg

Table 5.2b Comparison of Oblate Spheroidal NZ-FZT Algorithmic Results with Theoretical Results for the Filament Dipole of $l_\lambda = 0.1$ (Offset with Respect to Transformation Surface): $\varphi = 0^o$

Offset: $(x'_\lambda, y'_\lambda, z'_\lambda) = (0.1, 0.3, 0.05)$

$l_\lambda = 0.1;\ a_\lambda = 1.0;$ $I \times J = 180 \times 360;$ $\Delta\vartheta' = \Delta\varphi' = 1^o$		Relative Error of $\lvert\overline{E}_{fz_\theta}(\theta,\varphi)\rvert$(ppm) and Phase Error of $\angle\overline{E}_{fz_\theta}(\theta,\varphi)$ (deg) where $\varphi = 0^o$								
Oblate ξ_o	Convrgce L	$\theta = 10^o$	$\theta = 20^o$	$\theta = 30^o$	$\theta = 40^o$	$\theta = 50^o$	$\theta = 60^o$	$\theta = 70^o$	$\theta = 80^o$	$\theta = 90^o$
0.15	15	154 ppm; 0.0035 deg	74 ppm; 0.0009 deg	8 ppm; 0.0014 deg	64 ppm; 0.0007 deg	102 ppm; 0.0005 deg	133 ppm; 0.0020 deg	159 ppm; 0.0032 deg	176 ppm; 0.0039 deg	181 ppm; 0.0041 deg
0.20	15	91 ppm; 0.0080 deg	56 ppm; 0.0017 deg	8 ppm; 0.0004 deg	58 ppm; 0.0009 deg	95 ppm; 0.0003 deg	129 ppm; 0.0009 deg	158 ppm; 0.0022 deg	178 ppm; 0.0031 deg	184 ppm; 0.0035 deg
0.30	15	57 ppm; 0.0092 deg	12 ppm; 0.0037 deg	34 ppm; 0.0008 deg	62 ppm; 0.0008 deg	89 ppm; 0.0009 deg	120 ppm; 0.0001 deg	150 ppm; 0.0014 deg	173 ppm; 0.0025 deg	181 ppm; 0.0031 deg
0.40	15	133 ppm; 0.0058 deg	60 ppm; 0.0026 deg	58 ppm; 0.0002 deg	70 ppm; 0.0013 deg	89 ppm; 0.0013 deg	114 ppm; 0.0003 deg	142 ppm; 0.0012 deg	164 ppm; 0.0024 deg	172 ppm; 0.0030 deg
0.60	15	137 ppm; 0.0002 deg	78 ppm; 0.0007 deg	72 ppm; 0.0019 deg	78 ppm; 0.0025 deg	87 ppm; 0.0021 deg	103 ppm; 0.0007 deg	124 ppm; 0.0009 deg	143 ppm; 0.0023 deg	150 ppm; 0.0031 deg
0.80	15	100 ppm; 0.0024 deg	69 ppm; 0.0026 deg	70 ppm; 0.0030 deg	77 ppm; 0.0029 deg	83 ppm; 0.0023 deg	94 ppm; 0.0010 deg	110 ppm; 0.0007 deg	126 ppm; 0.0021 deg	131 ppm; 0.0029 deg

Table 5.2b (cont.) Comparison of Oblate Spheroidal NZ-FZT Algorithmic Results with Theoretical Results for the Filament Dipole of $l_\lambda = 0.1$ (Offset with Respect to Transformation Surface): $\varphi = 0^o$

Offset: $(x'_\lambda, y'_\lambda, z'_\lambda) = (0.1, 0.3, 0.05)$

$l_\lambda = 0.1;\ a_\lambda = 1.0;$ $I \times J = 180 \times 360;$ $\Delta\vartheta' = \Delta\varphi' = 1^o$		Relative Error of $\lvert\overline{E}_{fz_\theta}(\theta,\varphi)\rvert$(ppm) and Phase Error of $\angle\overline{E}_{fz_\theta}(\theta,\varphi)$ (deg) where $\varphi = 0^o$								
Oblate ξ_o	Convrgce L	$\theta = 90^o$	$\theta = 100^o$	$\theta = 110^o$	$\theta = 120^o$	$\theta = 130^o$	$\theta = 140^o$	$\theta = 150^o$	$\theta = 160^o$	$\theta = 170^o$
0.15	15	181 ppm; 0.0041 deg	171 ppm; 0.0036 deg	146 ppm; 0.0027 deg	111 ppm; 0.0014 deg	76 ppm; 0.0002 deg	43 ppm; 0.0013 deg	10 ppm; 0.0011 deg	20 ppm; 0.0016 deg	3 ppm; 0.0090 deg
0.20	15	184 ppm; 0.0035 deg	173 ppm; 0.0033 deg	146 ppm; 0.0025 deg	109 ppm; 0.0012 deg	74 ppm; 0.0001 deg	45 ppm; 0.0011 deg	24 ppm; 0.0007 deg	12 ppm; 0.0020 deg	63 ppm; 0.0080 deg
0.30	15	181 ppm; 0.0031 deg	169 ppm; 0.0030 deg	141 ppm; 0.0023 deg	104 ppm; 0.0011 deg	70 ppm; 0.0003 deg	50 ppm; 0.0011 deg	45 ppm; 0.0009 deg	55 ppm; 0.0008 deg	126 ppm; 0.0038 deg
0.40	15	172 ppm; 0.0030 deg	161 ppm; 0.0030 deg	133 ppm; 0.0022 deg	97 ppm; 0.0009 deg	66 ppm; 0.0006 deg	50 ppm; 0.0016 deg	52 ppm; 0.0017 deg	71 ppm; 0.0008 deg	141 ppm; 0.0002 deg
0.60	15	150 ppm; 0.0031 deg	139 ppm; 0.0030 deg	114 ppm; 0.0022 deg	83 ppm; 0.0007 deg	60 ppm; 0.0011 deg	49 ppm; 0.0025 deg	52 ppm; 0.0029 deg	68 ppm; 0.0026 deg	120 ppm; 0.0026 deg
0.80	15	131 ppm; 0.0029 deg	120 ppm; 0.0029 deg	97 ppm; 0.0020 deg	73 ppm; 0.0004 deg	57 ppm; 0.0013 deg	51 ppm; 0.0026 deg	51 ppm; 0.0033 deg	57 ppm; 0.0032 deg	85 ppm; 0.0032 deg

Table 5.3b Comparison of Oblate Spheroidal NZ-FZT Algorithmic Results with Theoretical Results for the Filament Dipole of $l_\lambda = 0.1$ (Offset with Respect to Transformation Surface): $\varphi = 45^o$

Offset: $(x'_\lambda, y'_\lambda, z'_\lambda) = (0.1, 0.3, 0.05)$

$l_\lambda = 0.1;\ a_\lambda = 1.0;$ $I \times J = 180 \times 360;$ $\Delta\vartheta' = \Delta\varphi' = 1^o$		Relative Error of $\lvert\bar{E}_{fz_\theta}(\theta,\varphi)\rvert$ (ppm) and Phase Error of $\angle\bar{E}_{fz_\theta}(\theta,\varphi)$ (deg) where $\varphi = 45^o$								
Oblate ξ_o	Convrgce L	$\theta = 10^o$	$\theta = 20^o$	$\theta = 30^o$	$\theta = 40^o$	$\theta = 50^o$	$\theta = 60^o$	$\theta = 70^o$	$\theta = 80^o$	$\theta = 90^o$
0.15	15	119 ppm; 0.0127 deg	179 ppm; 0.0013 deg	236 ppm; 0.0052 deg	265 ppm; 0.0057 deg	279 ppm; 0.0041 deg	286 ppm; 0.0013 deg	291 ppm; 0.0018 deg	290 ppm; 0.0041 deg	281 ppm; 0.0053 deg
0.20	15	186 ppm; 0.0206 deg	131 ppm; 0.0030 deg	160 ppm; 0.0031 deg	189 ppm; 0.0050 deg	214 ppm; 0.0041 deg	234 ppm; 0.0016 deg	247 ppm; 0.0013 deg	252 ppm; 0.0036 deg	247 ppm; 0.0047 deg
0.30	15	368 ppm; 0.0207 deg	133 ppm; 0.0062 deg	94 ppm; 0.0006 deg	106 ppm; 0.0037 deg	133 ppm; 0.0039 deg	162 ppm; 0.0020 deg	186 ppm; 0.0005 deg	199 ppm; 0.0026 deg	198 ppm; 0.0037 deg
0.40	15	429 ppm; 0.0125 deg	146 ppm; 0.0044 deg	79 ppm; 0.0006 deg	74 ppm; 0.0033 deg	95 ppm; 0.0036 deg	123 ppm; 0.0021 deg	148 ppm; 0.0001 deg	163 ppm; 0.0021 deg	166 ppm; 0.0031 deg
0.60	15	338 ppm; 0.0012 deg	126 ppm; 0.0002 deg	66 ppm; 0.0022 deg	53 ppm; 0.0034 deg	64 ppm; 0.0034 deg	86 ppm; 0.0021 deg	107 ppm; 0.0002 deg	119 ppm; 0.0015 deg	122 ppm; 0.0025 deg
0.80	15	236 ppm; 0.0024 deg	100 ppm; 0.0021 deg	56 ppm; 0.0029 deg	44 ppm; 0.0034 deg	52 ppm; 0.0032 deg	68 ppm; 0.0020 deg	84 ppm; 0.0004 deg	93 ppm; 0.0011 deg	93 ppm; 0.0019 deg

Table 5.3b (cont.) Comparison of Oblate Spheroidal NZ-FZT Algorithmic Results with Theoretical Results for the Filament Dipole of $l_\lambda = 0.1$ (Offset with Respect to Transformation Surface): $\varphi = 45^o$

Offset: $(x'_\lambda, y'_\lambda, z'_\lambda) = (0.1, 0.3, 0.05)$

$l_\lambda = 0.1;\ a_\lambda = 1.0;$ $I \times J = 180 \times 360;$ $\Delta\vartheta' = \Delta\varphi' = 1^o$		Relative Error of $\lvert\bar{E}_{fz_\theta}(\theta,\varphi)\rvert$ (ppm) and Phase Error of $\angle\bar{E}_{fz_\theta}(\theta,\varphi)$ (deg) where $\varphi = 45^o$								
Oblate ξ_o	Convrgce L	$\theta = 90^o$	$\theta = 100^o$	$\theta = 110^o$	$\theta = 120^o$	$\theta = 130^o$	$\theta = 140^o$	$\theta = 150^o$	$\theta = 160^o$	$\theta = 170^o$
0.15	15	281 ppm; 0.0053 deg	260 ppm; 0.0051 deg	226 ppm; 0.0036 deg	182 ppm; 0.0011 deg	136 ppm; 0.0014 deg	100 ppm; 0.0030 deg	84 ppm; 0.0023 deg	98 ppm; 0.0027 deg	257 ppm; 0.0187 deg
0.20	15	247 ppm; 0.0047 deg	227 ppm; 0.0045 deg	194 ppm; 0.0030 deg	149 ppm; 0.0007 deg	102 ppm; 0.0016 deg	69 ppm; 0.0026 deg	65 ppm; 0.0014 deg	111 ppm; 0.0034 deg	337 ppm; 0.0162 deg
0.30	15	198 ppm; 0.0037 deg	183 ppm; 0.0035 deg	152 ppm; 0.0022 deg	109 ppm; 0.0001 deg	66 ppm; 0.0017 deg	40 ppm; 0.0024 deg	51 ppm; 0.0011 deg	127 ppm; 0.0022 deg	391 ppm; 0.0080 deg
0.40	15	166 ppm; 0.0031 deg	152 ppm; 0.0030 deg	125 ppm; 0.0018 deg	87 ppm; 0.0001 deg	50 ppm; 0.0018 deg	28 ppm; 0.0025 deg	44 ppm; 0.0016 deg	120 ppm; 0.0003 deg	361 ppm; 0.0016 deg
0.60	15	122 ppm; 0.0025 deg	112 ppm; 0.0024 deg	91 ppm; 0.0013 deg	62 ppm; 0.0003 deg	35 ppm; 0.0019 deg	21 ppm; 0.0027 deg	33 ppm; 0.0026 deg	88 ppm; 0.0021 deg	255 ppm; 0.0031 deg
0.80	15	93 ppm; 0.0019 deg	86 ppm; 0.0018 deg	71 ppm; 0.0009 deg	49 ppm; 0.0005 deg	29 ppm; 0.0018 deg	19 ppm; 0.0026 deg	31 ppm; 0.0028 deg	70 ppm; 0.0027 deg	178 ppm; 0.0034 deg

related to the offset vector $\vec{r}' = (x', y', z')$ and the observation angle (θ, φ) by the following expression:

$$\Delta\Phi \text{ (radians)} = \frac{2\pi}{\lambda_o}\left[x' \sin\theta\cos\varphi + y' \sin\theta\sin\varphi + z'\cos\theta\right]. \qquad (5\text{-}11)$$

By adding this phase difference to the phase of equation (5-7), we compute the theoretical phase data necessary to conduct the phase error analysis for the offset dipole numerical tests. Presented in Tables 5.2a, 5.2b, 5.3a, and 5.3b is a compilation of the overall error analysis for both spheroidal cases of this second set of numerical tests. Both Tables 5.2a and 5.3a provide the overall error analysis of the prolate spheroidal algorithm for the $\varphi = 0^o$ and $\varphi = 45^o$ planar cuts, respectively. Likewise, Tables 5.2b and 5.3b respectively address the overall error analysis for the oblate spheroidal algorithm for the $\varphi = 0^o$ and $\varphi = 45^o$ planar cuts.

Upon review of these findings, we see that both algorithms respond differently to the offset dipole numerical tests when compared to that of the centered dipole numerical tests. Included in these differences is the fact that significantly more analysis data is presented in the case of the offset dipole numerical tests. This increase of data occurs because both algorithms now deliver varying performances for each observation angle (θ, φ) under consideration. As a result, the performance of the algorithms is no longer the same when predicting the far-zone E-field in the upper and lower hemisphere. Moreover, both algorithms now deliver performances that differ when comparing their results for the $\varphi = 0^o$ planar cut with those for the $\varphi = 45^o$ planar cut. It must be pointed out that this asymmetric performance of the algorithms is what should be expected when addressing a problem setup that has no angular and azimuthal (rotational) symmetry.

Further inspection of the error analysis data reveals that the worst case magnitude and phase error for our offset dipole numerical tests (i.e., for both planar cuts) is as follows: (a) prolate, 143 ppm and 0.0215 deg; (b) oblate, 429 ppm and 0.0207 deg. The performance of the prolate spheroidal algorithm appears to slightly degrade when

compared to its centered dipole counterpart; however, the opposite is true for the performance of the oblate spheroidal algorithm. Furthermore, both algorithms converge at a slightly slower rate for the offset numerical tests, viz., L=7 for prolate cases and L=15 for the oblate cases, as compared to their centered dipole counterparts.

In a manner identical to that conducted for the centered dipole numerical tests, the next step in the analysis of the offset dipole numerical tests is to determine how well the algorithms approximate theoretical values of zero. Once again, this analysis not only applies to the nulls of the pattern $\overline{E}_{fz_\theta}(\theta,\varphi)$ at the observation angles $\theta = 0^o$ and $\theta = 180^o$, but also to the cross-polarized far-zone E-field $\overline{E}_{fz_\varphi}(\theta,\varphi)$. The worst case null computed with respect to the main beam peak is as follows for all of the offset dipole test cases: (a) prolate, -83.74 dB; (b) oblate, -78.79 dB. As for the cross-polarized far-zone E-field $\overline{E}_{fz_\varphi}(\theta,\varphi)$, its worst case magnitude (considering all offset dipole test cases) computed with respect to the main beam peak is as follows: (a) prolate, -83.23 dB; (b) oblate, -78.28 dB. Note that for each spheroidal algorithm the worst case approximation of the theoretical value of zero is roughly the same when computing either the far-zone E-field nulls or the cross-polarized E-field $\overline{E}_{fz_\varphi}(\theta,\varphi)$. Moreover, the results of the offset dipole numerical tests show that the numerical noise floor is significantly higher than that of the corresponding centered dipole numerical tests. In spite of this, the increased level of the numerical noise floor still remains quite acceptable for both spheroidal algorithms.

Having completed the analysis for both the offset and centered dipole numerical tests, we are now ready to summarize the overall performance of the NZ-FZT algorithms. We do so by combining the results of both sets of analysis data to establish an overall worst case performance for all of the numerical test cases. The outcome of this performance assessment is compiled and presented in Table 5.4.

Table 5.4 Overall Worst Case Performance of the Spheroidal NZ-FZT Algorithms for the Offset and Centered Dipole Numerical Tests

NZ-FZT Algorithm	Slowest Convrgce L	Worst Case Relative Error of $\lvert\overline{E}_{fz_\theta}(\theta,\varphi)\rvert$ (ppm)	Worst Case Phase Error of $\angle\overline{E}_{fz_\theta}(\theta,\varphi)$ (deg)	Highest Level of Zero Approximation (dB)
Prolate	7	143 ppm	0.0215 deg	-83.23 dB
Oblate	15	826 ppm	0.1105 deg	-78.28 dB

From this performance assessment we are able to draw several important conclusions about the newly developed NZ-FZT algorithms. Based on these results, it appears that the prolate spheroidal algorithm performs a little better than its oblate counterpart. On average, the prolate algorithm delivers more accurate results for both sets of numerical tests while maintaining a numerical noise floor that is a few decibels (dB) lower. Regardless, both algorithms perform remarkably well: both algorithms deliver far-zone E-field computations that are within $\pm 0.1\%$ (or ± 1000 ppm) in magnitude and ± 0.12 deg in phase with at least 78 dB of numerical dynamic range. As for the difference in the rate of convergence, it is most likely attributed to the fact that the prolate spheroidal transformation surface geometrically conforms to the filament dipole better than its oblate counterpart. Most importantly, the results of these numerical studies demonstrate that our overall NZ-FZT concept is sound both in theory and in implementation.

CHAPTER 6. DEVELOPMENT OF A COMPUTATIONAL ELECTROMAGNETIC FIELD SOLVER

This chapter addresses the development of an electromagnetic field solver capable of computing the surrounding near-zone fields for a variety of radiation structures. The purpose of this software development is essentially twofold. First, by combining a computational field solver with our NZ-FZT computer software, we are able to provide further validation of our newly developed NZ-FZT process. (Note that this additional validation is completed in the chapter that follows using the combined software to model an empirical benchmark.) Second, the coupling of this software allows us to illustrate a realistic example of an application that makes excellent use of our NZ-FZT process.

Although many different computational techniques exist that are able to calculate the surrounding near-zone fields for a given radiation structure, we have chosen to implement our electromagnetic field solver using a specific form of the finite-difference time-domain (FDTD) method. Since our prime objective is to further validate the newly developed NZ-FZT process, only one electromagnetic field solver needs to be developed; that is, the examination of other field solvers would prove nothing additional with respect to the verification of our algorithms. In particular, the FDTD method is chosen to fulfill this function in our validation process because it is an extremely versatile technique that has become quite popular in most recent years. However, it is important to note that any one of the many other well-abled computational techniques, e.g., the finite element method (FEM), could have equally been chosen to serve as our electromagnetic field solver.

Initially, we begin our discussion by examining the relevant basics of the FDTD method and how they pertain to our particular application. We follow this by discussing the development of a FDTD field solver that is designed to interface with our NZ-FZT software. Finally, we conclude this chapter by conducting an end-to-end test of the combined NZ-FZT/FDTD software using a computational model of our analytical benchmark (initially described and used in Chapter 5).

6.1 FDTD FUNDAMENTALS

6.1.1 Overview of Computational Technique

In the field of computational electromagnetics, the term FDTD applies to all techniques that employ a finite-difference scheme both in time and space to numerically approximate the time-dependent differential form of Maxwell's equations. The technique of finite-differencing is not new to numerical analysis and is often considered the method of choice when computing a numerical solution for a system of partial differential equations. However, the use of the finite-difference method to treat partial differential equations is in itself quite an expansive subject: one that is too vast to even begin considering here. Consequently, the reader is referred to texts [37], [43], [44] for the many schemes and intricate details associated with this technique of numerical analysis. To further complicate matters, many finite-difference schemes and mesh configurations (used to approximate Maxwell's equations) exist that come under the umbrella of the FDTD method. These various approaches range from higher-order techniques to non-uniform grid configurations (all of which are too numerous to mention here). In general, this ever-growing diversity of FDTD stems from the continual desire to improve one or more of the following performance factors: accuracy, dispersion, stability, memory storage, and total computation time. For a comprehensive survey of the many variations of this computational technique and their advantages, we refer the interested reader to references [45], [46] (both presently considered the foremost texts on FDTD) and the literature survey article [47] (which points to the myriad of various FDTD techniques available in the literature). It is because of the sheer volume of these methods that our attention remains focused on the specific variation of FDTD utilized by our electromagnetic field solver.

In developing the field solver, we elect to make use of the most basic form of FDTD originally pioneered by Yee [48]. As we shall see, this approach combined with the second-order Mur absorbing boundary condition (ABC) [49] proves to be quite sufficient for our purposes of demonstrating the performance and effectiveness of the

newly developed NZ-FZT process. Yee's approach makes use of a two-step finite-difference explicit scheme with central differencing both in time and space (often referred to as a leapfrog scheme [45]) to represent both E- and H-fields in Cartesian coordinates. As a result, this scheme leads to a mesh configuration that represents a given solution volume with samples of E- and H-fields that are interleaved both spatially and temporally. Since this particular finite-differencing scheme only retains first-order terms, it provides second-order accuracy with respect to spatial and temporal sample periods. Furthermore, because the samples are uniformly distributed with respect to each Cartesian dimension, we are able to partition the solution volume into a set of uniform cells (also known as Yee cells). Each of these Yee cells consists of a set of E- and H-field samples with a spatial arrangement of that shown in Figure 6.1 (which results from central differencing in space). Upon inspection of the Yee cell geometry, one should notice that the E-field samples in each Cartesian plane surround the corresponding orthogonal H-field samples and vice-versa. Intuitively this arrangement makes sense because it remains consistent with both curl equations contained within the differential form of Maxwell's equations. Alternatively, one can recognize by inspection that the arrangement of the fields is also consistent with the integral form of Maxwell's equations (as should be expected). Likewise, it is also important to realize that the arrangements for each Cartesian component of the E- and H-fields do not coincide and are all spatially offset with respect to one another. Referring to Figure 6.1, we summarize the spatial locations of the indexed field samples as follows:

$$E_x(i+\tfrac{1}{2}, j, k) \text{ is at } ((i+\tfrac{1}{2})\Delta x, j\Delta y, k\Delta z);$$

$$E_y(i, j+\tfrac{1}{2}, k) \text{ is at } (i\Delta x, (j+\tfrac{1}{2})\Delta y, k\Delta z);$$

$$E_z(i, j, k+\tfrac{1}{2}) \text{ is at } (i\Delta x, j\Delta y, (k+\tfrac{1}{2})\Delta z);$$

$$H_x(i, j+\tfrac{1}{2}, k+\tfrac{1}{2}) \text{ is at } (i\Delta x, (j+\tfrac{1}{2})\Delta y, (k+\tfrac{1}{2})\Delta z);$$

$$H_y(i+\tfrac{1}{2}, j, k+\tfrac{1}{2}) \text{ is at } ((i+\tfrac{1}{2})\Delta x, j\Delta y, (k+\tfrac{1}{2})\Delta z);$$

$$H_z(i+\tfrac{1}{2}, j+\tfrac{1}{2}, k) \text{ is at } ((i+\tfrac{1}{2})\Delta x, (j+\tfrac{1}{2})\Delta y, k\Delta z).$$

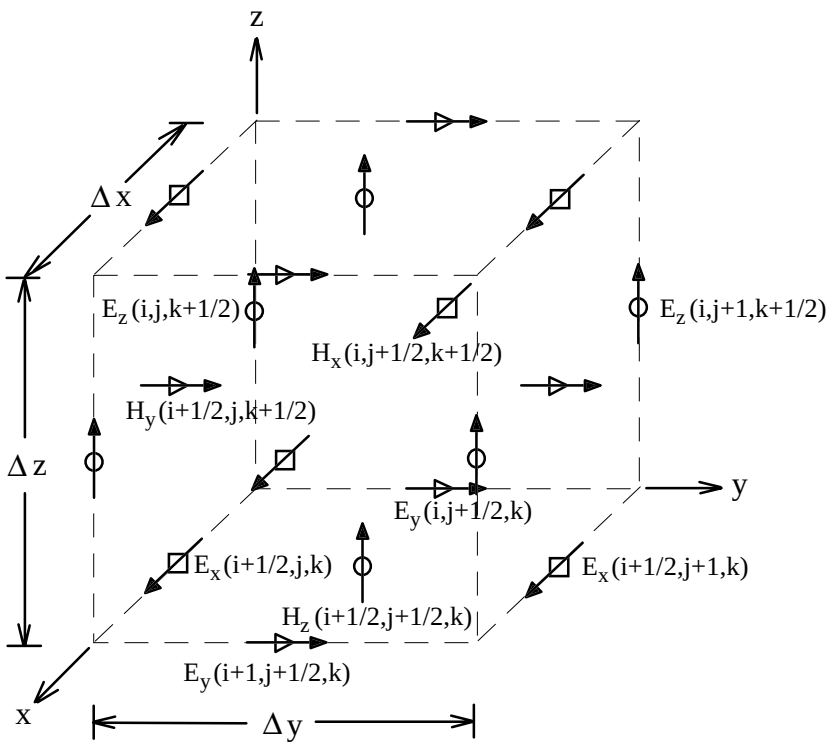

Figure 6.1 Yee cell geometry with index (*i*, *j*, *k*).

As we can see, each Yee cell is referenced in the solution volume by the spatial index (i, j, k) and is actually made up of twelve E-field samples and six H-field samples. By duality, the three-dimensional lattice can be viewed as a set of magnetic cells that instead contain twelve H-field samples and six E-field samples. Nonetheless, partitioning the solution volume into electrically defined Yee cells is much more suitable for our particular application; that is, the electrical approach is intrinsically better able to model a radiation structure solely made of non-magnetic materials (i.e., materials possessing a permeability of μ_o).

The modeling of a non-magnetic (electrical) structure using the FDTD method requires that each E-field sample be computed using a distinct formulation that corresponds to the medium present: (1) free-space (or non-lossy dielectric materials), (2) perfect electric conductor, and (3) lossy dielectric materials. Yet because all media required for our particular application are considered non-magnetic, computation of the respective H-field samples only requires a single formulation. Each of these resulting FDTD formulations is detailed in the sections that follow. Nevertheless, it is by specifying different materials at E-field sample points and subsequently using the proper formulations that effectively allow the construction of a FDTD electrical structure.

Now that we have a basic understanding of how FDTD functions spatially, we need to focus on its operation with respect to time. The technique is considered a time-marching algorithm that starts at some point in time (i.e., $t = 0$ in our case) with an initially defined solution volume and continues calculating the fields until some designated stop-point is reached. For our purposes of modeling radiation structures, the solution volume is considered at rest (i.e., all fields at zero) prior to the start of the FDTD simulation (i.e., $t < 0$). By receiving some form of excitation during the simulation, the FDTD field solver is then able to compute the resulting E- and H-field samples in the time-domain as the fields propagate throughout the entire three-dimensional lattice.

In a manner similar to the partitioning of the solution volume, the overall simulation time is first divided into uniform time-steps of duration Δt. At each of these time-steps there exists a distinct set of E- and H-field samples that represents the entire

solution volume. Moreover, these E- and H-field samples are staggered in time with respect to one another by a half time-step (i.e., $\Delta t/2$). For a given time-step (indexed with respect to *n*), the set of E-field samples is computed using the set of H-field samples from a half time-step back and the set of E-field samples from a whole time-step back. Likewise, the immediately following set of H-field samples is then found by using the recently computed set of E-field samples (now a half time-step back) and the set of H-fields samples from a whole time-step back. This two-step process is more easily understood by examining Figure 6.2. By repeating this multistep process, the field solver progresses through all of the time-steps until the designated stop-point index has been reached. The finite-difference scheme employed (i.e., leapfrog) is considered explicit because any given field sample is computed using only prior-time field samples [45].

Having reviewed both the spatial and temporal operation of this computational method, we now appropriately include a time-step index *n* in addition to the spatial index (i, j, k) when describing both E- and H-field samples (see Figure 6.2). It is important to note that within the literature there are a number of other notations that describe this multistep process. For the most part, the differences occur in the way that the indices refer to a particular sample both spatially and temporally. Nevertheless, all of the other notations are essentially describing the same process.

We now turn our attention to the fact that our three-dimensional lattice of E- and H-field samples is not infinite in extent. Although this limitation has no bearing on the modeling of closed electromagnetic problems (e.g., cavity type problems), it does pose some difficulties when modeling open electromagnetic problems (e.g., free-space radiation problems). In short, truncation of the three-dimensional lattice gives rise to unwanted reflections at the boundaries of the solution volume that will ultimately corrupt the results of a FDTD simulation. Because our particular application requires us to compute the near-zone fields of a radiation structure situated in free-space, these unwanted reflections can seriously impact the validity of our results. In order to attenuate these boundary reflections, we apply what is referred to as an absorbing boundary

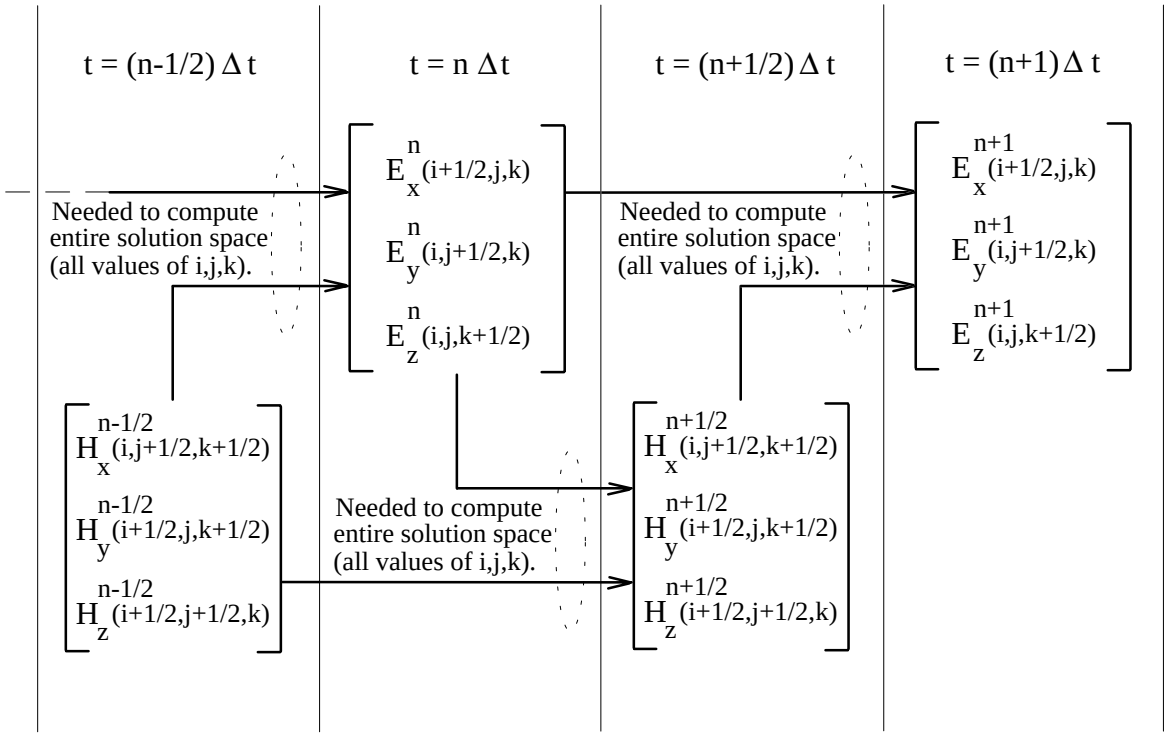

Figure 6.2 Temporal operation of FDTD.

condition (ABC) at the perimeter of the solution volume. Essentially, the ABC mathematically absorbs electromagnetic waves that are propagating outward with respect to the solution volume. Since there are so many accepted ABC techniques (including their respective variations), we will not even attempt to review them here. For a comprehensive examination of these existing techniques, the reader is referred to the extensive survey provided by Taflove [46] that details the theory and performance level for each respective ABC. However, in addition to these techniques, new ABCs are continually under development by the research community; for the most part, all of these efforts are directed toward finding the ideal method able to provide the quietest boundary reflections using the fewest computations. As mentioned earlier, our electromagnetic field solver makes use of the second-order ABC put forth by Mur [49]: experience shows that it provides a level of attenuation (of the boundary reflections) that is quite acceptable for our particular application.

Modern-day FDTD simulations typically make use of formulations based upon scattered-fields only, total-fields only, or some combination of both [45], [46]. The scattered-field formulation is based upon separating all E- and H-fields within the solution volume into incident and scattered components (this decomposition is justified by the linearity of Maxwell's equations [46]). In doing so, the incident field (serving as the excitation) can be specified analytically throughout the solution volume such that the field solver only has to compute the scattered fields. Moreover, an added benefit of the scattered-field formulation is that only the scattered fields need to be absorbed at the perimeter of the solution volume. According to Kunz and Luebbers [45], this feature is important because the scattered fields can be more readily absorbed by the ABC than the corresponding total fields; thus, the scattered-field formulation provides more accurate results in cases where the amplitude of the scattered fields is much less than that of the total fields. It is for these reasons that the scattered-field approach is better suited to model the scattering of incident waves impinging upon material objects. To the contrary, our application requires us to model a given radiation structure that is considered the sole source of any field disturbances (i.e., no incident fields). By internally exciting the

radiation structure, the total-field formulation allows the field solver to directly compute the total radiated fields. The total-field formulation is a special case of the scattered-field formulation where the incident fields are set to zero; that is, the scattered-field formulation inherently becomes the total-field formulation in the absence of incident fields. Accordingly, the total-field approach is the most logical choice for our purposes of validating the developed NZ-FZT algorithms. It is important to note that each of the FDTD formulations detailed in the sections that follow is particular to the total-field formulation and reflects the fact that the incident E- and H-fields are assumed to be zero. Finally, we dispense with the combination approach because it too, like the scattered-field formulation, is better suited for the modeling of scattering problems.

6.1.2 Free-Space (or Non-Lossy Dielectric) E-Field Formulation

In applications where FDTD is used to model electromagnetic radiation, a portion of the solution volume must be reserved for a free-space buffer that completely surrounds the entire radiation structure. This spatial buffer must be present in order to properly simulate the interaction of the radiation structure with free-space; without it, the modeled radiation structure improperly reacts with the ABC (situated at the perimeter of the solution volume) to yield inaccurate numerical results. Hence, all E-field samples that are part of this spatial buffer must be computed using a FDTD formulation that corresponds to free-space. In addition, this free-space formulation not only applies to E-field samples situated in the spatial buffer, but also to E-field samples that represent the absence of materials internal to a radiating structure (e.g., the internal space of a horn antenna).

In order to get a basic understanding of the rationale behind the free-space E-field formulation, we begin by considering the time-dependent differential form of the Maxwell-Ampere equation for free-space (assuming $\sigma = 0$):

$$\frac{\partial}{\partial t}\vec{E} = \frac{1}{\varepsilon_0}\left(\nabla \times \vec{H}\right). \tag{6-1}$$

As we can see, the vector equation contains derivatives with respect to both time and space (with the curl operator giving rise to the spatial derivatives). Operating in Cartesian coordinates, we are able to separate the vector equation of (6-1) into its three scalar components. By applying finite-differencing to approximate the temporal and spatial derivatives of each of the resulting scalar equations, we obtain the following FDTD update equations for free-space (using the total-field formulation) [45]:

$$E_x^{n+1}(i+\tfrac{1}{2},j,k) = E_x^{n}(i+\tfrac{1}{2},j,k) + \frac{\Delta t}{\varepsilon_o}\left[\begin{array}{l}\dfrac{H_z^{n+1/2}(i+\frac{1}{2},j+\frac{1}{2},k)-H_z^{n+1/2}(i+\frac{1}{2},j-\frac{1}{2},k)}{\Delta y} \\ -\dfrac{H_y^{n+1/2}(i+\frac{1}{2},j,k+\frac{1}{2})-H_y^{n+1/2}(i+\frac{1}{2},j,k-\frac{1}{2})}{\Delta z}\end{array}\right] \tag{6-2}$$

$$E_y^{n+1}(i,j+\tfrac{1}{2},k) = E_y^{n}(i,j+\tfrac{1}{2},k) + \frac{\Delta t}{\varepsilon_o}\left[\begin{array}{l}\dfrac{H_x^{n+1/2}(i,j+\frac{1}{2},k+\frac{1}{2})-H_x^{n+1/2}(i,j+\frac{1}{2},k-\frac{1}{2})}{\Delta z} \\ -\dfrac{H_z^{n+1/2}(i+\frac{1}{2},j+\frac{1}{2},k)-H_z^{n+1/2}(i-\frac{1}{2},j+\frac{1}{2},k)}{\Delta x}\end{array}\right] \tag{6-3}$$

$$E_z^{n+1}(i,j,k+\tfrac{1}{2}) = E_z^{n}(i,j,k+\tfrac{1}{2}) + \frac{\Delta t}{\varepsilon_o}\left[\begin{array}{l}\dfrac{H_y^{n+1/2}(i+\frac{1}{2},j,k+\frac{1}{2})-H_y^{n+1/2}(i-\frac{1}{2},j,k+\frac{1}{2})}{\Delta x} \\ -\dfrac{H_x^{n+1/2}(i,j+\frac{1}{2},k+\frac{1}{2})-H_x^{n+1/2}(i,j-\frac{1}{2},k+\frac{1}{2})}{\Delta y}\end{array}\right]. \tag{6-4}$$

Our electromagnetic field solver makes use of these update equations to compute the E-field for all samples that are situated in free-space. A given sample for each Cartesian component of the E-field is computed by using its previous sample (a whole time-step back) together with several neighboring orthogonal H-field samples (a half time-step

back). Note how these update equations conform to the spatial and temporal format of FDTD examined earlier in Figures 6.1 and 6.2. Furthermore, this free-space formulation can be easily made to address other non-lossy dielectric media by replacing the free-space permittivity with that of the desired dielectric material (i.e., $\varepsilon_o \rightarrow \varepsilon$).

6.1.3 Perfect Electric Conductor E-Field Formulation

The parts of a radiation structure that are made of metal are typically modeled in FDTD simulations using a perfect electric conductor (i.e., $\sigma \rightarrow \infty$). For most applications, this approximation is quite valid and often yields extremely good numerical results. In which case, we need a FDTD formulation able to compute E-field samples corresponding to this ideal material. Fortunately, we are able to make use of the fact that the total E-field in a perfect electric conductor must vanish; this fundamental property thus allows us to obtain the following update equations (using the total-field formulation) [45]:

$$E_x^{n+1}(i+\tfrac{1}{2}, j, k) = 0 \tag{6-5}$$

$$E_y^{n+1}(i, j+\tfrac{1}{2}, k) = 0 \tag{6-6}$$

$$E_z^{n+1}(i, j, k+\tfrac{1}{2}) = 0. \tag{6-7}$$

At each time step, our electromagnetic field solver computes the E-field samples corresponding to a perfect electric conductor by simply setting them equal to zero.

6.1.4 Lossy Dielectric E-Field Formulation

The third and final medium that our electromagnetic field solver must be able to address is a lossy dielectric possessing a finite conductivity of σ and a permittivity of ε. As we shall see, simulating this particular type of material is critical in the modeling of our empirical benchmark (which is used in Chapter 7 to further validate our newly developed NZ-FZT process). Consequently, we need an additional FDTD formulation

able to compute E-field samples for a variety of lossy dielectrics. Once again, we begin to understand the rationale behind this E-field formulation by evoking the time-dependent differential form of the Maxwell-Ampere equation; however, this time assuming a nonzero finite conductivity (i.e., $0 < \sigma < \infty$):

$$\frac{\partial}{\partial t}\vec{E} = -\frac{\sigma}{\varepsilon}\vec{E} + \frac{1}{\varepsilon}\left(\nabla \times \vec{H}\right). \tag{6-8}$$

Accordingly, the vector equation now contains an additional term when compared to equation (6-1) that is proportional to the conduction current density, i.e., $\vec{J} = \sigma\vec{E}$. By separating the vector equation of (6-8) into its three scalar equations (in Cartesian coordinates) and then applying finite-differencing to approximate the temporal and spatial derivatives, we obtain the following FDTD update equations for a lossy dielectric (using the total-field formulation) [45]:

$$E_x^{n+1}(i+\tfrac{1}{2}, j, k) = \left(\frac{\varepsilon}{\varepsilon + \sigma\Delta t}\right) E_x^{n}(i+\tfrac{1}{2}, j, k)$$
$$+ \frac{\Delta t}{\varepsilon + \sigma\Delta t}\left[\begin{array}{l} \dfrac{H_z^{n+1/2}(i+\frac{1}{2}, j+\frac{1}{2}, k) - H_z^{n+1/2}(i+\frac{1}{2}, j-\frac{1}{2}, k)}{\Delta y} \\ -\dfrac{H_y^{n+1/2}(i+\frac{1}{2}, j, k+\frac{1}{2}) - H_y^{n+1/2}(i+\frac{1}{2}, j, k-\frac{1}{2})}{\Delta z} \end{array}\right] \tag{6-9}$$

$$E_y^{n+1}(i, j+\tfrac{1}{2}, k) = \left(\frac{\varepsilon}{\varepsilon + \sigma\Delta t}\right) E_y^{n}(i, j+\tfrac{1}{2}, k)$$
$$+ \frac{\Delta t}{\varepsilon + \sigma\Delta t}\left[\begin{array}{l} \dfrac{H_x^{n+1/2}(i, j+\frac{1}{2}, k+\frac{1}{2}) - H_x^{n+1/2}(i, j+\frac{1}{2}, k-\frac{1}{2})}{\Delta z} \\ -\dfrac{H_z^{n+1/2}(i+\frac{1}{2}, j+\frac{1}{2}, k) - H_z^{n+1/2}(i-\frac{1}{2}, j+\frac{1}{2}, k)}{\Delta x} \end{array}\right] \tag{6-10}$$

$$E_z^{n+1}(i,j,k+\tfrac{1}{2}) = \left(\frac{\varepsilon}{\varepsilon+\sigma\Delta t}\right) E_z^{n}(i,j,k+\tfrac{1}{2})$$

$$+\frac{\Delta t}{\varepsilon+\sigma\Delta t}\left[\begin{array}{l}\dfrac{H_y^{n+1/2}(i+\frac{1}{2},j,k+\frac{1}{2}) - H_y^{n+1/2}(i-\frac{1}{2},j,k+\frac{1}{2})}{\Delta x} \\ -\dfrac{H_x^{n+1/2}(i,j+\frac{1}{2},k+\frac{1}{2}) - H_x^{n+1/2}(i,j-\frac{1}{2},k+\frac{1}{2})}{\Delta y}\end{array}\right]. \quad (6\text{-}11)$$

During the formulation of these update equations, it is important to use the most recent samples of the E-field, viz., $E_x^{n+1}(i+\frac{1}{2},j,k)$, $E_y^{n+1}(i,j+\frac{1}{2},k)$, or $E_z^{n+1}(i,j,k+\frac{1}{2})$, to determine each respective Cartesian component of the term $(-\frac{\sigma}{\varepsilon}\vec{E})$; Kunz and Luebbers [45] stress that this approach is key to obtaining numerical stability for large conductivity values. Note how in the limiting cases of $\sigma \to 0$ and $\sigma \to \infty$, these FDTD update equations reduce to those for free-space (or non-lossy dielectric), i.e., (6-2)-(6-4), and those for the perfect electric conductor, i.e., (6-5)-(6-7), respectively.

Our electromagnetic field solver makes use of update equations (6-9)-(6-11) to compute the E-field for all samples corresponding to a lossy dielectric. Different values of σ and ε are then used to represent each lossy dielectric that is part of a given FDTD simulation. In a manner that is quite similar to the formulation for free-space, each individual Cartesian component of the E-field is computed by using its previous sample (a whole time-step back) together with several neighboring orthogonal H-field samples (a half time-step back).

6.1.5 Non-Magnetic H-Field Formulation

Having addressed how to compute E-field samples corresponding to a variety of non-magnetic media, we now concentrate on computation of their respective H-field samples. As stated earlier, our electromagnetic field solver only needs one FDTD formulation to compute all H-field samples for the three types of non-magnetic media

under consideration. We begin by considering the time-dependent differential form of the Maxwell-Faraday equation with a non-magnetic permeability (assuming $\mu = \mu_o$):

$$\frac{\partial}{\partial t}\vec{H} = -\frac{1}{\mu_0}\left(\nabla \times \vec{E}\right). \tag{6-12}$$

Once again, we are able to separate the vector equation into its three Cartesian scalar equations. Applying finite-differencing to approximate the temporal and spatial derivatives of each of the resulting scalar equations, we obtain the following FDTD update equations to compute all H-field samples corresponding to non-magnetic media (using the total-field formulation) [45]:

$$H_x^{n+1/2}(i, j+\tfrac{1}{2}, k+\tfrac{1}{2}) = H_x^{n-1/2}(i, j+\tfrac{1}{2}, k+\tfrac{1}{2}) + \frac{\Delta t}{\mu_o}\left[\begin{array}{l} \dfrac{E_y^n(i, j+\frac{1}{2}, k+1) - E_y^n(i, j+\frac{1}{2}, k)}{\Delta z} \\ -\dfrac{E_z^n(i, j+1, k+\frac{1}{2}) - E_z^n(i, j, k+\frac{1}{2})}{\Delta y} \end{array}\right] \tag{6-13}$$

$$H_y^{n+1/2}(i+\tfrac{1}{2}, j, k+\tfrac{1}{2}) = H_y^{n-1/2}(i+\tfrac{1}{2}, j, k+\tfrac{1}{2}) + \frac{\Delta t}{\mu_o}\left[\begin{array}{l} \dfrac{E_z^n(i+1, j, k+\frac{1}{2}) - E_z^n(i, j, k+\frac{1}{2})}{\Delta x} \\ -\dfrac{E_x^n(i+\frac{1}{2}, j, k+1) - E_x^n(i+\frac{1}{2}, j, k)}{\Delta z} \end{array}\right] \tag{6-14}$$

$$H_z^{n+1/2}(i+\tfrac{1}{2}, j+\tfrac{1}{2}, k) = H_z^{n-1/2}(i+\tfrac{1}{2}, j+\tfrac{1}{2}, k)$$

$$+\frac{\Delta t}{\mu_o}\left[\begin{array}{c}\dfrac{E_x^n(i+\tfrac{1}{2}, j+1, k) - E_x^n(i+\tfrac{1}{2}, j, k)}{\Delta y} \\ -\dfrac{E_y^n(i+1, j+\tfrac{1}{2}, k) - E_y^n(i, j+\tfrac{1}{2}, k)}{\Delta x}\end{array}\right]. \qquad (6\text{-}15)$$

Since our particular application only requires non-magnetic media, our electromagnetic field solver uses these update equations to compute the H-field for all samples regardless of the media type. A given sample for each Cartesian component of the H-field is computed by using its previous sample (a whole time-step back) together with several neighboring orthogonal E-field samples (a half time-step back). As we can see, these update equations closely resemble the form of the free-space E-field formulation; the similarity of the two formulations should be expected by virtue of duality.

6.1.6 Second-Order Mur Absorbing Boundary Condition

The second-order Mur ABC used by our electromagnetic field solver is based upon applying an approximation of a one-way wave equation at the planar boundaries of the FDTD solution volume to numerically absorb impinging radiating waves. The approach can be traced back to a theory of one-way equations originally developed by Engquist and Majda [50] and can be understood in terms of the factoring of partial differential operators. Citing this theory in his seminal paper, Mur [49] devises an ABC for the FDTD method that is both practical and effective.

We begin our understanding of the second-order Mur ABC by considering the time-dependent three-dimensional wave equation [46]:

$$\frac{\partial^2 U}{\partial x^2} + \frac{\partial^2 U}{\partial y^2} + \frac{\partial^2 U}{\partial z^2} - \frac{1}{c^2}\frac{\partial^2 U}{\partial t^2} = 0 \qquad (6\text{-}16)$$

where U is a scalar field quantity and c is the free-space phase velocity (i.e., speed of light). Based on this equation, we are able to define the corresponding partial differential operator [46]:

$$L \equiv \frac{\partial^2}{\partial x^2} + \frac{\partial^2}{\partial y^2} + \frac{\partial^2}{\partial z^2} - \frac{1}{c^2}\frac{\partial^2}{\partial t^2} \equiv D_x^2 + D_y^2 + D_z^2 - \frac{1}{c^2} D_t^2 . \tag{6-17}$$

Thus, the three-dimensional wave equation can be concisely represented as follows [46]:

$$LU = 0 . \tag{6-18}$$

According to Taflove, the partial differential operator L can then be factored in the following manner [46]:

$$LU = L^+ L^- U = 0 \tag{6-19}$$

$$\text{where} \quad L^- \equiv D_x - \frac{D_t}{c}\sqrt{1 - S^2} \tag{6-20}$$

$$L^+ \equiv D_x + \frac{D_t}{c}\sqrt{1 - S^2} \tag{6-21}$$

$$\text{and} \qquad S \equiv \sqrt{\left(\frac{D_y}{D_t / c}\right)^2 + \left(\frac{D_z}{D_t / c}\right)^2} . \tag{6-22}$$

At this point, we now make use of an important finding by Engquist and Majda: Application of L^- to the field quantity U exactly absorbs a plane wave propagating toward the $x = 0$ planar boundary at any incident angle [50]. In mathematical terms,

$$L^- U = 0 . \tag{6-23}$$

As a result, the L^- operator applied at $x = 0$ acts as an exact analytical ABC for plane waves impinging on this particular planar boundary of the solution volume. Likewise, the

L^+ operator proceeds to absorb plane waves propagating at an arbitrary angle toward the opposite planar boundary of the solution volume.

The radical contained within equations (6-20) and (6-21) classifies both L^- and L^+ as pseudodifferential operators that are nonlocal in both the space and time variables [46]. Unfortunately, this particular feature prevents the direct numerical implementation of both operators as an ABC. However, the square root function can be approximated by creating a set of conventional partial differential equations able to be numerically evaluated using finite-differences. Since this approach is not exact, the resulting ABC does allow a small amount of reflection as the waves reach each planar boundary of the solution volume. Nonetheless, Taflove [46] reports that the second-order Mur ABC is able to truncate the FDTD lattice with an overall level of spurious reflections in the range of 1% to 5%. This level of performance proves to be sufficient for our purposes of providing further validation of the newly developed NZ-FZT algorithms.

For the sake of clarity and brevity, we limit our discussion to the planar boundary of the solution volume situated at $x = 0$. As we shall see, the equations for the first- and second-order Mur ABCs at this particular boundary are easily extended to formulate those required by the five other planar boundaries of the solution volume. Note that the first-order version of the ABC has been included in our discussion because it is still required by a FDTD simulation even if the second-order Mur ABC is being applied [45].

We begin by considering the one- and two-term Taylor series approximations for the square root function contained in equation (6-20) [46]:

$$\sqrt{1-S^2} \cong 1 \qquad \text{(first-order)} \qquad (6\text{-}24)$$

$$\sqrt{1-S^2} \cong 1-\frac{1}{2}S^2 \qquad \text{(second-order).} \qquad (6\text{-}25)$$

Applying these one- and two-term expansions to (6-20), we obtain the following approximations for the L^- operator [46]:

$$L^{-} \equiv D_x - \frac{D_t}{c} \qquad \text{(first-order)} \qquad (6\text{-}26)$$

$$L^{-} \equiv D_x - \frac{D_t}{c} + \frac{cD_y^2}{2D_t} + \frac{cD_z^2}{2D_t} \qquad \text{(second-order).} \qquad (6\text{-}27)$$

These equations are then used to approximate the L^{-} operator of equation (6-23) to yield the following first- and second-order ABCs at the $x = 0$ planar boundary [46]:

$$\frac{\partial U}{\partial x} - \frac{1}{c}\frac{\partial U}{\partial t} = 0 \qquad \text{(first-order)} \qquad (6\text{-}28)$$

$$\frac{\partial^2 U}{\partial x \partial t} - \frac{1}{c}\frac{\partial^2 U}{\partial t^2} + \frac{c}{2}\frac{\partial^2 U}{\partial y^2} + \frac{c}{2}\frac{\partial^2 U}{\partial z^2} = 0 \qquad \text{(second-order).} \qquad (6\text{-}29)$$

In order to apply these mathematical ABCs, they must first be put into a numerical form that is compatible with the FDTD method. Fortunately, Mur [49] is able to do just this by finding a stable finite-difference scheme to discretize both of these partial differential equations.

Partitioning the solution volume into electrically defined Yee cells as described earlier causes E_y and E_z to be the only electrical field components at the $x = 0$ planar boundary (see Figure 6.1). Having knowledge of these two field components along this planar boundary is sufficient to compute the H_x-field samples located at $x = 0$ as well as the E_x-, H_y-, and H_z-field samples located at $x = \Delta x/2$. Unfortunately, both E_y and E_z components at the $x = 0$ planar boundary cannot be calculated using the standard FDTD update equations because the needed H-field samples at $x = -\Delta x/2$ lie outside the solution volume. As a result, both of these field components are computed at the $x = 0$ planar boundary using Mur's finite-difference expressions to numerically approximate the mathematical ABCs of (6-28) and (6-29).

During the development of the finite-difference expressions, Mur chooses to approximate the partial differential equations of (6-28) and (6-29) using central

differencing both in time and space to expand the partial derivatives about an auxiliary sample point. Although the auxiliary sample points are spatially the same for both the first- and second-order Mur expressions, they do differ with respect to time: $(\frac{1}{2}, j, k+\frac{1}{2})\Big|^{n+1/2}$ for the first-order ABC (6-28); and $(\frac{1}{2}, j, k+\frac{1}{2})\Big|^{n}$ for the second-order ABC (6-29). Utilizing this approach, we obtain the first- and second-order Mur finite-difference expressions for the E_z samples situated at the $x = 0$ planar boundary [45]:

$$E_z^{n+1}(0, j, k+\tfrac{1}{2}) = E_z^{n}(1, j, k+\tfrac{1}{2}) + \frac{c\Delta t - \Delta x}{c\Delta t + \Delta x}\left[E_z^{n+1}(1, j, k+\tfrac{1}{2}) - E_z^{n}(0, j, k+\tfrac{1}{2})\right] \quad \text{(first-order)} \quad (6\text{-}30)$$

$$\begin{aligned} E_z^{n+1}(0, j, k+\tfrac{1}{2}) = {} & -E_z^{n-1}(1, j, k+\tfrac{1}{2}) \\ & + \frac{c\Delta t - \Delta x}{c\Delta t + \Delta x}\left[E_z^{n+1}(1, j, k+\tfrac{1}{2}) + E_z^{n-1}(0, j, k+\tfrac{1}{2})\right] \\ & + \frac{2\Delta x}{c\Delta t + \Delta x}\left[E_z^{n}(0, j, k+\tfrac{1}{2}) + E_z^{n}(1, j, k+\tfrac{1}{2})\right] \\ & + \frac{\Delta x (c\Delta t)^2}{2(\Delta y)^2 (c\Delta t + \Delta x)}\begin{bmatrix} E_z^{n}(0, j+1, k+\tfrac{1}{2}) - 2E_z^{n}(0, j, k+\tfrac{1}{2}) \\ +E_z^{n}(0, j-1, k+\tfrac{1}{2}) + E_z^{n}(1, j+1, k+\tfrac{1}{2}) \\ -2E_z^{n}(1, j, k+\tfrac{1}{2}) + E_z^{n}(1, j-1, k+\tfrac{1}{2}) \end{bmatrix} \\ & + \frac{\Delta x (c\Delta t)^2}{2(\Delta z)^2 (c\Delta t + \Delta x)}\begin{bmatrix} E_z^{n}(0, j, k+\tfrac{3}{2}) - 2E_z^{n}(0, j, k+\tfrac{1}{2}) \\ +E_z^{n}(0, j, k-\tfrac{1}{2}) + E_z^{n}(1, j, k+\tfrac{3}{2}) \\ -2E_z^{n}(1, j, k+\tfrac{1}{2}) + E_z^{n}(1, j, k-\tfrac{1}{2}) \end{bmatrix} \text{ (second-order).} \end{aligned} \quad (6\text{-}31)$$

Regarding the corresponding Mur expressions for the E_y samples situated at the $x = 0$ planar boundary, both can be found by applying the same central differencing approach.

Generally speaking, we can now repeat the entire procedure (with the proper modifications) to determine the corresponding first- and second-order Mur expressions for the remaining five planar boundaries of the solution volume. As a matter of fact, the first- and second-order Mur expressions required by these other planar boundaries can be subsequently found by properly modifying expressions (6-30) and (6-31) using coordinate symmetry arguments to permute all subscripts and spatial indices [46].

Upon inspection of (6-30) and (6-31), we point out that the first-order Mur expression only requires samples from a single time-step back while the second-order Mur expression needs samples from two time-steps back. Moreover, the second-order expression also requires samples from adjacent Yee cells (in both directions along the planar boundary to approximate the second-order spatial derivatives). Consequently, it is for this reason that the second-order ABC cannot be applied at the intersection of any two planar boundaries. To sidestep this difficulty, we make use of the approach recommended by Kunz and Luebbers [45]: The first-order Mur expressions update all field samples situated at the edges of the rectangular solution volume; meanwhile, the second-order Mur expressions update the other remaining samples along the faces of the planar boundaries.

6.1.7 Modeling Guidelines

Equipped with a fundamental understanding of FDTD, we now review key modeling guidelines that need to be observed when modeling a radiation structure using this computational method. Although there is always room for exceptions depending upon the application, compliance with these guidelines, more often than not, will allow us to escape the many numerical pitfalls that often crop up during a FDTD simulation. Development of these modeling guidelines is the product of many years of intense work conducted by the research community. As a result, we have prudently chosen to take advantage of this research and construct all of our FDTD models (in this chapter and the next) in a manner that carefully adheres to these established guidelines.

We begin by understanding the choice of Yee cell size for a given FDTD simulation. Fundamentally, the size of the cell must be significantly smaller that that of the shortest wavelength under consideration in order to obtain accurate results [45]. Of course basic sampling theory does impose a limit on the cell size based on the Nyquist sampling theorem (to avoid any aliasing):

$$\Delta x, \Delta y, \text{and } \Delta z \leq \frac{\lambda}{2}. \tag{6-32}$$

Nevertheless, it is important to understand that this limit is only a theoretically maximum for size of the cell. Instead, Kunz and Luebbers [45] advise using a cell size that corresponds to ten or more samples (cells) per wavelength at the highest frequency (or shortest wavelength) of interest in order to achieve accurate and stable results:

$$\Delta x, \Delta y, \text{and } \Delta z \leq \frac{\lambda}{10}. \tag{6-33}$$

Because FDTD is a volumetric computational method, the wavelength used in the modeling guideline of (6-33) must correspond to that which exists in the most electrically-dense penetrable medium that is part of a given simulation [45]. Accordingly, models containing dielectric materials will need to have smaller cells than those containing only free-space and perfect electrical conductors. Failure to observe this particular modeling guideline can result in grid dispersion errors that can severely impact the accuracy and stability of a given simulation (depending on the structure being modeled).

Another factor that must be considered when choosing the cell size is the geometry of the structure under consideration. In cases where the structures have minute geometrical features, the cell size must be made small enough to properly model the intricate details. When modeling such electrically detailed structures, one must understand that all cells in the solution volume are forced to be relatively small;

consequently, the total number of cells required to partition the solution volume may be significantly increased depending upon the structure being modeled.

Having understood the factors behind choosing the cell size for a particular FDTD simulation, we now turn our attention to determining the maximum duration for each time-step Δt. From a finite-difference perspective, the choice of time-step duration is crucial to establishing numerical stability for a given simulation. In short, a plane wave propagating through the FDTD lattice (of samples) must not pass through more than 1 cell during a single time-step [45]. Consequently, the length of each time-step Δt must comply with the stability criterion for the full three-dimensional Yee algorithm (rigorously derived by Taflove and Brodwin [51]):

$$\Delta t \leq \frac{1}{c\sqrt{\frac{1}{(\Delta x)^2}+\frac{1}{(\Delta y)^2}+\frac{1}{(\Delta z)^2}}} \tag{6-34}$$

where c represents the maximum phase velocity for a given FDTD simulation. For our application of modeling radiating structures situated in free-space, the maximum phase velocity c is taken as the speed of light.

Kunz and Luebbers [45] indicate that their experience has shown that for actual computations, the Δt value given by the equality of (6-34) does yield accurate results. Ironically, in most circumstances a smaller time-step does not necessarily provide results that are more accurate. As a matter of fact, they state that when the equality holds, simulated wave propagation most closely approximates actual wave propagation such that grid dispersion errors are minimized [45]. Nonetheless, it must be mentioned that there are always certain circumstances where numerical stability requires time-steps that are smaller than this limiting value. The interested reader is referred to [45] for details regarding these special cases. Fortunately, these anomalies have no direct bearing on our particular application; thus, we use the equality of (6-34) to compute the time-step duration Δt for all of our FDTD simulations (in this chapter and the next).

The final modeling guideline needed to be addressed is the distance the radiation structure must be from the boundaries of the solution volume. The more distant the modeled structure is from the ABC (situated at the boundaries of the solution volume) the greater the absorption of outward traveling waves [45]. This improvement in performance occurs because outward traveling waves become much more like plane waves as they get farther from the radiation structure. However, increasing the size of the free-space buffer does not come without the expense of more computation time and greater memory storage. Keeping this engineering tradeoff in mind, Kunz and Luebbers [45] quote a minimum of 10 cells between the radiation structure and all boundaries of the solution volume. Failure to comply with this modeling guideline can result in instabilities of the ABC implementation.

6.2 NZ-FZT/FDTD SOFTWARE DEVELOPMENT

6.2.1 Overview of Software

Using the FDTD approach described in the preceding sections along with the second-order Mur ABC, we are now able to put together a computational electromagnetic field solver capable of meeting the demands of our validation objective. We start this development by building upon an already existing single precision FDTD scattering code put forth by Kunz and Luebbers [45]. It is through modifications and additions to this code that we are able to construct a field solver capable of being coupled with our NZ-FZT computer software.

The code already applies the desired second-order Mur ABC at the boundaries of the solution volume using the procedure described earlier (see 6.1.6). However, during the computation of the field samples, the existing code makes use of formulations based on scattered-fields only and thus requires a specified incident E-field as its excitation. Because our application requires us to model a radiation structure that is the sole source of any field disturbances, we proceed to modify the code so that it uses the total-field

formulations (described in the preceding sections) instead to update all field samples. Furthermore, the FDTD field solver must now have the ability to handle localized field sources so that the modeled radiation structure can be excited. This capability is necessary for our particular application because we are not using a specified incident plane wave as the excitation mechanism. Included in this basic feature is the ability to use a variety of spatial configurations and temporal waveforms in order to model almost any localized field source (electric and/or magnetic) that presents itself.

Regarding the interface between the field solver and our NZ-FZT computer software, it is accomplished by spatially sampling the near-zone E-field along the prolate/oblate spheroidal transformation surface using the spheroidal sample grid specified in equations (2-106a)-(2-109a) (see also Figure 2.2). However, the FDTD algorithm delivers E-field samples corresponding to a Cartesian lattice that conforms to the geometry specified in Figure 6.1. Fortunately, we are able to reconcile this difference in sample grids by using a multidimensional interpolation scheme to extract the near-zone E-field samples along the spheroidal surface from their neighboring Cartesian samples. The extracted near-zone E-field samples are then converted to the frequency-domain for a specified frequency by applying a complex running discrete Fourier transform (DFT). At the end of the FDTD simulation, the field solver renders samples of the near-zone E-field along the prolate/oblate spheroidal surface at this specified frequency. (Note that multiple concurrent running DFTs can be used if additional frequencies are desired.) This near-zone information is then passed from the field solver to the NZ-FZT computer software by way of a single precision ASCII data file. Further details behind this involved extraction process are given in the section that follows.

Depicted in Figure 6.3 is a top-level flowchart indicating the overall process implemented by the FDTD electromagnetic field solver. Initially, the developed software reads the simulation setup (specified by the user) from multiple ASCII input data files. Contained in these files is the following setup information: (1) dimensions of the cell size and the solution volume; (2) definition of dielectric materials used; (3) configuration of electrical materials to form the radiation structure; (4) configuration of electric and

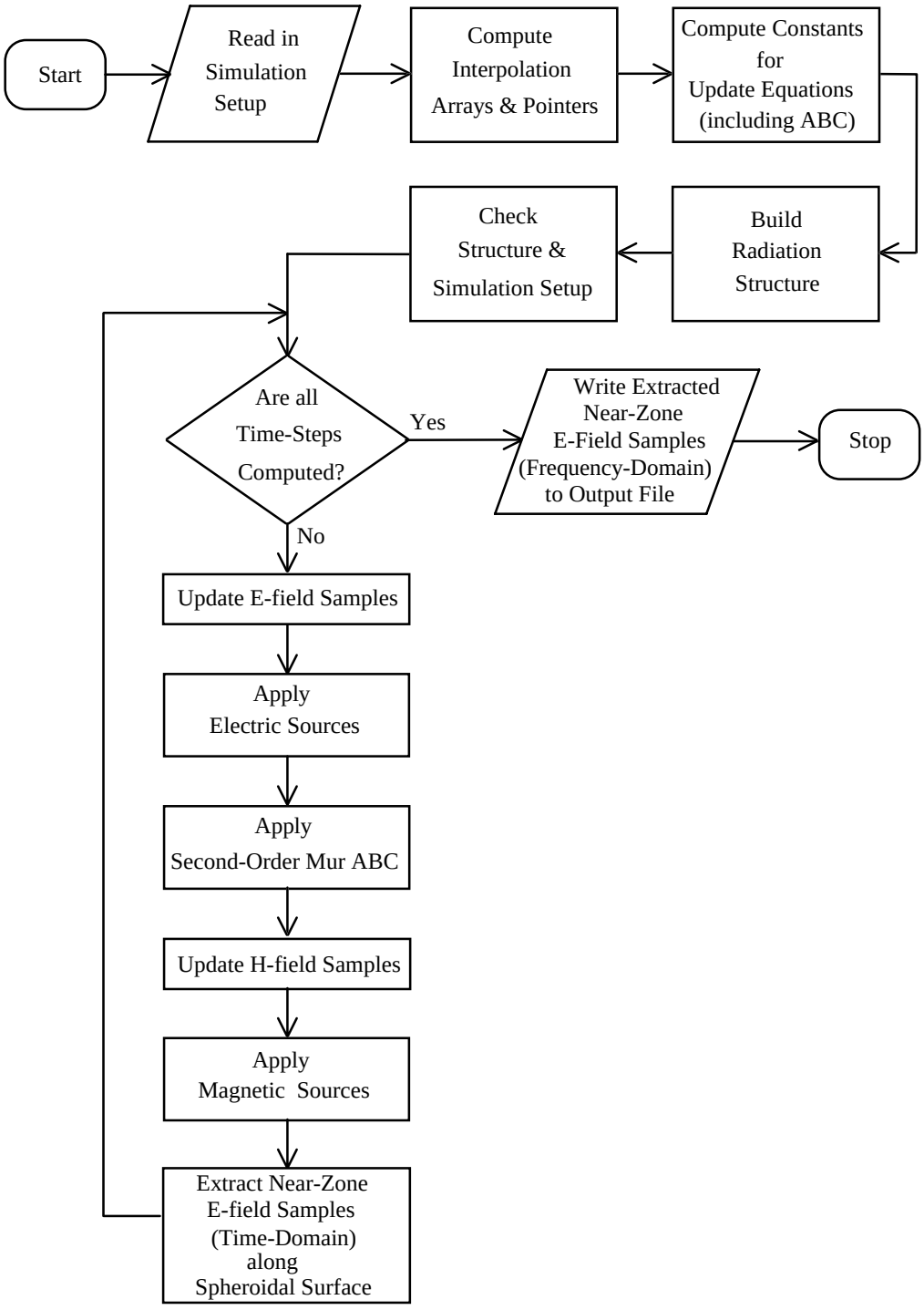

Figure 6.3 Flowchart of FDTD electromagnetic field solver.

magnetic sources (spatially and temporally); (5) number of time-steps in the simulation; (6) choice of prolate or oblate spheroidal transformation surface; (7) location and shape of the prolate/oblate spheroidal surface; (8) fineness of corresponding spheroidal sample grid; and (9) configuration of the DFT (viz., observation interval, window type, and frequency index at which the near-zone E-field samples are to be extracted).

After reading all of this information, the field solver begins by computing the parameters necessary to launch a successful FDTD simulation of the radiation structure. First, the interpolation arrays and pointers associated with the near-zone E-field extraction process must be computed and stored. This step is followed by computing and storing the constants required to implement the FDTD update equations (described earlier in this chapter) as well as those required for the first- and second-order Mur ABCs. For obvious reasons, storage of all of this information at the start of the process has a dramatic effect on reducing total computation time.

The field solver then proceeds to build the specified radiation structure by locating differently defined electric materials at various points of the lattice as per the user's specifications. This step is accomplished by creating a set of pointers for each Cartesian component that indicates the material located at each lattice point. When updating the E-field samples, the field solver looks at these material pointers to determine the proper FDTD formulation to use. In addition, the field solver also utilizes these pointers to efficiently retrieve from storage the constants necessary to implement each respective E-field formulation.

The last step before starting the computation of the E- and H-field samples is to check that the modeled radiation structure and corresponding simulation setup are free of errors due to invalid input data. By checking the data at the start of a simulation, the field solver is able to flag the user of obvious errors before any lengthy computations are made. Toward this end, this step in the process can help avoid many needless hours of computation time.

With the preliminary computations and the simulation setup completed, the field solver is ready to implement the two-step finite-difference process described earlier in

Figure 6.2. For our application, it is assumed that all E- and H-fields are at rest before the start of the simulation. The field solver begins the computations associated with each time-step by first updating the set of E-field samples. For each E-field sample, the proper formulation must be used based upon the material present at its respective lattice point (specified by the material pointers). If any electric sources are present, they are at this time applied to the simulation by forcing all E-fields that make up a given spatial configuration to values that depend on a user specified temporal waveform. Following this, the field solver then proceeds to apply the second-order Mur ABC to update the E-field samples situated at the boundaries of the solution volume. We recall that the E-field samples located at the edges of the solution volume (i.e., the intersection of two planar boundaries) must be computed using the corresponding first-order Mur expressions. The second part of this two-step finite-difference process requires computation of the corresponding H-field samples. Because our application only addresses non-magnetic media, the field solver always uses the non-magnetic H-field formulation to update all H-field samples. It is at this point in the procedural sequence that magnetic sources, if any, are applied to the corresponding H-field samples in much of the same way that the electric sources are handled. With the computation of all E- and H-field samples for a given time-step completed, the field solver now proceeds to interpolate the near-zone E-field samples along the spheroidal surface using neighboring Cartesian E-field samples. All interpolated values then contribute to their own individual running complex summation that ultimately implements a DFT at the end of the simulation run. This entire two-step finite-difference process is then repeated until the desired number of computed time-steps has been performed. At the completion of this loop, the field solver proceeds to place the extracted near-zone E-field phasor data (along the prolate/oblate spheroidal transformation surface) in a single precision ASCII data file that is suitable for processing by our NZ-FZT software.

6.2.2 Extraction of Near-Zone E-Field Samples Along the Prolate/Oblate Spheroidal Surface

As previously mentioned, a multidimensional interpolation scheme is used to extract near-zone E-field samples along the spheroidal surface from the Cartesian samples provided by the FDTD algorithm. Our field solver evokes this interpolation scheme each and every time-step to form the required set of near-zone E-field samples that coincides with the spheroidal sample grid. Each of these samples is then converted to the frequency-domain for a particular frequency through the use of a complex running DFT. In short, all three vector components (Cartesian) of each spheroidal E-field sample contribute on-the-fly (at each time-step) to their own individual complex running summations such that their DFTs (for a specified frequency) are effectively implemented at the end of the simulation. As required by our NZ-FZT software, the final result of this extraction process is a phasor representation (corresponding to the specified frequency) of the near-zone E-field samples along the spheroidal transformation surface (coinciding with the user specified spheroidal sample grid).

The first step in the interpolation process is to assign Cartesian coordinates to the spheroidal sample grid as well as to the FDTD three-dimensional lattice of the E-field. Initially, the user defines the shape of the prolate/oblate spheroidal surface by providing the parameters ξ_o and a (both introduced in Chapter 2), and specifies its location by defining its center with respect to the reference corner of the solution volume, viz., the corner that corresponds to the origin. In addition to these parameters, the number of samples in the azimuthal direction and the number of samples in the angular direction are then supplied in order to specify the desired fineness of the spheroidal sample grid. Using this information together with the respective prolate/oblate spheroidal-to-Cartesian transformation provided in equations (2-1)-(2-5), the field solver then computes the Cartesian coordinates of the spheroidal sample grid in relation to the reference corner of the solution volume (using the proper translation vector to account for the location of the spheroidal surface). Whereas only one set of Cartesian coordinates is required to describe the spheroidal sample grid, three sets of Cartesian coordinates are necessary to describe

the FDTD E-field lattice. Referring to Figure 6.1, one can see that the need for three sets of coordinates arises from the fact that the spatial locations of the E-field samples are offset with respect to one another. That is, the three-dimensional E-field lattice can, in effect, be viewed as three separate grids (offset from one another) with each corresponding to a vector component of the computed E-field. Cartesian coordinates for each of these grids are easily found by employing the definition of the Yee cell geometry discussed earlier in this chapter (see 6.1.1). In order to maintain a coordinate system that is consistent with the spheroidal sample grid, the coordinates of these three separate grids are also computed in relation to the reference corner of the solution volume.

Mathematically speaking, the FDTD algorithm delivers sampled representations of three distinct scalar functions (for a given time-step) that happen to correspond to the vector components of the computed E-field: $E_x^{n+1}(i+\frac{1}{2}, j, k)$, $E_y^{n+1}(i, j+\frac{1}{2}, k)$, and $E_z^{n+1}(i, j, k+\frac{1}{2})$. Meanwhile, the desired spheroidal samples (in the time-domain), i.e., $E_x^{n+1}(\vartheta_i', \varphi_j')$, $E_y^{n+1}(\vartheta_i', \varphi_j')$, and $E_z^{n+1}(\vartheta_i', \varphi_j')$, represent samples of the same three scalar functions that are spatially situated in-between these computed data points. (Note that although both sets of E-field samples are referenced using the indices *i* and *j*, the symbols represent entirely different sample indices. Ambiguity is easily avoided by considering the context of usage.) Accordingly, we are able to utilize an interpolation scheme in three-dimensions to approximate these in-between values for each vector component at a given time-step: more precisely, we find $E_x^{n+1}(\vartheta_i', \varphi_j')$ through interpolation of $E_x^{n+1}(i+\frac{1}{2}, j, k)$, $E_y^{n+1}(\vartheta_i', \varphi_j')$ through interpolation of $E_y^{n+1}(i, j+\frac{1}{2}, k)$, and $E_z^{n+1}(\vartheta_i', \varphi_j')$ through interpolation of $E_z^{n+1}(i, j, k+\frac{1}{2})$.

Because each vector component makes use of the same interpolation process, we need only discuss the method with respect to a given sampled scalar function *g* (where *g* represents any one of the field components E_x, E_y, and E_z computed by the field solver). The interpolation process continues by overlaying the spheroidal sample grid with the Cartesian grid corresponding to the field component under consideration. By

comparing the Cartesian coordinates of these two overlaid grids, the field solver is able to determine which eight FDTD data points immediately surround each spheroidal sample. For the sake of clarity, the geometry of this three-dimensional interpolation scheme for a given spheroidal sample $g_s^{n+1} = g(x_s, y_s, z_s)|^{n+1}$ is illustrated in Figure 6.4. Employing a shorthand notation, we designate the values of the eight neighboring data points (for a given time-step) with the variables g_1^{n+1}, g_2^{n+1}, ... , g_8^{n+1} and define them as follows with respect to the scalar function *g*:

$$g_1^{n+1} = g(x_i, y_j, z_k)|^{n+1}, \qquad g_2^{n+1} = g(x_{i+1}, y_j, z_k)|^{n+1},$$

$$g_3^{n+1} = g(x_{i+1}, y_{j+1}, z_k)|^{n+1}, \qquad g_4^{n+1} = g(x_i, y_{j+1}, z_k)|^{n+1},$$

$$g_5^{n+1} = g(x_i, y_j, z_{k+1})|^{n+1}, \qquad g_6^{n+1} = g(x_{i+1}, y_j, z_{k+1})|^{n+1},$$

$$g_7^{n+1} = g(x_{i+1}, y_{j+1}, z_{k+1})|^{n+1}, \qquad g_8^{n+1} = g(x_i, y_{j+1}, z_{k+1})|^{n+1}.$$

(Note how the configuration of these eight data points corresponds to the arrangement shown in Figure 6.4.)

The next step in the interpolation process is to determine where each spheroidal sample is situated in relation to its set of eight neighboring data points. For each spheroidal sample point, we do this by creating the following three auxiliary parameters:

$$t \equiv \frac{x_s - x_i}{x_{i+1} - x_i} \equiv \frac{x_s - x_i}{\Delta x} \tag{6-35}$$

$$u \equiv \frac{y_s - y_j}{y_{j+1} - y_j} \equiv \frac{y_s - y_j}{\Delta y} \tag{6-36}$$

$$v \equiv \frac{z_s - z_k}{z_{k+1} - z_k} \equiv \frac{z_s - z_k}{\Delta z}. \tag{6-37}$$

(Note that the variable *t* does not refer to time in this context.) In essence, these auxiliary parameters represent the fractional distance (with respect to all eight data points) between

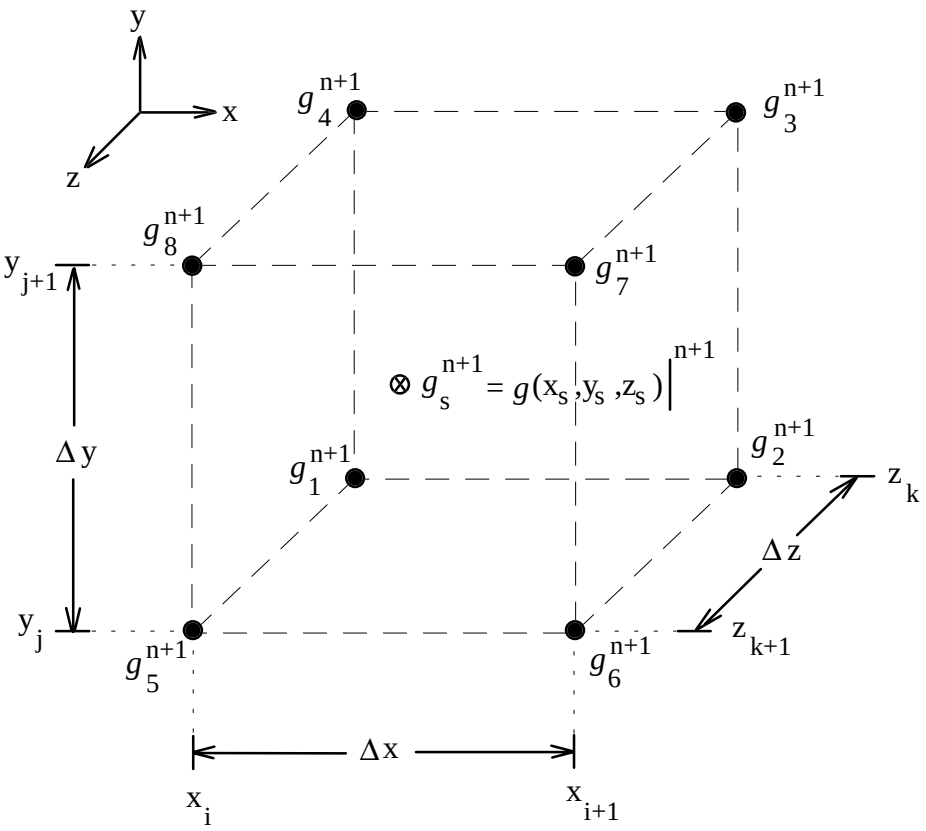

Figure 6.4 Geometry of the three-dimensional interpolation scheme for a given spheroidal sample g_s^{n+1}.

the spheroidal sample g_s^{n+1} and the reference data point g_1^{n+1}. Furthermore, parameters *t*, *u*, and *v* respectively represent all three Cartesian components of this fractional distance. As a result, these auxiliary parameters must always assume values on the interval between zero and unity including at least one of these two endpoints. Use of an endpoint is essential to representing a spheroidal sample point that happens to lie in any of the planes that coincide with the Cartesian sample grid under consideration. Because our FDTD field solver uses a uniform E-field lattice, we can replace the denominators of equations (6-35)-(6-37) with their respective spatial sample periods, viz., Δx, Δy, and Δz.

Using these auxiliary parameters along with the set of eight neighboring data points, we are able to define the following function to interpolate a spheroidal sample at a given time-step:

$$\begin{aligned} g_s^{n+1} = g(x_s, y_s, z_s)\,|^{n+1} = \\ & (1-t)(1-u)(1-v)g_1^{n+1} + t(1-u)(1-v)g_2^{n+1} \\ & + tu(1-v)g_3^{n+1} + (1-t)u(1-v)g_4^{n+1} + (1-t)(1-u)vg_5^{n+1} \\ & + t(1-u)vg_6^{n+1} + tuvg_7^{n+1} + (1-t)uvg_8^{n+1}. \end{aligned} \tag{6-38}$$

This three-dimensional interpolation scheme is the natural extension of the two-dimensional version provided in *Numerical Recipes in FORTRAN* [37]. It can be rigorously derived by fitting a three-variable polynomial of the third degree to the eight neighboring data points. For the special case where the spheroidal sample g_s^{n+1} is situated equidistant from all eight data points, parameters *t*, *u*, and *v* all assume a value of one-half, and the result is the sum of g_1^{n+1}, g_2^{n+1}, ... , g_8^{n+1} divided by eight. Although there are higher-order interpolation techniques that can provide more accurate results (at the expense of having to conduct substantially more computations), our experience has shown that this particular one performs quite well for our purposes.

Once again, the field solver must individually carryout the described interpolation process for all three vector components E_x, E_y, and E_z during each time-step. For each

vector component, the field solver begins by finding which eight FDTD data points immediately surround each spheroidal sample (note that the spatial indices for g_1^{n+1}, g_2^{n+1}, ... , g_8^{n+1} must be made to properly correspond to each respective FDTD sample grid). Consequently, the field solver must somehow store the information of which twenty-four data points (i.e., eight data points per vector component) are necessary to interpolate each spheroidal E-field sample. Even though the same twenty-four Cartesian sample points are used to interpolate each spheroidal sample regardless of the time-step, storage of this information can become quite cumbersome depending upon the desired fineness of the spheroidal sample grid. Fortunately, the arrangement of each set of eight data points is always the same by definition (see Figure 6.4); thus, knowledge of which FDTD samples constitute g_2^{n+1}, g_3^{n+1}, ... , g_8^{n+1} is implied based upon the reference data point g_1^{n+1}. As a result, only one pointer per Cartesian component is needed to convey the given set of surrounding eight data points. In total, the field solver only has to store three pointers per spheroidal sample point to indicate all three sets of surrounding eight data points. As one can see, this approach is a significant improvement over storing twenty-four pointers per spheroidal sample point. Finally, each of these pointers naturally must contain three indices in order to properly point to a given reference data point.

Having determined which twenty-four data points are necessary to interpolate each spheroidal E-field sample, the field solver must then determine where each spheroidal sample point lies in relation to these known data points. It does this by computing and storing three sets of auxiliary parameters *t*, *u*, and *v* (using equations (6-35)-(6-37)) with each set corresponding to the vector components E_x, E_y, and E_z. In summary, the field solver requires a total of three pointers and nine auxiliary parameters per spheroidal sample point in order to conduct the interpolation for all time-steps during a given simulation.

As indicated by the flowchart shown in Figure 6.3, the field solver computes and stores this interpolation information only once during a particular FDTD simulation. This approach is possible because the set of all pointers and auxiliary parameters is the same

for all time-steps. At the end of every time-step, the field solver uses this stored information together with equation (6-38) to interpolate the near-zone E-field samples along the prolate/oblate spheroidal surface from the computed FDTD lattice. In procedural terms, the field solver performs this operation for each time-step by computing g_s^{n+1} for all three vector components and then assigning the results to their respective spheroidal samples $E_x^{n+1}(\vartheta_i', \varphi_j')$, $E_y^{n+1}(\vartheta_i', \varphi_j')$, and $E_z^{n+1}(\vartheta_i', \varphi_j')$. It is worth noting that equation (6-38) can be more efficiently implemented than that which is written by factoring and then locally storing some of its constituent subexpressions.

With a grasp of the interpolation part of the extraction process, we now proceed to focus our attention on converting the interpolated time-domain data to the frequency-domain for a specified frequency. Specifically, this is done for every spheroidal grid point by individually applying a complex running DFT to the temporal sequences of the interpolated vector components: $E_x^{n+1}(\vartheta_i', \varphi_j')$, $E_y^{n+1}(\vartheta_i', \varphi_j')$, and $E_z^{n+1}(\vartheta_i', \varphi_j')$. Thus, three separate running DFTs must be conducted for each spheroidal grid point $(\vartheta_i', \varphi_j')$. Once again, because this part of the extraction process is the same for each vector component, we need only examine it in terms of a given time-sampled sequence g_s^{n+1} (where g_s^{n+1} represents either $E_x^{n+1}(\vartheta_i', \varphi_j')$, $E_y^{n+1}(\vartheta_i', \varphi_j')$, or $E_z^{n+1}(\vartheta_i', \varphi_j')$).

The purpose of using a DFT during our extraction process is to compute the analog spectrum of the spheroidal sample g_s from its corresponding time-sampled sequence g_s^{n+1}. However, it must be emphasized that the DFT will only yield an approximation of the analog spectrum belonging to g_s. As we shall see, the accuracy of this approximation shall depend upon the spectral content of the sequence being processed. Consequently, the user cannot blindly apply the transform to a given sample sequence and confidently expect reasonable results. An understanding of the transform method as well as the sequence under consideration is required.

In order to avoid the pitfalls typically associated with DFT processing, it is necessary for the user to have total control over the transform operation. Accordingly, the

user must configure the DFT operation during the simulation setup by specifying the following transform parameters: the observation interval, the window type, and the frequency index at which the near-zone E-field samples are to be extracted (all of which are included in the simulation setup files). As for the sample period Δt used during the DFT process, it naturally conforms to the time-step duration employed by the FDTD simulation (i.e., computed using the equality of (6-34)).

Because g_s^{n+1} is a time-sampled version of the scalar function g_s, its spectrum actually corresponds to the spectrum of g_s repeated about integer multiples of the sample rate f_s (where $f_s = 1/\Delta t$) [52]. Furthermore, the spectrum of g_s^{n+1} is also scaled in amplitude by a multiplying factor of f_s as compared to the original spectrum of g_s (due to the sampling process; see [52]). In other words, the periodic spectrum of g_s^{n+1} is made up of a superposition of the scaled spectrum of g_s (multiplied by f_s) and an infinite number of its translated images which are each centered about integer multiples of f_s. Unfortunately, this superposition can lead to unwanted overlapping of the spectrum of g_s with its translated images. In cases where this unwanted effect crops up, the spectrum of g_s^{n+1} becomes a corrupted version of the original spectrum of g_s in the region where the overlapping occurs. Degradation of the spectrum due to this particular effect is often referred to as aliasing. Fundamental digital signal processing theory indicates that one may avoid the problem of aliasing by satisfying the Nyquist sampling theorem and ensuring that the sample rate f_s is always greater than twice the highest frequency component contained within the original spectrum of g_s (assuming that the original spectrum is bandlimited) [52].

Practical application of the DFT requires that the sequence under consideration be finite in length over some observation interval T with some sort of window function w^n applied. Consequently, the resulting spectrum computed by the DFT is a version of the analog spectrum of g_s that is further modified from the spectrum of g_s^{n+1}. More specifically, the spectrum delivered by the DFT is the convolution (in the frequency-

domain) of the Fourier transform of the window function with the periodic spectrum of g_s^{n+1} [52]. In essence, the DFT process delivers a sampled version of this convolved spectrum with samples at a discrete set of frequencies separated by the reciprocal of the observation interval, i.e., $\Delta f = 1/T$ [52]. As one can see, DFT processing significantly alters the original spectrum of g_s. Fortunately, with prudent and careful application of this transform, we are able to compute a fairly accurate approximation of the analog spectrum belonging to the spheroidal spatial sample g_s. As always, the accuracy of the approximation can be improved at the expense of performing significantly more calculations.

The user indirectly specifies the observation interval T by indicating the number of samples N to use during DFT processing. For all of our computational models (in this chapter and the next), the number of DFT samples is always made to equal the number of time-steps in the FDTD simulation. Thus, we shall not discriminate between these two parameters for the remainder of our discussion. However, the values of both parameters can be made to differ if the use of zero padding were to become necessary.

Unfortunately, truncating (or windowing) the time-domain response of the spheroidal sample g_s can cause an additional unwanted effect on the results of our DFT processing: spectral leakage. We begin by understanding that spectral components that are not part of the DFT basis set are not periodic in the observation window (that is, their respective periods do not fit exactly into the observation interval T). These non-basis set spectral components cause the periodic extension of the spheroidal sample g_s to exhibit discontinuities at the boundaries of the observation interval. In turn, these discontinuities are then responsible for unwanted spectral contributions (or leakage) over the entire basis set. Depending upon the sequence being processed, windowing of the spheroidal sample g_s can cause spectral energy to leak from one frequency to another when using the DFT to approximate its spectrum. For a more detailed understanding of the theory behind this unwanted effect, we direct the interested reader to the comprehensive survey article on windowing by Harris [53].

The basic window that is often used is the rectangular (or Dirichlet) and is defined as unity over the observation interval [53]:

$$w^n = 1 \qquad \text{where } n = 0,1,\ldots,N-1. \tag{6-39}$$

Unfortunately, this particular window does not provide much in the way of mitigating spectral leakage. In order to minimize this unwanted processing effect, the sampled sequence can be weighted by a non-rectangular window that smoothly approaches zero at the beginning and end of the observation interval [52]. The non-rectangular window must be designed to match as many orders of derivative (of the weighted data) as possible at the boundaries of the observation interval [53]. Furthermore, the window should also be designed to be an even function centered about the $N/2$ sequence position (i.e., including the implied sample at $n = N$; see [53]).

For our particular application, we need to truncate the time-domain E-field samples along the spheroidal transformation surface (computed using the FDTD algorithm) in a manner that is as smooth as possible. Although Harris [53] catalogues over twenty windows able to successfully reduce spectral leakage, we will only make use of one of them to derive the benefits of non-rectangular windowing: the Hamming window. We choose this particular window because Ziemer *et al.* [52] recommend using it when wanting to resolve closely spaced frequency components while minimizing leakage from one component to another (note that it has a highest sidelobe level of -43 dB and a 3 dB bandwidth of 1.30 bins [53]). Typically, the Hamming window is defined as follows over the observation interval [53]:

$$w^n = 0.54 - 0.46\cos\left[\frac{2\pi}{N}n\right] \quad \text{where } n = 0,1,\ldots,N-1. \tag{6-40}$$

For each of these window functions, we must consider its normalized coherent gain (*NCG*). Harris [53] defines this parameter as the sum of all window terms normalized with respect to the total number of terms N:

$$NCG = \frac{1}{N}\sum_{n} w^n \qquad \text{where } n = 0,1,\ldots,N-1. \tag{6-41}$$

Applying this definition to the windows given in (6-39) and (6-40), we are able to determine their respective *NCG*: rectangular window, $NCG = 1.0$; and Hamming window, $NCG = 0.54$. Because all windows are defined in a manner where the weighting coefficients are between zero and unity, i.e., $0 \le w^n \le 1$, the rectangular window intrinsically has the largest *NCG*. Thus, in general, the *NCG* for any other window is reduced (from unity) due to the window function smoothly approaching zero near the boundaries. This reduction of the *NCG* is important because it represents a known bias on spectral amplitudes [53]. As we shall see, we will need to make use of this parameter to remove this bias when approximating the analog spectrum of the spheroidal sample g_s.

In the process of converting the interpolated time-domain data to the frequency-domain, we make use of the following definition of the DFT [52]:

$$X^k = \frac{1}{N}\sum_{n=0}^{N-1} x^n\, e^{-j(2\pi/N)nk} \qquad \text{where } k = 0,1,\ldots,N-1. \tag{6-42}$$

We have elected to use this particular form of the DFT where there is a negative sign in the complex exponential because it remains consistent with our phasor (or time-harmonic) convention that assumes a $e^{+j\omega t}$ time dependence. Secondly, the $1/N$ factor is included outside the finite summation in order to account for the difference in amplitude between the analog spectrum and its corresponding windowed/time-sampled version (i.e., obtained by convolving in the frequency-domain the periodic spectrum of the time-sampled sequence with the Fourier transform of the rectangular window function).

It is important to understand that the DFT operation defined in (6-42) computes the spectrum in the following format: zero frequency corresponds to $k = 0$; positive

frequencies $0 < f < \frac{1}{2} f_s$ correspond to values where $1 \le k < N/2$; negative frequencies $-\frac{1}{2} f_s < f < 0$ correspond to values where $N/2 < k \le N-1$; and the spectral position at $k = N/2$ corresponds to both $f = \frac{1}{2} f_s$ and $f = -\frac{1}{2} f_s$. Because our NZ-FZT algorithms have been designed to operate on E-field samples conforming to a $e^{+j\omega t}$ time-harmonic convention (i.e., a positive-rotating phasor), our FDTD field solver only has to address non-negative frequencies. Recalling that the sampled frequencies are separated by the reciprocal of the observation interval, i.e., $\Delta f = 1/T = 1/(N\Delta t)$, we use the following expression to determine which index *k* corresponds to the desired non-negative spectral component:

$$f_k = k\,\Delta f = \frac{k}{N\Delta t} \quad \text{where } 0 \le k < N/2 \text{ and } 0 \le f_k < \tfrac{1}{2} f_s. \qquad (6\text{-}43)$$

(Note that all of the discussed expressions apply to both even and odd values of N. In the case where N is even, $N/2$ is of integer value and as such, has a sequence position that coincides with an actual sample. To the contrary, when N is odd, $N/2$ is not an integer and the sequence position actually exists in-between two samples.)

We continue our discussion by understanding that the time-sampled sequence g_s^{n+1} is a real sequence with no imaginary components. Consequently, the resulting spectrum computed by the DFT is double-sided and includes both positive and negative frequencies. However, our NZ-FZT algorithms have been designed to accept E-field samples in the frequency-domain that are single-sided and comply with the $e^{+j\omega t}$ time-harmonic convention. Fortunately, we have a simple way to reconcile this difference in time-domain representations: double the amplitude of the DFT results and only use non-negative frequencies where $0 \le f_k < \frac{1}{2} f_s$. The reason for applying the factor of two can be easily understood by decomposing a real sinusoidal signal into its complex exponentials and comparing it to its time-harmonic counterpart (i.e., a positive-rotating phasor).

Equipped with an understanding of fundamental DFT processing, we are now able to approximate the analog spectrum of the spheroidal sample g_s using the DFT operation defined in (6-42):

$$G_s^k = \frac{2}{N(NCG)} \sum_{n=0}^{N-1} w^n g_s^n \, e^{-j(2\pi/N)nk} \qquad (6\text{-}44)$$

where $0 \le k < N/2$ and $0 \le f_k < \frac{1}{2} f_s$.

As we can see, the DFT process of (6-44) allows the user to apply additional window functions other than rectangular so that spectral leakage can be reduced. Correspondingly, the expression must be then divided by the *NCG* of the applied window function in order to remove its resulting bias on the spectral amplitude. All of our computational models (in this chapter and the next) utilize the Hamming window as defined in (6-40) for this part of the extraction process. As for the factor of two that is outside the finite summation of (6-44), it is included to account for the difference in time-domain representations (i.e., phasor versus real signal format).

The field solver uses the described DFT process to carry out the latter portion of the extraction process that converts the interpolated time-domain data to the frequency-domain for a single frequency. The software performs this conversion by individually applying (6-44) for a given frequency index *k* (specified by the user) to the temporal sequences of the interpolated vector components: $E_x^{n+1}(\vartheta_i', \varphi_j')$, $E_y^{n+1}(\vartheta_i', \varphi_j')$, and $E_z^{n+1}(\vartheta_i', \varphi_j')$ (where in the process g_s^{n+1} represents each vector component). This procedure is then performed for each grid point $(\vartheta_i', \varphi_j')$ situated along the spheroidal transformation surface. Experience has shown that in order to get single precision results from the DFT process, the complex summation must be conducted in double precision. At the conclusion of the simulation, the results of the individual DFT processes yield the extracted near-zone E-field samples along the spheroidal surface: $E_x(\vartheta_i', \varphi_j')$,

$E_y(\vartheta_i', \varphi_j')$, and $E_z(\vartheta_i', \varphi_j')$ (where in the process G_s^k represents each vector component). The time-step superscript has been dropped from the notation because the extracted quantities have been converted to the frequency domain; more specifically, the near-zone E-field samples along the spheroidal surface are now phasor quantities at the frequency corresponding to the user specified index *k* (found using equation (6-43)). These extracted near-zone E-field samples are then passed from the FDTD field solver to the NZ-FZT computer software by way of a single precision ASCII data file.

Regarding the implementation of the time- to frequency-domain conversion process, one may wonder as to why we elected to use a DFT instead of a fast Fourier transform (FFT). Conventional wisdom indicates that the FFT algorithm is always more computationally efficient than the DFT. This statement is true if our application required the entire spectrum corresponding to all indices of *k*. However, this is not the case. As we have already seen, our NZ-FZT process only calls for the near-zone E-field samples along the spheroidal transformation surface for a single frequency. Conducting a full FFT would involve many additional computations in order to obtain the same result as the DFT for a single frequency index. Ultimately, the field solver would end up wasting the FFT computed results for the other $N-1$ frequencies.

Another important advantage that the DFT approach has is that it can be computed in an on-the-fly manner. For each time-step, the field solver applies the respective window coefficient to the interpolated spheroidal sample and then adds it to a complex partial sum that is stored in a running accumulator. At the end of the simulation after all time-samples of g_s^{n+1} have contributed to the finite summation of (6-44), the outcome of the running DFT is inherently found sitting in the accumulator. The reason for using this on-the-fly DFT method is that it greatly improves memory storage efficiency: the field solver is only required to store one complex quantity per each time-sampled sequence g_s^{n+1} instead of *N*. (Note that with three individual DFTs for each spheroidal grid point $(\vartheta_i', \varphi_j')$, memory storage of *N* complex quantities per each time-sampled sequence can become quite cumbersome.) Finally, illustrated in Figure 6.5 is a

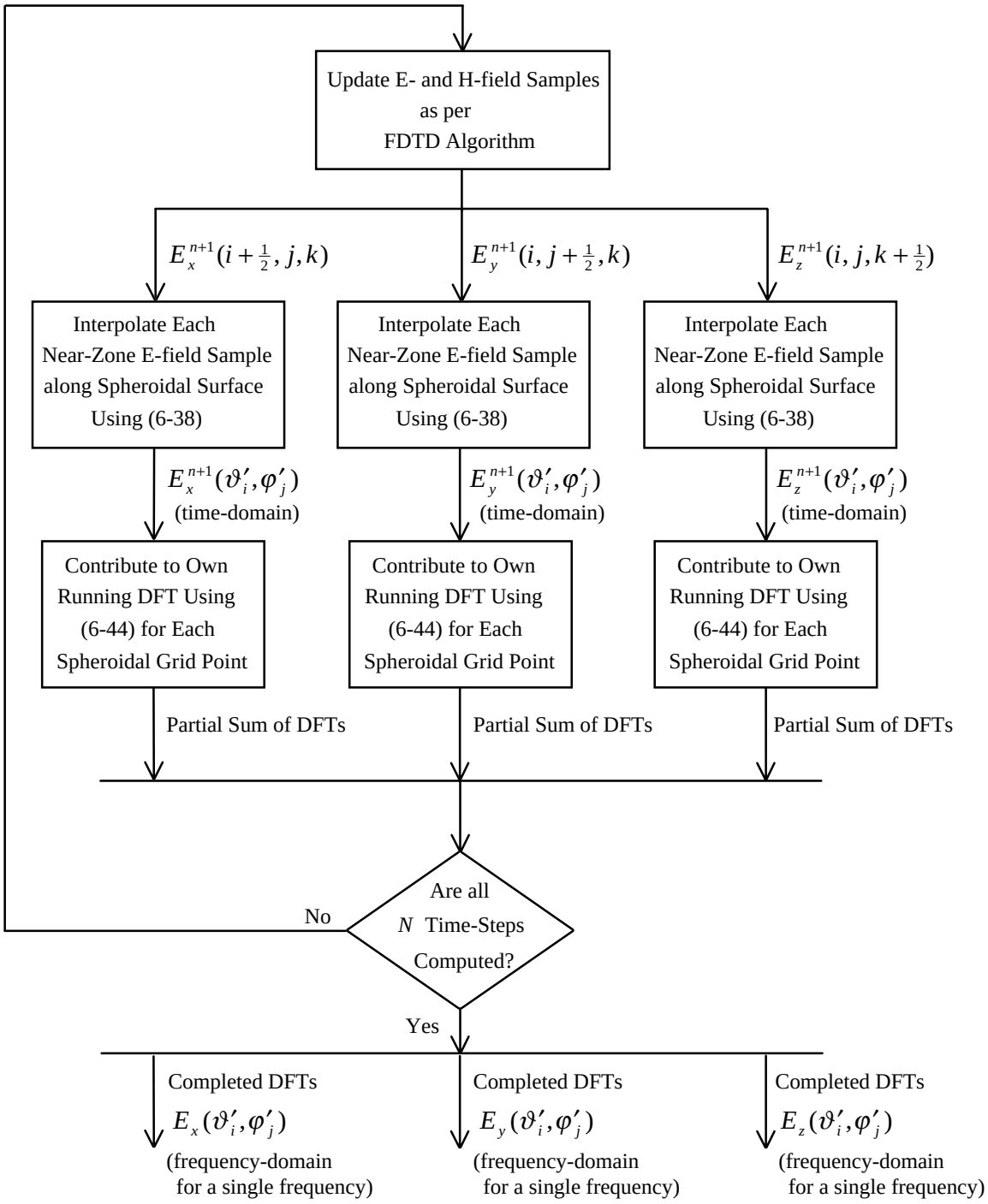

Figure 6.5 Block diagram depicting the overall extraction process of near-zone E-field samples along the prolate/oblate spheroidal transformation surface.

block diagram depicting the overall extraction process of near-zone E-field samples along the prolate/oblate spheroidal transformation surface.

6.3 NZ-FZT/FDTD END-TO-END TEST EMPLOYING THE ANALYTICAL BENCHMARK

6.3.1 NZ-FZT/FDTD Model of the Analytical Benchmark

Once again, the objective of this end-to-end test is to validate and assess the overall performance of the combined NZ-FZT/FDTD software. As we shall see, the combined software performs extremely well when computing the far-zone E-field of the analytical benchmark dipole. It is because of this level of performance that we have a great deal of confidence when modeling other radiation structures with our combined software package. In addition, by characterizing the accuracy of the NZ-FZT/FDTD model of the analytical benchmark, we also gain some insight into how well the combined software package models radiation from our empirical benchmark (see Chapter 7).

In order to maintain a control in our numerical experiment, we choose to make use of the same test setups that are employed during our centered dipole numerical tests (see 5.4.1 for the specifics). However, this time the near-zone E-field along the spheroidal surface is computed by our FDTD model of the analytical benchmark dipole (using the developed field solver) as opposed to the analytical benchmark software driver. Conducting the end-to-end test in this fashion allows us to understand how much of the resulting error in the combined process truly stems from the FDTD portion of our NZ-FZT/FDTD model.

We continue assembling our end-to-end test by developing the required NZ-FZT/FDTD model of the benchmark dipole. From Chapter 5, the z-directed dipole is of infinitesimal radius with a sinusoidal current distribution. To be more specific, the distribution of the current along the filament dipole of length l is defined in terms of the free-space propagation constant k as follows [27]:

$$I(z) = \begin{cases} I_o \sin\left[k\left(\frac{l}{2} - z\right)\right] & 0 \le z \le l/2, \\ I_o \sin\left[k\left(\frac{l}{2} + z\right)\right] & -l/2 \le z \le 0. \end{cases} \tag{6-45}$$

Note that it is this particular current distribution that leads to the closed form representation of the near-zone E-field presented in equations (5-1)-(5-6). Thus, in order to simulate the analytical benchmark dipole, our model must emulate a filament of current that obeys the distribution of (6-45). We do so by representing samples of current along the dipole with a series of five magnetic loops that surrounds a perfect electric conductor (PEC) core. However, before we can proceed, the layout of the FDTD solution volume must first be considered.

The first step in developing the setup of the solution volume is determining the size of the Yee cells. For the sake of simplicity, we shall choose to make the free-space wavelength of our NZ-FZT/FDTD model equal to unity, i.e., $\lambda_o = 1\,m$. Since we want five magnetic loops to exactly represent the tenth of a wavelength dipole, it is necessary to employ 4 cells over its entire length in the z-direction. To achieve this resolution, the FDTD spatial sample period in the z-direction must be as follows:

$$\Delta z = \frac{(0.1\lambda_o)}{4} = 2.500000 \times 10^{-2}\,m. \tag{6-46}$$

Regarding the spatial sample periods in the x- and y-directions, they have been made to equal one another and are taken as follows:

$$\Delta x = \Delta y = \frac{\lambda_o}{15} = 6.666667 \times 10^{-2}\,m. \tag{6-47}$$

Note how all three spatial sample periods satisfy the modeling guideline of (6-33) that suggests always using a cell size that corresponds to ten or more samples (cells) per wavelength.

Having addressed the cell size for our NZ-FZT/FDTD model of the benchmark dipole, we now must determine the overall size of the solution volume. In doing so, we must ensure that the FDTD solution volume is broad enough to accommodate the largest spheroidal surface used during our end-to-end test, viz., the oblate spheroidal transformation surface of $a = 1.0\lambda_o$ and $\xi_o = 0.80$. In order to keep the test setup consistent with the centered dipole numerical tests of the previous chapter, the model of the dipole (five magnetic loops surrounding a PEC core) and the spheroidal transformation surface both have their centers coincide with that of the rectangular FDTD solution volume. Since we desire at least a 2 cell margin between the surface and the boundaries of the solution volume, our model makes use of the following number of cells in each dimension: 44 cells in both the x- and y-directions, and 69 cells in the z-direction. As we can see, the modeled dipole has more than 20 cells between itself and the boundaries of the solution volume; this is well beyond the 10 cell minimum recommended by Kunz and Luebbers [45].

At this point in our discussion, we now direct the reader to Figure 6.6 in order to get a better understanding of the FDTD model of the analytical benchmark dipole. Just as described earlier, the current along the z-directed dipole is approximated by using a series of five magnetic loops that surrounds a PEC core. During the FDTD simulation, it is these five magnetic loops that actually serve as the source of the radiating fields. Each magnetic loop is 1 cell in width in both the x- and y-directions and surrounds a z-directed E-field sample that is equal to zero, i.e., $E_S^{n+1} = 0$. We set this enclosed z-directed E-field sample to zero by telling the FDTD field solver that there is PEC material located at the corresponding grid point. The five magnetic loops are uniformly distributed along the filament dipole (separated by Δz) as follows: loops 1 and 5 are exactly at the ends of the dipole; loops 2 and 4 are in from the ends of the dipole by a quarter of its total length; and loop 3 is exactly at the midpoint of the dipole. Accordingly, the current through each of the magnetic loops is made to obey the sinusoidal current distribution defined in (6-45) where the central loop, i.e., loop 3, is taken as the center reference. As for the four H-

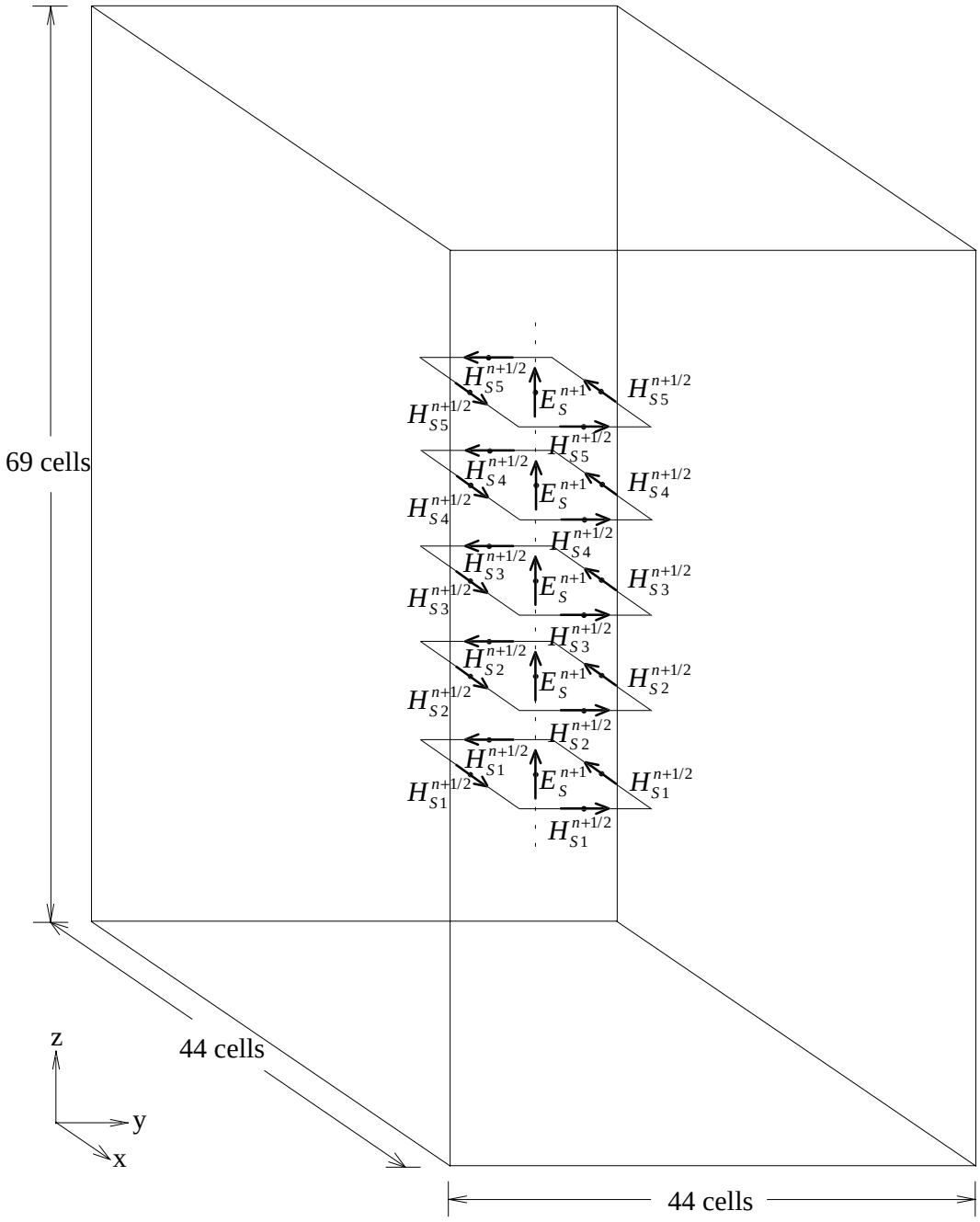

Figure 6.6 FDTD model of analytical benchmark dipole that is used during the NZ-FZT/FDTD end-to-end test (diagram not to scale).

field samples that make up each magnetic loop, they are considered equal in magnitude because the dipole is rotationally symmetric and the loop forms a square contour. We are then able to use the integral form of the Maxwell-Ampere equation (with the displacement current taken as zero due to the PEC core) to determine the four H-field time-domain sources that make up each magnetic loop:

$$H_{S1}^{n+1/2} = 0 \tag{6-48}$$

$$H_{S2}^{n+1/2} = \left[\frac{I_o}{4\Delta x}\right]\sin(2\pi(l_\lambda/2 - \Delta z/\lambda_o))\cos(2\pi\, f_{exc}(n+\tfrac{1}{2})\Delta t) \tag{6-49}$$

$$H_{S3}^{n+1/2} = \left[\frac{I_o}{4\Delta x}\right]\sin(2\pi(l_\lambda/2)\cos(2\pi\, f_{exc}(n+\tfrac{1}{2})\Delta t) \tag{6-50}$$

$$H_{S4}^{n+1/2} = \left[\frac{I_o}{4\Delta x}\right]\sin(2\pi(l_\lambda/2 - \Delta z/\lambda_o))\cos(2\pi\, f_{exc}(n+\tfrac{1}{2})\Delta t) \tag{6-51}$$

$$H_{S5}^{n+1/2} = 0 \tag{6-52}$$

where $n = 0,1,\ldots,N-1$.

(Note that Δt is computed using the equality of (6-34) and spatial sample periods defined in (6-46) and (6-47).) It is important to understand that these expressions are formulated assuming a source H-field that is uniform along the entire length of the square contour. The H-field sources associated with loops 1 and 5 are zero because the current must vanish at both ends of the filament dipole in accordance with the distribution of (6-45). As for loops 2, 3, and 4, the sine term contained within each of their respective expressions comes directly from the distribution of (6-45) and is based on the position of the magnetic loop with respect to the center of the dipole. Recalling that FDTD is a time-domain technique, we have included the $\cos(2\pi\, f_{exc}(n+\tfrac{1}{2})\Delta t)$ term in the expressions of (6-49)-(6-51) so that we may excite the NZ-FZT/FDTD model at a particular frequency of

interest. Notice how the sampling of the cosine term is delayed by a half time-step; we do so in order to properly account for the half time-step difference between the E- and H-field samples. It is important to point out that disregarding this offset in time will cause phase errors in the final results that could have easily been avoided. In addition, when implementing each magnetic loop, we must be careful to properly account for the direction of the four H-field sources along the square contour in relation to the FDTD field convention; that is, we must apply the proper sign to each H-field source in accordance with the right-hand rule. Regarding the value of I_o to use when implementing the H-field sources of (6-49)-(6-51), we have elected to use $I_o = 1\,A$ in order to remain consistent with the centered dipole numerical tests of Chapter 5.

The next step in setting up our NZ-FZT/FDTD model of the benchmark dipole involves configuration of the DFT and the choice of excitation frequency. Using the equality of (6-34) together with (6-43), we obtain the following expression for finding the free-space wavelength that corresponds to the center of the DFT frequency bin:

$$\lambda_{bin} = \left(\frac{k}{N}\right)^{-1}\left(\frac{1}{\Delta x^2} + \frac{1}{\Delta y^2} + \frac{1}{\Delta z^2}\right)^{-\frac{1}{2}}. \tag{6-53}$$

Our objective is to use equation (6-53) to find values of *k* (i.e., the frequency index of the DFT) and *N* that make the free-space wavelength corresponding to the center of the DFT frequency bin, i.e., λ_{bin}, as close as possible to the free-space wavelength of our NZ-FZT/FDTD model, i.e., $\lambda_o = 1\,m$. Although it is actually the ratio of *k* to *N* that determines λ_{bin}, care must be taken to ensure that there are a sufficient number of time-steps to fully characterize the response of the FDTD simulation. Satisfying these requirements, our NZ-FZT/FDTD model uses a frequency index of $k = 14$ and a total number of time-steps $N = 634$. Employing these values of *k* and *N*, the values of the spatial sample periods defined in (6-46) and (6-47), and the equation of (6-53), we find that $\lambda_{bin} = 1.000194\,m$ (which is within 194 ppm of $\lambda_o = 1\,m$). At last, we must

Table 6.1 Summary of NZ-FZT/FDTD Model of Analytical Benchmark Dipole

Dipole Model:

Free-space wavelength: $\lambda_o = 1\ m$.
Length of benchmark dipole: $l = 0.1m$.
Current distribution constant: $I_o = 1\ A$.
Excitation frequency: $f_{exc} = 2.997382 \times 10^8\ Hz$.

Description: Five magnetic loops surrounding a PEC core centered in the FDTD solution volume that obey the current distribution of (6-45).

FDTD Solution Volume:

Size of Yee cell: $\Delta x = 6.666667 \times 10^{-2}\ m$,
$\Delta y = 6.666667 \times 10^{-2}\ m$,
$\Delta z = 2.500000 \times 10^{-2}\ m$.
Number of cells in each dimension (x, y, z): $44 \times 44 \times 69$ cells.
Time-step duration: $\Delta t = 7.367101 \times 10^{-11}$ sec.

Spheroidal Transformation Surface:

Frequency index: $k = 14$.
Total number of time-steps (and observation interval): $N = 634$.
Free-space wavelength corresponding to center of bin: $\lambda_{bin} = 1.000194\ m$.
Window type: Hamming.
Sample grid: $\Delta\vartheta' = \Delta\varphi' = 1^o$ ($I \times J = 180 \times 360$ samples).
Position: Centered in the solution volume and centered about the dipole model.

Prolate tests:	Oblate tests:
$a = 0.1m$	$a = 1.0\ m$
$\xi_o = 1.5$, 2.0, 3.0, 4.0, and 5.0.	$\xi_o = 0.15$, 0.2, 0.3, 0.4, 0.6, and 0.8.

determine the frequency at which to excite the NZ-FZT/FDTD model, i.e., the parameter f_{exc} in the expressions of (6-49)-(6-51). Initially, one might think that the best choice of frequency would be that which corresponds to the free-space wavelength of our NZ-FZT/FDTD model. However, because this frequency does not lie in the center of the frequency bin, the results will incur a slight phase error due to the DFT processing. Instead, this potential phase error is eliminated by exciting the model using the frequency at the center of the bin that corresponds to λ_{bin}:

$$f_{exc} = \frac{k}{N\Delta t} = 2.997382 \times 10^8 \; Hz \, . \tag{6-54}$$

Although the modeled dipole no longer operates at exactly $\lambda_o = 1\, m$, the slight shift in operating frequency is worth the numerical tradeoff. Finally, all related DFT processing during the end-to-end test exclusively makes use of the Hamming window. Provided in Table 6.1 is a summary of the NZ-FZT/FDTD model of our analytical benchmark dipole.

6.3.2 Comparison of NZ-FZT/FDTD Results with Theoretical Results

We now use the just developed model of the benchmark dipole to carry out the end-to-end test of the combined NZ-FZT/FDTD software. The overall performance of the combined software package is characterized by comparing the computed far-zone E-field of the model to that which is theoretically known (described by the closed form expressions of (5-7) and (5-8)). Still, it must be made clear that the performance of this end-to-end test intrinsically depends on the accuracy of our NZ-FZT/FDTD model of the benchmark dipole. To be more specific, the level of detail used to construct the dipole model and the distance it is from the ABC (situated at the boundaries of the solution volume) both have a direct bearing on the accuracy of the computed results. Bearing this in mind, using this specific model of our analytical benchmark still allows us to draw some valid conclusions about the overall performance of the combined NZ-FZT/FDTD software.

Performance of the combined NZ-FZT/FDTD software is evaluated much in the same way as that which is done in Chapter 5 for both of the developed NZ-FZT algorithms. Essentially, the performance evaluation follows the same format utilized in the centered dipole numerical tests (see 5.4.1) and is accomplished by conducting the following numerical studies: (1) an error analysis of the NZ-FZT/FDTD computed results, (2) an analysis of how well the model approximates theoretical values of zero, and (3) a convergence study of the computed results. So that we may avoid being redundant, the reader is referred to Section 5.4.1 to understand the many details behind this performance assessment process. However, this time around some of the performance parameters have been slightly altered. First, we choose to quantify the relative error in magnitude of $\overline{E}_{fz_\theta}(\theta,\varphi)$ in terms of percent (%) instead of parts per million (ppm). This is done by using a slightly modified version of equation (5-9) which replaces the written 10^6 factor with a 10^2 factor. As we shall see, the percent error quantity more appropriately describes the performance of the combined software during the end-to-end test. Second, we have also chosen to include the relative error in magnitude of $\overline{E}_{fz_\theta}(\theta,\varphi)$ in terms of decibels (dB) so as to get a more intuitive feel of the model's performance:

$$\text{Relative Error of } |\overline{E}_{fz_\theta}(\theta,\varphi)| \text{ (dB)} = 20\log\left[\frac{|computed|}{|theoretical|}\right]. \qquad (6\text{-}55)$$

Notice how (6-55) expresses the relative error in dB using both positive and negative quantities. As for the corresponding phase error of $\overline{E}_{fz_\theta}(\theta,\varphi)$, its evaluation remains unchanged and is still computed in terms of degrees using equation (5-10).

Presented in Tables 6.2a, 6.3a, 6.2b and 6.3b is a compilation of the error analysis for both the prolate and oblate test cases of the end-to-end test. Once again, it is important to emphasize that this error analysis makes use of computed and theoretical

Table 6.2a Comparison of Prolate Spheroidal End-to-End Test Results from the NZ-FZT/FDTD Model of the Analytical Benchmark Dipole with Theoretical Results: $\varphi = 0^o$

$l = 0.1m$; $a = 0.1m$; $I \times J = 180 \times 360$; $\Delta\vartheta' = \Delta\varphi' = 1^o$		Relative Error of $\lvert\overline{E}_{fz_\theta}(\theta,\varphi)\rvert$ (% and dB) and Phase Error of $\angle\overline{E}_{fz_\theta}(\theta,\varphi)$ (deg) where $\varphi = 0^o$								
Prolate ξ_o	Convrgce L	$\theta = 10^o$ $\theta = 170^o$	$\theta = 20^o$ $\theta = 160^o$	$\theta = 30^o$ $\theta = 150^o$	$\theta = 40^o$ $\theta = 140^o$	$\theta = 50^o$ $\theta = 130^o$	$\theta = 60^o$ $\theta = 120^o$	$\theta = 70^o$ $\theta = 110^o$	$\theta = 80^o$ $\theta = 100^o$	$\theta = 90^o$
1.5	6	8.4% (-0.8 dB); 0.8 deg	7.8% (-0.7 dB); 0.8 deg	6.9% (-0.6 dB); 0.8 deg	5.8% (-0.5 dB); 0.8 deg	4.8% (-0.4 dB); 0.7 deg	3.8% (-0.3 dB); 0.7 deg	3.1% (-0.3 dB); 0.7 deg	2.6% (-0.2 dB); 0.7 deg	2.5% (-0.2 dB); 0.7 deg
2.0	6	2.0% (+0.2 dB); 0.3 deg	1.8% (+0.2 dB); 0.3 deg	1.3% (+0.1 dB); 0.3 deg	0.8% (+0.1 dB); 0.3 deg	0.2% (~ 0 dB); 0.3 deg	0.3% (~ 0 dB); 0.4 deg	0.8% (-0.1 dB); 0.4 deg	1.1% (-0.1 dB); 0.4 deg	1.2% (-0.1 dB); 0.4 deg
3.0	6	3.7% (+0.3 dB); 0.6 deg	3.2% (+0.3 dB); 0.6 deg	2.4% (+0.2 dB); 0.6 deg	1.4% (+0.1 dB); 0.7 deg	0.5% (~ 0 dB); 0.7 deg	0.4% (~ 0 dB); 0.8 deg	1.1% (-0.1 dB); 0.8 deg	1.6% (-0.1 dB); 0.8 deg	1.7% (-0.2 dB); 0.8 deg
4.0	6	4.5% (+0.4 dB); 0.2 deg	3.9% (+0.3 dB); 0.2 deg	2.9% (+0.3 dB); 0.2 deg	1.9% (+0.2 dB); 0.2 deg	0.7% (+0.1 dB); 0.2 deg	0.3% (~ 0 dB); 0.2 deg	1.1% (-0.1 dB); 0.2 deg	1.6% (-0.1 dB); 0.3 deg	1.8% (-0.2 dB); 0.3 deg
5.0	6	5.9% (+0.5 dB); 0.9 deg	5.3% (+0.4 dB); 0.7 deg	4.3% (+0.4 dB); 0.5 deg	3.2% (+0.3 dB); 0.2 deg	1.9% (+0.2 dB); < 0.1 deg	0.8% (+0.1 dB); 0.1 deg	0.1% (~ 0 dB); 0.2 deg	0.7% (-0.1 dB); 0.2 deg	0.9% (-0.1 dB); 0.2 deg

Table 6.3a Comparison of Prolate Spheroidal End-to-End Test Results from the NZ-FZT/FDTD Model of the Analytical Benchmark Dipole with Theoretical Results: $\varphi = 45^o$

$l = 0.1m$; $a = 0.1m$; $I \times J = 180 \times 360$; $\Delta\vartheta' = \Delta\varphi' = 1^o$		Relative Error of $\lvert\overline{E}_{fz_\theta}(\theta,\varphi)\rvert$(% and dB) and Phase Error of $\angle\overline{E}_{fz_\theta}(\theta,\varphi)$ (deg) where $\varphi = 45^o$								
Prolate ξ_o	Convrgce L	$\theta = 10^o$ $\theta = 170^o$	$\theta = 20^o$ $\theta = 160^o$	$\theta = 30^o$ $\theta = 150^o$	$\theta = 40^o$ $\theta = 140^o$	$\theta = 50^o$ $\theta = 130^o$	$\theta = 60^o$ $\theta = 120^o$	$\theta = 70^o$ $\theta = 110^o$	$\theta = 80^o$ $\theta = 100^o$	$\theta = 90^o$
1.5	6	8.5% (-0.8 dB); 0.8 deg	7.9% (-0.7 dB); 0.8 deg	7.0% (-0.6 dB); 0.8 deg	5.9 % (-0.5 dB); 0.8 deg	4.9% (-0.4 dB); 0.7 deg	3.9% (-0.3 dB); 0.7 deg	3.1% (-0.3 dB); 0.7 deg	2.6% (-0.2 dB); 0.7 deg	2.4% (-0.2 dB); 0.7 deg
2.0	6	2.0% (+0.2 dB); 0.3 deg	1.8% (+0.2 dB); 0.3 deg	1.3% (+0.1 dB); 0.3 deg	0.8% (+0.1 dB); 0.3 deg	0.2% (~ 0 dB); 0.3 deg	0.3% (~ 0 dB); 0.4 deg	0.7% (-0.1 dB); 0.4 deg	1.0% (-0.1 dB); 0.4 deg	1.1% (-0.1 dB); 0.4 deg
3.0	6	3.7% (+0.3 dB); 0.6 deg	3.2% (+0.3 dB); 0.6 deg	2.4% (+0.2 dB); 0.6 deg	1.4% (+0.1 dB); 0.7 deg	0.4% (~ 0 dB); 0.7 deg	0.5% (~ 0 dB); 0.8 deg	1.2% (-0.1 dB); 0.8 deg	1.7% (-0.2 dB); 0.8 deg	1.9% (-0.2 dB); 0.8 deg
4.0	6	4.5% (+0.4 dB); 0.2 deg	3.8% (+0.3 dB); 0.2 deg	2.9% (+0.2 dB); 0.2 deg	1.7% (+0.1 dB); 0.2 deg	0.5% (~ 0 dB); 0.3 deg	0.6% (-0.1 dB); 0.3 deg	1.6% (-0.1 dB); 0.3 deg	2.2% (-0.2 dB); 0.4 deg	2.4% (-0.2 dB); 0.4 deg
5.0	6	5.9% (+0.5 dB); 0.9 deg	5.2% (+0.4 dB); 0.8 deg	4.1% (+0.3 dB); 0.6 deg	2.7% (+0.2 dB); 0.4 deg	1.1% (+0.1 dB); 0.3 deg	0.3% (~ 0 dB); 0.3 deg	1.5% (-0.1 dB); 0.3 deg	2.3% (-0.2 dB); 0.3 deg	2.6% (-0.2 dB); 0.3 deg

Table 6.2b Comparison of Oblate Spheroidal End-to-End Test Results from the NZ-FZT/FDTD Model of the Analytical Benchmark Dipole with Theoretical Results: $\varphi = 0^o$

$l = 0.1m$; $a = 1m$; $I \times J = 180 \times 360$; $\Delta\vartheta' = \Delta\varphi' = 1^o$		Relative Error of $\lvert\overline{E}_{fz_\theta}(\theta,\varphi)\rvert$(% and dB) and Phase Error of $\angle\overline{E}_{fz_\theta}(\theta,\varphi)$ (deg) where $\varphi = 0^o$								
Oblate ξ_o	Convrgce L	$\theta = 10^o$ $\theta = 170^o$	$\theta = 20^o$ $\theta = 160^o$	$\theta = 30^o$ $\theta = 150^o$	$\theta = 40^o$ $\theta = 140^o$	$\theta = 50^o$ $\theta = 130^o$	$\theta = 60^o$ $\theta = 120^o$	$\theta = 70^o$ $\theta = 110^o$	$\theta = 80^o$ $\theta = 100^o$	$\theta = 90^o$
0.15	14	2.0% (+0.2 dB); 1.3 deg	3.3% (+0.3 dB); 1.5 deg	4.6% (+0.4 dB); 1.6 deg	5.5% (+0.5 dB); 1.5 deg	5.6% (+0.5 dB); 1.2 deg	5.2% (+0.4 dB); 1.0 deg	4.5% (+0.4 dB); 0.8 deg	3.9% (+0.3 dB); 0.7 deg	3.7% (+0.3 dB); 0.6 deg
0.20	14	1.0% (+0.1dB); 2.0 deg	2.8% (+0.2 dB); 1.9 deg	4.7% (+0.4 dB); 1.8 deg	5.7% (+0.5 dB); 1.6 deg	5.8% (+0.5 dB); 1.3 deg	5.3% (+0.4 dB); 1.1 deg	4.6% (+0.4 dB); 1.0 deg	4.1% (+0.3 dB); 0.9 deg	3.9% (+0.3 dB); 0.9 deg
0.30	14	2.8% (-0.2 dB); 3.2 deg	1.1% (+0.1 dB); 2.7 deg	4.5% (+0.4 dB); 2.2 deg	6.2% (+0.5 dB); 1.9 deg	6.1% (+0.5 dB); 1.6 deg	5.3% (+0.5 dB); 1.5 deg	4.5% (+0.4 dB); 1.4 deg	4.0% (+0.3 dB); 1.4 deg	3.8% (+0.3 dB); 1.4 deg
0.40	14	8.5% (-0.8 dB); 3.6 deg	1.8% (-0.2 dB); 3.1 deg	4.0% (+0.3 dB); 2.6 deg	6.5% (+0.5 dB); 2.2 deg	6.3% (+0.5 dB); 1.9 deg	5.0% (+0.4 dB); 1.8 deg	4.0% (+0.3 dB); 1.8 deg	3.5% (+0.3 dB); 1.9 deg	3.3% (+0.3 dB); 1.9 deg
0.60	14	19.7% (-1.9 dB); 2.6 deg	7.2% (-0.7 dB); 0.8 deg	3.1% (+0.3 dB); 2.6 deg	6.5% (+0.5 dB); 2.8 deg	4.9% (+0.4 dB); 2.3 deg	2.4% (+0.2 dB); 2.0 deg	1.0% (+0.1 dB); 2.0 deg	0.7% (+0.1 dB); 2.3 deg	0.7% (+0.1 dB); 2.4 deg
0.80	14	16.1% (-1.5 dB); 10.4 deg	5.4% (-0.5 dB); 1.6 deg	3.9% (+0.3 dB); 2.7 deg	5.9% (+0.5 dB); 2.6 deg	2.7% (+0.2 dB); 0.6 deg	1.0% (-0.1 dB); 0.7 deg	2.5% (-0.2 dB); 0.5 deg	2.0% (-0.2 dB); 0.7 deg	1.5% (-0.1 dB); 1.3 deg

Table 6.3b Comparison of Oblate Spheroidal End-to-End Test Results from the NZ-FZT/FDTD Model of the Analytical Benchmark Dipole with Theoretical Results: $\varphi = 45^o$

$l = 0.1m$; $a = 1m$; $I \times J = 180 \times 360$; $\Delta\vartheta' = \Delta\varphi' = 1^o$		Relative Error of $\lvert\overline{E}_{fz_\theta}(\theta,\varphi)\rvert$(% and dB) and Phase Error of $\angle\overline{E}_{fz_\theta}(\theta,\varphi)$ (deg) where $\varphi = 45^o$								
Oblate ξ_o	Convrgce L	$\theta = 10^o$ $\theta = 170^o$	$\theta = 20^o$ $\theta = 160^o$	$\theta = 30^o$ $\theta = 150^o$	$\theta = 40^o$ $\theta = 140^o$	$\theta = 50^o$ $\theta = 130^o$	$\theta = 60^o$ $\theta = 120^o$	$\theta = 70^o$ $\theta = 110^o$	$\theta = 80^o$ $\theta = 100^o$	$\theta = 90^o$
0.15	14	1.6% (+0.1 dB); 1.4 deg	1.2% (+0.1 dB); 1.6 deg	0.5% (~ 0 dB); 1.6 deg	3.2% (-0.3 dB); 1.4 deg	5.8% (-0.5 dB); 0.9 deg	7.6% (-0.7 dB); 0.4 deg	8.6% (-0.8 dB); <0.1 deg	8.9% (-0.8 dB); 0.3 deg	9.0% (-0.8 dB); 0.4 deg
0.20	14	0.4% (~ 0 dB); 2.0 deg	0.2% (~ 0 dB); 1.9 deg	1.1% (-0.1 dB); 1.7 deg	3.6% (-0.3 dB); 1.2 deg	6.2% (-0.6 dB); 0.6 deg	8.0% (-0.7 dB); <0.1 deg	8.9% (-0.8 dB); 0.5 deg	9.3% (-0.8 dB); 0.7 deg	9.3% (-0.8 dB); 0.8 deg
0.30	14	3.7% (-0.3 dB); 3.1 deg	2.5% (-0.2 dB); 2.3 deg	2.6% (-0.2 dB); 1.4 deg	4.3% (-0.4 dB); 0.5 deg	6.6% (-0.6 dB); 0.4 deg	8.4% (-0.8 dB); 1.1 deg	9.3% (-0.8 dB); 1.6 deg	9.7% (-0.9 dB); 1.9 deg	9.7% (-0.9 dB); 2.0 deg
0.40	14	9.8% (-0.9 dB); 3.2 deg	6.2% (-0.6 dB); 1.9 deg	3.9% (-0.3 dB); 0.6 deg	4.2% (-0.4 dB); 0.5 deg	6.0% (-0.5 dB); 1.5 deg	7.8% (-0.7 dB); 2.3 deg	8.9% (-0.8 dB); 3.0 deg	9.3% (-0.9 dB); 3.4 deg	9.4% (-0.9 dB); 3.5 deg
0.60	14	20.8% (-2.0 dB); 4.3 deg	10.8% (-1.0 dB); 3.3 deg	2.7% (-0.2 dB); 2.2 deg	<0.1% (~ 0 dB); 1.6 deg	1.1% (-0.1 dB); 1.9 deg	3.3% (-0.3 dB); 3.1 deg	4.9% (-0.4 dB); 4.6 deg	5.6% (-0.5 dB); 5.7 deg	5.8% (-0.5 dB); 6.1 deg
0.80	14	15.3% (-1.4 dB); 12.9 deg	5.3% (-0.5 dB); 7.2 deg	2.0% (+0.2 dB); 1.8 deg	3.5% (+0.3 dB); 1.7 deg	1.7% (+0.1 dB); 2.2 deg	0.3% (~ 0 dB); 0.1 deg	0.7% (-0.1 dB); 2.9 deg	0.3% (~ 0 dB); 5.2 deg	<0.1% (~ 0 dB); 6.0 deg

data that are unnormalized with respect to both magnitude and phase. Notice how the NZ-FZT/FDTD model of the benchmark dipole performs the same when computing the E-field in the upper and lower hemisphere of the far-zone. This occurrence is naturally what should be expected due to the fact that the spheroidal transformation surface, the model of the dipole, and the rectangular FDTD solution volume all have centers that coincide with each other. Yet, this is where the symmetry of the model's performance ends. Because the benchmark dipole is modeled in FDTD using a Cartesian lattice and a rectangular solution volume, the computed far-zone E-field for all of the prolate and oblate test cases does not possess the azimuthal (rotational) symmetry that is theoretically expected for the analytical benchmark. As a result, we have chosen to include in all of our test cases both the $\varphi = 0^o$ and $\varphi = 45^o$ planar cuts so as to demonstrate these asymmetrical differences. The other six cardinal and intercardinal planes have not been included in our numerical studies since the model will essentially yield the same results as the $\varphi = 0^o$ and $\varphi = 45^o$ planar cuts (a single test case for each type of spheroidal surface has been conducted to corroborate this assertion). Furthermore, by invoking symmetry arguments, one can intuitively understand as to why the model performs in this manner: (1) the FDTD sample lattice is square in the x-y plane, and (2) the dipole model and the spheroidal transformation surface are both situated exactly in the middle of the rectangular FDTD solution volume.

Inspection of Tables 6.2a and 6.3a reveals that the NZ-FZT/FDTD model of the benchmark dipole computes the far-zone E-field within $\pm 8.5\%$ (or ± 0.8 dB) and ± 0.9 deg for the prolate test cases. In addition, all of the prolate tests converge with $L = 6$ (i.e., the degree at which the spheroidal wave-harmonic expansion is truncated). The reason for excluding the $\xi_o = 1.2$ test case from the prolate numerical study is that some sample points along the spheroidal surface lie within one spatial sample period from the modeled dipole. As a result, the simulated radiating field is not able to properly form along the transformation surface in so little a number of Yee cells. If we wanted to accommodate this specific test case, resolution of the entire NZ-FZT/FDTD model would

have to be increased to a point that would ultimately preclude the model from addressing the larger of the oblate surfaces under consideration.

Regarding the oblate test results, Tables 6.2b and 6.3b indicate that the NZ-FZT/FDTD model of the benchmark dipole performs much better when the oblate spheroidal surface is situated closer to the modeled source. For the oblate test cases where $\xi_o =$ 0.15, 0.20, 0.30, and 0.40, the model of the dipole computes the far-zone E-field within $\pm 9.8\%$ (or ± 0.9 dB) and ± 3.6 deg. As for the outermost test cases where $\xi_o =$ 0.60 and 0.80, the NZ-FZT/FDTD model computes the far-zone E-field within $\pm 20.8\%$ (or ± 2.0 dB) and ± 12.9 deg. All of the oblate test cases converge with $L = 14$.

Upon review of these results, we can gather that the combined NZ-FZT/FDTD model does not perform as well as either spheroidal NZ-FZT algorithm operating in a stand-alone manner. Logically speaking, this degradation of performance must be expected because the FDTD portion of the model only approximates the radiation from the benchmark dipole; to the contrary, the analytical benchmark software driver provides the exact near-zone E-field for the benchmark dipole using closed form expressions (5-1)-(5-6). In Chapter 5, both NZ-FZT algorithms (while operating on theoretically generated near-zone E-field samples for the benchmark dipole) deliver the magnitude of the far-zone E-field within $\pm 0.1\%$ for the same exact test cases that are used in this end-to-end test. As a result, these findings imply that most of the resulting error of the NZ-FZT/FDTD model stems from the FDTD portion of the model rather than the developed NZ-FZT algorithms. We are only able to draw this conclusion because the centered dipole numerical tests of Chapter 5 establish isolated performances of the NZ-FZT algorithms for comparison (i.e., stand-alone from the FDTD field solver).

Having concluded that most of the error arises from the FDTD portion of the NZ-FZT/FDTD model, we now turn our attention to the differences in performance between the prolate and oblate test cases. As we can see, the NZ-FZT/FDTD model overall performs better for the prolate cases than it does for the oblate cases. Yet, both NZ-FZT

algorithms have been shown to compute the magnitude of the far-zone E-field within $\pm 0.1\%$ when isolated from the FDTD portion of the model. Although a certain amount of error can be attributed to the discretizing of the benchmark dipole, the bulk of the resulting error does not appear to originate from this approximation. We draw this conclusion because all of our end-to-end test cases use the same exact FDTD simulation and still achieve a wide range of performances (see Tables 6.2a, 6.3a, 6.2b and 6.3b). Indeed, the only difference between all of the end-to-end test cases is the actual location of the spheroidal sample points. Also note that the prolate spheroidal transformation surfaces are closer on average to the modeled dipole than their oblate counterparts. All of these facts together suggest that the performance of the NZ-FZT/FDTD model must somehow be linked to the position of the spheroidal sample points with respect to both the modeled dipole and the solution volume boundaries. We have already concluded that our NZ-FZT/FDTD model does not function well when using a transformation surface situated within a limited number of Yee cells from the modeled radiation source. Likewise, performance of the model appears to degrade as the transformation surface gets farther away from the modeled dipole and closer to the ABC situated at the boundary of the solution volume, viz., the oblate test cases where $\xi_o = 0.60$ and 0.80.

All things considered, there are several possible reasons as to why the NZ-FZT/FDTD model behaves in this manner. First, we must consider the effects of numerical dispersion on a FDTD simulation. In short, the phase velocity of a simulated wave can differ from that of free-space. Moreover, the speed at which the simulated wave may propagate varies with the modal wavelength, the direction of propagation in the grid, and the grid discretization [46]. As a result, fields emanating from our modeled dipole can experience different free-space phase velocities depending upon the direction of propagation: the result being unwanted phase errors along our spheroidal transformation surface. According to Taflove [46], these phase errors are cumulative and increase linearly with wave propagation distance. Second, we consider the effects of unwanted reflections from the ABC. In essence, these unwanted reflections from the boundary of the solution volume can produce erroneous traveling waves that pass through

a given spheroidal transformation surface and ultimately corrupt the NZ-FZT process. As the transformation surface gets closer to the ABC, the true outgoing waves have to compete with unwanted reflections that are closer in magnitude (i.e., the outgoing waves decrease in intensity at the spheroidal transformation surface as the surface gets farther from the modeled dipole due to spherical spreading loss).

Note that the lack of rotational symmetry observed in the relative error for all of the test cases is also consistent with the presence of both of these unwanted effects. The ABC does not uniformly absorb outgoing waves at the boundaries of the solution volume. Simulated waves that are perpendicularly incident upon the planar boundaries are better absorbed by this particular ABC than those that are incident upon the corners and edges of the solution volume. Likewise, the effects of numerical dispersion also vary with regard to the direction of outgoing waves.

Once again, we examine how well the NZ-FZT/FDTD model of the benchmark dipole approximates the null at the far-zone observation angles $\theta = 0^o$ and $\theta = 180^o$. For all of the prolate and oblate test cases, the model computes the null as values that are below -110 dB from the main beam peak (i.e., which exists at $\theta = 90^o$). Regarding the cross-polarized far-zone E-field, the model computes the theoretical zero of $\overline{E}_{fz_\varphi}(\theta,\varphi)$ as values that are well below -120 dB from the main beam peak. For all practical purposes, the NZ-FZT/FDTD model of the benchmark dipole approximates theoretical values of zero comparable to either NZ-FZT algorithm operating in a stand-alone manner. Like before, the corresponding phase is ignored because it essentially represents some form of numerical phase noise.

Overall, the results of the end-to-end test indicate that the combined NZ-FZT/FDTD software performs extremely well. With the exception of the outermost oblate test cases where $\xi_o =$ 0.60 and 0.80, the fact that this specific NZ-FZT/FDTD model of the analytical benchmark dipole computes the magnitude of the far-zone E-field within $\pm 10\%$ error demonstrates the validity and robustness of the overall NZ-FZT/FDTD combined process. However, like all numerical processes, a full

understanding of its inner-workings as well as its limitations is essential to its successful application. As we have discovered, the user must be judicious when placing the spheroidal transformation surface with respect to both the modeled radiation structure and the boundaries of the solution volume. Note that in addition to this consideration, the user must not forget to observe guidelines for the FDTD algorithm (see 6.1.7) as well as those for the DFT portion of the extraction process (see 6.2.2).

CHAPTER 7. FURTHER VALIDATION VIA AN EMPIRICAL BENCHMARK

We are now ready to proceed with the final step of this research project: applying the developed NZ-FZT process to a computational model of a physically constructed radiating structure. In doing so, we are able to provide further validation of our newly developed process as well as demonstrate a practical example of its application. First, this task requires us to select and fabricate a radiation structure that is to serve as our empirical benchmark. Once constructed, this benchmark structure proceeds to undergo pattern testing at the NASA Langley research facility and the Virginia Tech antenna laboratory in order to empirically characterize its far-zone performance. With both sets of pattern measurements established as a basis for comparison, we then move forward to construct our computational model of the benchmark structure using the developed NZ-FZT/FDTD software. Computed results are then compared to those obtained from the NASA Langley and Virginia Tech measurements, and conclusions are drawn as to how well the combined software package is able to model radiation from the developed empirical benchmark.

An important consideration when selecting the radiating structure to use as our empirical benchmark is its ability to be physically realized within tight electrical and mechanical tolerances. Practically speaking, a radiating structure that cannot be accurately constructed is not worth much as a comparison standard; the last thing we want to do is introduce additional significant sources of error into our comparative study. Moreover, we desire a radiating structure that is not too complicated to build, excite, or test. Satisfying all of these prerequisites, an edge-fed microstrip patch antenna makes an excellent choice for our empirical benchmark. Its construction is relatively simple and employs standard fabrication techniques for printed circuit boards that are presently considered quite mature in the field of antenna design.

7.1 MICROSTRIP PATCH ANTENNA

7.1.1 Design Layout and Fabrication

Having selected an edge-fed microstrip patch antenna as our empirical benchmark, we now turn our attention toward its design. When considering its frequency of operation, we prefer that our empirical benchmark not operate below microwave frequencies. The reason for imposing such a requirement is essentially twofold. First, from a fabrication and material perspective, we naturally want to limit the physical size of the antenna. Second, pattern testing at these lower frequencies usually requires a range facility that is quite large in size and, more often than not, is limited in terms of availability. Similarly, we also cannot permit our benchmark structure to operate at too high a frequency. For obvious reasons, fabrication errors have a much greater effect on the overall accuracy of measured results as mechanical tolerances get electrically larger with respect to the operating modal wavelength (which not only depends on the fabrication material, but also the radiating structure itself). Accordingly, designing our microstrip patch antenna to operate at 3.0 GHz allows us to create an empirical benchmark that achieves a reasonable balance between all of these considerations.

We choose to fabricate our microstrip patch antenna with a substrate of RT/duroid 5870 which is manufactured and made available from the Rogers Corporation. The advantage of this particular material is that it maintains close tolerances on all of its mechanical and electrical parameters. As a result, RT/duroid 5870 makes an excellent choice of substrate for our comparison standard. From a mechanical standpoint, its glass microfiber reinforced polytetrafluoroethylene (PTFE) composite is specifically designed for exacting microstrip circuit applications [54]. Furthermore, the material has excellent dimensional stability and is resistant to all solvents and reagents hot or cold, normally used in etching printed circuits [54]. With regard to electrical properties, its dielectric constant remains quite uniform throughout the material, and its low dissipation factor extends its usefulness to X-band applications and above [54]. The material comes in a variety of thicknesses for both the dielectric substrate and the double-sided copper

Table 7.1 Summary of Pertinent Mechanical and Electrical Parameters for the RT/duroid 5870 Substrate Used in the Construction of the Empirical Benchmark [54]

Parameter	Nominal Value
Relative Dielectric Constant, ε_r	1 MHz: 2.35 10 GHz: 2.33
Dissipation Factor (Loss Tangent), $\tan\delta$	1 MHz: 0.005 10 GHz: 0.0012
Thickness of Dielectric Substrate, *h*	45 mils (0.045 in.)
Weight/Thickness of Copper Cladding	1 oz./ft.^{2} or 1.4 mils (0.0014 in.)

cladding. For our particular application, the thickness of the dielectric substrate is 45 mils, and the weight of the copper cladding is 1 oz./ft.^{2} (i.e., a thickness of 1.4 mils [55]). Displayed in Table 7.1 is a summary of all pertinent electrical and mechanical parameters for the RT/duroid 5870 substrate specific to the construction of our microstrip patch antenna.

With the substrate and operating frequency selected, we now shift our focus to the actual design of our 3.0 GHz edge-fed microstrip patch antenna. We begin this effort by considering the simple, yet useful, transmission line model of a rectangular patch antenna described by Bhartia *et al.* [56]. Although there are other more accurate models that describe this type of antenna, this specific one, as we shall see, is quite sufficient for our purpose of determining the dimensions of our empirical benchmark (note that the interested reader is directed to [56] for the details regarding the other models available for this particular radiating structure). In accordance with the transmission line model, the resonant frequency of a rectangular patch antenna is determined using the following expressions [56]:

$$f_r = \frac{c}{2(L + 2\Delta l_{oc})\sqrt{\varepsilon_{re}}} \tag{7-1}$$

where

$$\varepsilon_{re} = \frac{\varepsilon_r + 1}{2} + \frac{\varepsilon_r - 1}{2}\left(1 + \frac{10}{(W/h)}\right)^{-\frac{1}{2}} \tag{7-2}$$

$$\Delta l_{oc} = 0.412h\frac{(\varepsilon_{re} + 0.3)(W/h + 0.264)}{(\varepsilon_{re} - 0.258)(W/h + 0.813)}. \tag{7-3}$$

Within these expressions the parameters are defined as follows: *L* and *W*, the length and width of the patch antenna; *h*, the thickness of the substrate (and subsequently the distance between the etched metalization and the ground plane); ε_r, the relative dielectric constant of the substrate; ε_{re}, the effective relative dielectric constant of the microstrip patch; and Δl_{oc}, the line extension (due to fringing fields at the radiating edges of the patch antenna). For the sake of simplicity, we have chosen to make our patch antenna square in shape. Given the fact that the length and width of the patch antenna are considered equal, expressions (7-1)-(7-3) are then used to calculate the dimensions of the square patch antenna necessary to achieve resonance at 3.0 GHz for the given RT/duroid 5870 substrate. Results of these calculations yield the following dimensions for the patch antenna: $L = W = 1252$ mils. Note that these calculations utilize the $\varepsilon_r = 2.33$ value (see Table 7.1) since the antenna is designed to operate at microwave frequencies.

Next, we follow with the design of the antenna feed. An edge feed is selected to excite our patch antenna because of its ability to be constructed with a great deal of precision. It is this feature that allows the dimensional differences between our NZ-FZT/FDTD model and the fabricated benchmark structure to be minimized, thus reducing the amount of additional error introduced. The feed design makes use of a microstrip transmission line that perpendicularly feeds the square patch in the middle of one of its radiating edges. Furthermore, the characteristic impedance of this transmission line is designed to be $50\,\Omega$ in order to maintain commonality with the reference impedance of

the range measurement system (note that $50\,\Omega$ is considered the industry standard for microwave measurement systems). As a result, we must determine the width W_{feed} necessary to construct the $50\,\Omega$ microstrip feed for the given RT/duroid 5870 substrate. To do so, we apply the following formula for impedance of a microstrip transmission line [55]:

$$Z_o = \frac{120\pi \left[\sqrt{\varepsilon_{re}}\right]^{-1}}{W_{feed}/h + 1.393 + 0.667\ln(1.444 + W_{feed}/h)} \text{ for } W_{feed}/h \geq 1. \quad (7\text{-}4)$$

It should be understood that when applying this equation the effective dielectric constant ε_{re} of the $50\,\Omega$ microstrip feed is also found by using equation (7-2); however, W (the width of the patch) must now be replaced with W_{feed} (the width of the microstrip feed). Employing both (7-2) and (7-4), we determine that a line width of $W_{feed} = 133$ mils yields approximately the desired $50\,\Omega$ microstrip transmission line for our particular substrate (i.e., precisely $50.2\,\Omega$ as calculated by (7-2) and (7-4)).

At this point, it must be mentioned that a typical microstrip patch antenna design would operate with a matching network between itself and the $50\,\Omega$ transmission line feed. However, our objective is to accurately characterize the performance of the empirical benchmark, not to make it achieve the most efficient radiation. Accordingly, we directly excite the radiation structure from the standard reference impedance in order to isolate its performance from the effects of additional microwave circuitry. Unfortunately, we still cannot get away from the fact that the $50\,\Omega$ microstrip feed does contribute some radiation to the overall far-zone performance of the empirical benchmark structure.

The empirical benchmark is fabricated on a finite piece of substrate that maintains at least a half-wavelength (in the substrate) between the printed patch antenna and the edge of the ground-plane backed substrate. Consequently, the $50\,\Omega$ transmission line is required to travel 1417 mils to reach the edge of the substrate. It is here where the printed

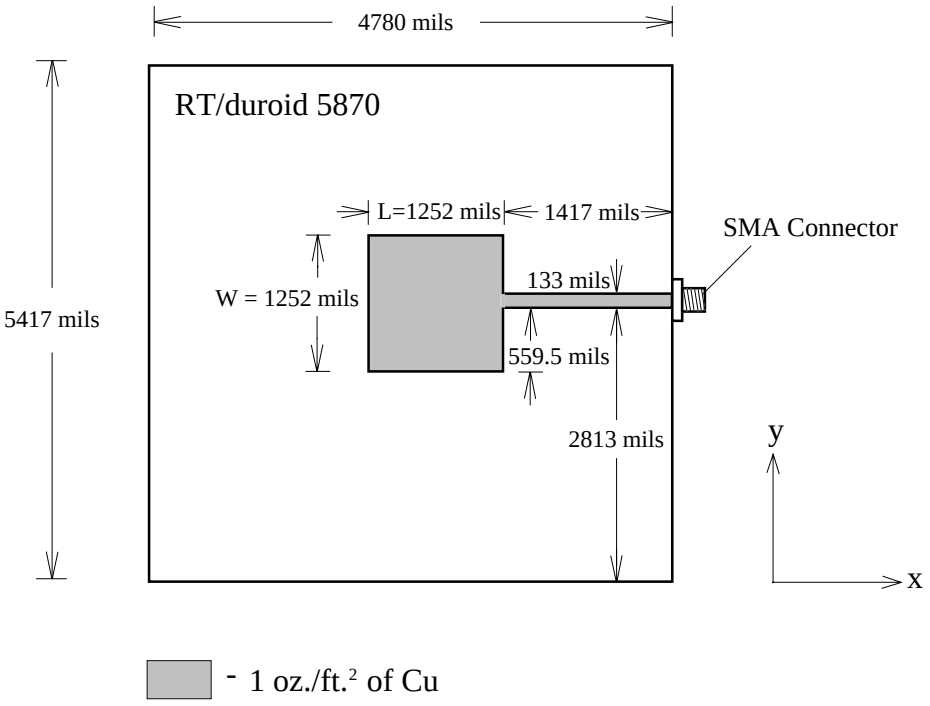

Figure 7.1 Overall layout of the fabricated empirical benchmark (top-view; not to scale).

circuit assembly interfaces with the measurement system by way of a standard subminiature (SMA) coaxial connector. This interface between the SMA connector and the microstrip transmission line is physically realized as follows: first, the center conductor of the connector is soldered to the upper metalization of the microstrip feed; and second, the outer conductor of the connector (specifically the flange) is soldered to the ground-plane. Depicted in Figure 7.1 is the overall layout of the fabricated empirical benchmark. Note that the fabrication tolerances for the constructed benchmark structure are on the order of ± 1 mil for the printed dimensions, i.e., the etched metalization, and ± 20 mils for dimensions describing the overall size (or edges) of the ground-plane backed substrate.

7.1.2 NASA Langley and Virginia Tech Measurements of Far-Zone Radiation Patterns

Pattern testing of the empirical benchmark structure is conducted in an anechoic chamber at the NASA Langley research facility and on an outdoor range at the Virginia Tech antenna laboratory. Measurements of the far-zone radiation patterns are taken at the 3.0 GHz resonant frequency of the microstrip patch and consist of both E- and H-plane linear co-polarization cuts. (Note that the E-plane for a microstrip patch antenna is parallel to its length and perpendicular to the substrate; meanwhile, the corresponding H-plane is parallel to its width and also perpendicular to the substrate. See Figure 7.1.) The resulting pattern data is comprised of relative power measurements (i.e., no phase) that are expressed in terms of decibels (dB) and are normalized with respect to the peak of its main lobe. Pattern measurements are made over the full 360^o for both planar cuts and are taken with the following angular resolution: in 1.00^o increments at NASA Langley and in 0.352^o increments at Virginia Tech. Both sets of measured radiation patterns are subsequently shown in the section that compares them to the computed results of our NZ-FZT/FDTD model (see 7.2.2).

7.2 EMPIRICAL VALIDATION OF THE NZ-FZT PROCESS

7.2.1 NZ-FZT/FDTD Model of the Empirical Benchmark

In creating a NZ-FZT/FDTD model of our benchmark patch antenna, we must first consider the layout of the FDTD solution volume. Once again, the first step in developing the setup of the solution volume is determining the size of the Yee cells. As we can see from the design layout of our fabricated empirical benchmark (see Figure 7.1), there are many geometrical details necessary to physically describe its construction. Consequently, we need to select a cell size that is best able to represent the geometry of the entire radiating structure as defined by the coordinate system of Figure 7.1. We begin this process by first establishing critical dimensions of the structure in each Cartesian direction that would best be represented exactly by the model. The size of the Yee cell is then designed to fit into each of these three critical dimensions using an integral number of cell widths; in other words, the critical dimension in each Cartesian direction is exactly divisible by its respective FDTD spatial sample period. Unfortunately, choosing the cell size in this manner generally precludes the remainder of the geometrical features from being modeled exactly. Nevertheless, this difficulty can be easily overcome by choosing a cell size that is able to closely approximate all of the other less critical dimensions.

The first critical dimension that we consider is the thickness h of the dielectric substrate. Referring to expressions (7-1)-(7-3), one can plainly see that the distance at which the upper metalization is situated above the ground plane has a profound impact on the operation of a microstrip patch antenna. In addition, our experience shows that using three cells (in the z-direction) to represent the thickness of the substrate is quite sufficient to accurately model a microstrip structure. Accordingly, we have selected the FDTD spatial sample period in the z-direction to be as follows:

$$\Delta z = \frac{45 mils}{3} = 15 mils = 3.810000 \times 10^{-4}\ m . \tag{7-5}$$

Focusing our attention on the remaining two critical dimensions, we naturally conclude that they should be the length L and width W of our microstrip patch antenna. Again referring to expressions (7-1)-(7-3), we are able to recognize that both of these dimensions are also crucial to the operation of a microstrip patch antenna. Because both of these critical dimensions are equal, the spatial sample periods in the x- and y-directions can be made to equal one another. Having chosen to represent both the length and width of the patch using 29 cells in each direction, we determine the spatial sample periods in the x- and y-directions as follows:

$$\Delta x = \Delta y = \frac{1252\,mils}{29} = 43.2\,mils = 1.096579 \times 10^{-3}\,m. \qquad (7\text{-}6)$$

It is important to note that partitioning the length and width of the patch into exactly 29 cells is not completely arbitrary. First, it is necessary to have a significant number of spatial samples along the patch antenna in order to accurately simulate its operation. Second, using 3 cells (in the y-direction) of this particular spatial sample period enables us to closely approximate the line width of the microstrip feed (i.e., $W_{feed} = 133$ mils). Our experience has shown that using 3 cells along the width of the microstrip transmission line is quite sufficient. Due to the intricate geometrical features of our overall model, all three spatial sample periods do turn out to be much less than the tenth of a wavelength maximum cell width recommended by the modeling guideline of (6-33).

With the size of the Yee cell designed to exactly meet the critical dimensions of the microstrip patch antenna, we now proceed to model the remainder of the fabricated empirical benchmark. Each of the other less critical dimensions is represented by using the integral number of cells that most closely approximates the given spatial measurement. Thus, the spatial extent of the modeled radiation structure without the free-space buffer is determined to be as follows: 111 cells in the x-direction, 125 cells in the y-direction, and 3 cells in the z-direction. Regarding the surrounding free-space buffer, we have chosen to equidistantly space the modeled radiation structure from the boundaries of the solution volume as follows: a 37 cell border in the x-direction, a 30 cell

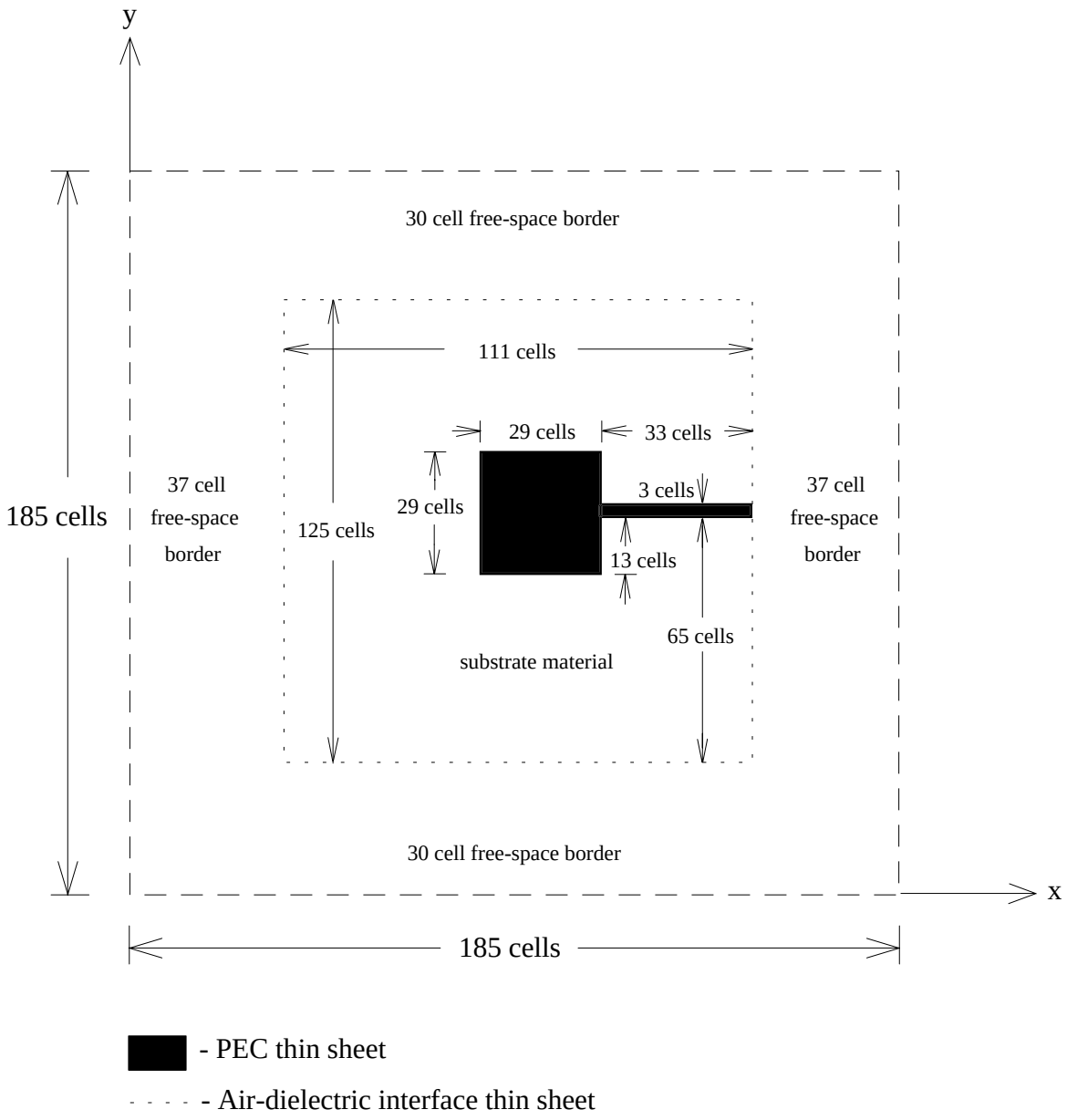

Figure 7.2 Overall layout of NZ-FZT/FDTD model of the fabricated empirical benchmark (top-view; not to scale).

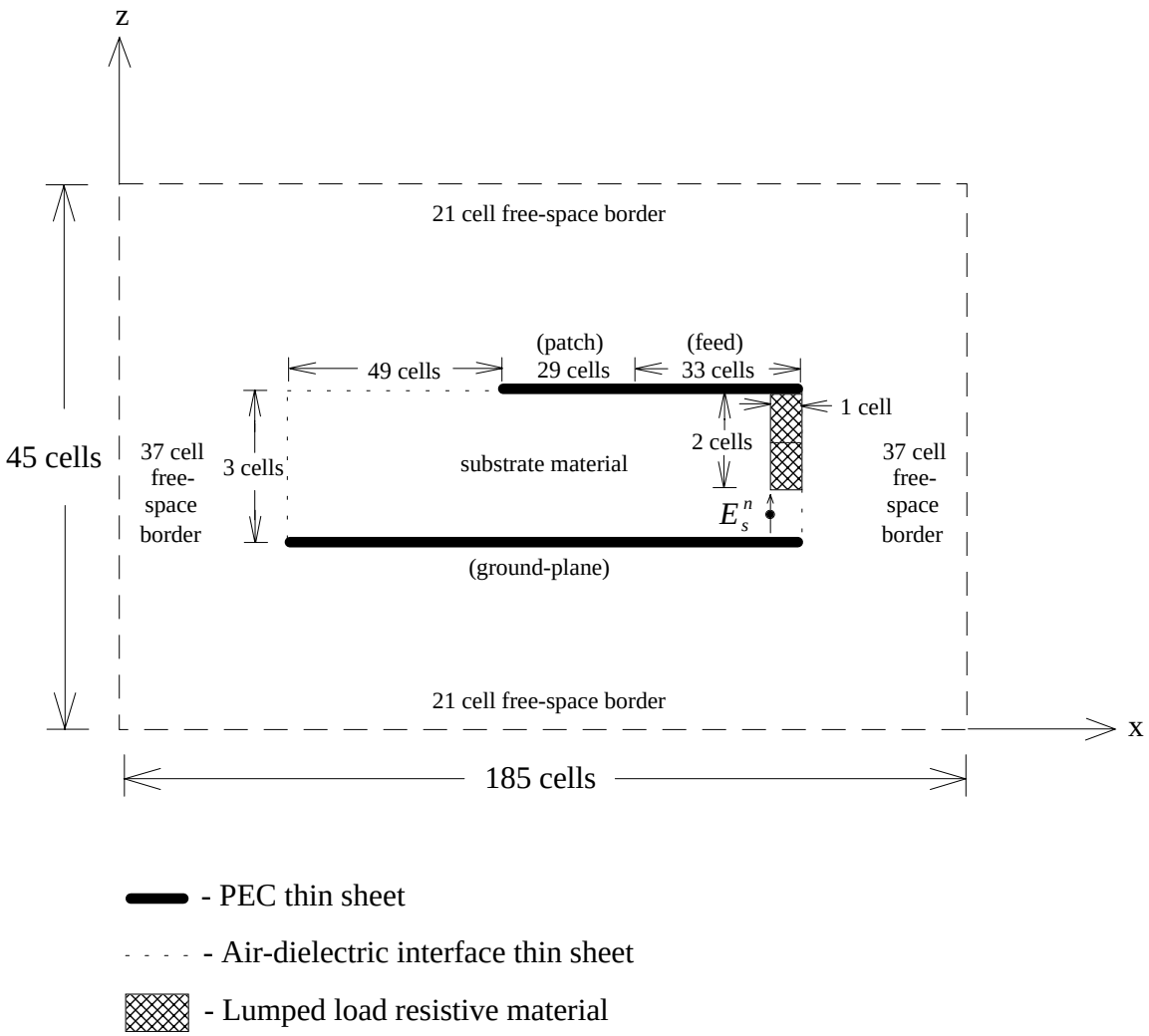

Figure 7.3 Overall layout of NZ-FZT/FDTD model of the fabricated empirical benchmark (side-view along mid-section of solution volume; not to scale).

border in the y-direction, and a 21 cell border in the z-direction. As we can see, this choice of free-space buffer allows the modeled radiation structure to be situated exactly in the center of a FDTD solution volume with 185 cells in both the x- and y-directions, and 45 cells in the z-direction. Furthermore, notice how the shortest distance between the radiation structure and all boundaries of the solution volume well exceed the 10 cell minimum suggested by the FDTD modeling guideline (see 6.1.7). Illustrated in Figures 7.2 and 7.3 is the overall layout (depicting different views) of our NZ-FZT/FDTD model of the fabricated empirical benchmark.

As shown in Figures 7.2 and 7.3, the upper metalization and the ground-plane of the patch antenna are both modeled using thin sheets of perfect electric conductor (PEC) that are respectively situated at the top and bottom of the modeled substrate. Note that both PEC thin sheets are of infinitesimal thickness and are modeled by setting the tangential components of the E-field samples in their respective planes to zero (see 6.1.3).

Regarding the RT/duroid 5870 substrate, it is modeled as a lossy dielectric. As mentioned earlier, we use $\varepsilon_r = 2.33$ as the relative dielectric constant of the substrate because our radiating structure operates at microwave frequencies (see Table 7.1). Furthermore, the loss of the substrate is specified by the manufacturer in terms of its loss tangent and has the following value at microwave frequencies: $\tan\delta = 0.0012$ (see Table 7.1). Yet, the FDTD lossy dielectric E-field formulation of our electromagnetic field solver requires us to represent loss in a material using a finite conductivity σ (see 6.1.4). Fortunately, we are able to reconcile this difference in the representation of loss. First, we must understand that loss (or power dissipation) in a dielectric material can stem from either of the two following sources or a combination of both: (1) a time lag in the D-field relative to the E-field that is attributable to damping effects of the medium (which thus leads to loss resulting from a complex permittivity); and (2) the finite conductivity σ of the medium (which thus leads to ohmic loss) [57]. Basic electromagnetic theory reveals that the two loss mechanisms are virtually indistinguishable as far as external effects related to power dissipation are concerned [57]. As a result, Collin [57] states that the combination of both loss effects can be lumped under a total effective conductivity or

under an effective imaginary part of the permittivity. In order to maintain consistency with our electromagnetic field solver, we opt to represent the total loss in our substrate using an effective conductivity σ_{eff}. At the 3.0 GHz resonant frequency, the total effective conductivity of the substrate is determined from its loss tangent $\tan\delta$ and relative dielectric constant ε_r as follows [57]:

$$\sigma_{eff} = 2\pi f \varepsilon_r \varepsilon_o \tan\delta = 4.666355 \times 10^{-4}\ S/m. \tag{7-7}$$

Modeling of the air-dielectric interface of the substrate is achieved by placing a thin sheet (i.e., of infinitesimal thickness) of a special dielectric along all substrate surfaces absent of metalization. Specifically, the relative dielectric constant of this air-dielectric interface thin sheet is taken as the average of the two dielectric constants:

$$\varepsilon_{\text{int}} = (1+\varepsilon_r)/2 = 1.665. \tag{7-8}$$

This modeling technique allows the tangential FDTD E-field samples that are on the air-dielectric interface to simultaneously account for the tangential E-field on both sides of the interface. The air-dielectric interface thin sheet is approximated as lossless. Treating the air-dielectric interface in this manner is consistent with that which is done in [58] and is further explained in [59].

As stated earlier, the fabricated empirical benchmark is actually excited by way of a SMA coaxial connector. Unfortunately, incorporating the fine geometrical details of the connector into our overall model would ultimately cause our entire NZ-FZT/FDTD simulation to become quite cumbersome. Consequently, we have chosen to simulate excitation of the radiating structure using an alternative approach that is much more computationally efficient. As revealed in Figures 7.2 and 7.3, our approach makes use of two adjacent, z-directed, E-field sources that are situated internal to the modeled radiating structure as follows: both are 1 cell (in the x-direction) in from the edge of the substrate; both are $\frac{1}{2}$ cell (in the z-direction) up above the ground-plane; and each is situated 1 cell

(in the y-direction) in from either of the two respective edges of the $50\,\Omega$ microstrip feed (the width of which is modeled using 3 cells). The overall NZ-FZT/FDTD model of our empirical benchmark is excited by driving both of these E-field sources using the following sinusoidal waveform:

$$E_s^n = \cos(2\pi\, f_{exc}\, n\Delta t) \text{ where } n = 0,1,\ldots,N-1. \tag{7-9}$$

(Note that the time-step duration Δt is computed using the equality of (6-34) and spatial sample periods defined in (7-5) and (7-6).) Even though we have conveniently chosen to excite our model using a sinusoidal waveform of unity amplitude, for all practical purposes, the choice of amplitude has no real bearing on the computed results. This is true for this particular application because the computed far-zone radiation patterns are ultimately normalized with respect to the peak of its main lobe. In this instance, the NZ-FZT/FDTD model performs pattern normalization so that its computed results can be compared directly to both sets of measured far-zone radiation patterns (which are also normalized; see 7.1.2).

Included in our source model is a $50\,\Omega$ lumped load sandwiched between both z-directed E-field sources and the upper metalization of the microstrip feed. The load is modeled as a lossy dielectric and is part of the source model because it simulates the $50\,\Omega$ output impedance of the range measurement system. In accordance with Figure 7.3, our lumped load is form-factored as follows: 1 cell in the x-direction, 3 cells in the y-direction, and 2 cells in the z-direction. Naturally, we want this size block of resistive material to simulate $50\,\Omega$ in the z-direction. To do so, the conductivity of the lumped load resistive material must be as follows:

$$\sigma_{load} = \frac{(2\Delta z)}{(\Delta x)(3\Delta y)} R^{-1} = 4.224581\ S/m. \tag{7-10}$$

Since the $50\,\Omega$ lumped load is imbedded within the substrate of our modeled structure, we have chosen to make its relative dielectric constant match that of the substrate.

The next step in constructing the NZ-FZT/FDTD model of our fabricated empirical benchmark involves configuration of the DFT (see 6.2.2) and the choice of excitation frequency. Employing the time-step duration Δt, our objective is to find values of *k* (the frequency index of the DFT) and *N* (the number of time-steps in the simulation to be processed by the DFT) that allow the center of the resulting DFT frequency bin to be situated as close as possible to the 3.0 GHz resonant frequency of the microstrip patch. In doing so, we are able to excite the model at the frequency corresponding to the center of the bin so that we can minimize the unwanted effects of DFT processing. Although the modeled patch antenna no longer operates at exactly 3.0 GHz, the trivial shift in operating frequency is worth the numerical tradeoff. Once again, care must be taken to ensure that there are a sufficient number of time-steps to fully characterize the response of the FDTD simulation. Satisfying all of these requirements, our NZ-FZT/FDTD model uses a frequency index $k = 14$ and a total number of time-steps $N = 4091$. Employing these values of *k* and *N*, the time-step duration Δt, and equation (6-43), we find that the center of the resulting DFT frequency bin and, hence, the excitation frequency of (7-9) is as follows:

$$f_{exc} = \frac{k}{N\Delta t} = 3.000282\,GHz\,. \tag{7-11}$$

Note that the excitation frequency of the model is within 94 ppm of the 3.0 GHz resonant frequency. As for the window function applied during DFT processing, the NZ-FZT/FDTD model of our fabricated empirical benchmark exclusively makes use of the Hamming window (see 6.2.2).

When selecting the spheroidal transformation surface to use during the NZ-FZT/FDTD simulation of our fabricated empirical benchmark, we must consider several key elements. First, the spheroidal transformation surface must be able to completely surround the entire benchmark structure without intersecting any part of it. Due to the shape of our empirical benchmark, one can easily see that the oblate spheroid is much more suitable for this particular model than its prolate counterpart. Furthermore,

Table 7.2 Summary of NZ-FZT/FDTD Model of the Fabricated Empirical Benchmark

Microstrip Patch Model:

Size of entire radiation structure (x, y, z): $111 \times 125 \times 3$ cells.
Thickness of modeled substrate: 3 cells.
Length and width of patch antenna: 29 cells.
Width of microstrip feed: 3 cells.
Length of microstrip feed: 33 cells.
Substrate: Modeled with a lossy dielectric using $\varepsilon_r = 2.33$ and $\sigma_{eff} = 4.666355 \times 10^{-4}\ S/m$.
Metalization: Modeled using a PEC thin sheet (infinitesimal thickness).
Air-dielectric interface: Modeled using a lossless dielectric thin sheet (infinitesimal thickness) of $\varepsilon_{\text{int}} = (1 + \varepsilon_r)/2 = 1.665$.
Excitation: Modeled using two E-field sources that drive the microstrip feed against the ground-plane through a $50\,\Omega$ lumped load.
Lumped load: Modeled with $1 \times 3 \times 2$ cells (x, y, z) of lossy dielectric with $\varepsilon_r = 2.33$ and $\sigma_{load} = 4.224581 S/m$ to yield $50\,\Omega$ in z-direction.
Excitation frequency: $f_{exc} = 3.000282\,GHz$.
Position: Entire radiation structure is centered in the FDTD solution volume.

FDTD Solution Volume:

Size of Yee cell: $\Delta x = \Delta y = 1.096579 \times 10^{-3}\ m$ and $\Delta z = 3.810000 \times 10^{-4}\ m$.
Number of cells in each dimension (x, y, z): $185 \times 185 \times 45$ cells.
Time-step duration: $\Delta t = 1.140608 \times 10^{-12}$ sec.

Oblate Spheroidal Transformation Surface:

Size of oblate spheroidal surface: 24 cells in total height (in the z-direction) and 170 cells in diameter (in the x-y plane).
Corresponding oblate spheroidal parameters: $a = 9.309704 \times 10^{-2}\ m$ and $\xi_o = 4.911005 \times 10^{-2}$.
Frequency index: $k = 14$.
Total number of time-steps (and observation interval): $N = 4091$.
Window type: Hamming.
Sample grid: $\Delta\vartheta' = \Delta\varphi' = 1^o$ ($I \times J = 180 \times 360$ samples).
Position: Centered in the solution volume and about the entire radiation structure.

experience gained from our end-to-end test (see 6.3.2) indicates that it is best not to situate the transformation surface too close to the boundaries of the solution volume nor too close to the radiating structure. Taking into account all of these factors, we choose to use an oblate spheroidal transformation surface that is 24 cells in total height (in the z-direction) and 170 cells in diameter (in the x-y plane). This particular oblate spheroid can be described in terms of the following oblate spheroidal parameters: $a = 9.309704 \times 10^{-2}\ m$ and $\xi_o = 4.911005 \times 10^{-2}$ (found by employing the oblate coordinate transformation of (2-1)-(2-5) and the FDTD spatial sample periods defined in (7-5) and (7-6)). Regarding the placement of the oblate spheroidal transformation surface, it is centered both in the solution volume and about the entire radiation structure. Lastly, the NZ-FZT/FDTD model of our empirical benchmark makes use of a uniform sample grid along the spheroidal surface with 1^o intervals in both the ϑ and φ dimensions (i.e., $I \times J = 180 \times 360$). Provided in Table 7.2 is a summary of the NZ-FZT/FDTD model of our fabricated empirical benchmark.

7.2.2 Comparison of NZ-FZT/FDTD Model Results with Measured Results

At last, we are now able to compare the far-zone radiation patterns computed by the just developed NZ-FZT/FDTD model with the patterns measured at NASA Langley and Virginia Tech. The computed results are in 1^o increments over the full 360^o for both E- and H-plane linear co-polarization cuts. Like the measured data, the computed radiation patterns also consist of relative power measurements that are normalized with respect to the peak of the main lobe. Specifically, the computed results are found by expressing the relative magnitude of the far-zone E-field in decibels (dB). Regarding the convergence of our NZ-FZT/FDTD model, numerical tests indicate that the computed far-zone radiation patterns converge at the point where $L = 16$ (i.e., the degree at which the spheroidal wave-harmonic expansion is truncated; see 2.3.1).

Both Figures 7.4 and 7.5 graphically depict a direct comparison of all three sets of pattern data for both the E- and H-plane linear co-polarization cuts. Notice that there are

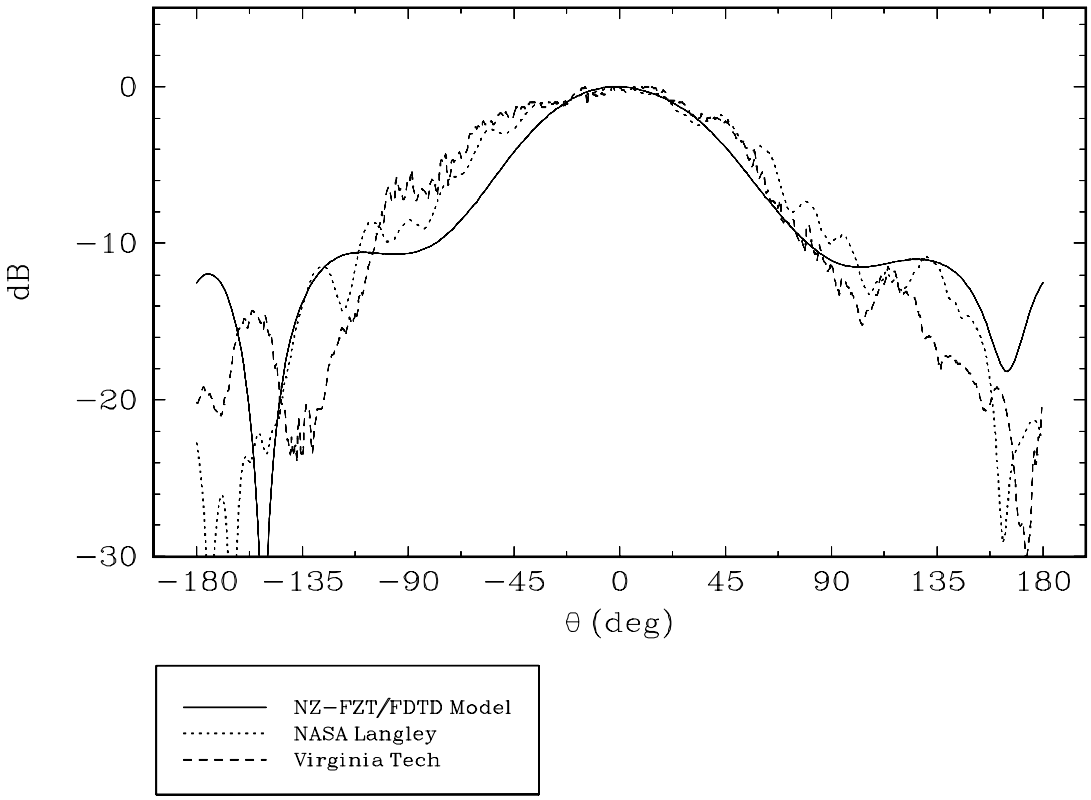

Figure 7.4 Comparison of NZ-FZT/FDTD model results (of the empirical benchmark) with NASA Langley and Virginia Tech measured results for the E-plane linear co-polarization pattern at 3.0 GHz.

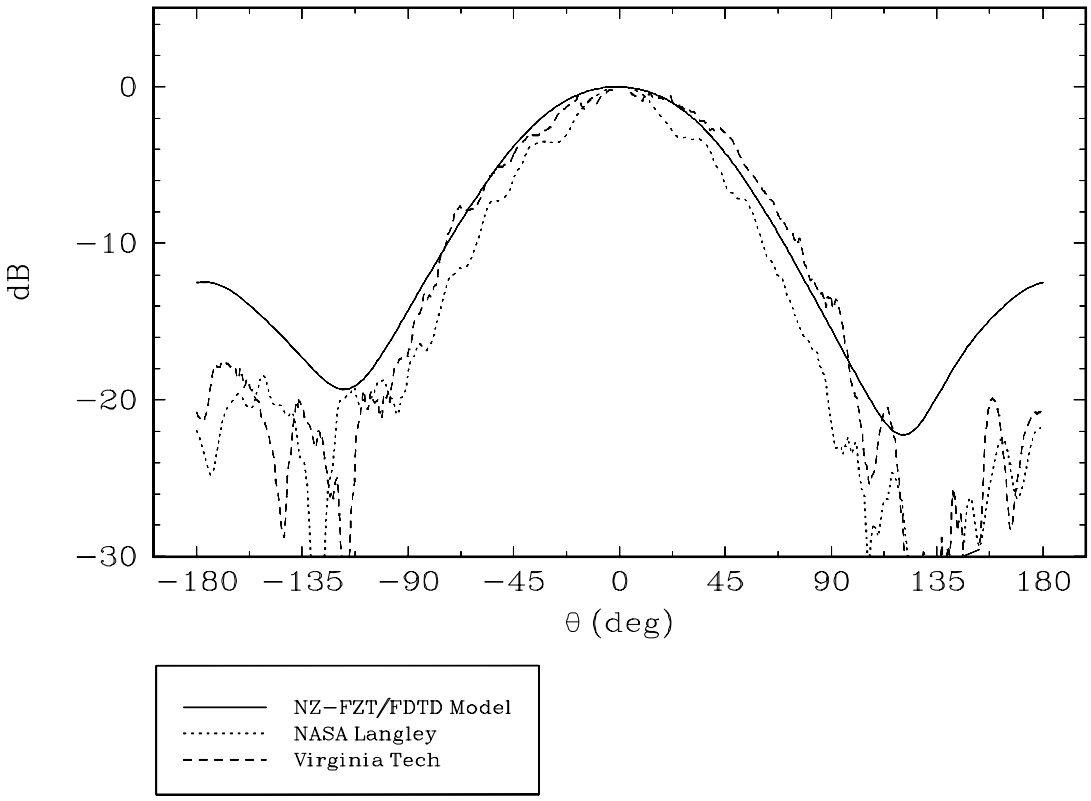

Figure 7.5 Comparison of NZ-FZT/FDTD model results (of the empirical benchmark) with NASA Langley and Virginia Tech measured results for the H-plane linear co-polarization pattern at 3.0 GHz.

some inconsistencies between the patterns measured at NASA Langley and those measured at Virginia Tech. In essence, these differences demonstrate that a certain amount of measurement error is introduced by each range measurement system together with its respective range design. Part of this measurement error can be attributed to unwanted reflections from both the antenna positioner and the range surroundings. Consequently, we have included both sets of measured data in order to give us a more complete picture of the actual far-zone behavior of the fabricated empirical benchmark.

For the most part with a few exceptions, the far-zone radiation patterns computed by our NZ-FZT/FDTD model are in fairly good agreement with both sets of measured data for the forward-looking region where $-120^o \leq \theta \leq 120^o$. Naturally, we exclude the region behind the benchmark microstrip patch from consideration because of the measurement error introduced by the presence of an antenna positioner and its associated measurement equipment. To put it briefly, our NZ-FZT/FDTD model simulates the fabricated benchmark antenna situated in free-space, not mounted on a positioner. Furthermore, inspection of Figure 7.4 reveals that both sets of measured E-plane data have an asymmetry with respect to the far-zone observation angle θ that is more pronounced than the slight asymmetry exhibited by the computed results. Although the computed results are in good agreement with the measured results for the positive half of the forward-looking region and in the broadside direction where $-22.5^o \leq \theta \leq 22.5^o$, some differences do exist over some of the observation angles in the corresponding negative half of the forward-looking region. The cause of these differences can most likely be attributed to the fact that the SMA connector and its attached coaxial cable are present during the actual measurements whereas both microwave structures are not part of our NZ-FZT/FDTD simulation (see 7.2.1). As a result, unwanted coupling, scattering, and radiation from both the connector (including its flange) and the coaxial cable all ultimately alter the true far-zone performance of the fabricated empirical benchmark. The fact that the actual test setup has a connector and a cable on only one side of the fabricated structure is consistent with the asymmetry found in the E-plane measured

results. In addition, the slight asymmetry present in the computed results is consistent with the microstrip patch being fed from only one side. Finally, Figure 7.5 indicates that the computed results for the H-plane pattern cut are in good agreement with the measured results for the entire forward looking region where $-120^o \leq \theta \leq 120^o$. The fact that no significant asymmetries are found in either of the measured H-plane pattern results or in the computed results is also consistent with the configuration of the actual test setup and the layout of the fabricated empirical benchmark. On the whole, our NZ-FZT/FDTD model does a good job of numerically simulating radiation from the empirical benchmark.

CHAPTER 8. SUMMARY AND CONCLUSIONS

There are several important conclusions that can be drawn from this research. First, our findings show that it is possible to construct a practical NZ-FZT process that makes use of a spheroidal transformation surface and requires knowledge of only one of the two near-zone electromagnetic fields, not both. Furthermore, it should be emphasized that the process is quite successful despite the fact that both spheroidal transformation surfaces do not support orthogonal vector wave functions. As shown in Chapter 2, we are able to sidestep this difficulty by employing a differential equation approach that solves the three-dimensional vector Helmholtz equation using a hybrid of coordinate systems. Although our algorithms are defined throughout the dissertation in terms of the radiating E-field (both near- and far-zone), it is important to realize that the overall NZ-FZT process also applies to the radiating H-field (this assertion is easily understood by evoking the duality theorem of electromagnetics).

Throughout our investigation the newly developed NZ-FZT process is shown to have several noteworthy features that are considered quite beneficial. Since the entire process is very efficient from a computational standpoint, the developed algorithms are capable of being successfully mapped to an IBM compatible personal computer (see Chapters 3 and 4). As a result, we need not have the computational power of a supercomputer or of some other type of specialized hardware to carry out our numerical process. Also, because our NZ-FZT process is formulated in a generalized manner, it is not just limited to addressing radiation problems with rotational symmetry. The capacity to handle radiation problems that are rotationally asymmetric is numerically demonstrated with the offset dipole numerical tests (in Chapter 5) and with the NZ-FZT/FDTD model of the empirical benchmark (in Chapter 7). Lastly, an additional feature that is afforded to us by our NZ-FZT process is the ability to compute the far-zone in terms of its correct absolute quantity, and not some relative quantity; that is, the far-zone is accurately rendered without any magnitude and phase normalization. Note that being able to

compute far-zone field quantities in an unnormalized format is often necessary depending upon the given application (e.g., computation of antenna gain).

Regarding the performance of our NZ-FZT process, the numerical studies of Chapter 5 indicate that the algorithms (operating on the analytical benchmark radiation structure for a given set of spheroidal transformation surfaces) provide unnormalized far-zone results that match theory within $\pm 0.1\%$ in magnitude and ± 0.12 deg in phase. In addition, both algorithms demonstrate that they provide at least 78 dB of numerical dynamic range with regard to pattern computations. And finally, the rate of convergence is shown to be more than acceptable for algorithmic expansions of this nature. Citing these results, we conclude that our newly developed NZ-FZT process is extremely sound both in theory and implementation.

However, although both algorithms perform extremely well during the numerical tests of Chapter 5 for a specific radiating structure and a specific set of spheroidal transformation surfaces, the possibility exists that the numerical process may breakdown in some extreme cases. It is important to emphasize that this shortcoming is not caused by the underlying theory behind the developed NZ-FZT process, but rather the inability of the algorithms to accurately compute all orders and degrees of the required special functions necessary to achieve convergence. Naturally, this particular situation can arise when applying the algorithms to very large radiating structures.

In Chapter 6, we are able to successfully integrate our NZ-FZT process with a FDTD electromagnetic field solver. We do so in order to create a tool that allows us to further validate our newly developed process. The entire combined process is initially verified by using a computational model of our analytical benchmark to conduct an end-to-end test. From this numerical study we also gain an understanding of both the limitations and expected performance of the NZ-FZT/FDTD combined process. Finally, the linking of both processes allows us to successfully demonstrate a novel application of our newly developed NZ-FZT process.

Our research concludes in Chapter 7 by applying the developed NZ-FZT process to a computational model of our fabricated empirical benchmark. Far-zone radiation

patterns computed by the NZ-FZT/FDTD model of the empirical benchmark are then compared to those measured at NASA Langley and Virginia Tech. Overall with a few exceptions, both the computed and measured sets of far-zone radiation patterns are in fairly good agreement for the forward-looking region. Ultimately, it is this additional numerical/empirical experiment that provides further validation of our newly developed NZ-FZT process.

In the end, it is our hope that the work presented in this dissertation, in part or as a whole, is able to further serve the research community as both a tool and a springboard for a variety of other uses. Regardless of their application, the numerical routines developed in Chapter 3 provide an efficient way to compute all of the special functions pertaining to prolate and oblate spheroidal wave-harmonics. In addition, both developed benchmarks are able to provide other researchers with a means through which to test their own computational algorithms. Finally, computational strategies and approaches used to develop our NZ-FZT process may also be of aid in addressing other electromagnetic problems with spheroidal based geometries.

APPENDIX A. PROLATE AND OBLATE SPHEROIDAL COORDINATE SYSTEMS

Prolate Spheroidal Coordinates (with z-axis preference)

Independent coordinates and their domain:

(ξ, η, φ) or $(\xi, \vartheta, \varphi)$, where $\eta = \cos\vartheta$

and

$1 \le \xi < \infty$, $-1 \le \eta \le 1$ or $0 \le \vartheta \le \pi$, $0 \le \varphi \le 2\pi$.

Prolate spheroidal-to-Cartesian transformation [23]:

$$x = a\sqrt{\xi^2 - 1}\sqrt{1 - \eta^2}\cos\varphi = a\sqrt{\xi^2 - 1}\sin\vartheta\cos\varphi \tag{A-1}$$

$$y = a\sqrt{\xi^2 - 1}\sqrt{1 - \eta^2}\sin\varphi = a\sqrt{\xi^2 - 1}\sin\vartheta\sin\varphi \tag{A-2}$$

$$z = a\xi\eta = a\xi\cos\vartheta \tag{A-3}$$

where a is the distance between the focal point of the coordinate system and the origin.

Prolate spheroidal scale factors (metric coefficients) [22]:

$$h_\xi = a\sqrt{\frac{\xi^2 - \eta^2}{\xi^2 - 1}} = a\sqrt{\frac{\xi^2 - \cos^2\vartheta}{\xi^2 - 1}}, \tag{A-4}$$

$$h_\eta = a\sqrt{\frac{\xi^2 - \eta^2}{1 - \eta^2}} \quad \text{or} \tag{A-5}$$

$$h_\vartheta = a\sqrt{\xi^2 - \cos^2\vartheta}, \tag{A-6}$$

$$h_\varphi = a\sqrt{\xi^2 - 1}\sqrt{1 - \eta^2} = a\sqrt{\xi^2 - 1}\sin\vartheta. \tag{A-7}$$

Prolate spheroidal unit vector representations:

$$\begin{aligned}\hat{\xi} &= \xi\sqrt{\frac{1-\eta^2}{\xi^2-\eta^2}}\cos\varphi\,\hat{x} + \xi\sqrt{\frac{1-\eta^2}{\xi^2-\eta^2}}\sin\varphi\,\hat{y} + \eta\sqrt{\frac{\xi^2-1}{\xi^2-\eta^2}}\,\hat{z} \\ &= \frac{\xi\sin\vartheta}{\sqrt{\xi^2-\cos^2\vartheta}}\cos\varphi\,\hat{x} + \frac{\xi\sin\vartheta}{\sqrt{\xi^2-\cos^2\vartheta}}\sin\varphi\,\hat{y} + \sqrt{\frac{\xi^2-1}{\xi^2-\cos^2\vartheta}}\cos\vartheta\,\hat{z}\,, \qquad \text{(A-8)}\end{aligned}$$

$$\hat{\eta} = -\eta\sqrt{\frac{\xi^2-1}{\xi^2-\eta^2}}\cos\varphi\,\hat{x} - \eta\sqrt{\frac{\xi^2-1}{\xi^2-\eta^2}}\sin\varphi\,\hat{y} + \xi\sqrt{\frac{1-\eta^2}{\xi^2-\eta^2}}\,\hat{z} \quad \text{or} \qquad \text{(A-9)}$$

$$\begin{aligned}\hat{\vartheta} &= \sqrt{\frac{\xi^2-1}{\xi^2-\cos^2\vartheta}}\cos\vartheta\cos\varphi\,\hat{x} \\ &\quad + \sqrt{\frac{\xi^2-1}{\xi^2-\cos^2\vartheta}}\cos\vartheta\sin\varphi\,\hat{y} - \frac{\xi\sin\vartheta}{\sqrt{\xi^2-\cos^2\vartheta}}\hat{z} \quad (\text{note that } \hat{\eta} = -\hat{\vartheta}\,), \qquad \text{(A-10)}\end{aligned}$$

$$\hat{\varphi} = -\sin\varphi\,\hat{x} + \cos\varphi\,\hat{y}\,, \qquad \text{(A-11)}$$

and

$$\begin{aligned}\hat{x} &= \xi\sqrt{\frac{1-\eta^2}{\xi^2-\eta^2}}\cos\varphi\,\hat{\xi} - \eta\sqrt{\frac{\xi^2-1}{\xi^2-\eta^2}}\cos\varphi\,\hat{\eta} - \sin\varphi\,\hat{\varphi} \\ &= \frac{\xi\sin\vartheta}{\sqrt{\xi^2-\cos^2\vartheta}}\cos\varphi\,\hat{\xi} + \sqrt{\frac{\xi^2-1}{\xi^2-\cos^2\vartheta}}\cos\vartheta\cos\varphi\,\hat{\vartheta} - \sin\varphi\,\hat{\varphi}\,, \qquad \text{(A-12)}\end{aligned}$$

$$\begin{aligned}\hat{y} &= \xi\sqrt{\frac{1-\eta^2}{\xi^2-\eta^2}}\sin\varphi\,\hat{\xi} - \eta\sqrt{\frac{\xi^2-1}{\xi^2-\eta^2}}\sin\varphi\,\hat{\eta} + \cos\varphi\,\hat{\varphi} \\ &= \frac{\xi\sin\vartheta}{\sqrt{\xi^2-\cos^2\vartheta}}\sin\varphi\,\hat{\xi} + \sqrt{\frac{\xi^2-1}{\xi^2-\cos^2\vartheta}}\cos\vartheta\sin\varphi\,\hat{\vartheta} + \cos\varphi\,\hat{\varphi}\,, \qquad \text{(A-13)}\end{aligned}$$

$$\begin{aligned}\hat{z} &= \eta\sqrt{\frac{\xi^2-1}{\xi^2-\eta^2}}\,\hat{\xi} + \xi\sqrt{\frac{1-\eta^2}{\xi^2-\eta^2}}\,\hat{\eta} \\ &= \sqrt{\frac{\xi^2-1}{\xi^2-\cos^2\vartheta}}\cos\vartheta\,\hat{\xi} - \frac{\xi\sin\vartheta}{\sqrt{\xi^2-\cos^2\vartheta}}\hat{\vartheta}\,. \qquad \text{(A-14)}\end{aligned}$$

Definition of cross product in prolate spheroidal coordinates:

The unit vectors $\hat{\xi}$, $\hat{\vartheta}$, and $\hat{\varphi}$ form a right-handed coordinate system that is defined by the cross products

$$\hat{\xi} \times \hat{\vartheta} = \hat{\varphi} \tag{A-15}$$

$$\hat{\varphi} \times \hat{\xi} = \hat{\vartheta} \tag{A-16}$$

$$\hat{\vartheta} \times \hat{\varphi} = \hat{\xi} \tag{A-17}$$

where $\hat{\eta} = -\hat{\vartheta}$.

Far-zone behavior ($\xi \to \infty$) of prolate spheroidal coordinates [23]:

In the far-zone, viz., large arguments of ξ, the prolate spheroidal coordinate system approaches the spherical coordinate system in the following manner:

$$\xi \to r/a \,, \tag{A-18}$$

$$\eta \to \cos\theta \quad \text{or} \tag{A-19}$$

$$\vartheta \to \theta \,, \tag{A-20}$$

$$\varphi \equiv \varphi \,, \tag{A-21}$$

and $$\hat{\xi} \to \hat{r} \,, \tag{A-22}$$

$$\hat{\eta} \to -\hat{\theta} \quad \text{or} \tag{A-23}$$

$$\hat{\vartheta} \to \hat{\theta} \,, \tag{A-24}$$

$$\hat{\varphi} \equiv \hat{\varphi} \,. \tag{A-25}$$

Oblate Spheroidal Coordinates (with z-axis preference)

Independent coordinates and their domain:

(ξ, η, φ) or $(\xi, \vartheta, \varphi)$, where $\eta = \cos\vartheta$

and

$0 \le \xi < \infty$, $-1 \le \eta \le 1$ or $0 \le \vartheta \le \pi$, $0 \le \varphi \le 2\pi$.

Oblate spheroidal-to-Cartesian transformation [23]:

$$x = a\sqrt{\xi^2 + 1}\sqrt{1 - \eta^2}\cos\varphi = a\sqrt{\xi^2 + 1}\sin\vartheta\cos\varphi \tag{A-26}$$

$$y = a\sqrt{\xi^2 + 1}\sqrt{1 - \eta^2}\sin\varphi = a\sqrt{\xi^2 + 1}\sin\vartheta\sin\varphi \tag{A-27}$$

$$z = a\xi\eta = a\xi\cos\vartheta \tag{A-28}$$

where a is the distance between the focal point of the coordinate system and the origin.

Oblate spheroidal scale factors (metric coefficients) [22]:

$$h_\xi = a\sqrt{\frac{\xi^2 + \eta^2}{\xi^2 + 1}} = a\sqrt{\frac{\xi^2 + \cos^2\vartheta}{\xi^2 + 1}}, \tag{A-29}$$

$$h_\eta = a\sqrt{\frac{\xi^2 + \eta^2}{1 - \eta^2}} \quad \text{or} \tag{A-30}$$

$$h_\vartheta = a\sqrt{\xi^2 + \cos^2\vartheta}, \tag{A-31}$$

$$h_\varphi = a\sqrt{\xi^2 + 1}\sqrt{1 - \eta^2} = a\sqrt{\xi^2 + 1}\sin\vartheta. \tag{A-32}$$

Oblate spheroidal unit vector representations:

$$\begin{aligned}\hat{\xi} &= \xi\sqrt{\frac{1-\eta^2}{\xi^2+\eta^2}}\cos\varphi\,\hat{x} + \xi\sqrt{\frac{1-\eta^2}{\xi^2+\eta^2}}\sin\varphi\,\hat{y} + \eta\sqrt{\frac{\xi^2+1}{\xi^2+\eta^2}}\,\hat{z} \\ &= \frac{\xi\sin\vartheta}{\sqrt{\xi^2+\cos^2\vartheta}}\cos\varphi\,\hat{x} + \frac{\xi\sin\vartheta}{\sqrt{\xi^2+\cos^2\vartheta}}\sin\varphi\,\hat{y} + \sqrt{\frac{\xi^2+1}{\xi^2+\cos^2\vartheta}}\cos\vartheta\,\hat{z}\,, \qquad \text{(A-33)}\end{aligned}$$

$$\hat{\eta} = -\eta\sqrt{\frac{\xi^2+1}{\xi^2+\eta^2}}\cos\varphi\,\hat{x} - \eta\sqrt{\frac{\xi^2+1}{\xi^2+\eta^2}}\sin\varphi\,\hat{y} + \xi\sqrt{\frac{1-\eta^2}{\xi^2+\eta^2}}\,\hat{z} \quad \text{or} \qquad \text{(A-34)}$$

$$\begin{aligned}\hat{\vartheta} &= \sqrt{\frac{\xi^2+1}{\xi^2+\cos^2\vartheta}}\cos\vartheta\cos\varphi\,\hat{x} \\ &\quad + \sqrt{\frac{\xi^2+1}{\xi^2+\cos^2\vartheta}}\cos\vartheta\sin\varphi\,\hat{y} - \frac{\xi\sin\vartheta}{\sqrt{\xi^2+\cos^2\vartheta}}\,\hat{z} \quad (\text{note that } \hat{\eta} = -\hat{\vartheta}\,), \qquad \text{(A-35)}\end{aligned}$$

$$\hat{\varphi} = -\sin\varphi\,\hat{x} + \cos\varphi\,\hat{y}\,, \qquad \text{(A-36)}$$

and

$$\begin{aligned}\hat{x} &= \xi\sqrt{\frac{1-\eta^2}{\xi^2+\eta^2}}\cos\varphi\,\hat{\xi} - \eta\sqrt{\frac{\xi^2+1}{\xi^2+\eta^2}}\cos\varphi\,\hat{\eta} - \sin\varphi\,\hat{\varphi} \\ &= \frac{\xi\sin\vartheta}{\sqrt{\xi^2+\cos^2\vartheta}}\cos\varphi\,\hat{\xi} + \sqrt{\frac{\xi^2+1}{\xi^2+\cos^2\vartheta}}\cos\vartheta\cos\varphi\,\hat{\vartheta} - \sin\varphi\,\hat{\varphi}\,, \qquad \text{(A-37)}\end{aligned}$$

$$\begin{aligned}\hat{y} &= \xi\sqrt{\frac{1-\eta^2}{\xi^2+\eta^2}}\sin\varphi\,\hat{\xi} - \eta\sqrt{\frac{\xi^2+1}{\xi^2+\eta^2}}\sin\varphi\,\hat{\eta} + \cos\varphi\,\hat{\varphi} \\ &= \frac{\xi\sin\vartheta}{\sqrt{\xi^2+\cos^2\vartheta}}\sin\varphi\,\hat{\xi} + \sqrt{\frac{\xi^2+1}{\xi^2+\cos^2\vartheta}}\cos\vartheta\sin\varphi\,\hat{\vartheta} + \cos\varphi\,\hat{\varphi}\,, \qquad \text{(A-38)}\end{aligned}$$

$$\begin{aligned}\hat{z} &= \eta\sqrt{\frac{\xi^2+1}{\xi^2+\eta^2}}\,\hat{\xi} + \xi\sqrt{\frac{1-\eta^2}{\xi^2+\eta^2}}\,\hat{\eta} \\ &= \sqrt{\frac{\xi^2+1}{\xi^2+\cos^2\vartheta}}\cos\vartheta\,\hat{\xi} - \frac{\xi\sin\vartheta}{\sqrt{\xi^2+\cos^2\vartheta}}\,\hat{\vartheta}\,. \qquad \text{(A-39)}\end{aligned}$$

Definition of cross product in oblate spheroidal coordinates:

The unit vectors $\hat{\xi}$, $\hat{\vartheta}$, and $\hat{\varphi}$ form a right-handed coordinate system that is also defined by the cross-products specified in expressions (A-15)-(A-17).

Far-zone behavior ($\xi \to \infty$) of oblate spheroidal coordinates [23]:

In the far-zone, viz., large arguments of ξ, the oblate spheroidal coordinate system approaches the spherical coordinate system in a manner that is similar to its prolate counterpart. Accordingly, the far-zone expressions provided in (A-18)-(A-25) also apply to the oblate spheroidal coordinate system.

APPENDIX B. SCALAR LAPLACIAN IN SPHEROIDAL COORDINATES

The generalized Laplacian for a scalar function defined in terms of an orthogonal curvilinear coordinate system is as follows [60]:

$$\nabla^2 f(u_1,u_2,u_3) =$$

$$\frac{1}{h_1 h_2 h_3}\left[\frac{\partial}{\partial u_1}\left(\frac{h_2 h_3}{h_1}\frac{\partial f}{\partial u_1}\right)+\frac{\partial}{\partial u_2}\left(\frac{h_3 h_1}{h_2}\frac{\partial f}{\partial u_2}\right)+\frac{\partial}{\partial u_3}\left(\frac{h_1 h_2}{h_3}\frac{\partial f}{\partial u_3}\right)\right] \qquad \text{(B-1)}$$

where h_1, h_2, and h_3 are the respective scale factors.

In the prolate spheroidal case, we employ the scale factors of (A-4)-(A-7) with (B-1) to yield the following representation of the Laplacian in prolate spheroidal coordinates [22]:

$$\nabla^2 \psi^P(\xi,\eta,\varphi)$$

$$= \frac{1}{h_\xi h_\eta h_\varphi}\left[\frac{\partial}{\partial \xi}\left(\frac{h_\eta h_\varphi}{h_\xi}\frac{\partial \psi^P}{\partial \xi}\right)+\frac{\partial}{\partial \eta}\left(\frac{h_\varphi h_\xi}{h_\eta}\frac{\partial \psi^P}{\partial \eta}\right)+\frac{\partial}{\partial \varphi}\left(\frac{h_\xi h_\eta}{h_\varphi}\frac{\partial \psi^P}{\partial \varphi}\right)\right]$$

$$= \frac{1}{a^2(\xi^2-\eta^2)}\left[\frac{\partial}{\partial \xi}\left(\left(\xi^2-1\right)\frac{\partial \psi^P}{\partial \xi}\right)+\frac{\partial}{\partial \eta}\left(\left(1-\eta^2\right)\frac{\partial \psi^P}{\partial \eta}\right)+\frac{\left(\xi^2-\eta^2\right)}{\left(\xi^2-1\right)\left(1-\eta^2\right)}\frac{\partial^2 \psi^P}{\partial \varphi^2}\right].$$

(B-2)

Likewise, we employ the scale factors of (A-29)-(A-32) with (B-1) to yield the following representation of the Laplacian in oblate spheroidal coordinates [22]:

$$\nabla^2 \psi^O(\xi,\eta,\varphi)$$

$$= \frac{1}{h_\xi h_\eta h_\varphi}\left[\frac{\partial}{\partial \xi}\left(\frac{h_\eta h_\varphi}{h_\xi}\frac{\partial \psi^O}{\partial \xi}\right)+\frac{\partial}{\partial \eta}\left(\frac{h_\varphi h_\xi}{h_\eta}\frac{\partial \psi^O}{\partial \eta}\right)+\frac{\partial}{\partial \varphi}\left(\frac{h_\xi h_\eta}{h_\varphi}\frac{\partial \psi^O}{\partial \varphi}\right)\right]$$

$$= \frac{1}{a^2(\xi^2+\eta^2)}\left[\frac{\partial}{\partial \xi}\left(\left(\xi^2+1\right)\frac{\partial \psi^O}{\partial \xi}\right)+\frac{\partial}{\partial \eta}\left(\left(1-\eta^2\right)\frac{\partial \psi^O}{\partial \eta}\right)+\frac{\left(\xi^2+\eta^2\right)}{\left(\xi^2+1\right)\left(1-\eta^2\right)}\frac{\partial^2 \psi^O}{\partial \varphi^2}\right].$$

(B-3)

APPENDIX C. SEPARATION OF VARIABLES OF THE SCALAR HELMHOLTZ EQUATION IN SPHEROIDAL COORDINATES

For the prolate spheroidal case, we apply the separation of variables method to the scalar Helmholtz partial differential equation expressed in terms of coordinate specific differential operators [23]:

$$\frac{\partial}{\partial\xi}\left(\left(\xi^2-1\right)\frac{\partial\psi^P}{\partial\xi}\right)+\frac{\partial}{\partial\eta}\left(\left(1-\eta^2\right)\frac{\partial\psi^P}{\partial\eta}\right)+\frac{\left(\xi^2-\eta^2\right)}{\left(\xi^2-1\right)\left(1-\eta^2\right)}\frac{\partial^2\psi^P}{\partial\varphi^2}+h^2(\xi^2-\eta^2)\psi^P=0 \tag{C-1}$$

where $h \equiv ka \equiv (2\pi/\lambda_o)\,a \equiv 2\pi\, a_\lambda$.

We begin this process by assuming the solution of the partial differential equation to be the product of three distinct functions with each being only dependent on its respective variable:

$$\psi^P(\xi,\eta,\varphi) = R_P(\xi)S_P(\eta)\Phi_P(\varphi) \tag{C-2}$$

where $R_P(\xi)$ is the radial solution, $S_P(\eta)$ is the angular solution, and $\Phi_P(\varphi)$ is the azimuthal (rotational) solution. Substituting (C-2) into the partial differential equation of (C-1), we obtain the following:

$$\frac{1}{R_p}\frac{\partial}{\partial\xi}\left(\left(\xi^2-1\right)\frac{\partial R_P}{\partial\xi}\right)+\frac{1}{S_p}\frac{\partial}{\partial\eta}\left(\left(1-\eta^2\right)\frac{\partial S_p}{\partial\eta}\right)$$

$$+\frac{\left(\xi^2-\eta^2\right)}{\left(\xi^2-1\right)\left(1-\eta^2\right)}\left(\frac{1}{\Phi_p}\frac{\partial^2\Phi_p}{\partial\varphi^2}\right)+h^2(\xi^2-\eta^2)=0\,. \tag{C-3}$$

Upon review of (C-3), one can see that Φ_P, which is a function of φ only, can be made to equal a function of the other two variables:

$$\frac{1}{\Phi_p}\frac{\partial^2 \Phi_p}{\partial \varphi^2} =$$

$$-\frac{\left(\xi^2-1\right)\left(1-\eta^2\right)}{\left(\xi^2-\eta^2\right)}\left[\frac{1}{R_p}\frac{\partial}{\partial \xi}\left(\left(\xi^2-1\right)\frac{\partial R_P}{\partial \xi}\right)+\frac{1}{S_p}\frac{\partial}{\partial \eta}\left(\left(1-\eta^2\right)\frac{\partial S_p}{\partial \eta}\right)+h^2(\xi^2-\eta^2)\right].$$

(C-4)

However, all three variables are suppose to be independent of one another. This paradox can be resolved by setting each side of (C-4) equal to the same separation constant. Although theory allows this constant to be represented by any mathematical symbol, it is convenient to select the separation constant as $-m^2$. Consequently, we are able to reduce the partial differential equation of (C-1) into an ordinary differential equation that depends on φ only, viz.,

$$\frac{d^2}{d\varphi^2}\Phi_P(\varphi)+m^2\Phi_P(\varphi)=0 \quad \text{where} \quad 0\le\varphi\le 2\pi\,, \tag{C-5}$$

and a partial differential equation that depends on both ξ and η only, viz.,

$$\frac{1}{R_p}\frac{\partial}{\partial \xi}\left(\left(\xi^2-1\right)\frac{\partial R_P}{\partial \xi}\right)+\frac{1}{S_p}\frac{\partial}{\partial \eta}\left(\left(1-\eta^2\right)\frac{\partial S_p}{\partial \eta}\right)$$

$$-\frac{\left(\xi^2-\eta^2\right)}{\left(\xi^2-1\right)\left(1-\eta^2\right)}m^2+h^2(\xi^2-\eta^2)=0\,. \tag{C-6}$$

With some mathematical manipulation, the partial differential equation of (C-6) can be written as follows:

$$\frac{1}{R_p}\frac{\partial}{\partial\xi}\left(\left(\xi^2-1\right)\frac{\partial R_P}{\partial\xi}\right)-\frac{m^2}{\xi^2-1}+h^2\xi^2 =$$

$$-\frac{1}{S_p}\frac{\partial}{\partial\eta}\left(\left(1-\eta^2\right)\frac{\partial S_p}{\partial\eta}\right)+\frac{m^2}{1-\eta^2}+h^2\eta^2 . \qquad \text{(C-7)}$$

At this point, we have the two remaining independent variables represented as a function of one another. Once again, we resolve the paradox by setting both sides equal to a second separation constant λ (not to be confused with free-space wavelength). As a result, we are able to reduce the intermediate partial differential equation of (C-6) into two separate ordinary differential equations:

$$\frac{d}{d\xi}\left[\left(\xi^2-1\right)\frac{d}{d\xi}R_P(\xi)\right]-\left[\lambda-h^2\xi^2+\frac{m^2}{\left(\xi^2-1\right)}\right]R_P(\xi)=0 \text{ where } 1\le\xi<\infty ,$$

(C-8)

$$\frac{d}{d\eta}\left[\left(1-\eta^2\right)\frac{d}{d\eta}S_P(\eta)\right]+\left[\lambda-h^2\eta^2-\frac{m^2}{\left(1-\eta^2\right)}\right]S_P(\eta)=0 \text{ where } -1\le\eta\le 1 .$$

(C-9)

In short, the partial differential equation of (C-1) is reduced to three separate ordinary differential equations, namely (C-4), (C-8), and (C-9), by way of introducing two separation constants, namely $-m^2$ and λ.

Similarly, we can apply the same method to reduce the scalar Helmholtz partial differential equation in oblate spheroidal coordinates [23]:

$$\frac{\partial}{\partial\xi}\left(\left(\xi^2+1\right)\frac{\partial\psi^O}{\partial\xi}\right)+\frac{\partial}{\partial\eta}\left(\left(1-\eta^2\right)\frac{\partial\psi^O}{\partial\eta}\right)+\frac{\left(\xi^2+\eta^2\right)}{\left(\xi^2+1\right)\left(1-\eta^2\right)}\frac{\partial^2\psi^O}{\partial\varphi^2}+h^2(\xi^2+\eta^2)\psi^O=0$$

(C-10)

where $h\equiv ka\equiv(2\pi/\lambda_o)\,a\equiv 2\pi\,a_\lambda$.

Adopting the same separation constants as the prolate spheroidal case, we are able to reduce (C-10) to the following three ordinary differential equations:

$$\frac{d^2}{d\varphi^2}\Phi_O(\varphi) + m^2\Phi_O(\varphi) = 0 \text{ where } 0 \le \varphi \le 2\pi\,, \tag{C-11}$$

$$\frac{d}{d\xi}\left[\left(\xi^2+1\right)\frac{d}{d\xi}R_O(\xi)\right] - \left[\lambda - h^2\xi^2 - \frac{m^2}{\left(\xi^2+1\right)}\right]R_O(\xi) = 0 \text{ where } 0 \le \xi < \infty\,, \tag{C-12}$$

$$\frac{d}{d\eta}\left[\left(1-\eta^2\right)\frac{d}{d\eta}S_O(\eta)\right] + \left[\lambda + h^2\eta^2 - \frac{m^2}{\left(1-\eta^2\right)}\right]S_O(\eta) = 0 \text{ where } -1 \le \eta \le 1\,. \tag{C-13}$$

APPENDIX D. LEGENDRE FUNCTIONS

Legendre Polynomials and Functions

Legendre's differential equation (where order $m = 0$) [29], [40]:

$$\frac{d}{dz'}\left[(1-z'^2)\frac{dy}{dz'}\right] + l(l+1)y = 0 \quad \text{where } l \text{ is an integer and } z' \text{ is} \tag{D-1}$$

complex; regular singularities exist at $z' = \pm 1$ and $z' = \infty$.

Definition of domain:

In the following, z represents any arbitrary point in the finite complex plane with the exception of those points on the real axis that lie on the $-1 < x < 1$ branch cut; meanwhile, x represents all points on the branch cut.

Independent solutions of Legendre's differential equation:

Legendre polynomials (or Legendre functions of the first kind):

$P_l(z)$ (off the branch cut) and $P_l(x)$ (on the branch cut);

Legendre functions of the second kind:

$Q_l(z)$ (off the branch cut) and $Q_l(x)$ (on the branch cut).

Definition of Legendre polynomials [29], [40]:

$$P_l(z) = \sum_{q=0}^{Int[l/2]} (-1)^q \frac{(2l-2q)!}{2^l q!(l-q)!(l-2q)!} z^{l-2q} \qquad \text{(D-2)}$$

$$P_l(z) = \frac{1}{2^l l!} \frac{d^l}{dz^l}(z^2-1)^l \quad \text{(Rodrigues' formula)} \qquad \text{(D-3)}$$

where both equations are valid on and off the branch cut, i.e., z can be replaced with x; and $Int[x]$ is the greatest integer function, e.g., $Int[7/2] = 3$ and $Int[2] = 2$.

Table D.1 Legendre Polynomials

$P_0(z) = 1$
$P_1(z) = z$
$P_2(z) = \frac{1}{2}(3z^2 - 1)$
$P_3(z) = \frac{1}{2}(5z^3 - 3z)$
$P_4(z) = \frac{1}{8}(35z^4 - 30z^2 + 3)$
$P_5(z) = \frac{1}{8}(63z^5 - 70z^3 + 15z)$
$P_6(z) = \frac{1}{16}(231z^6 - 315z^4 + 105z^2 - 5)$

(Note: Polynomials are valid on and off the branch cut, i.e., z can be replaced with x.)

Definition of Legendre functions of the second kind [29], [40]:

Off the branch cut:

$$Q_l(z) = \tfrac{1}{2} P_l(z) \ln\frac{z+1}{z-1} - \sum_{q=0}^{Int\left[\frac{1}{2}(l-1)\right]} \frac{(2l-4q-1)}{(2q+1)(l-q)} P_{l-2q-1}(z) \quad \text{for } l \geq 1, \qquad \text{(D-4)}$$

and $Q_0(z) = \frac{1}{2}\ln\frac{z+1}{z-1}$ for $l = 0$; (D-5)

On the branch cut:

$$Q_l(x) = \frac{1}{2}P_l(x)\ln\frac{1+x}{1-x} - \sum_{q=0}^{Int\left[\frac{1}{2}(l-1)\right]}\frac{(2l-4q-1)}{(2q+1)(l-q)}P_{l-2q-1}(x) \quad \text{for } l \geq 1, \tag{D-6}$$

and $Q_0(x) = \frac{1}{2}\ln\frac{1+x}{1-x}$ for $l = 0$. (D-7)

From these expressions, one can see that the Legendre functions of the second kind exhibit singularities at $z = \pm 1$.

Special values and relationships between Legendre polynomials [28], [29], [40]:

$$P_l(-z) = (-1)^l P_l(z) \tag{D-8}$$

$$P_{-l-1}(z) = P_l(z) \tag{D-9}$$

where both equations are valid on and off the branch cut, i.e., z can be replaced with x; and

$$P_l(0) = \begin{cases} 0 & l \text{ odd}, \\ (-1)^{l/2}\dfrac{1\cdot 3\cdot 5\cdots(l-1)}{2\cdot 4\cdot 6\cdots l} = (-1)^{l/2}\dfrac{(l-1)!!}{l!!} & l \text{ even}; \end{cases} \tag{D-10}$$

$$P_l(1) = 1; \tag{D-11}$$

$$P_l(-1) = \begin{cases} -1 & l \text{ odd}, \\ 1 & l \text{ even}. \end{cases} \tag{D-12}$$

Special values and relationships between Legendre functions of the second kind [28], [40]:

$$Q_l(-z) = (-1)^{l+1} Q_l(z) \tag{D-13}$$

where the equation remains valid on and off the branch cut, i.e., z can be replaced with x; and

$$Q_l(1) = +\infty; \tag{D-14}$$

$$Q_l(-1) = \begin{cases} +\infty & l \text{ odd}, \\ -\infty & l \text{ even}. \end{cases} \tag{D-15}$$

Orthogonality relation [29]:

$$\int_{-1}^{1} P_l(x) P_{l'}(x)\, dx = \frac{2}{2l+1} \delta_{l,l'}. \tag{D-16}$$

Recurrence relations [29], [40]:

$$(2l+1) z P_l(z) = (l+1) P_{l+1}(z) + l\, P_{l-1}(z) \tag{D-17}$$

$$\begin{aligned} (z^2 - 1) \frac{d}{dz} P_l(z) &= (l+1) P_{l+1}(z) - (l+1) z P_l(z) \\ &= l\, z P_l(z) - l P_{l-1}(z) \end{aligned} \tag{D-18}$$

where both recurrence relations are also valid for $Q_l(z)$; in addition, both equations are valid on and off the branch cut, i.e., z can be replaced with x.

Associated Legendre Functions

Associated Legendre's differential equation (where order $m \neq 0$) [29], [40]:

$$\frac{d}{dz'}\left[(1-z'^2)\frac{dy}{dz'}\right]+\left[l(l+1)-\frac{m^2}{1-z'^2}\right]y=0 \quad \text{where } l \text{ and } m \text{ are} \tag{D-19}$$

integers and z' is complex; regular singularities exist at $z'=\pm 1$ and $z'=\infty$.

Definition of domain:

As before, z represents any arbitrary point in the finite complex plane with the exception of those points on the real axis that lie on the $-1<x<1$ branch cut; meanwhile, x represents all points on the branch cut.

Independent solutions of the associated Legendre's differential equation:

Associated Legendre functions of the first kind:

$P_l^m(z)$ (off the branch cut) and $P_l^m(x)$ (on the branch cut)

where $P_l^0(z)=P_l(z)$ and $P_l^0(x)=P_l(x)$ (by definition);

Associated Legendre functions of the second kind:

$Q_l^m(z)$ (off the branch cut) and $Q_l^m(x)$ (on the branch cut)

where $Q_l^0(z)=Q_l(z)$ and $Q_l^0(x)=Q_l(x)$ (by definition).

Definition of associated Legendre functions of the first kind [29], [40], [41]:

Off the branch cut:

$$P_l^m(z) = (z^2-1)^{m/2}\frac{d^m}{dz^m}P_l(z) \qquad \text{(Hobson's definition)}$$

$$= \frac{(z^2-1)^{m/2}}{2^l l!}\frac{d^{m+l}}{dz^{m+l}}(z^2-1)^l; \qquad \text{(D-20)}$$

On the branch cut:

$$P_l^m(x) = (1-x^2)^{m/2}\frac{d^m}{dx^m}P_l(x) \qquad \text{(Ferrer's definition)}$$

$$= \frac{(1-x^2)^{m/2}}{2^l l!}\frac{d^{m+l}}{dx^{m+l}}(x^2-1)^l. \qquad \text{(D-21)}$$

(Note that $P_l^m(x)$ is sometimes alternatively defined with an additional factor of $(-1)^m$. As a consequence, some of the expressions that follow (namely, those that pertain to arguments on the branch cut) may or may not directly apply when using this other definition. However, with some slight modifications, those expressions that are affected by this alternative definition can be made to account for the additional $(-1)^m$ factor.)

Table D.2 Associated Legendre Functions of the First Kind

Off the branch cut	On the branch cut
$P_1^1(z) = (z^2-1)^{1/2}$	$P_1^1(x) = (1-x^2)^{1/2}$
$P_2^1(z) = 3z(z^2-1)^{1/2}$	$P_2^1(x) = 3x(1-x^2)^{1/2}$
$P_2^2(z) = 3(z^2-1)$	$P_2^2(x) = 3(1-x^2)$
$P_3^1(z) = \frac{3}{2}(5z^2-1)(z^2-1)^{1/2}$	$P_3^1(x) = \frac{3}{2}(5x^2-1)(1-x^2)^{1/2}$
$P_3^2(z) = 15z(z^2-1)$	$P_3^2(x) = 15x(1-x^2)$
$P_3^3(z) = 15(z^2-1)^{3/2}$	$P_3^3(x) = 15(1-x^2)^{3/2}$
$P_4^1(z) = \frac{5}{2}(7z^3-3z)(z^2-1)^{1/2}$	$P_4^1(x) = \frac{5}{2}(7x^3-3x)(1-x^2)^{1/2}$
$P_4^2(z) = \frac{15}{2}(7z^2-1)(z^2-1)$	$P_4^2(x) = \frac{15}{2}(7x^2-1)(1-x^2)$
$P_4^3(z) = 105z(z^2-1)^{3/2}$	$P_4^3(x) = 105x(1-x^2)^{3/2}$
$P_4^4(z) = 105(z^2-1)^2$	$P_4^4(x) = 105(1-x^2)^2$

Definition of associated Legendre functions of the second kind [40], [61]:

Off the branch cut:

$$Q_l^m(z) = (z^2-1)^{m/2}\frac{d^m}{dz^m}Q_l(z); \tag{D-22}$$

On the branch cut:

$$Q_l^m(x) = (1-x^2)^{m/2}\frac{d^m}{dx^m}Q_l(x); \tag{D-23}$$

note that the associated Legendre functions of the second kind exhibit singularities at $z = \pm 1$. (Just like $P_l^m(x)$, $Q_l^m(x)$ is sometimes alternatively defined with an additional factor of $(-1)^m$. Likewise, some of the following expressions (namely, those that pertain to arguments on the branch cut) also may or may not directly apply when using this other definition. Nevertheless, those expressions that are affected by this alternative definition can also be made to account for the additional $(-1)^m$ factor).

Special values and relationships between associated Legendre functions [23], [29], [40], [61]:

$$P_l^m(-z) = (-1)^{l-m} P_l^m(z) \tag{D-24}$$

$$Q_l^m(-z) = (-1)^{l+m+1} Q_l^m(z) \tag{D-25}$$

$$P_{-l-1}^m(z) = P_l^m(z) \tag{D-26}$$

where all three equations are valid on and off the branch cut, i.e., z can be replaced with x.

Off the branch cut:

$$P_l^{-m}(z) = \frac{(l-m)!}{(l+m)!} P_l^m(z) \tag{D-27}$$

$$P_m^m(z) = \frac{(2m)!}{2^m m!}(z^2-1)^{m/2} = (2m-1)!!(z^2-1)^{m/2}; \tag{D-28}$$

On the branch cut:

$$P_l^{-m}(x) = (-1)^m \frac{(l-m)!}{(l+m)!} P_l^m(x) \tag{D-29}$$

$$P_m^m(x) = \frac{(2m)!}{2^m m!}(1-x^2)^{m/2} = (2m-1)!!(1-x^2)^{m/2}. \tag{D-30}$$

Additionally,

$$P_l^m(0) = \begin{cases} 0 & (l-m) \text{ odd}, \\ (-1)^{(l-m)/2} \dfrac{(l+m)!}{2^l \left(\dfrac{l-m}{2}\right)! \left(\dfrac{l+m}{2}\right)!} & \\ = (-1)^{(l-m)/2} \dfrac{(l+m-1)!!}{(l-m)!!} & (l-m) \text{ even}; \end{cases} \tag{D-31}$$

$$P_l^m(\pm 1) = 0 \text{ for } m \neq 0. \tag{D-32}$$

Orthogonality relation [29]:

$$\int_{-1}^{1} P_l^m(x) P_{l'}^m(x)\, dx = \frac{2}{2l+1} \frac{(l+m)!}{(l-m)!} \delta_{l,l'}. \tag{D-33}$$

Recurrence relations [29], [35], [40]:

$$(2l+1) z P_l^m(z) = (l-m+1) P_{l+1}^m(z) + (l+m) P_{l-1}^m(z) \tag{D-34}$$

$$\frac{d}{dz} P_l^m(z) = \frac{l z}{z^2-1} P_l^m(z) - \frac{(l+m)}{z^2-1} P_{l-1}^m(z) \tag{D-35}$$

where both recurrence relations are valid on and off the branch cut, i.e., z can be replaced with x.

Off the branch cut:

$$\frac{d}{dz}P_l^m(z) = \frac{(l+m)(l-m+1)}{\sqrt{z^2-1}}P_l^{m-1}(z) - \frac{mz}{z^2-1}P_l^m(z)$$

$$= \frac{P_l^{m+1}(z)}{\sqrt{z^2-1}} + \frac{mz}{z^2-1}P_l^m(z); \tag{D-36}$$

On the branch cut:

$$\frac{d}{dx}P_l^m(x) = -\frac{(l+m)(l-m+1)}{\sqrt{1-x^2}}P_l^{m-1}(x) + \frac{mx}{1-x^2}P_l^m(x)$$

$$= \frac{P_l^{m+1}(x)}{\sqrt{1-x^2}} - \frac{mx}{1-x^2}P_l^m(x). \tag{D-37}$$

Note that all recurrence relations, i.e., (D-34)-(D-37), are also valid for $Q_l^m(z)$ and $Q_l^m(x)$.

Useful Formulas and Definitions

Double factorial notation [29]:

$$(2n)!! = 2\cdot 4\cdot 6\cdots(2n) = 2^n n! \tag{D-38}$$

$$(2n-1)!! = 1\cdot 3\cdot 5\cdots(2n-1) = \frac{(2n)!}{2^n n!}. \tag{D-39}$$

Leibnitz's formula for the n^{th} derivative of a product [29]:

$$\frac{d^n}{dx^n}\left[A(x)B(x)\right] = \sum_{s=0}^{n}\binom{n}{s}\frac{d^{n-s}}{dx^{n-s}}A(x)\frac{d^s}{dx^s}B(x) \tag{D-40}$$

where $\binom{n}{s} = \frac{n!}{s!(n-s)!}$ is a binomial coefficient.

APPENDIX E. DOUBLE- TO SINGLE-SIDED SPHEROIDAL WAVE-HARMONIC IDENTITY

Employing the prolate spheroidal wave-harmonic defined in Chapter 2 (see 2.2.7), we can write the following:

$$\sum_{m=-l}^{+l} \frac{Y_{m,l}(h,\vartheta_1,\varphi_1)Y_{m,l}^{*}(h,\vartheta_2,\varphi_2)}{R_{m,l}^{(4)}(h,\xi)}$$

$$= \sum_{m=-l}^{+l} \left[\frac{S_{m,l}(h,\cos\vartheta_1)}{\sqrt{2\pi N_{m,l}(h)}} e^{+jm\varphi_1} \right] \left[\frac{S_{m,l}(h,\cos\vartheta_2)}{\sqrt{2\pi N_{m,l}(h)}} e^{-jm\varphi_2} \right] \left[R_{m,l}^{(4)}(h,\xi) \right]^{-1}$$

$$= \frac{1}{2\pi} \sum_{m=-l}^{+l} \frac{S_{m,l}(h,\cos\vartheta_1)S_{m,l}(h,\cos\vartheta_2)}{N_{m,l}(h)R_{m,l}^{(4)}(h,\xi)} e^{+jm(\varphi_1-\varphi_2)} . \qquad \text{(E-1)}$$

We now express the right-hand side of (E-1) in terms of non-negative indices of m:

$$\sum_{m=-l}^{+l} \frac{Y_{m,l}(h,\vartheta_1,\varphi_1)Y_{m,l}^{*}(h,\vartheta_2,\varphi_2)}{R_{m,l}^{(4)}(h,\xi)}$$

$$= \frac{1}{2\pi} \frac{S_{0,l}(h,\cos\vartheta_1)S_{0,l}(h,\cos\vartheta_2)}{N_{0,l}(h)R_{0,l}^{(4)}(h,\xi)} + \frac{1}{2\pi} \sum_{m=1}^{+l} \left[\begin{array}{l} \dfrac{S_{m,l}(h,\cos\vartheta_1)S_{m,l}(h,\cos\vartheta_2)}{N_{m,l}(h)R_{m,l}^{(4)}(h,\xi)} e^{+jm(\varphi_1-\varphi_2)} \\ + \dfrac{S_{-m,l}(h,\cos\vartheta_1)S_{-m,l}(h,\cos\vartheta_2)}{N_{-m,l}(h)R_{-m,l}^{(4)}(h,\xi)} e^{-jm(\varphi_1-\varphi_2)} \end{array} \right]. \qquad \text{(E-2)}$$

By definition (see Chapter 2), $S_{-m,l}(h,\cos\vartheta) \equiv S_{m,l}(h,\cos\vartheta)$, $R_{-m,l}^{(4)}(h,\xi) \equiv R_{m,l}^{(4)}(h,\xi)$, and $N_{-m,l}(h) \equiv N_{m,l}(h)$. Accordingly, we are able to simplify (E-2) and thus put forth the

following double- to single-sided spheroidal wave-harmonic identity for the prolate spheroidal case:

$$\sum_{m=-l}^{+l} \frac{Y_{m,l}(h,\vartheta_1,\varphi_1)Y_{m,l}^{*}(h,\vartheta_2,\varphi_2)}{R_{m,l}^{(4)}(h,\xi)}$$

$$= \frac{1}{2\pi}\left[\begin{array}{l} \dfrac{S_{0,l}(h,\cos\vartheta_1)S_{0,l}(h,\cos\vartheta_2)}{N_{0,l}(h)R_{0,l}^{(4)}(h,\xi)} \\ \quad + 2\displaystyle\sum_{m=1}^{l} \frac{S_{m,l}(h,\cos\vartheta_1)S_{m,l}(h,\cos\vartheta_2)}{N_{m,l}(h)R_{m,l}^{(4)}(h,\xi)}\cos m(\varphi_1-\varphi_2) \end{array}\right]. \quad \text{(E-3)}$$

In a manner that is quite similar, one can show that the form of (E-3) is also valid for oblate spheroidal wave-harmonics.

REFERENCES

[1] R. C. Johnson, H. A. Ecker, and J. S. Hollis, "Determination of far-field antenna patterns from near-field measurements," *Proc. IEEE*, vol. 61, pp. 1668-1694, Dec. 1973.

[2] A. D. Yaghjian, "An overview of near-field antenna measurements," *IEEE Trans. Antennas Propagat.*, vol. AP-34, pp. 30-45, Jan. 1986.

[3] J. H. Richmond and T. E. Tice, "Probes for microwave near-field measurements," *IRE Trans. Microwave Theory Tech.*, vol. MTT-3, pp. 32-34, Apr. 1955.

[4] J. H. Richmond, "Simplified calculation of antenna patterns with application to radome problems," *IRE Trans. Microwave Theory Tech.*, vol. MTT-3, pp. 9-12, July 1955.

[5] D. M. Kerns, "Analytical techniques for the correction of near-field antenna measurements made with an arbitrary but known measuring antenna," *URSI-IRE Mtg. Abstracts*, Washington, D.C., Apr. 1963, pp. 6-7.

[6] Y. Rahmat-Samii, V. Galindo-Israel, and R. Mittra, "A plane-polar approach for far-field construction from near-field measurements," *IEEE Trans. Antennas Propagat.*, vol. AP-28, pp. 216-230, Mar. 1980.

[7] L. I. Williams and Y. Rahmat-Samii, "Novel bi-polar planar near-field measurement scanner at UCLA," *IEEE Antennas Propagat. Soc. Int. Symp. Dig.*, London, Ontario, Canada, June 1991, pp. 1446-1449.

[8] J. Brown and E. V. Jull, "The prediction of aerial radiation patterns from near-field measurements," *Proc. Inst. Elect. Eng.*, vol. 108B, pp. 635-644, Nov. 1961.

[9] W. M. Leach and D. T. Paris, "Probe compensated near-field measurements on a cylinder," *IEEE Trans. Antennas Propagat.*, vol. AP-21, pp. 435-445, July 1973.

[10] F. Jensen, "Electromagnetic near-field-far-field correlations," Ph.D. dissertation, Technical University of Denmark, Lyngby, Denmark, July 1970.

[11] J. R. James and L. W. Longdon, "Prediction of arbitrary electromagnetic fields from measured data," *Alta. Freq.*, vol. 38 (special issue), pp. 286-290, May 1969.

[12] R. C. Baird, A. C. Newell, and C. F. Stubenrauch, “A brief history of near-field measurements of antennas at the National Bureau of Standards,” *IEEE Trans. Antennas Propagat.*, vol. AP-36, pp. 727-733, June 1988.

[13] E. B. Joy, “A brief history of the development of the near-field measurement technique at the Georgia Institute of Technology,” *IEEE Trans. Antennas Propagat.*, vol. AP-36, pp. 740-745, June 1988.

[14] J. E. Hansen and F. Jensen, “Spherical near-field scanning at the Technical University of Denmark,” *IEEE Trans. Antennas Propagat.*, vol. AP-36, pp. 734-739, June 1988.

[15] Y. Rahmat-Samii, L. I. Williams, and R. G. Yaccarino, “The UCLA bi-polar planar-near-field antenna-measurement and diagnostics range,” *IEEE Antennas Propagat. Mag.*, vol. 37, pp. 16-35, Dec. 1995.

[16] A. C. Ludwig, “Near-field far-field transformations using spherical-wave expansions,” *IEEE Trans. Antennas Propagat.*, vol. AP-19, pp. 214-220, Mar. 1971.

[17] J. J. Lee, E. M. Ferren, D. P. Woollen, and K. M. Lee, “Near-field probe used as a diagnostic tool to locate defective elements in an array antenna,” *IEEE Trans. Antennas Propagat.*, vol. AP-36, pp. 884-889, June 1988.

[18] Y. Rahmat-Samii and J. Lemanczyk, “Application of spherical near-field measurements to microwave holographic diagnosis of antennas,” *IEEE Trans. Antennas Propagat.*, vol. AP-36, pp. 869-878, June 1988.

[19] K. R. Umashankar and A. Taflove, “A novel method to analyze electromagnetic scattering of complex objects,” *IEEE Trans. Electromagn. Compat.*, vol. EMC-24, pp. 397-405, Nov. 1982.

[20] A. Taflove and K. R. Umashankar, “Radar cross section of general three-dimensional scatterers,” *IEEE Trans. Electromagn. Compat.*, vol. EMC-25, pp. 433-440, Nov. 1983.

[21] R. J. Luebbers, K. S. Kunz, M. Schneider, and F. Hunsberger, “A finite-difference time-domain near zone to far zone transformation,” *IEEE Trans. Antennas Propagat.*, vol. AP-39, pp. 429-433, Apr. 1991.

[22] P. M. Morse and H. Feshbach, *Methods of Theoretical Physics*. New York: McGraw-Hill, 1953.

[23] C. Flammer, *Spheroidal Wave Functions*. Stanford: Stanford University Press, 1957.

[24] C. T. Tai, *Generalized Vector and Dyadic Analysis: Applied Mathematics in Field Theory*. New York: IEEE Press, 1991.

[25] M. Abramowitz and I. A. Stegun (Eds.), *Handbook of Mathematical Functions with Formulas, Graphs, and Mathematical Tables,* Applied Mathematical Series-55 *(AMS-55)*, National Bureau of Standards. Washington, D.C.: U.S. Government Printing Office, 1964.

[26] W. L. Stutzman and G. A. Thiele, *Antenna Theory and Design*. New York: Wiley, 1981.

[27] C. A. Balanis, *Antenna Theory: Analysis and Design*. New York: Harper and Row, 1982.

[28] C. A. Balanis, *Advanced Engineering Electromagnetics*. New York: Wiley, 1989.

[29] G. Arfken, *Mathematical Methods for Physicists*, Third Edition. Orlando: Academic Press, 1985.

[30] W. E. Boyce and R. C. DiPrima, *Elementary Differential Equations and Boundary Value Problems*, Third Edition. New York: Wiley, 1977.

[31] H. Sagan, *Boundary and Eigenvalue Problems in Mathematical Physics*. New York: Dover, 1989.

[32] S. Hanish and B. King, "Tables of eigenvalues of the wave equation in prolate spheroidal coordinates," *Naval Research Laboratory Report FR-6856,* Apr. 1969.

[33] L. B. Felsen and N. Marcuvitz, *Radiation and Scattering of Waves*. New York: IEEE Press, 1994.

[34] B. J. King and L. Van Buren, "A Fortran computer program for calculating the prolate and oblate angle functions of the first kind and their first and second derivatives," *Naval Research Laboratory Report FR-7161*, Nov. 1970.

[35] B. J. King, R. V. Baier, and S. Hanish, "A Fortran computer program for calculating the prolate spheroidal radial functions of the first and second kind and their first derivatives," *Naval Research Laboratory Formal Report 7012*, Mar. 1970.

[36] A. L. Van Buren, R. V. Baier, and S. Hanish, "A Fortran computer program for calculating the oblate spheroidal radial functions of the first and second kind and their first derivatives," *Naval Research Laboratory Report 6959*, Jan. 1970.

[37] W. H. Press, S. A. Teukolsky, W. T. Vetterling, and B. P. Flannery, *Numerical Recipes in FORTRAN: The Art of Scientific Computing*, Second Edition. New York: Cambridge University Press, 1992.

[38] C. J. Bouwkamp, "Theoretische en numerieke behandeling van de buiging door een ronde opening," Diss. Groningen, Groningen-Batavia, 1941; also *J. Math. Phys.*, vol. 26, 1947.

[39] G. Blanch, "On the computation of Mathieu functions," *J. Math. Phys.*, vol. 25, pp. 1-20, 1946.

[40] A. Erdelyi, W. Magnus, F. Oberhettinger, and F. G. Tricomi, *Higher Transcendental Functions*, vol. 1, Bateman Manuscript Project, California Institute of Technology. New York: McGraw-Hill, 1953.

[41] "Tables of associated Legendre functions," Mathematical Tables Project (*MTP-1945*), National Bureau of Standards. New York: Columbia University Press, 1945.

[42] M. J. Maron, *Numerical Analysis: A Practical Approach*. New York: Macmillan, 1982.

[43] J. C. Strikwerda, *Finite Difference Schemes and Partial Differential Equations*. New York: Chapman and Hall, 1989.

[44] K. W. Morton and D. F. Mayers, *Numerical Solution of Partial Differential Equations*. New York: Cambridge University Press, 1994.

[45] K. S. Kunz and R. J. Luebbers, *The Finite Difference Time Domain Method for Electromagnetics.* Boca Raton: CRC Press, 1993.

[46] A. Taflove, *Computational Electrodynamics: The Finite-Difference Time-Domain Method*. Boston: Artech House, 1995.

[47] K. L. Shlager and J. B. Schneider, "A selective survey of the finite-difference time-domain literature," *IEEE Antennas Propagat. Mag.*, vol. 37, pp. 39-57, Aug. 1995.

[48] K. S. Yee, "Numerical solution of initial boundary value problems involving Maxwell's equations in isotropic media," *IEEE Trans. Antennas Propagat.*, vol. AP-14, pp. 302-307, May 1966.

[49] G. Mur, "Absorbing boundary conditions for the finite-difference approximation of the time-domain electromagnetic-field equations," *IEEE Trans. Electromagn. Compat.*, vol. EMC-23, pp. 377-382, Nov. 1981.

[50] B. Engquist and A. Majda, "Absorbing boundary conditions for the numerical simulation of waves," *Math. Comp.*, vol. 31, pp. 629-651, July 1977.

[51] A. Taflove and M. E. Brodwin, "Numerical solution of steady-state electromagnetic scattering problems using the time-dependent Maxwell's equations," *IEEE Trans. Microwave Theory Tech.*, vol. MTT-23, pp. 623-630, Aug. 1975.

[52] R. E. Ziemer, W. H. Tranter, and D. R. Fannin, *Signals and Systems: Continuous and Discrete*. New York: Macmillan, 1983.

[53] F. J. Harris, "On the use of windows for harmonic analysis with the discrete Fourier transform," *Proc. IEEE,* vol. 66, pp. 51-83, Jan. 1978.

[54] *RT/duroid 5870 Specification Sheet*, Rogers Corporation, Chandler, Arizona, Apr. 1993.

[55] E. A. Wolff and R. Kaul, *Microwave Engineering and Systems Applications.* New York: Wiley, 1988.

[56] P. Bhartia, K. V. S. Rao, and R. S. Tomar, *Millimeter-Wave Microstrip and Printed Circuit Antennas.* Boston: Artech House, 1991.

[57] R. E. Collin, *Foundations for Microwave Engineering.* New York: McGraw-Hill, 1966.

[58] H. S. Tsai and R. A. York, "FDTD analysis of CPW-fed folded-slot and multiple-slot antennas on thin substrates," *IEEE Trans. Antennas Propagat.*, vol. AP-44, pp. 217-226, Feb. 1996.

[59] G. C. Liang, Y. W. Liu, and K. K. Mei, "Full-wave analysis of coplanar waveguide and slotline using the time-domain finite-difference method," *IEEE Trans. Microwave Theory Tech.*, vol. MTT-37, pp. 1949-1957, Dec. 1989.

[60] M. R. Spiegel, *Vector Analysis and an Introduction to Tensor Analysis*, Schaum's Outline Series. New York: McGraw-Hill, 1959.

[61] E. Jahnke and F. Emde, *Tables of Functions with Formulae and Curves*, Fourth Edition. New York: Dover, 1945.

VITA

Gerald F. Ricciardi was born in Bronx, NY, in 1965. He received the B.S. degree in electrical engineering from Columbia University, New York, NY, in 1987, and the M.S. degree in electrical engineering from the Johns Hopkins University, Baltimore, MD, in 1991. From 1987 to 1992, he worked for Westinghouse Electric Corporation, Baltimore, MD, where he developed algorithms used in the testing of prototype defense missile systems. In August 1992, he came to Virginia Tech to pursue the Ph.D. degree in electrical engineering.

Gerald Ricciardi is a member of IEEE. His current research interests are in the areas of computational electromagnetics, numerical analysis, and antenna design.